Multi-distance and multi-frequency frequency-domain near-infrared spectroscopy - characterization and application

Abstract

Near-infrared spectroscopy and imaging are non-invasive optical methods, which measure various parameters such as the absorption and scattering coefficient of tissue and the concentration of oxy and deoxyhemoglobin, water and fat. Near-infrared spectroscopy and imaging offer the possibility to non-invasively measure hemodynamic responses of the brain to external stimuli. The ability of near-infrared spectroscopy and imaging to measure all these parameters makes this a promising technique for a broad field of applications. In the context of this thesis, two projects were carried out: i) assessing potential effects of UMTS electromagnetic fields on blood circulation in the human head and ii) monitoring structural and compositional changes of the human cervix in regular pregnancies.

DISS. ETH NO. 19006

Multi-Distance and Multi-Frequency Frequency-Domain Near-Infrared Spectroscopy: Characterization and Application

A dissertation submitted to
Swiss Federal Institute of Technology Zurich
for the degree of

Doctor of Sciences

presented by
SONJA SPICHTIG
Diploma in Natural Sciences, Swiss Federal Institute of Technology Zurich, 2006
born on the 1st of October, 1982
citizen of Sachseln OW

accepted on the recommendation of

Prof. Markus Rudin, examiner
PD Martin Wolf, co-examiner
Prof. Peter Achermann, co-examiner

2010

Table of contents

List of figures

List of tables

List of abbreviations

μ_s'	reduced scattering coefficient
μ_a	absorption coefficient
[HHb]	deoxyhemoglobin concentration
[O_2Hb]	oxyhemoglobin concentration
[tHb]	total hemoglobin concentration
APD	avalanche photo diodes
BOLD	blood oxygen level-dependent
BORL	Biomedical Optics Research Laboratory
CBF	cerebral blood flow
CBSI	correlation-based signal improvement
CBV	cerebral blood volume
$CMRO_2$	cerebral metabolic rate of oxygen
CW	continuous wave
dll	dynamic linked library
DOI	diffuse optical imaging
DPF	differential path length factor
ECG	electrocardiography
EEG	electroencephalography
EMF	electromagnetic field
EP	exploratory study
FD	frequency-domain
FFN	fetal fibronectin
FFT	fast fourier transform
fMRI	functional magnetic resonance imaging
fNIRS	functional near infrared spectroscopy
GSM	Global System for Mobile Communications
H_2O	water
HHb	deoxyhemoglobin
HR	heart rate
ICA	independent component analysis
MARA	movement artifact reduction algorithm
MDL	minimum description length
MRI	magnetic resonance imaging
MSD	moving standard deviation
NIRI	near infrared imaging
NIRS	near-infrared spectroscopy

O_2Hb	oxyhemoglobin
PET	positron emission tomography
PMI	photon migration imaging software
PMT	photomultiplier tube
rCBF	regional cerebral blood flow
RF-EMF	radio frequency electromagnetic fields
RTE	radiative transfer equation
SD	standard deviation
SIRT	simultaneous iterative reconstruction technique
SP	scatter power
SRS	spatially resolved spectroscopy
StO_2	tissue oxygen saturation
$tcPO_2$	transcutaneous partial pressure of oxygen
TD	time domain
tHb	total hemoglobin
TPSF	temporal point spread function
UMTS	Universal Mobile Telecommunication System

Summary

Near-infrared spectroscopy and imaging are non-invasive optical methods, which measure various parameters such as the absorption and scattering coefficient of tissue and the concentration of oxy and deoxyhemoglobin, water and fat. Near-infrared spectroscopy and imaging offer the possibility to non-invasively measure hemodynamic responses of the brain to external stimuli. The ability of near-infrared spectroscopy and imaging to measure all these parameters makes this a promising technique for a broad field of applications. In the context of this thesis, two projects were carried out: i) assessing potential effects of UMTS electromagnetic fields on blood circulation in the human head and ii) monitoring structural and compositional changes of the human cervix in regular pregnancies.

Potential effects of electromagnetic fields on blood circulation in the human head

The *UMTS exposure study* is motivated by the highly increasing number of mobile phone users worldwide and the lack of studies investigating effects of the new telecommunication standard UMTS. Until today, most human exposure studies applied a continuous exposure either due to low time resolution of the measurement method (e.g. positron emission tomography) or due to electromagnetic interference between electromagnetic fields and the measurement technique (e.g. in electroencephalography). Near-infrared imaging is the only measurement method suitable to investigate immediate short-term effects of intermittent electromagnetic fields. The potential immediate effects of UMTS electromagnetic fields on blood circulation have not yet been investigated either.
The *UMTS exposure study* was carried out with the ISS Oxiplex® (ISS Inc., Champaign, Illinois, USA). The commercially available instrument had to be modified to suit the study requirements. The commercial configuration of the instrument was enhanced by an additional mode, which quadrupled the number of source-detector combinations. The additional functionality was achieved by modifying the FPGA, uClinux and controller software and can be enabled for a measurement by flipping a dip-switch at the back of the instrument. A novel optical sensor was constructed to make use of all newly available sources and detectors. No active parts were integrated in the sensor to prevent interference between the electromagnetic fields and the near infrared imaging instrument. This sensor was built with 10 m optical cables in order to place the instrument itself outside of a sensitive area, e.g. an electromagnetic fields exposure chamber. In principle, the novel optical sensor could also be used in a magnetic resonance scanner. However, initial test measurements showed that iron particles are present within the color used to dye the sil-

icone elastomer shell of the sensor, resulting in huge artifacts in the magnetic resonance images.

The optical sensor was further developed in an additional side project, which was not within the scope of the UMTS exposure study. This optical sensor was successfully constructed with a different dye to enable simultaneous measurements with near-infrared imaging and magnetic resonance imaging. The novel optical sensor provides potential for a wide range of multi-modal applications to benefit both modalities.

The increased number of source-detector combinations of the novel sensors makes it possible to obtain horizontal and depth resolution. This ability was characterized by simulations, which showed that a good resolution in the horizontal plane can be obtained, whereas the depth resolution is quite non-linear over the volume probed. Therefore, different methods were used to test the ability of the novel sensors in discriminating between superficial and deep changes. This discrimination is very important for exposure studies, since the skin receives the highest electromagnetic field dose, but effects on the cerebral blood flow have also been reported in the literature. The modified Lambert-Beer law has proven to be the most reliable method to distinguish between superficial and deep changes in phantom and in-vivo measurements and was thus used for data analysis of the UMTS exposure study.

The UMTS exposure system was designed by Swisscom (Switzerland) Ltd. (Innovation Competence Centre, Environment & Electromagnetic Compatibility, 3050 Bern, Switzerland) to generate four different UMTS signal types having the same carrier frequency with three different exposure levels (0.0 W/kg (sham), 0.18 W/kg and 1.8 W/kg). These signals were applied at two exposure positions in a single-blind exploratory study on eight subjects, which investigated the potential effect of intermittent exposure (maximum peak SAR-value of 1.8 W/kg) on blood circulation. No significant short-term (shorter than 80 s) effects were found for any signal type or exposure position. Thus, the signal type *downlink* and exposure position *T3* were applied in the main study as this was the configuration which showed the strongest (yet not significant) change in the measurables due to electromagnetic fields. In the main study, 16 subjects were enrolled to investigate potential short and medium-term (from 80 s to 30 minutes) effects of intermittent UMTS electromagnetic fields. In the main study, small significant short-term effects on oxy and total hemoglobin concentrations for the low dose (0.18 W/kg) were found, as well as medium-term effects on deoxyhemoglobin concentration for the low and high dose (1.8 W/kg) and medium-term effects on the heart rate for the high dose. The effects were very small, but indicate that there may be an effect of intermittent UMTS electromagnetic field exposure, which justifies affording intermittent electromagnetic field exposure more scientific attention in the future.

Monitoring of structural and compositional changes of the uterine cervix

During pregnancy, the consistency of the uterine cervix changes to meet the changing requirements: i) during pregnancy it has to be ductile to ensure physical stability, protection against infections and to prevent preterm delivery and ii) towards the end of the pregnancy it has to become soft, to dilate and enable delivery. At present, there is no method reliable enough to predict cervical ripening and thus preterm labor over a broad population of patients. Near-infrared spectroscopy is able to measure changes in blood perfusion and tissue structure and thus it should be possible to assess structural and compositional changes during pregnancy. Near-infrared spectroscopy has the potential to become a more accurate method to predict preterm birth than any available today.

To measure a small tissue structure, such as the cervix, the multi-distance measurement instrument ISS Imagent® (ISS Inc., Champaign, Illinois, USA) had to be converted in a multi-frequency instrument with a single source-detector distance. The spectral range of the instrument was enhanced to measure water and lipid in addition to hemoglobin. Validation measurements were performed which showed that the modified instrument can determine reliable and accurate measures for total hemoglobin and water concentration, however not for lipid.

13 pregnant women were enrolled in the cervix study. Near-infrared spectroscopy measurements were carried out during their routine clinical examinations. Due to movement artifacts in the near-infrared spectroscopy data, the analysis software had to be improved to make it more robust. The measurement values obtained were analyzed in terms of their correlation to the weeks of gestation.

A significant increase in oxy and total hemoglobin was found between the second and the third trimester, which may be explained by the large increase in uterine perfusion that guarantees a sufficient supply for the growing fetus. No significant changes were observed for tissue oxygen saturation, deoxyhemoglobin and water concentration. The scatter power decreased significantly between the first and second trimester, which indicates an increase in the size of scatter particles. This may be explained by an increasing size and number of cervical cells and the consolidation and alignment of collagen.

Although, strong movement artifacts were present in near-infrared spectroscopy data, we have shown that structural and compositional changes in the uterine cervix during a normal pregnancy are reflected in changes of the optical signal.

Zusammenfassung

Nahinfrarot Spektroskopie ist eine nicht invasive, optische Methode, die mittels der Messung verschiedener Parameter wie z.B. der Absorptions- und Streukoeffizienten, die Konzentrationen von Oxy- und Deoxyhemoglobin, Wasser und Fett im Gewebe bestimmt. Nahinfrarot Spektroskopie ermöglicht auch die nicht invasive Messung hämodynamischer Antworten des Gehirns auf externe Stimuli. Die Möglichkeit all diese Parameter zu messen, macht Nahinrarot Spektroskopie zu einer vielversprechenden Messmethode mit einer Vielzahl möglicher Anwendungen. Werden mehrere Lichtquellen und Detektoren räumlich verteilt auf dem Gewebe angeordnet, wird auch von optischer Bildgebung gesprochen.

Im Rahmen dieser Doktorarbeit wurden zwei Projekte durchgeführt: i) die Untersuchung möglicher Effekte von UMTS elektromagnetischer Felder auf die Blutzirkulation im menschlichen Kopf und ii) die Messung von Veränderungen der Struktur und Zusammensetzung des Gebärmuttermundes über einen normalen Schwangerschaftsverlauf.

Mögliche Effekte von elektromagnetischen Feldern auf die Blutzirkulation des menschlichen Kopfes

Die *UMTS Expositionsstudie* ist motiviert durch die weltweit rasch ansteigende Zahl von Mobiltelefon-Nutzern und den Mangel an Studien, welche Effekte des neuen Telekommunikationsstandards UMTS untersucht haben. In der Vergangenheit wurden die meisten Expositionsstudien aufgrund der tiefen Zeitauflösung (z.B. für Positronen-Emissions-Tomographie) oder wegen auftretenden Interferenzen zwischen den elektromagnetischen Feldern und der Messmethode (z.B. für Elektroencephalographie) mit einer kontinuierlichen Befeldung durchgeführt. Optische Bildgebung ist die einzige Messmethode welche geeignet ist, unmittelbare kurzfristige Effekte von intermittierenden elektromagnetischen Feldern zu detektieren. Bis heute wurden mögliche unmittelbare Effekte von UMTS Feldern auf die Blutzirkulation noch nicht untersucht.

Die *UMTS Expositionsstudie* wurde mit dem ISS Oxiplex® (ISS Inc., Champaign, Illinois, USA) durchgeführt. Dieses kommerziell erhältliche Messinstrument musste modifiziert werden, um den Anforderungen der Studie gerecht zu werden. Das Messgerät wurde mit einem zusätzlichen Modus erweitert, welcher die Anzahl der Kombinationen von Lichtquellen und Detektoren vervierfachte. Die Funktionalitätserweiterung wurde mittels Modifizierung des FPGA, uClinux und der Kontrollsoftware erreicht und kann durch Betätigen des Kippschalters an der Rückseite des Gerätes aktiviert werden. Um alle zur Verfügung stehenden Lichtquellen und Detektoren nutzen zu können, wurde ein neuer optischer Sensor hergestellt. In den Sensor wurden keine aktiven Bauteile integriert, um Interferenzen zwischen den elektromagnetischen Feldern und dem optischen Messgerät zu verhindern. Der Sensor wurde mit 10 m langen Glasfaserkabeln hergestellt, damit das Messgerät ausserhalb eines empfindlichen Bereichs, in diesem Fall der Expositionskammer, platziert werden kann. Im Prinzip kann der neue optische Sensor auch im Magnetresonanz-Tomographen benutzt werden. Erste Testmessungen zeigten jedoch, dass die Farbe, welche benutzt wurde um die Silikonhülle einzufärben, Eisenpartikel enthält und deshalb zu starken Artefakten in den Magnetresonanz-Bildern führt.

Deshalb wurde der optische Sensor in einem Nebenprojekt, welches nicht im Rahmen der UMTS Expositionsstudie durchgeführt wurde, weiterentwickelt. Der optische Sensor wurde erfolgreich mit einem anderen Farbstoff hergestellt, um simultane Messungen mit optischer Bildgebung und Magnetresonanz-Tomographie zu ermöglichen, wovon beide Methoden profitieren können.

Dank der erhöhten Anzahl von Lichtquellen und Detektoren ist es mit dem neuen Sensor möglich Horizontal- und Tiefenauflösung zu erhalten. Diese Fähigkeit wurde anhand von Simulationen charakterisiert, welche gezeigt haben, dass zwar eine gute Horizontalauflösung erreicht werden kann, die Tiefenauflösung aber über das gemessene Volumen nicht-linear ist. Deshalb wurden verschiedene Methoden benutzt, um die Fähigkeit des neuen Sensors zu testen zwischen oberflächlichen und tiefen Veränderungen zu unterscheiden. Diese Unterscheidung ist wichtig für Expositionsstudien, weil zwar die Haut die höchste Dosis der elektromagnetischen Felder erhält, in der Literatur aber Effekte auf den cerebralen Blutfluss dokumentiert sind. Es hat sich gezeigt, dass das modifizierte Lambert-Beer Gesetz die zuverlässigste Methode ist, um zwischen oberflächlichen and tiefen Veränderungen in Phantom- und In-vivo-Messungen zu unterscheiden. Deshalb wurde es für die Datenanalyse der UMTS Expositionsstudie verwendet.

Das UMTS Expositionssystem wurde von der Swisscom (Switzerland) Ltd. (Innovation Competence Centre, Environment & Electromagnetic Compatibility, 3050 Bern, Switzerland) entwickelt, um vier verschiedene UMTS Signale mit der gleichen Trägerfrequenz und drei verschiedenen Expositionsdosen (0.0 W/kg (sham), 0.18 W/kg and 1.8 W/kg) zu generieren. Die verschiedenen UMTS Signale wurden an zwei Expositionspositionen am Kopf emittiert, um mögliche Effekte intermittierender Exposition (maximaler SAR-Spitzenwert von 1.8 W/kg) auf die Blutzirkulation zu untersuchen. Dazu wurde eine einfach-blinde Studie an acht Probanden durchgeführt. Es wurde für keine Kombination von UMTS Signalen und Expostionspositionen signifikante kurzfristige (kürzer als 80 s) Effekte gefunden. Für die Hauptstudie wurde der Signaltyp *downlink* und die Expositionsposition *T3* ausgewählt, da diese Kombination die stärksten (aber nicht signifikanten) Änderungen in den Messgrössen aufgrund der elektromagnetischen Feldern aufzeigte. In die Hauptstudie wurden 16 Probanden eingeschlossen, um mögliche kurzfristige und mittelfristige (innerhalb von 80 s bis 30 min) Effekte von intermittierenden UMTS elektromagnetischen Feldern zu untersuchen. In der Hauptstudie wurden kleine signifikante kurzfristige Konzentrationsänderungen in Oxyhämoglobin und totalem Hämoglobin für die tiefe Dosis (0.18 W/kg), mittlfristige Konzentrationsänderungen in Deoxyhämoglobin für die tiefe und hohe Dosis (1.8 W/kg) und mittelfristige Veränderungen in der Herzrate für die hohe Dosis festgestellt. Die gemessenen Effekte waren sehr klein, aber deuten darauf hin, das Effekte aufgrund einer Exposition mit intermittierenden UMTS elektromagnetischen Felder auftreten können. Dies rechtfertigt auch, dass intermittierende elektromagnetische Felder in der Zukunft mehr wissenschaftliche Aufmerksamkeit erhalten sollten.

Messung von Veränderungen in der Struktur und Zusammensetzung des Gebärmuttermundes über einen normalen Schwangerschaftsverlauf

Während der Schwangerschaft verändert sich die Konsistenz vom Gebärmutterhals, um sich den veränderten Anforderungen anzupassen: i) Während der Schwangerschaft muss er duktil sein, um die physikalische Stabilität und den Schutz vor Infektionen zu garantieren und um einer Frühgeburt vorzubeugen und ii) gegen Ende der Schwangerschaft muss das Gewebe nachgiebiger sein, um sich erweitern zu können und die Geburt zu ermöglichen. Momentan existiert keine Methode, welche zuverlässig genug ist, um eine Muttermundsreifung und somit eine Frühgeburt über eine breite Patientenpopulation vorherzusagen. Nahinfrarot-Spektroskopie kann Veränderungen in der Durchblutung und Gewebestruktur messen und es sollte somit möglich sein die Veränderungen in der Struktur und Zusammensetzung des Gebärmutterhalses über den Schwangerschaftsverlauf zu messen. Nahinfrarot-Spektroskopie hat das Potential Frühgeburten genauer vorherzusagen, als die momentan vorhandenen Methoden.

Um ein so kleines Gewebevolumen wie den Gebärmutterhals messen zu können, musste das Multi-Distanz Messgerät ISS Imagent® (ISS Inc., Champaign, Illinois, USA), in ein Multi-Frequenz Gerät mit einer einzigen Lichtquellen-Detektor Kombination umgebaut werden. Der spektrale Messbereich vom Gerät wurde erhöht, um zusätzlich zum Hämoglobin noch Wasser und Fett zu messen. Durchgeführte Validierungsmessungen haben gezeigt, dass das modifizierte Messgerät zuverlässig und genau die Konzentrationen von totalem Hämoglobin und Wasser messen kann, aber nicht die von Fett.

In die Cervix Studie wurden 13 schwangere Frauen eingeschlossen. Die Messungen mit Nahinfrarot Spektroskopie wurden während den klinischen Routineuntersuchungen durchgeführt. Aufgrund von Bewegungsartefakten in den Messdaten musste die Analysesoftware verbessert werden, um robuster gegenüber Artefakten zu sein. Die erhaltenen Messwerte wurden hinsichtlich ihrer Korrelation zu der Schwangerschaftswoche analysiert.

Es wurde ein signifikanter Anstieg im Oxy- und totalem Hämoglobin zwischen dem zweiten und dritten Trimester gefunden. Dies kann durch den starken Anstieg der Durchblutung in der Gebärmutter erklärt werden, welche eine genügende Versorgung vom Fötus garantieren muss. Für die Gewebesättigung, Deoxyhämoglobin und Wasserkonzentration wurden keine signifikanten Veränderungen beobachtet. Die *Scatter power* nahm signifikant zwischen dem ersten und zweiten Trimestern ab und deutet auf eine Grössenzunahme der Streupartikel hin. Dies kann durch eine zunehmende Grösse und Anzahl von Gebärmutterhalszellen und durch die Verdichtung und Ausrichtung von Kollagen erklärt werden.

Obwohl ausgeprägte Bewegungsartefakte in den Messdaten vorhanden waren, konnte gezeigt werden, dass sich die Veränderungen in der Struktur und Zusammensetzung des Gebärmuttermundes über einen normalen Schwangerschaftsverlauf in den Änderungen der optischen Signal niederschlägt.

Introduction

Near-infrared spectroscopy (NIRS) is a non-invasive optical method, which measures the concentration of optical absorbers in biological tissue (Jöbsis 1977). Within the near-infrared spectral range (650 – 950 nm), sometimes called "optical window", biological tissue is relatively transparent for light, which allows the detection of concentration changes in absorbers. The main absorbers are oxy and deoxyhemoglobin (O_2Hb and HHb), where O_2Hb is the hemoglobin state carrying oxygen and it is responsible for the oxygen transport in the blood to the cells. HHb is the deoxygenated hemoglobin state and changes in HHb can be correlated to the amount of oxygen consumed. Using two wavelengths, one below 700 nm and one higher or equal to 830 nm, the two hemoglobin species can be separated. From the sum of [O_2Hb] and [HHb], total hemoglobin ([tHb]) can be obtained and the tissue oxygen saturation (StO_2) is given by the fraction of [O_2Hb] to [tHb]. Spectra of O_2Hb and HHb are shown in Fig. 0.1 on the left side (multiplying the extinction coefficient given in the figure by the factor ln(10) results in the absorption coefficient).
In addition to [O_2Hb] and [HHb], the concentration of fat and water can be measured when two additional wavelengths, one around 920 nm (absorption peak of fat) and one around 970 nm (absorption peak of water), are incorporated in the measurement system. Spectra of water and fat are shown in Fig. 0.1 on the right side.

When doing NIRS measurements, near-infrared light is emitted into biological tissue and undergoes absorption and scattering. In the reflection mode, the light which is scattered back to the surface is measured at the detector, whereas in the transmission mode, the light transmitted through the tissue is measured. For large tissue thicknesses, transmitted light cannot be detected due to high absorption and thus the transmission mode is not practical for measurement on larger tissue structures, such as the brain.
When a NIRS sensor employs multiple, spatially distributed light sources and detectors, the term near-infrared imaging (NIRI) or diffuse optical imaging (DOI) is used. By that, it is then possible to reconstruct images of spatially resolved changes in [O_2Hb], [HHb], [tHb] and oxygenation (Gibson and Dehghani 2009). DOI or NIRI are mainly used for imaging of brain functions (Wolf et al. 2008) or breast cancer (Leff et al. 2008). If the time is also considered, which is of interest to visualize brain activity, spatiotemporal movies of the changes can be reconstructed. The spatial resolution of NIRI is not better than 0.5 to 1 cm^3, whereas the temporal resolution can be as high as a few ms.
Different NIRS techniques and sensors exist and the methodology is chosen depending on the desired application. These NIRS techniques are: continuous wave (CW), frequency-domain (FD) and time-domain (TD) (Tuchin 2000). In CW systems, light with a constant intensity I_0 is emitted into the tissue and from the attenuated detected intensity the change

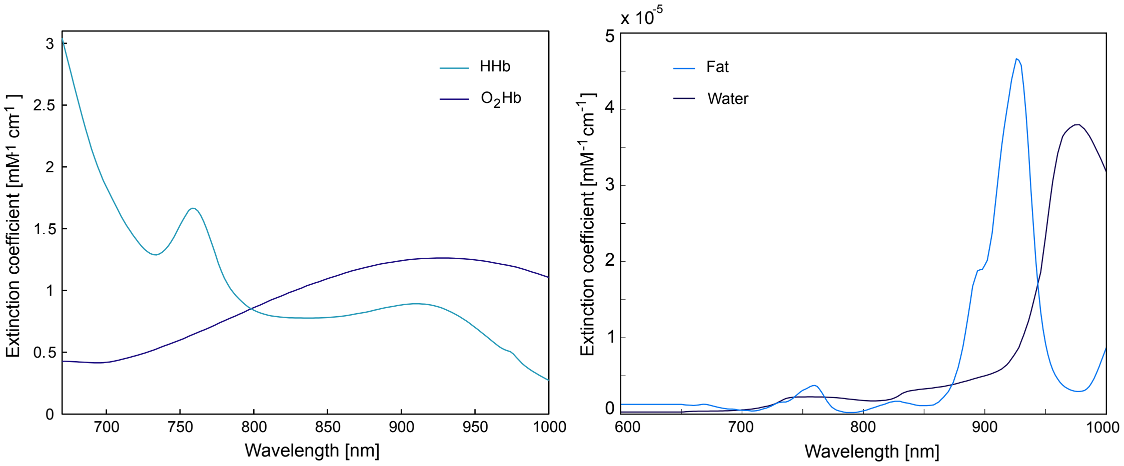

Figure 0.1 – Extinction coefficients for oxy and deoxyhemoglobin (Wray et al. 1988, *UCL, Departement of Medical Physics and Bioengineering* n.d.), water (*UCL, Departement of Medical Physics and Bioengineering* n.d.) and fat (*Oregon Medical Laser Center* n.d.). The extinction coefficients of water are multiplied with the factor 10 to enable a better comparison of the water and fat spectra.

in the absorption coefficients are calculated. From the absorption coefficients at different wavelengths the changes in the absorber concentrations can be obtained. However, if one would like to determine absolute absorption and reduced scattering coefficients and absolute absorber concentrations, FD or TD-NIRS instruments must be employed. FD-NIRS instruments are used in two different modes: multi-distance and multi-frequency. In the multi-distance mode, the intensity of the light is modulated at a single frequency between 50 and 500 MHz and the light sources and detectors are arranged in a way so that different source-detector distances are obtained. In the multi-frequency mode, a single source-detector distance is employed in the sensor and the modulation frequency is varied within the range of 50 to 500 MHz. Multi-distance sensors are more suitable for larger tissues (e.g. human head and muscles), whereas multi-frequency sensors can be employed for measurements on much smaller tissue structures, such as the tongue or the cervix.

Primarily, NIRS was applied to detect hypoxic ischemic brain injury in preterm neonates. Several performed studies (Obrig et al. 1996, Heekeren et al. 1997, Schecklmann et al. 2008) presented the possibility to measure hemodynamic responses of the brain to an external stimuli non-invasively with near-infrared spectroscopy and imaging.

When measuring hemodynamic responses, the term functional NIRS (fNIRS) is used. The measured concentration changes ($\Delta[O_2Hb]$, $\Delta[HHb]$ and $\Delta[tHb]$) are representing changes in cerebral blood flow (CBF), cerebral blood volume (CBV) and cerebral metabolic rate of oxygen ($CMRO_2$). NIRS and NIRI can measure changes in a depth of 2.5 cm in the human head, as Toronov et al. (2001) described. Thus, NIRS is able to assess the outer cortex, which is activated in response to an external stimuli.

Wolf and Greisen (2009) summarized the advances and applications when studying the brain of preterm and term neonates. In NIRS research, attention was mainly focused on the brain, since 21% of the total oxygen is consumed by the brain and as it reacts very sensitive to oxygen deficits, e.g. on high altitudes, during difficult childbirth or during sleep apnea.

To measure optical properties and oxygenation of biological tissue, NIRS was applied widely in medical research for neonates or adults, e.g. to monitor brain or tissue oxygenation (Wolf and Greisen 2009), in cardiac and major vascular surgery (Edmonds et al. 2004), cancer diagnosis (Kondepati et al. 2008) or to detect peripheral vascular diseases (Vardi and Nini 2008).

In addition, the scatter power (SP), defined as the exponential decay of the reduced scattering coefficient in dependency of the wavelength, is a measure for the size of scatter particles (Mourant et al. 1997). Thus, structural and compositional changes of tissue, which are accompanied by changes in the size of the scatter particles, should be reflected in changes of the SP. Therefore, monitoring absorption and reduced scattering coefficients over time can reveal structural and compositional tissue changes as well as the water, fat and hemoglobin content and the oxygenation state of the tissue.

Within this thesis two research questions were investigated, the first being of public interest and the second being of high clinical relevance:

- *Do Universal Mobile Telecommunication System electromagnetic fields (UMTS-EMF) alter the cerebral or superficial blood circulation in the human head?*

  This research topic is motivated by the highly increasing number of mobile phone users worldwide and the lack of studies investigating effects of the new telecommunication standard UMTS. Until today, most human exposure studies were using a continuous exposure either due to low time resolution of the measurement method (e.g. positron emission tomography (PET)) or due to electromagnetic interference between EMF and the measurement technique (e.g. electroencephalography (EEG)). NIRI is the only measurement method enabling to investigate immediate short-term effects of intermittent EMF. Furthermore, potential immediate effects of UMTS-EMF on blood circulation have not been investigated yet.

  Since the head is receiving the highest EMF dose during mobile phone calls, investigation of neurophysiological effects (Valentini et al. 2007) is of great importance. The major amount of studies was carried out using EEG and Global System for Mobile communications electromagnetic fields (GSM-EMF), some showing an effect (Huber et al. 2002, Regel, Tinguely, Schuderer, Adam, Kuster, Landolt and Achermann 2007, Regel, Gottselig, Schuderer, Tinguely, Retey, Kuster, Landolt and Achermann 2007, Croft et al. 2008) and some did not (Kleinlogel et al. 2008, Röschke and Mann 1997). Using PET, effects of GSM-EMF on regional CBF (rCBF) were detected (Huber et al. 2002, Huber et al. 2005, Aalto et al. 2006), but no effects on rCBF were found for UMTS-EMF (Mizuno et al. 2009). The low time resolution of PET (15 to 30 min) allows only to study slow effects of EMF on rCBF, whereas NIRI systems can measure with a time resolution up to a few ms, which enables to study not only slow effects but also immediate short-term effects of intermittent EMF. So far, two NIRI studies were carried out with GSM-EMF investigating immediate effects (Wolf et al. 2006) and slow effects of continuous exposure (Curcio et al. 2009). In these studies either borderline significant immediate changes of [O_2Hb] and [HHb] (Wolf et al. 2006) or a significant linear increase in [HHb] (Curcio et al. 2009) were found.

- *Are structural and compositional changes in the uterine cervix during a normal pregnancy reflected in optical changes measured by NIRS?*
  This research topic is motivated by the fact that preterm labor is the most common obstetric complication and can lead to infant's death or neurological disease. Until today, no method is enough reliable to predict cervical ripening and thus preterm labor, over a broad range of patients (Garfield et al. 2001). Any method that accurately determines the state of the cervical ripening has the potential to become a clinical routine investigation. Accurate diagnosis in preterm cervical ripening would allow to start the appropriate treatment and hence, to prevent preterm labor.
  The uterine cervix consists dominantly of connective tissue, which is composed of collagen with elastin and preoglycans (extracellular matrix) and smooth muscle and fibroblasts as the cellular substances (Ludmir and Sehdev 2000). The connective tissue is well perfused with blood. The constitution of the uterine cervix changes over pregnancy to fulfill the changing requirements: i) during pregnancy it has to be strong enough to ensure physical stability, protection against infections and to prevent preterm delivery and ii) at the end of pregnancy it has to be soft enough to dilate and enable delivery. Thus, the uterine cervix has to undergo enormous structural and compositional changes during pregnancy.
  Changes in blood perfusion, water content and the size of scatter particles are measurable non-invasively with NIRS and a previous study showed that changes in the constitution of cervical tissue during drug-induced cervical ripening are indeed reflected in changes in the optical NIRS signal (Baños et al. 2007). To assess the potential of the technology, normative data about inconspicuous pregnancies over all three trimesters must be available to compare it in a further study to pregnancies resulting in preterm delivery.

Objectives and Outline

Potential effects of electromagnetic fields on blood circulation in the human head

The *UMTS exposure study* was carried out in the framework of the Swiss National Research Programme NRP 57 entitled "Non-Ionising Radiation - Health and Environment". It was carried out in collaboration with Swisscom (Switzerland) Ltd. (Innovation Competence Centre, Environment & Electromagnetic Compatibility, 3050 Bern, Switzerland), which provided the exposure system (the electronics equipment, the antenna, the controlling computer and the EMF absorbers). The necessary antenna power output was assessed with dosimetric simulations. Verification measurement and measurement to validate the system were carried out at the industry-independent IT'IS foundation in Zurich. The responsibilities of Swisscom and the Biomedical Optics Research Laboratory (BORL) were separated and defined in a declaration to ensure that Swisscom had no influence on the data acquisition and analysis. Due to this collaboration, Swisscom's experience with RF-EMF and exposure systems could be incorporated in the study.
Within the *UMTS exposure study* different aims have to be achieved by BORL:

- **Aim 1:** Shielding of the NIRI measurement system against UMTS-EMF.
  This aim was based on the experience gained in the EMF study (GSM 900 MHz) previously carried out in our group (Wolf et al. 2006), where the electronics part of the optical sensor was susceptible to EMF. This caused interference in the optical signal during the time where GSM-EMF was emitted by the antenna. An optical sensor without any active parts was built to prevent interference between the optical sensor and the UMTS-EMF. In addition, the optical cables guiding the light from the sensor to the NIRI instrument had to be long enough to place the instrument outside of the measurement chamber. The degree of inertness had to be validated in phantom measurements. A detailed description of the named steps is given in chapter 2.

- **Aim 2:** Improving horizontal and depth resolution of the novel optical sensor.
  Achieving depth resolution was motivated by the objective to discriminate between superficial and deep effects of EMF, because on the one hand the skin receives the highest dose of EMF and on the other hand results of previous studies indicated effects on rCBF (Huber et al. 2002, Huber et al. 2005). For localization of absorption changes, a NIRI sensor must consist of spatially distributed sources and detectors with different separations. This was not possible with the commercially available

configuration of the ISS Oxiplex® (ISS Inc., Champaign, Illinois, USA), which incorporates only 4 light paths within one single sensor.
The aim was to enhance the range of applications for the instrument by increasing the number of sources and detectors available for a single optical sensor. To achieve this aim, hardware and software modifications to the ISS Oxiplex® had to be implemented and a novel optical sensor (*Imager16*) had to be constructed (section 2.1 and 2.1.2).

- **Aim 3:** Characterizing the *Imager16* in terms of the achievable horizontal and depth resolution.
  The third aim was to characterize the ability of the *Imager16* to localize absorption changes and to give a basis for the interpretation of results. Simulations based on solving the diffusion equation were carried out to characterize the ability of *Imager16* to localize an higher absorbing object and to determine the correlation between the *real* depth of an higher absorbing object to its *reconstructed* depth (section 2.2). In addition, different approaches were investigated in order to determine their ability to distinguish superficial from deep changes. The approaches were validated in phantom and in-vivo measurements (section 2.3).

- **Aim 4:** Performing an exploratory study on eight subjects to study potential short-term (shorter than 80 s) effects of various UMTS signals and exposure positions on blood circulation in the human head and to define a final protocol for the main study.
  This experimental phase was performed in a single-blind mode to gain experience in handling the setup (exposure and NIRI). A summary of the exploratory study can be found in section 4.2.

- **Aim 5:** Performing a main study to investigate potential short and medium-term (within 80 s to 30 minutes) effects of UMTS-EMF on blood circulation in the human head in a larger population (N=16)
  To achieve this aim a controlled, randomized, crossover and double-blind paradigm was applied. Three different dose-levels were used to check for an dose-dependent effect. In addition, functional measurements were planned to compare the amplitude of potential short-term effects to something known. A detailed description of the main study can be found in section 4.3.

Aside from these aims, a novel movement artifact reduction algorithm (MARA) was implemented to minimize the influence of movement artifacts (MAs) on the results. This algorithm can be applied on different NIRI data sets. More details about the MARA are given in section 4.1.
Multi-modal imaging gained more attention in recent years, since it enhances the understanding of physiology and diseases due to different constrasts of the employed imaging methods. In principle, the novel optical sensor (*Imager16*) could also be used in a magnetic resonance scanner, but initial test measurements showed that iron particles are present within the color used to dye the silicone elastomer shell of the sensor and produced severe artifacts in the magnetic resonance images.

The optical sensor was further developed in an additional side project, which was not within the scope of the *UMTS exposure study*. This second optical sensor (*Imager4MRT*) was successfully constructed with a different dye to enable simultaneous measurements with near-infrared imaging and magnetic resonance imaging (section 2.1.3). The *Imager4MRT* opens a wide range of multi-modal applications, which have the potential to benefit both modalities.

Monitoring of structural and compositional changes of the cervix

This study was carried out in collaboration with the gynecology clinic of the University Hospital of Zurich.

- **Aim 1:** Modification of the measurement instrument to suit the study requirements (responsibility: BORL).
  To assess a small tissue volume such as the uterine cervix with NIRS, it was necessary to use a single source-detector distance for the optical sensor. Since multi-frequency FD-NIRS instruments are not commercially available, the multi-distance FD-NIRS instrument ISS Imagent® (ISS Inc., Champaign, Illinois, USA) at BORL was modified to feature a multi-frequency mode. The optical probe was designed specifically for this study. To be able to measure water and fat, two light sources, one with 920 nm and one with 970 nm, have been integrated in the instrument. Since the photomultiplier tube (PMT) was not able to measure up to those wavelengths, one detector was exchanged with an avalanche photo diode (APD). A more detailed description of the modified instrument can be found in chapter 3.

- **Aim 2:** Verifications and validations of the modified instrument in phantom and in-vivo measurements (responsibility: BORL).
  The reliability, accuracy and repeatability of the modified instrument were determined in solid silicone and liquid intralipid phantoms. In addition, measurements on muscle tissue were performed and compared to literature values. The detailed measurement protocol and results are given in chapter 3.

- **Aim 3:** Enrolling pregnant women scheduled for clinical routine examinations to perform NIRS measurements of the cervix (responsibility: gynecology).

- **Aim 4:** Development of an easy-to-use analysis tool and the analysis of the NIRS data itself (responsibility: BORL).
  Based on a first version developed by Meerstetter and Jacoma (2004), the analysis was improved and enhanced (Spichtig 2006), which enabled to analyze multi-frequency measurements carried out on phantoms and humans.
  The first versions did not account for MAs, which were common in the cervix study. Thus the analysis was further improved to make it more robust to MAs.

- **Aim 5:** Statistical analysis of the measurement data in terms of their correlation to the weeks of gestation and publication (responsibility: gynecology) (chapter 5).

1 Introduction to frequency-domain instruments

Today, three different types of NIRS instrumentations are available: continuous wave (CW), time-domain (TD) and frequency-domain (FD) (Fig. 1.1). This chapter provides a short introduction to CW and TD-NIRS and covers the working principle, advantages and disadvantages of multi-distance and multi-frequency FD instruments. For more information about CW- and TD-NIRS and comparison between the different techniques see (Tuchin 2000, Hebden et al. 1997, Gibson et al. 2005).

In CW-NIRS, light with a constant intensity I_0 is emitted into tissue and undergoes absorption and scattering. In the reflection mode, the backscattered intensity I is measured at the detector, located on tissue's surface. In the transmission mode, the transmitted light is measured at the detector, located on the tissue surface opposite the sources. Relative changes between two time points can be calculated using the modified Lambert-Beer law, see Eq. 2.3.3 (Wray et al. 1988, Matcher, Elwell, Cooper, Cope and Delpy 1995). Assuming that the reduced scattering coefficient μ_s' is known and that the photon transport can be modeled by the diffusion equation, absolute values of the absorption coefficient μ_a can be calculated from the distance dependency of the attenuated intensity (Matcher, Kirkpatrick, Nahid, Dope and Delpy 1995). The first NIRS instrument (Jöbsis 1977) and most of the clinically used NIRS instruments are based on the CW method (Wolf et al. 2007). CW-NIRS systems are less expensive and complex than FD-NIRS or TD-NIRS instruments.

In TD-NIRS, a laser pulse (with durations of a pico, nano or femto seconds) is emitted into the tissue and the time-of-flight of single photons is measured at the detector. The number of detected photons as a function of time is also known as the temporal point spread function (TPSF) (Fig. 1.1). From the ascending slope of $log(TPSF)$, μ_a can be calculated and μ_s' from the time t_{max}, where $log(TPSF)$ reaches the maximum. Looking at the TPSF, one can obtain the average μ_a and μ_s' of the tissue, and the optical coefficients at different depths. This is done by selecting different time intervals of the TPSF for the

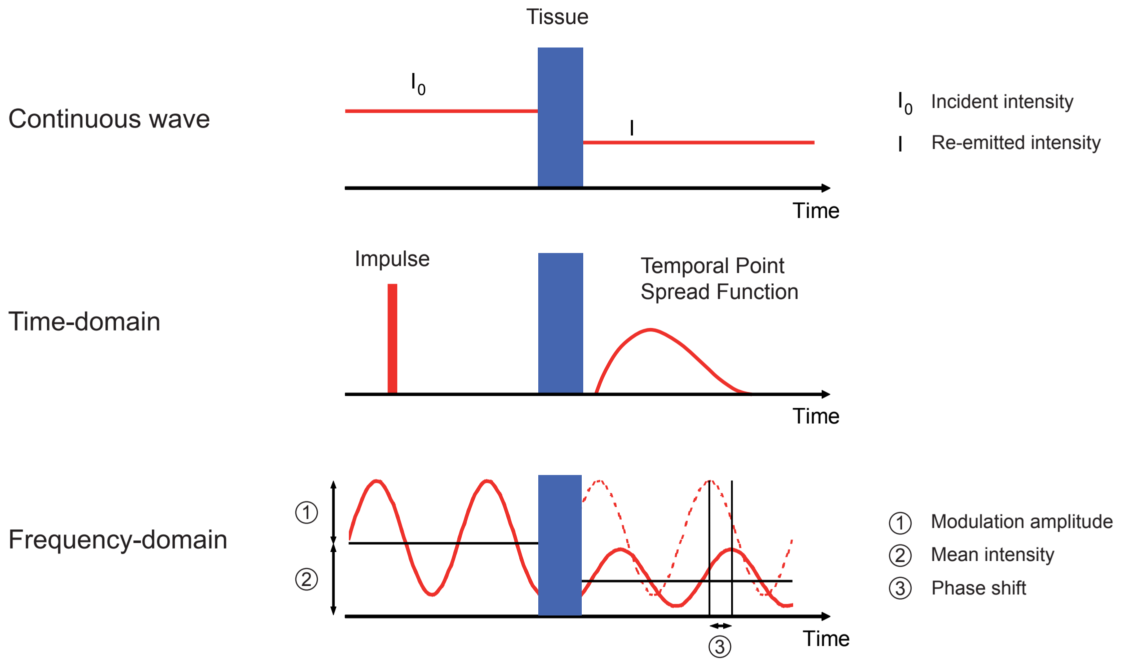

Figure 1.1 – Illustration of the temporal characteristic of light transmitted through a highly scattering tissue for the three types of NIRS instrumentation: continuous wave, time-domain and frequency-domain.

analysis (Liebert et al. 2004) and can be applied e.g. in measurements of a multi-layered tissue, which allows to calculate the optical coefficients of each layer.

TD-NIRS measurements are noisier than CW or FD-NIRS, because fewer photons are detected for the analysis. TD-NIRS is the most advanced and complex NIRS technique. It is highly demanding with respect to laser diodes and detectors, which makes it also to the most expensive technique. An overview of TD-NIRS instruments is given in Wolf et al. (2007).

The first FD-NIRS measurements were performed by Lakowicz and Berndt (1990) and since then, different companies and research groups developed their own FD-NIRS instruments. An overview of clinically used FD-NIRS instruments can be found in Wolf et al. (2007).

When doing NIRS in the frequency-domain, the intensity of the emitted light is amplitude-modulated at frequencies between 50 MHz to 500 MHz. Above 500 MHz, the accuracy decreases due to a decreasing detector sensitivity and attenuation, which leads to a lower signal-to-noise ratio. Since frequency synthesizers are necessary, so far, it is not possible to integrate the source and detector unit into the optical sensor itself. Thus, for FD-NIRS and some TD-NIRS instrumentations, the intensity-modulated light is coupled into glass fibres and guided to the tissue of interest. The light is sent into the tissue and undergoes absorption and scattering, which causes attenuation in the mean intensity and modulation amplitude and a longer light path length (Fig. 1.1). The light scattered back to the detector positions is collected and guided back to the instrument by glass fibres. The light is measured at the detector, which is modulated slightly above light's modulation frequency. From the heterodyne demodulated signal, a software computes intensity, modulation amplitude and phase shift. The measurement of the phase shift between incident and reference signal makes it possible to determine μ_s' (Fantini et al. 1995). But since some instrumental factors are not known, such as the intensity of the laser light, the detector sensitivity, the coupling and losses in the glass fibres, a calibration measurement on a phantom with known optical properties is required.

The light sources are time-multiplexed to allow a clear differentiation of the signals measured at the detector. Usually, laser diodes are used as light sources, since they can be intensity modulated with frequencies up to a few hundred MHz. Photomultiplier tubes (PMT) and avalanche photo diodes (APD) are the most common detectors.

The calculation of absolute values for μ_a and μ_s' is based on the diffusion equation

$$\left[\nabla^2 + \frac{i\omega - v\mu_a(r)}{D}\right]\Phi(r) = \frac{-v}{D}q_0(r), \tag{1.1}$$

where r is a position vector, q_0 stands for an modulated isotropic source (Eq. 1.2), μ_a is the spatially varying absorption coefficient, ω the modulation frequency of the laser light, $D = v/3\mu_s'$ the diffusion coefficient and v light's velocity in the medium defined by c_0/n with c_0 the vacuum light speed and n the index of refraction. Within the diffusion approximation the following assumptions are made:

- μ_s' of the tissue is much larger than μ_a.
- The source-detector distance is longer than 1 cm.
- The probed tissue is homogeneous.
- The modulation frequency is smaller than 1 GHz.

Two techniques for FD-NIRS instruments exist: multi-distance and multi-frequency. In the following, both techniques are described in detail.

1.1 Multi-distance frequency-domain instrument

In multi-distance FD-NIRS, laser light is modulated at a single frequency and the backscattered light is measured at different source-detector distances. This principle of measurement at different distances is also known as spatially resolved spectroscopy (SRS) and is not only used in FD-NIRS, but also in CW- and TD-NIRS. The first multi-distance FD-NIRS instrument was presented by Fantini et al. (1995). For a summary of multi-distance FD-NIRS instruments used in the clinical environment see Wolf et al. (2007).

For a semi-infinite medium and a modulated isotropic light source q_0

$$q_0 = \delta(r_s)\, S\left(1 + Ae^{-i\omega t}\right), \tag{1.2}$$

with $\delta(r_s)$ the Dirac delta function located at the source position r_s, S the fluence of the source [photons/s], A the source's modulation amplitude and ω the modulation frequency, a solution to the diffusion equation (Eq. 1.1) for the photon density $U(r,t)$ is (Fishkin and Gratton 1993)

$$U(r,t) = U_{dc}(r) + U_{ac}(r)e^{-i\omega t + \varphi}. \tag{1.3}$$

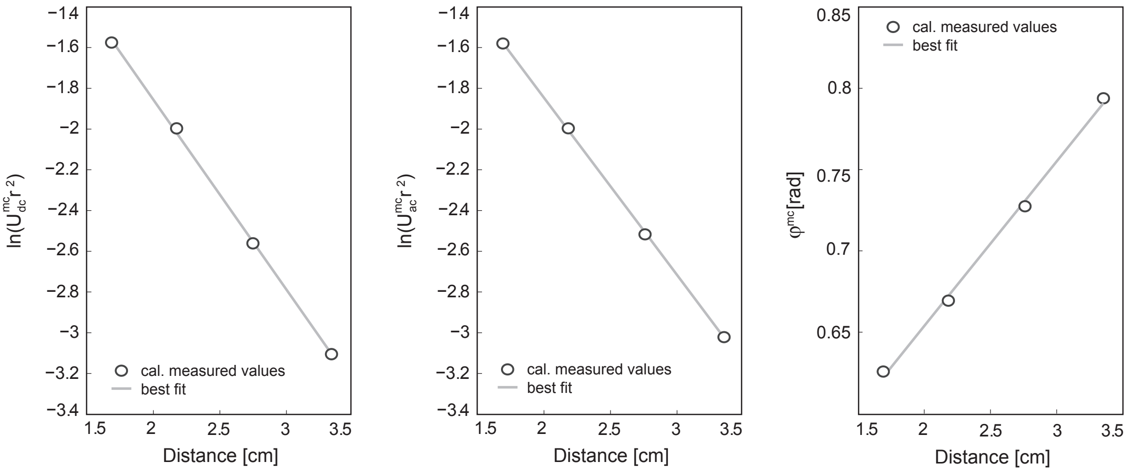

Figure 1.2 – Illustration of the linear relationship between $\ln(U_{dc} \cdot r^2)$, $\ln(U_{ac} \cdot r^2)$, φ and the source-detector distance r. Measured values from a solid silicone phantom measurement are indicated with dark blue circles and the best linear fit with a bright blue.

U_{dc} is the mean intensity of the backscattered light, U_{ac} the modulation amplitude and φ the phase shift between the emitted and detected light. For the different measurable components of $U(r,t)$, a linear relationship to the source-detector distance was derived by (Fantini, Franceschini and Gratton 1994) and given in a more explicit form by (Hueber, Franceschini, Ma, Zhang, Ballesteros, Fantini, Wallace, Ntziachristos and Chance 2001)

$$\ln\left(r^2 \cdot U_{dc}(r)\right) = \ln\left(\frac{S}{4\pi v D}\right) - r\left(\frac{\mu_a}{D}\right)^{\frac{1}{2}}, \tag{1.4}$$

$$\ln\left(r^2 \cdot U_{ac}(r)\right) = \ln\left(\frac{SA}{4\pi v D}\right) - r\left(\frac{\mu_a}{D}\right)^{\frac{1}{2}}\left[\left(1+\left(\frac{\omega}{v\mu_a}\right)^2\right)^{\frac{1}{2}} + 1\right]^{\frac{1}{2}}, \tag{1.5}$$

$$\varphi(r) = \alpha + r\left(\frac{\mu_a}{2D}\right)^{\frac{1}{2}}\left[\left(1+\left(\frac{\omega}{v\mu_a}\right)^2\right)^{\frac{1}{2}} - 1\right]^{\frac{1}{2}}, \tag{1.6}$$

where α is the phase source term. The fluence S and the modulation A of the light coupled into the tissue differs from light source to light source. Since S and A are not known and different light influx has to be corrected, a calibration measurement on a phantom with known optical properties is needed. $U^c_{dc}(r)$, $U^c_{ac}(r)$ and $\varphi^c(r)$, measured for the calibration phantom, are compared to the theoretical values for the phantom's optical coefficients μ_a and μ_s' to obtain the distance-dependent calibration factors for the mean intensity, the modulation amplitude and phase shift ($C_{dc}(r)$, $C_{ac}(r)$ and $C_\varphi(r)$). The calibrated measurement variables $U^{mc}_{dc}(r)$, $U^{mc}_{ac}(r)$ and $\varphi^{mc}(r)$ (Fig. 1.2) are thus

$$U^{mc}_{dc}(r) = \frac{U_{dc}(r)}{C_{dc}(r)}, \quad U^{mc}_{ac}(r) = \frac{U_{ac}(r)}{C_{ac}(r)} \quad and \quad \varphi^{mc}(r) = \varphi(r) - C_\varphi(r). \tag{1.7}$$

From the slopes of $\ln\left(r^2 \cdot U^{mc}_{dc}(r)\right)$, $\ln\left(r^2 \cdot U^{mc}_{ac}(r)\right)$ and $\varphi^{mc}(r)$ (S_{dc}, S_{ac} and S_φ), μ_a and

μ_s' of the tissue under investigation can be calculated:

$$\mu_a = \frac{\omega}{2v} \cdot \left(\frac{S_\varphi}{S_{ac}} - \frac{S_{ac}}{S_\varphi} \right) = \frac{\omega}{2v} \cdot \frac{S_{dc}}{S_\varphi} \cdot \left(\frac{S_\varphi^2}{S_{dc}^2} + 1 \right)^{-\frac{1}{2}}, \tag{1.8}$$

$$\mu_s' = \frac{S_{ac}^2 - S_\varphi^2}{3\mu_a} - \mu_a = \frac{S_{dc}^2}{3\mu_a} - \mu_a. \tag{1.9}$$

Thus, the optical coefficients can either be calculated from S_φ and S_{ac} or S_φ and S_{dc}. Compared to the multi-frequency method, the multi-distance method features a higher signal-to-noise ratio (Fantini, Francheschini, Fishkin, Barbieri and Gratton 1994) and due to the shorter duration of a measurement cycle it is much more robust to movement artifacts (MA) occurring in in-vivo measurements. The probed tissue volume depends on the sensor configuration, but is usually several times larger than for the multi-frequency setup. This means that the assumption of a homogeneous medium must be valid for larger tissue volumes. Small heterogeneities, which are probed by only one measurement path, will be visible as outliers in the linear multi-distance plots and can be excluded from the analysis. However, most biological tissues, like for example muscle or brain tissue, are macroscopically homogeneous and thus mean optical properties are obtained. In the case of a superficial layer, like for example the human head, Franceschini et al. (1998) showed that the optical changes in a superficial layer and the layer's optical properties cancel out for certain specific measurement configurations.

Multi-distance measurements do not only enable measurements of absolute optical coefficients, but also allow estimations about the depth of occurring optical changes. Since the mean penetration depth is dependent on the source-detector distance r (Choi et al. 2004)

$$z(r) = \frac{1}{2} \left(\frac{r}{(3\mu_s'(r)\mu_a(r))^{\frac{1}{2}}} \right)^{\frac{1}{2}}, \tag{1.10}$$

photons originating from larger source-detector distances penetrate deeper into tissue structures than from smaller source-detector distances.

Using a multi-distance sensor with spatially distributed sources and detectors, it is possible to obtain horizontal and depth resolution. Using a perturbation approach, where the medium is assumed to be homogeneous and absorption changes are described as perturbations, which are localized disturbances in the optical coefficients, changes in the absorption coefficient can be reconstructed (O'Leary 1996). Also other methods exist to reconstruct the optical coefficients by diffuse optical imaging (DOI) (chapter 2.2.2).

1.2 Multi-frequency frequency-domain instrument

In multi-frequency FD-NIRS, a single source-detector separation is employed and the modulation frequency of the laser light is varied within the range of 50 to 500 MHz. The amplitude modulation $A_{att}(\omega)$ and phase shift $\Theta_{lag}(\omega)$ as functions of modulation frequency are calibrated (Eq. 3.3) and μ_a and μ_s' with the best fit determined (Eq. 3.4). An example of calibrated measurement amplitude attenuation A_{att}^{mc} and phase shift Θ_{lag}^{mc}

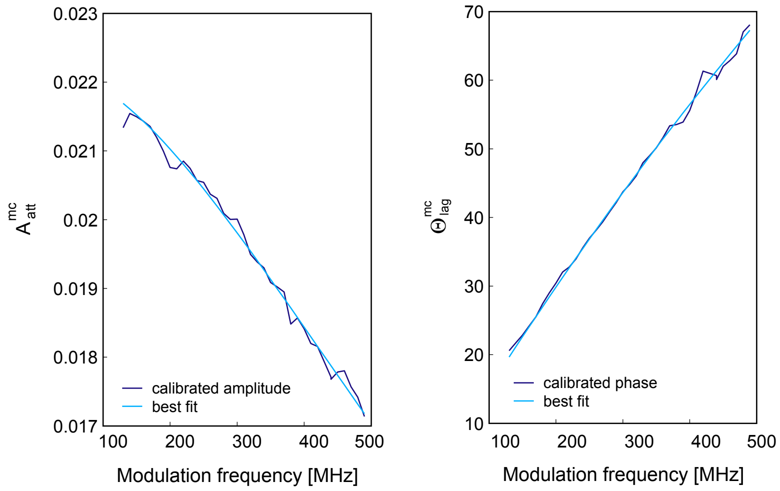

Figure 1.3 – Calibrated amplitude attenuation A_{att}^{mc} and calibrated phase shift Θ_{lag}^{mc}. In addition the theoretical curves of the absorption and scattering coefficient which minimize Eq. 3.4 are shown.

and the best theoretical fit are shown in Fig. 1.3. For a more detailed description refer to the theory section in chapter 3. Multi-frequency instruments are not yet commercially available and have a relatively low time resolution (≈10 to 40 s) compared to CW-NIRS or multi-distance FD-NIRS (≈10 to 50 ms). Since the multi-frequency method uses only a single source-detector distance, the contact area needed for sensor placement on the tissue is relatively small (≈1 to 2 cm^2). This extends the range of applications to smaller organs and tissue structures, such as the tongue or the cervix.

2 Characterization of the multi-distance FD-NIRS instrument

The ISS Oxiplex® instrument (ISS Inc., Champaign, Illinois, USA) (Fig. 2.1) is compact, portable and able to measure μ_a, μ_s', [O_2Hb], [HHb], [tHb] and [StO_2] of the tissue. The instrument is mainly used in clinical research, especially in premature infants, sports medicine, sleep research and the monitoring of the brain oxygenation.

The ISS Oxiplex® instrument features two laser boards and two PMT detectors. Each laser board contains eight laser diodes, four emitting at a wavelength of 690 nm and four emitting at a wavelength of 830 nm. The laser diodes of each laser board are controlled in a time-multiplexed manner. Both laser boards are used simultaneously, one laser diode from each laser board is in an on-state simultaneously. To prevent interference between the signals of the different laser boards, only one laser board can be used for a single optical sensor. Due to the time-multiplexing of 8 laser diodes, this measurement mode is called the *switch8* mode. The intensity of the laser light is amplitude-modulated at a frequency of 110 MHz. The temporal resolution in the *switch8* mode is 20 ms.

The commercial optical sensor consists of four source and one detector position (Fig. 2.1). For each source position, light at both wavelengths is guided by individual glass fibres to a prism, which deflects the light by 90° into the tissue. The glass fibres and the prisms are casted in silicone to obtain a flexible planar sensor, which can easily be placed on the tissue of interest. The silicone is dyed black to prevent direct light traveling from source to detector within the silicone and to absorb light re-emitted by the skin at other locations than the detector's.

In contrast to CW instruments, all source and detector electronics are located inside the instrument and the optical sensor itself contains no active parts. Glass fibres with a length of 1.5 m are used to deliver the light to the optical sensor and the recollected light back to the instrument.

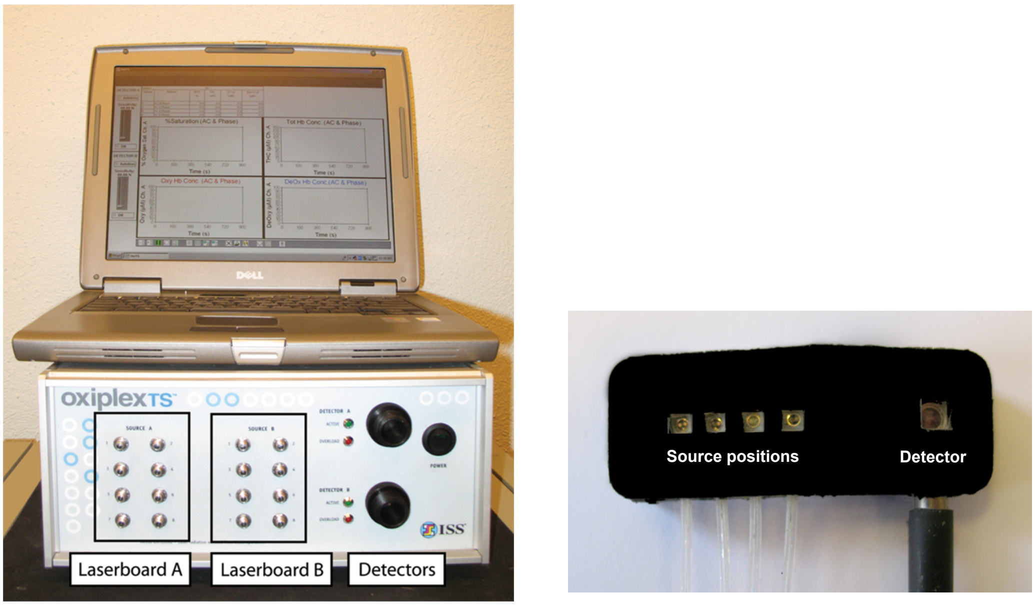

Figure 2.1 – Left side: Frontal view of ISS Oxiplex® with control computer. The couplings for the glass fibre connectors both for the laser diodes and the detectors are located at the front. Right side: Commercially available optical sensor with four source positions and one detector. Glass fibres enter the flexible black silicone from below and are attached to the source and detector prisms.

The *switch8* mode of the commercial instrument has some limitations:

- Due to the one-dimensional arrangement of the detector and the sources and their low number, no spatial resolution can be obtained.
- The volume of the probed tissue is relatively small and thus localized concentration changes can easily be missed.

However, the commercial configuration of the instrument provides also some advantages:

- With the implemented multi-distance paradigm, depth resolution can be obtained (Choi et al. 2004) since longer source-detector distances are more sensitive to deeper concentration changes than shorter source-detector distances.
- Maintaining a certain distance between both sensors, they can simultaneously be used for a measurement. This enables e.g. to investigate both brain hemisphere at the same time or to measure the lateralization of different brain functions.

For the *UMTS exposure study*, different aims had to be achieved:

1. To enable NIRI recording during EMF exposure, the NIRI instrument must be sufficiently inert to EMF. This means that the sensor cannot contain any active parts. Furthermore, the glass fibres had to be long enough to be able to place the measurement instrument itself outside of the exposure chamber.

2. To resolve absorption changes spatially and in order to be able to distinguish between superficial and deep changes, the optical sensor must provide horizontal and depth resolution. This can be achieved by increasing the number of sources and detectors used for the optical sensor. Furthermore, the sources and detectors must be arranged in a way that horizontal and depth resolution can be obtained.

3. To obtain depth resolution the multi-distance setup must be maintained for the optical sensor. In addition, available depth resolution algorithms must be optimized and tested.

To realize these aims, extensive modifications were needed: hardware and software had to be adapted (2.1.1) and a new optical sensor had to be built (2.1.2). Simulations were carried out to characterize the ability of the novel optical sensor (*Imager16*) to localize an activation and to determine the correlation between the *real* depth of an activation and its *reconstructed* depth (section 2.2). Different depth resolution algorithms were optimized and tested in phantom and in-vivo measurements (2.3).

2.1 Modifications

2.1.1 Hardware and software changes

The core of the ISS Oxiplex® is a uClinux operating system, which controls the whole electronics including laser diode activation, light detection and data processing. A FPGA, programmed in Verilog, is used to activate and switch the laser diodes, which is time critical, in the predefined order. The control computer is connected via USB port to the ISS Oxiplex®.

The adjustment of the ISS Oxiplex® to suit the requirements of the *UMTS exposure study* was based on modifying FPGA, uClinux and the source code of a dynamically linked library (DLL) which transcodes the recorded measurement data into the format required in the end by the recording software. Since the hardware and software design of the instrument is very complex, the aim was to achieve the desired modifications with as little interventions as possible.

In this novel mode, one laser board is switched on after the other, which enables to use all 16 laser diodes and both detectors for a single optical sensor. This is called *switch16* mode. The sampling rate is reduced from 50 Hz to 25 Hz, since twice the time is needed to switch through all laser diodes.

A dip-switch was added at the back of the instrument to enable measurements with both modes. Prior the power-on of the instrument, the user can select between *switch8* or *switch16* mode. The state of the dip-switch tells the uClinux processor, which protocol has to be used to initialize the FPGA.

Two programs are installed on the control laptop: Boxy4Oxi and OxiTS®. OxiTS® is the original software belonging to the ISS Oxiplex®, whereas Boxy4Oxi was specifically adapted for the *switch16* mode. The choice of the software depends on the user's demands. OxiTS provides no on-line data monitoring, whereas Boxy4Oxi does. Tab. 2.1

Software	record data	view data on-line	save data
OxiTS	Yes	Yes	Yes
Boxy4Oxi	No	No	No

Table 2.1 – Feasible software applications for the *switch8* mode.

Software	record data	view data on-line	save data
OxiTS	Yes	No	Yes
Boxy4Oxi	Yes	Yes	Yes

Table 2.2 – Feasible software applications for the *switch16* mode.

and 2.2 summarize the restrictions of both softwares running the instrument in the *switch8* and the *switch16* mode, respectively.

2.1.2 Optical sensor for the UMTS exposure study: *Imager16*

Since the commercial sensor contains no active parts, the aim was to build the *Imager16* for the *switch16* mode made from similar parts as used for the commercial sensor (Fig. 2.1). The necessary material included: 10 m long glass fibres to guide light from the source to the tissue (part number: BFL37-400, Thorlabs, Newton, New Jersey, USA), 10 m long glass fibres to guide light from the tissue to the detectors (part number: LP3, Fiberoptic-Heim, Bühler, Schweiz), protective cover for the glass fibres, prisms for source and detector fibres (part number: 65413, Balboa Scientific, Costa Mesa, CA, USA), two-component silicone elastomer (part number: LSR-05, Factor II, Lakeside, AZ, USA), black colour to dye the silicone elastomer (part number: FI-205, Factor II, Lakeside, AZ, USA) and connectors attached at the other end of the fibres (part number: 10410A, Thorlabs, Newton, New Jersey, USA) to connect the source fibres with the ISS Oxiplex®.
Arranging source and detector positions for the *Imager16* was done to fulfill several requirements:

- Eight sources and two detectors must be arranged in an optimal way to obtain spatial resolution.
- The sources must be arranged at different distances from the detectors so that the multi-distance paradigm can be applied.
- Due to the limited dynamic range of the detector electronics, each source position should have the same distance to both detectors. This guarantees that the signal quality is optimal at both detectors.
- The space clearance needed for the optical fibres with the prisms at one end must be taken into account when defining source and detector positions.

The sensor geometry fulfilling the requirements is shown in Fig. 2.2. The shortest distance is given by the place needed for the optical fibres and prisms of both detectors. The

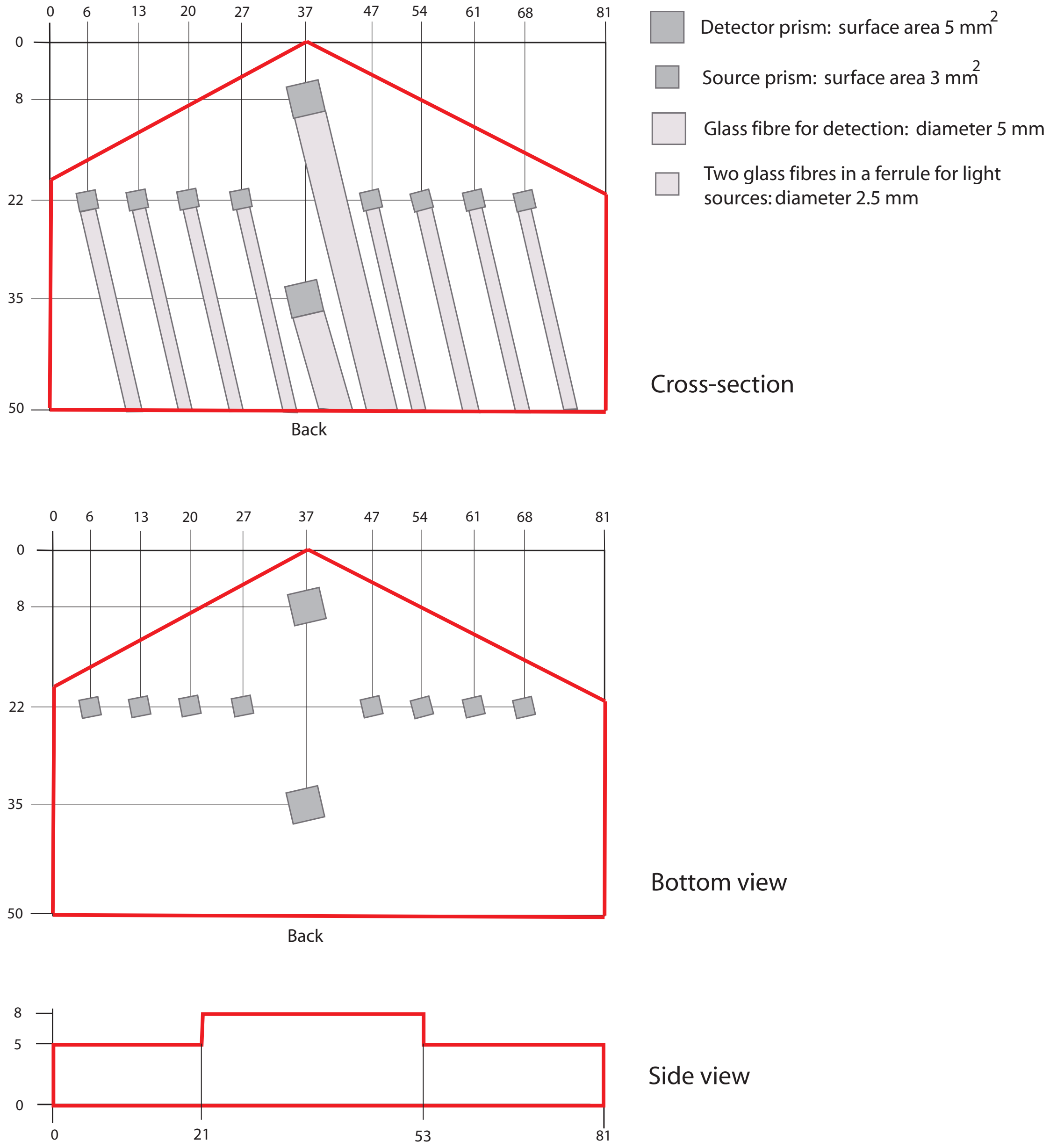

Figure 2.2 – Cross-section, bottom view and side view of the *Imager16*. Sizing units are mm. Larger squares represent the detectors, smaller squares the source positions. A total of 16 sources-detector combinations can be measured with 4 different distances. This sensor design enables a spatial and depth resolution.

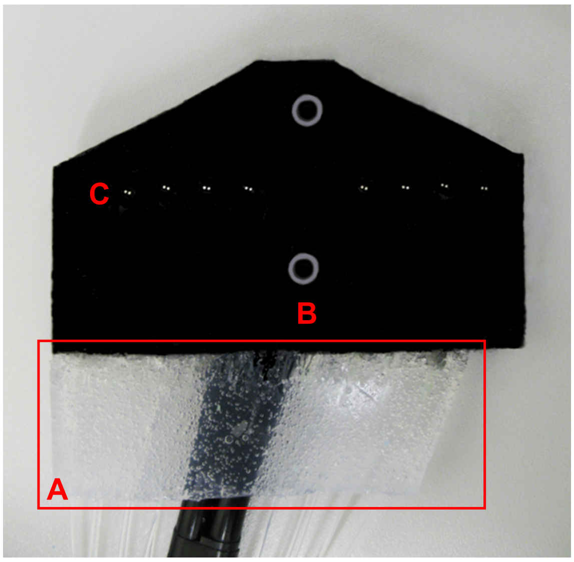

Figure 2.3 – Bottom view of the *Imager16*. A: glass fibre fixture to enhance sensor's stability, B: detectors and C: emission points of laser light.

maximum source-detector distance present is the largest distance still leading to acceptable signal quality.

An image of the *Imager16* with an additional glass fibre fixture to enhance sensor's stability and detector and source positions is shown in Fig. 2.3 (bottom view). One source position consists of two emitters, one for 690 nm and one for 830 nm. Since the measurement principle of the instrument was not changed and the analysis is the same, the determination of the optical coefficients is as accurate as with the commercial sensor. This was verified with measurements on commercially available solid silicone phantoms (ISS Inc., Champaign, Illinois, USA).

Multi-modal imaging gained more attention in recent years, since it enhances the understanding of physiology and diseases due to different constrasts of the employed imaging methods. Several research groups have published optical NIRI sensors feasible for usage in the MR scanner (Kleinschmidt et al. 1996, Strangman et al. 2002, Toronov et al. 2001, Zhang et al. 2005). The construction principle is mostly based on single glass fibres for each source and detector, which are arranged with some kind of holder or with velcro band resulting in a bulky optical sensor. For combined NIRI and MRI measurements on sensitive subjects, such as term or pre-term neonates, the simple handling of a measurement instrument is very important. For these subjects it is desirable to have an optical sensor, which is simple to attach and compatible for usage in the MR scanner. Planar patch sensors, like the *Imager16*, are simple to handle and therefore, in principle, suitable for this multi-modal application. Test measurements with the *Imager16* revealed artifacts in the MR images (Fig. 2.4C) caused by iron particles within the black color used to dye the silicone elastomer.

Therefore, a second NIRI sensor (called in the following *Imager4MRT*) was designed and manufactured with the same source-detector arrangement but different components.

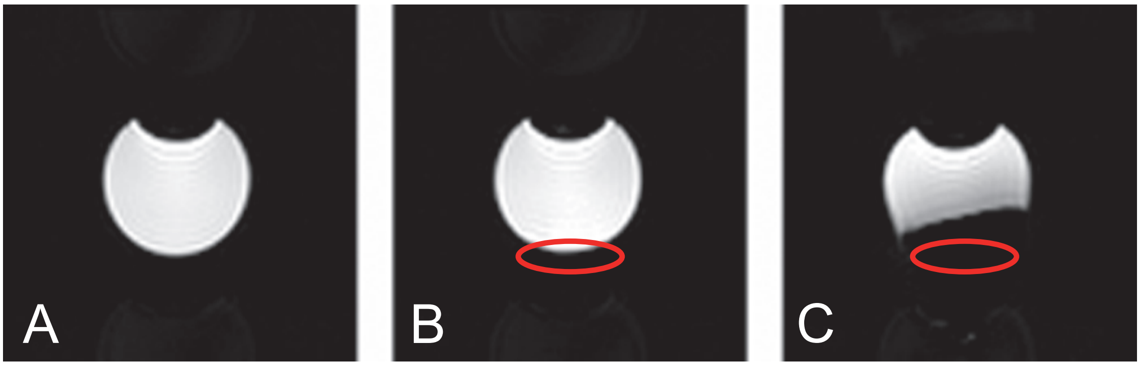

Figure 2.4 – MRI of a spherical water phantom with different optical sensors attached (marked with a red ellipse). A: without any optical sensor, B: with *Imager4MRT* and C: with *Imager16*.

2.1.3 Further development: optical sensor for combined NIRI-MRI measurements: *Imager4MRT*

Carbon black powder (part number: 45527, Alfa Aesar, MA, USA) was found to be a suitable dye for usage in the MR scanner. To prevent skin irritations and staining of color, a different black dye (ELASTOSIL® pigment paste PT 9005, Wacker Silicone, Munchen, Germany) was used for the contact area between the sensor and the skin. The other sensor sides were covered with a thin transparent silicone film. The silicone elastomer was exchanged by a health care grade silicone rubber (Silpuran 6000/10, Wacker Silicone, Munchen, Germany) to comply with EN/ISO 10993 (biocompatibility), which is necessary to get an approval for potential future clinical applications.

Phantom measurements

To assess if the *Imager4MRT* causes artifacts in the MR scanner (Philips Achieva 3.0T Quasar Dual Scanner, Philips Healthcare, Best, The Netherland), test measurements on a spherical water phantom (A Sphere water-phantom, Philips Healtcare, Best, The Netherland) were performed. The phantom was placed in the head coil (SENSE 8-Channel Headcoil, Philips Healtcare, Best, The Netherland) and positioned close to the center of the coil with foam pads. It was then secured with foam wedges and a sandbag was placed over the top of the coil. The MR sequence applied was a modified BIRN (Friedman and Glover 2006), which is a gradient-echo BOLD fMRI T2*-weighted sequence, with strong encoding gradients for a long EPI readout. Other sequence parameters are listed in Tab. 2.3.

The MR images are shown in Fig. 2.4A for the measurement without any optical sensor, Fig. 2.4B for the measurement with the *Imager4MRT* and, for comparison, the *Imager16* in Fig. 2.4C. Whereas the *Imager16* produces artifacts, no artifacts are present for the *Imager4MRT*.

This comparison shows that introducing a foreign object such as the sensor in the MR scanner can influence the image quality to a high degree or can even destroy part of the image. Although, this behaviour depends highly on the constituent parts of the sensor, it is also dependent on the MR sequence and the object the sensor gets attached to. To test the *Imager4MRT* in a real experimental situation, anatomical head scans and functional

Parameter	Values used for phantom meas.	Values used for anatomical scan	Values used for functional meas.
Scan Duration [s]	453.68	298.54	424.98
Number of slices/locations	23	301	30
Scan resolution (aquisition matrix)	80x79	228x227	96x96
Repetition time (TR) [ms]	2000.00	7.45	1950.18
FOV (ap,fh,rl) [mm]	(240, 91, 240)	(250, 250, 180.6)	(230, 89.5, 240)
Slice thickness [mm]	3	1.2	2.5
Slice gap [mm]	1	-0.6	0.5
Slice Orientation	transversal	sagittal	transversal
Water Fat shift [pixels]	14.78	2.07	16.07
Echo time (TE) [ms]	30	3.399	30
Image flip angle [degree]	90	8	90

Table 2.3 – MR sequence parameters used for the phantom and functional measurements and the anatomical scan. A negative slice gap describes overlapping slices.

measurements were also performed.
Due to the small amplitude of the blood oxygen level-dependent (BOLD) signal, a stable performance of the MR scanner is required. To assess if the *Imager4MRT* influences the spatial (e.g. increasing the spatial noise) and temporal (e.g. discharges in and around the optical sensor) stability of the MR scanner, the obtained images (Fig. 2.4A and 2.4B) were analyzed and compared according to Friedman and Glover (2006). The results are shown in Fig. 2.5 with a short description of the parameters. For a more detailed description refer to Friedman and Glover (2006). It is important to note that no significant difference for any parameter was found using a two-sided t-test with a significance level of 0.05. This means that the *Imager4MRT* does not influence the spatial and temporal stability of the MR scanner.

Anatomical scan and fMRI

To determine the subject-specific localization of the motor cortex, a functional measurement applying a finger tapping paradigm was performed before the combined measurements. This allowed a positioning of the *Imager4MRT* over the targeted cortex area. The stimulus sequence consisted of finger tapping, 16 s tapping and 16 s recovery, which was repeated 13 times. The software Presentation® (Neurobehavioral Systems Inc., Albany, CA, USA) was used to generate an auditory signal for the subject to indicate each single tapping event. The time between two tapping events was varied between 475 to 525 ms. The auditory signal was transmitted through the headphones, which subjects generally wear during MR scanning.

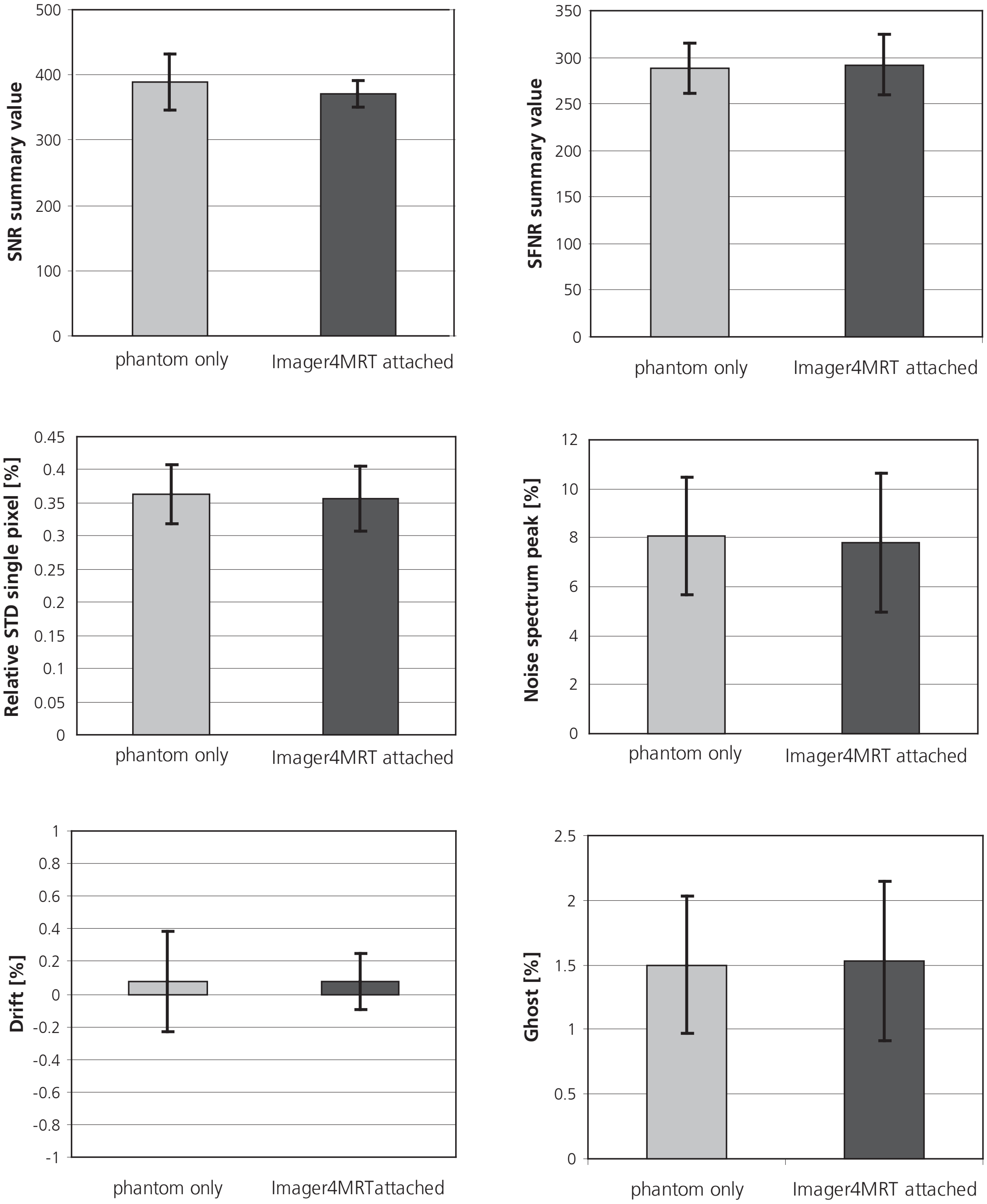

Figure 2.5 – Quantitative comparison of the spatial and temporal signal stability of the MR scanner assessed for a spherical phantom only and the spherical phantom with atteched *Imager4MRT*. *SNR summary value*: static spatial noise variance, *SFNR*: signal-to-temporal fluctuation-noise ratio, *Relative STD single pixel*: relative standard deviation for single pixels, *Noise spectrum peak*: maximum aplitude of temporal noise spectrum, *Drift*: Drift of MR signal, *Ghost*: percentage of ghost signal to the real signal (Friedman and Glover 2006)

The computer running Presentation®, the MR scanner and the ISS Oxiplex® were time-synchronized by using an analog trigger signal issued by the MR scanner. This setup and stimulus paradigm was used for all functional measurements.

Using a custom-built headband with holes for detectors and sources enabled to shift hair aside, which would have blocked the detectors and sources, and hence reduced light attenuation by hair. Elastic bandages (Derma Plast®, IVF Hartmann AG, Neuhausen, Switzerland) were used to attach the *Imager4MRT* at the head.

After attaching the *Imager4MRT* over the left motor cortex area, the anatomical head scan was performed using a T1-weighted TFE sequence. Further scan parameters are given in Tab. 2.3. Six slices of the anatomical scan are shown in Fig. 2.6. One slice is located below the position of the *Imager4MRT* and five slices are located within the position of the sensor. The optical sensor is clearly visible on the MR scans and produces no visible artifacts.

The data set of the anatomical scan was imported to MRIcro (Rorden n.d.), a freely available image processing software. A 3D model of the head with attached optical NIRI-MRI sensor was generated from the anatomical scan (Fig. 2.7), using the surface render function of MRIcro. The figure shows that using an anatomical scan the *Imager4MRT* is clearly visible at subject's head and thus co-registration between NIRI and MR data is simple to perform. In addition, the exerted pressure from the headband is apparent at the forehead and below sensor's location the crumpled skin and fat layer can be seen.

For the functional measurements, the BOLD signal was analyzed online using IviewBold (Philips Healthcare, Best, The Netherland) with the following constraints: the *minimal cluster size* was 9 pixels, the *threshold value* 5% and the noise discard level *mask* was 79 arbitrary units. The results of a representative activation are displayed in Fig. 2.8. The comparison between the activation without and with *Imager4MRT* attached has shown that the sensor does not influence the BOLD signal (data not shown). In contrast to the anatomical scan, the *Imager4MRT* can not be seen in the functional MR scan due to different contrast of the sequences.

In conclusion, the *Imager4MRT* allows the simultaneous acquisition of fNIRI and fMRI data in a simple setup. Furthermore, the visibility of the optical sensor in an anatomical scan allows the experimenter to co-registrate fNIRI and fMRI data.

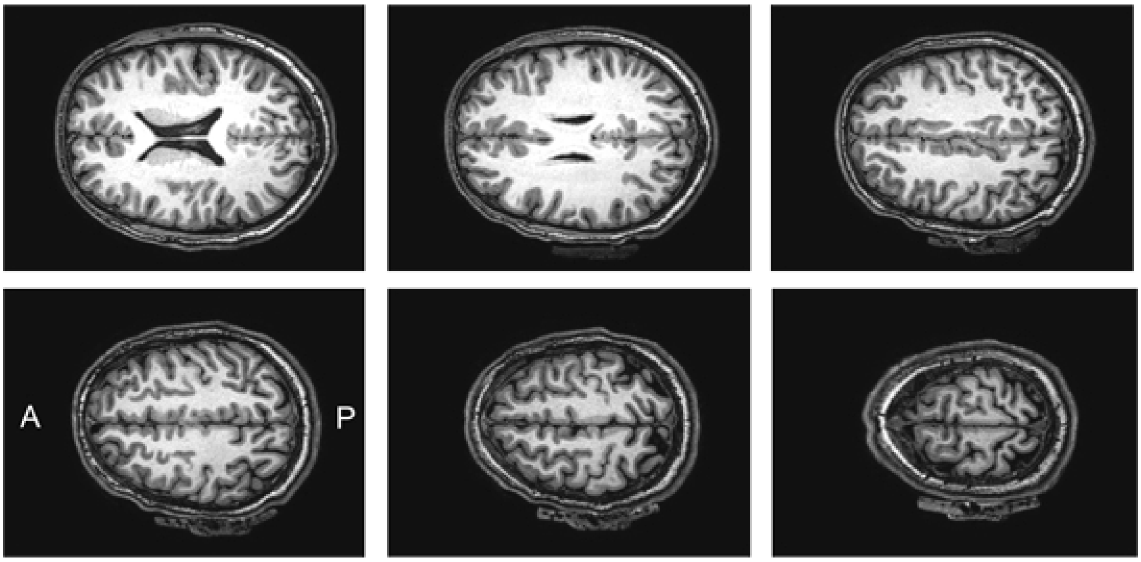

Figure 2.6 – Displayed are six slices of an anatomical MR head scan with *Imager4MRT* attached to the head. For the orientation, A: anterior and P: posterior.

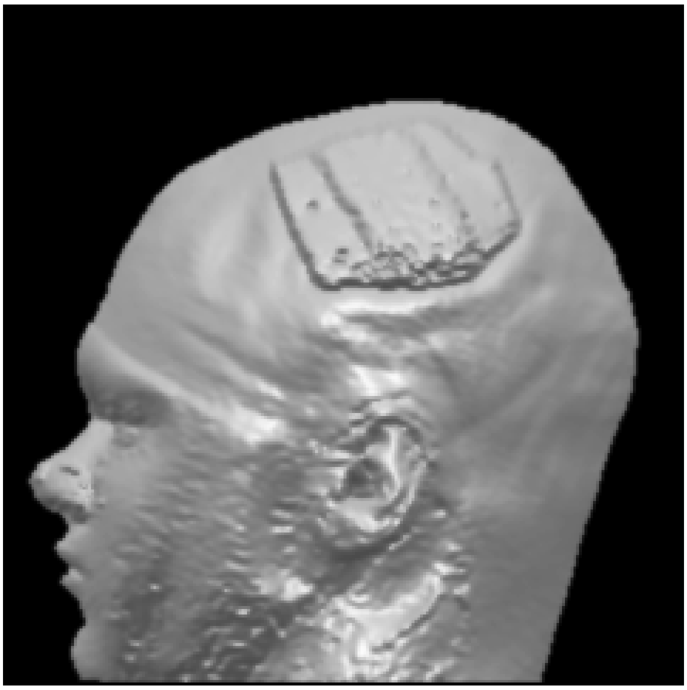

Figure 2.7 – 3D model of the head with attached *Imager4MRT* reconstructed from the anatomical scan.

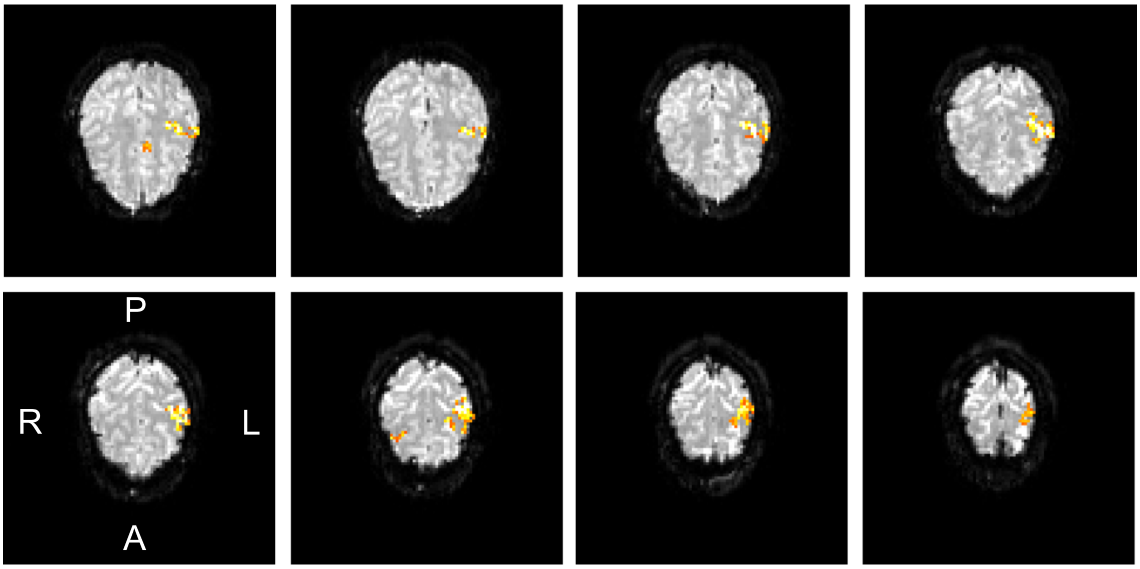

Figure 2.8 – Functional activation maps for a finger tapping paradigm. For the orientation, A: anterior, P: posterior, L: left and R: right.

2.2 Characterization using diffuse optical imaging

2.2.1 Background

This section describes the ability of the *Imager16* and *Imager4MRT* to localize an object with higher absorption than the medium it is contained in. For this purpose, simulations were performed with varying position of the object. This simulations give a best case estimate for the reconstruction of in-vivo measurements, since instrumental and physiological noise and the heterogenity of the tissue is neglected.

For the *UMTS exposure study*, only relative changes in O_2Hb and HHb concentrations were of interest, which are calculated from changes in μ_a. Therefore, changes in μ_s' were not considered in the characterization of the sensor with DOI. Furthermore, scattering was assumed to be constant, which is a common assumption in DOI and near infrared spectroscopy (Matcher, Elwell, Cooper, Cope and Delpy 1995, Wray et al. 1988). This is a valid assumption, since the only scatterers with time-varying concentrations are blood constituents - erythrocytes, leukocytes and thrombocytes - representing only a small fraction of total tissue scattering (Matcher, Elwell, Cooper, Cope and Delpy 1995).

In the majority of older DOI studies, the image was reconstructed with measurements using single source-detector distances and without overlapping light paths (Franceschini et al. 2000, Fantini, Franceschini, Gratton, Hueber, Rosenfeld, Maulik, Stubblefield and Stankovic 1999). This restricts the spatial resolution to the source-detector distance, which is usually between 2 and 4 cm. In the past ten years, optical systems were developed providing overlapping light paths and an increased spatial resolution better than 1 cm^3 (Boas, Dale and Franceschini 2004, Dehghani et al. 2009).

Due to high scattering of near-infrared light in biological tissue, resolution in the horizontal plane and in depth is restricted. Multiple scattering per photon occurs in tissue and causes features to blur. Beside these physical restrictions, other factors such as the number of source-detector combinations integrated in a sensor and the arrangement of source and detector positions determine the resolution. Furthermore, due to the limited number of sources and detectors in DOI, the volume of interest located under the sensor is not probed homogeneously. This means that the sensitivity of DOI to absorption changes is not homogeneous over the probed volume and depends highly on the sensor geometry used and on the position of the absorption change with respect to source and detector positions. This is the reason, why one should perform a sensitivity analysis for all novel sensors, taking into account the resolution in the horizontal plane and in depth.

Not only the resolution depends on the position of the absorption change relative to sources and detectors, but also its amplitude. Depending on the position of a higher absorbing volume in respect to source and detector positions, it will get probed by more or less light and leads to a higher or lower reconstructed absorption change. This is known as the *partial volume effect*. Thus, when measurements are only performed with NIRS or DOI, it is not possible to obtain accurate quantitative measures for the absorption changes. However, (Boas, Dale and Franceschini 2004) showed that the quantitative accuracy of DOI can be improved when it is used in combination with structural and functional magnetic resonance imaging (MRI). The structural MRI will provide constraints to the image reconstruction so that it is cortically restricted and the functional MRI will provide information about the location of the brain activation.

2.2.2 Introduction to DOI

Performing optical imaging depends on the usage of an appropriate model of photon transport and on solving an inverse problem. A very good synopsis about models and image reconstruction methods is given by Arridge and Hebden (1997). The modeling of photon transport through the tissue and the amount of light collected by the detectors is known as the *forward problem*. The reconstruction of changes in the optical coefficients using the information from the detected light, is the so-called *inverse problem*.

To describe photon transport in highly scattering media, the radiative transfer equation (RTE) (Chandrasekhar 1950) can be approximated by the diffusion equation. The photon fluence rate $\Phi(r)$ $(photons/[cm^2 \cdot s])$ can be described by the diffusion equation (Furutsu 1980) given in Eq. 1.1

$$\left[\nabla^2 + \frac{i\omega - v\mu_a(r)}{D}\right]\Phi(r) = \frac{-v}{D}q_0(r),$$

where r is a position vector, q_0 stands for an modulated isotropic source (Eq. 1.2), μ_a is the spatially varying absorption coefficient, ω the modulation frequency of the laser light, $D = v/3\mu_s'$ the diffusion coefficient and v light's velocity in the medium defined by c_0/n with c_0 the vacuum light speed and n the index of refraction. The photon fluence rate $\Phi(r,t)$ is proportional to the photon density $U(r,t)$ [photons/cm^3] used in chapter 1.1: $\Phi(r,t) = v \cdot U(r,t)$ (Boas, Dale and Franceschini 2004).

The diffusion approximation is the most widely used approach in the field of DOI and differences to approximations considering higher-order terms are neglectable for modulation frequencies below 1 GHz and high-scattering tissues (Arridge 1999).

To image the optical properties of heterogeneous tissue a *perturbation approach* is applied, where the absorption coefficient μ_a is divided into a homogeneous background component and a spatially varying part $\delta\mu_a(r)$

$$\mu_a(r) = \mu_{a,0} + \delta\mu_a(r). \tag{2.1}$$

The scattering coefficient is assumed to be homogeneous for the following explanations and simulations. The photon fluence rate $\Phi(r_d, r_s)$ can as well be separated in an incident photon fluence rate $\Phi_i(r_d, r_s)$ and a scattered photon fluence rate $\Phi_{sc}(r_d, r_s)$. $\Phi_i(r_d, r_s)$ is the incident photon fluence rate on the detector due to interactions with the background medium and $\Phi_{sc}(r_d, r_s)$ due to the inhomogeneities. r_s is the position of the source for which the photon fluence rate is measured at the detector positioned at r_d. Using the *Rytov approximation*, which is much more suitable for most biological situations than the *Born approximation* (O'Leary 1996), $\Phi(r_d, r_s)$ can be expressed as

$$\Phi(r_d, r_s) = \Phi_i(r_d, r_s) \cdot e^{\Phi_{sc}(r_d, r_s)}. \tag{2.2}$$

The first-order scattered photon fluence rate $\Phi_{sc}^{l=0}(r_s, r_s)$ in the *Rytov approximation* is

$$\Phi_{sc}^{l=0}(r_d, r_s) = -\frac{1}{\Phi_i(r_d, r_s)} \int_V G(r_d, r)\Phi_i(r, r_s)\frac{v\Delta\mu_a(r)}{D} d^3r. \tag{2.3}$$

In the following, $\Phi_{sc}^{l=0}(r_s, r_s)$ is abbreviated as $\Phi_{sc}(r_s, r_s)$. For measurements at the human head it is justified to assume a semi-infinite medium (Boas, Dale and Franceschini 2004). To find the Green function for this geometry, the method of images was applied. The source was modeled one mean free path length l_{tr} ($\sim 1/\mu'_{sp}$) into the medium (Haskell et al. 1994). In the so-called extrapolated boundary condition, the photon fluence rate is non-zero at the physical boundary, but zero at a distance z_b out of the medium,

$$z_b = \frac{2}{3\mu'_s}\left(\frac{1 + R_{eff}}{1 - R_{eff}}\right). \tag{2.4}$$

R_{eff} is the effective reflection coefficient from inside of the medium. For the method of images and a semi-infinite medium the following Green function is obtained

$$G(r_d, r) = \frac{-1}{4\pi\,|r_d - r|} e^{ik_0|r_d - r|} + \frac{1}{4\pi\,|r_d - r_i|} e^{ik_0|r_d - r_i|}, \tag{2.5}$$

where r is the position of the source one mean free path length below the surface of the medium and r_i the position of the image source located $z_b + l_{tr}$ above the surface. In practice, the *perturbation approach* is realized by performing difference measurements to estimate $\Phi_{sc}(r)$ as the difference between two known states. Performing a measurement of the homogeneous medium and one of the homogeneous medium with inhomogeneity or an activation, $\Phi_{sc}(r)$ can be calculated as

$$\Phi_{sc}(r) = ln\frac{\Phi(r)}{\Phi_i(r)}. \tag{2.6}$$

Replacing the integral in Eq. 2.3 by a discretization of the volume and considering only the real part of Φ_{sc}, the following system of linear equations($Ax = b$) is obtained (O'Leary

1996)

$$\begin{pmatrix} \Re(\Phi_{sc}(\vec{r}_{d1},\vec{r}_{s1})) \\ \vdots \\ \Re(\Phi_{sc}(\vec{r}_{dm},\vec{r}_{s1})) \end{pmatrix} = \begin{pmatrix} ln\left(\frac{A}{A_0}\right)(\vec{r}_{d1},\vec{r}_{s1}) \\ \vdots \\ ln\left(\frac{A}{A_0}\right)(\vec{r}_{dm},\vec{r}_{sm}) \end{pmatrix} = \begin{pmatrix} \Re(W_{11}) & \dots & \Re(W_{1N}) \\ \vdots & \ddots & \vdots \\ \Re(W_{m1}) & \dots & \Re(W_{mN}) \end{pmatrix} \begin{pmatrix} \delta\mu_a(\vec{r}_1) \\ \vdots \\ \delta\mu_a(\vec{r}_N) \end{pmatrix}, \tag{2.7}$$

with

$$W_{ij} = \frac{V_{voxel}}{D \cdot \Phi_i(\vec{r_{di}},\vec{r_{si}})} G(\vec{r_{di}},\vec{r_j})\Phi_i(\vec{r_{di}},\vec{r_{si}}). \tag{2.8}$$

Considering also the imaginary part of Φ_{sc} leads to

$$\begin{pmatrix} \Re(\Phi_{sc}(\vec{r}_{d1},\vec{r}_{s1})) \\ \vdots \\ \Re(\Phi_{sc}(\vec{r}_{dm},\vec{r}_{s1})) \\ \Im(\Phi_{sc}(\vec{r}_{d1},\vec{r}_{s1})) \\ \vdots \\ \Im(\Phi_{sc}(\vec{r}_{dm},\vec{r}_{s1})) \end{pmatrix} = \begin{pmatrix} ln\left(\frac{A}{A_0}\right)(\vec{r}_{d1},\vec{r}_{s1}) \\ \vdots \\ ln\left(\frac{A}{A_0}\right)(\vec{r}_{dm},\vec{r}_{sm}) \\ (\phi-\phi_0)(\vec{r}_{d1},\vec{r}_{s1}) \\ \vdots \\ (\phi-\phi_0)(\vec{r}_{dm},\vec{r}_{sm}) \end{pmatrix} = \begin{pmatrix} \Re(W_{11}) & \dots & \Re(W_{1N}) \\ \vdots & \ddots & \vdots \\ \Re(W_{m1}) & \dots & \Re(W_{mN}) \\ \Im(W_{11}) & \dots & \Im(W_{1N}) \\ \vdots & \ddots & \vdots \\ \Im(W_{m1}) & \dots & \Im(W_{mN}) \end{pmatrix} \begin{pmatrix} \delta\mu_a(\vec{r}_1) \\ \vdots \\ \delta\mu_a(\vec{r}_N) \end{pmatrix}. \tag{2.9}$$

A_0 and ϕ_0 are the amplitude and phase measured at the detector for the homogeneous case and A and ϕ for the total system (homogeneous plus inhomogeneity or activation).

The linear equations 2.7 and 2.9 are ill posed and underdetermined, since the discretization of the volume of interest leads usually to more voxels than the number of measurements. To solve the system of linear equations, a linear reconstruction technique, namely the *Simultaneous Iterative Reconstruction Technique* (SIRT) (Kak and Slaney 2001) is applied. A comparison of different linear reconstruction technique is given by Gaudette et al. (2000). Since the system of linear equations is ill-posed, it can lead to artifacts in the reconstructed image.

Boas et al. (1997) performed an extensive analysis about detecting and characterizing optical inhomogeneities within a homogeneous medium. A slab geometry was used and measurements were carried out in the transmission mode. They examined the influence of different moments of the scattered fluence rate Φ_{sc} on the reconstruction. They showed that for reconstructions using only the monopole moment of the scattered fluence rate $\Phi_{sc}^{l=0}$ (Boas 1997), objects as small as 0.3 cm in diameter can be detected. Above this limit, a small, highly absorbing object cannot be discriminated from a larger, less-absorbing object. In the case, where the inhomogeneity with volume a^3 and the medium exhibit an absorption difference of $\delta\mu_a$, but the same scattering coefficient, one can only reconstruct the product of $a^3\delta\mu_a$. All the possibilities of a^3 and $\delta\mu_a$ combinations define a family of solutions. O'Leary (1996) mentioned that the higher the number of iterations for solving the linear equation system the smaller and more absorbing the object was. This was explained such that increasing the number of iterations moved the reconstruction through this family of solutions; notably always in the same way if the initial guess is the same.

Boas et al. (1997) mentioned that a scanning of source and detector along three orthogonal axis allows the detection of the central (X/Y/Z) coordinates of the object. This is possible for setups based on the transmission mode, but not for the ones based on the reflection mode. This is the reason why absorbing objects can be localized in depth for the transmission mode, whereas depth localization is very restricted in the reflection mode. In reflection mode, the resolution decreases also rapidly with increasing depth into the brain. Several research groups showed that depth resolution in reflection mode can be improved by providing overlapping light paths (Dehghani et al. 2009, Boas, Chen, Grebert and Franceschini 2004).

Thus, it is necessary to perform simulations for a novel NIRI sensor to obtain a qualitative measure of its ability to localize optical changes. In addition, correlations between *real* and *reconstructed* depth were carried out to characterize a best case scenario of depth reconstructions for the *Imager16*. The characterization applies also to the *Imager4MRT*, since the sensor geometry is the same as for the *Imager16*. Other approaches to achieve depth resolution are covered in chapter 2.3.

2.2.3 Simulation settings

The following simulations were carried out for the novel sensor:

- Simulation A: the three-dimensional reconstruction of a local activation volume (a sphere) in a depth of 1.5 cm was simulated. The volume was positioned at different locations. These simulations mimic a local activation in the human cortex and assess the ability to localize activation volumes with the *Imager16*.

- Simulation B: simulations with a higher absorbing sphere at different depths were carried out to estimate the ability to obtain depth information using the *Imager16* and image reconstruction. The *real* depth of the absorbing sphere was correlated with the *reconstructed* depth.

All simulations were carried out with the photon migration imaging software (PMI). PMI is freely available on the website of *Martinos center for biomedical imaging*. The simulation is based on solving the diffusion equation, which was described earlier in the introduction. The parameters were set to simulate measurements at the human head, but neglected the influence of blood circulation in the skin.

The SIRT algorithm was applied with 200 iterations. The medium properties were set as follows: $\mu_a = 0.15\ \mathrm{cm}^{-1}$, $\mu_s' = 5.0\ \mathrm{cm}^{-1}$ (Choi et al. 2004) and the index of refraction was set to 1.37. Since $\mu_s' >> \mu_a$ and the source-detector distance $\rho > 1$ cm, the assumption of the photon propagation as a diffusive process is valid.

2.2.4 Simulation A: reconstruction of local activation volumes

Within the homogeneous medium a sphere with a radius of 0.5 cm was placed at a depth of 1.5 cm. μ_a was 0.05 cm^{-1} higher than μ_a of the medium and μ_s' of the sphere and the medium were equal. The position of the sphere was altered within one sensor quadrant to test the reconstruction performance and space resolution.
The following representative sphere positions were selected for the simulation:

- Position A: (X/Y) = (0/0) cm, where the sphere is located in the middle of both detectors and the closest source positions.
- Position B: (X/Y) = (-1/0) cm, where the sphere is located under the closest source position.
- Position C: (X/Y) = (-2/0) cm, where the sphere is located in the middle of four source position.
- Position D: (X/Y) = (-3/0) cm, where the sphere is located under the farthest source position.
- Position E: (X/Y) = (0/0.7) cm, where the sphere is located horizontally at the right side and vertically in the middle of the sensor quadrant.
- Position F: (X/Y) = (-1/0.7) cm, where the sphere is located horizontally on the same height as the closest source position and vertically in the middle of the sensor quadrant.
- Position G: (X/Y) = (-2/0.7) cm, where the sphere is located horizontally in the middle of four source positions and vertically in the middle of the sensor quadrant.
- Position H: (X/Y) = (-3/0.7) cm, where the sphere is located horizontally at the left side and vertically in the middle of the sensor quadrant.
- Position I: (X/Y) = (0/1.4) cm, where the sphere is located under a detector.

The depth of the sphere was -1.5 cm. The voxel size for the simulations was 0.1 cm^3. The absorption difference $\Delta\mu_a$ was reconstructed in the horizontal plane at a depth of -1.5 cm (Fig. 2.9A - 2.11A). The position of the sphere is given in the captions of the subfigures. In addition, the maximum absorption change in all horizontal planes is plotted in dependency of the depth z. These reconstructed depth profiles are shown in Fig. 2.9B - 2.11B, where the real sphere position is shaded in grey.

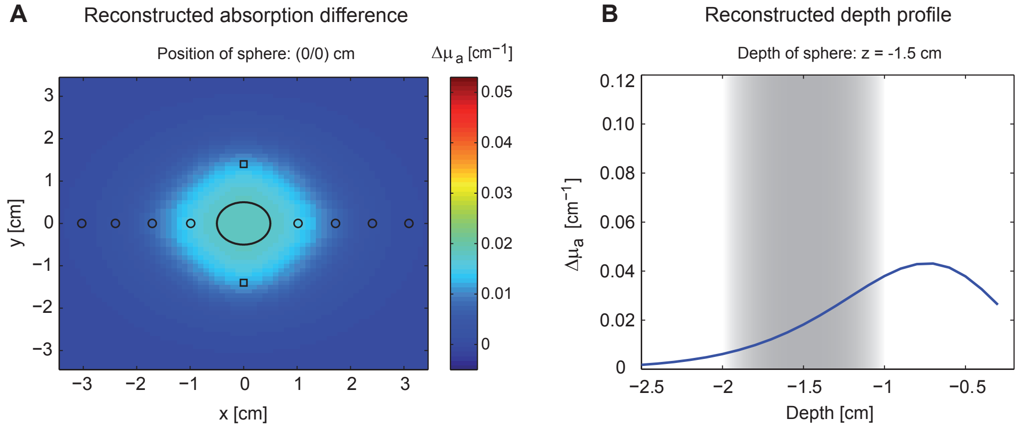

(a) Sphere position A

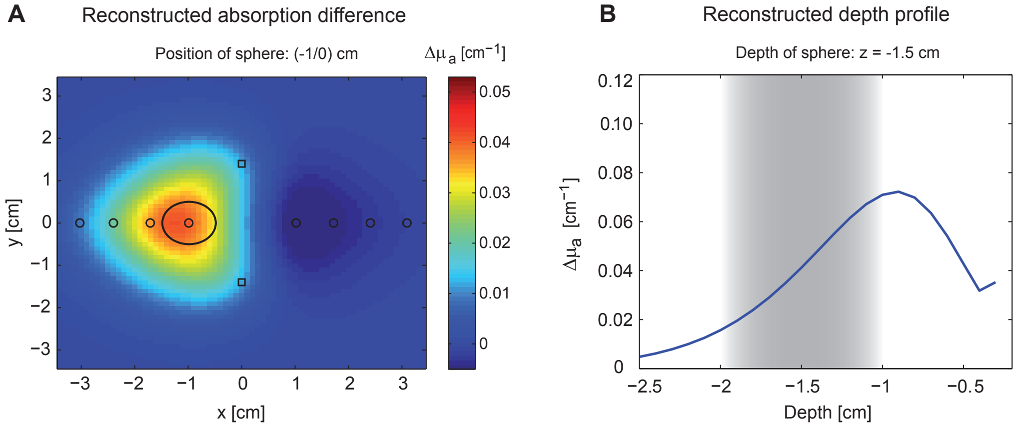

(b) Sphere position B

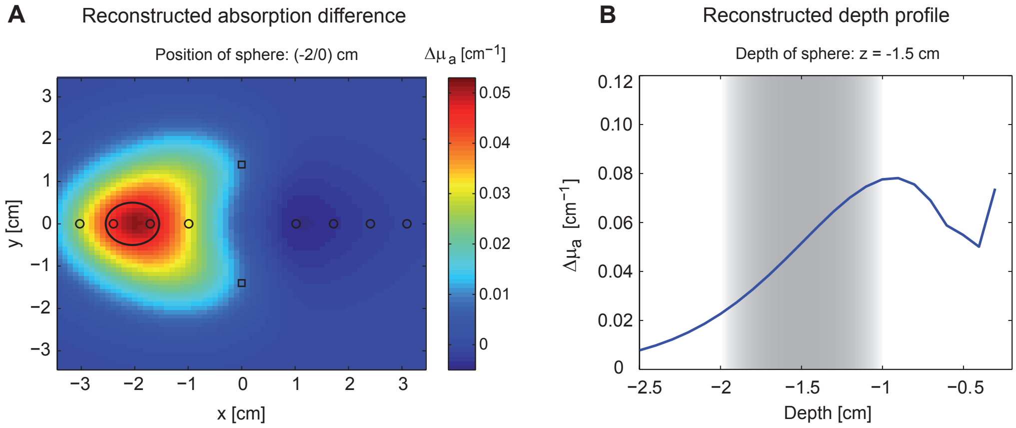

(c) Sphere position C

Figure 2.9 – Simulation of the image reconstruction process for three different sphere positions: A, B and C. **A**: reconstructed absorption difference in the horizontal plane at a depth of 15 mm. The smaller black ellipses represent the position of the light sources and the black rectangle the position of the detectors. The larger black ellipse marks sphere's position. **B**: reconstructed depth profile (z axis) of the absorption difference. The location of the sphere is shaded in grey.

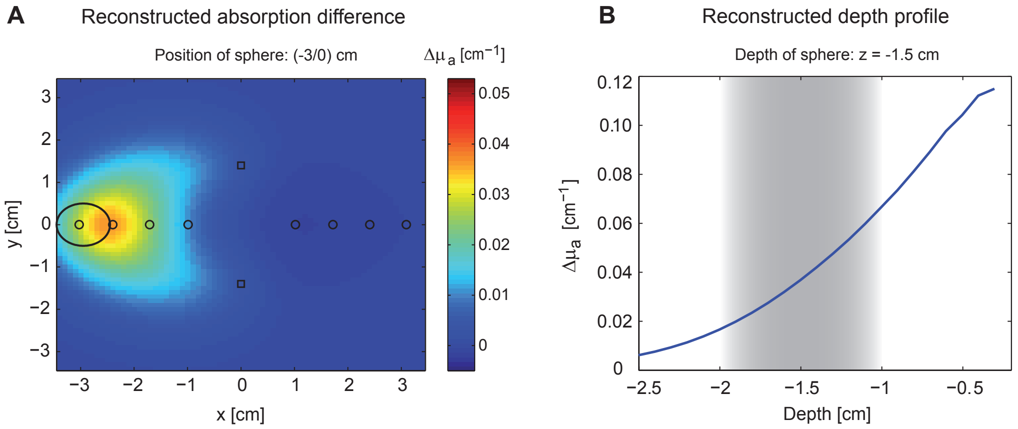

(a) Sphere position D

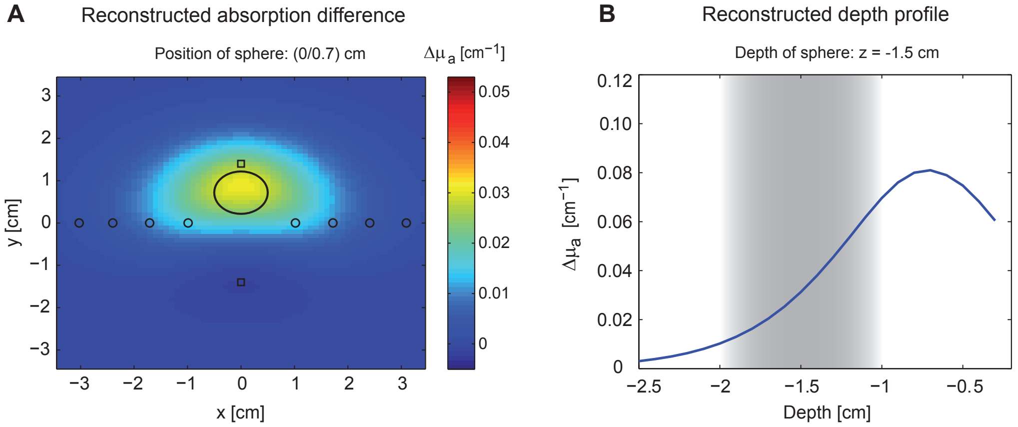

(b) Sphere position E

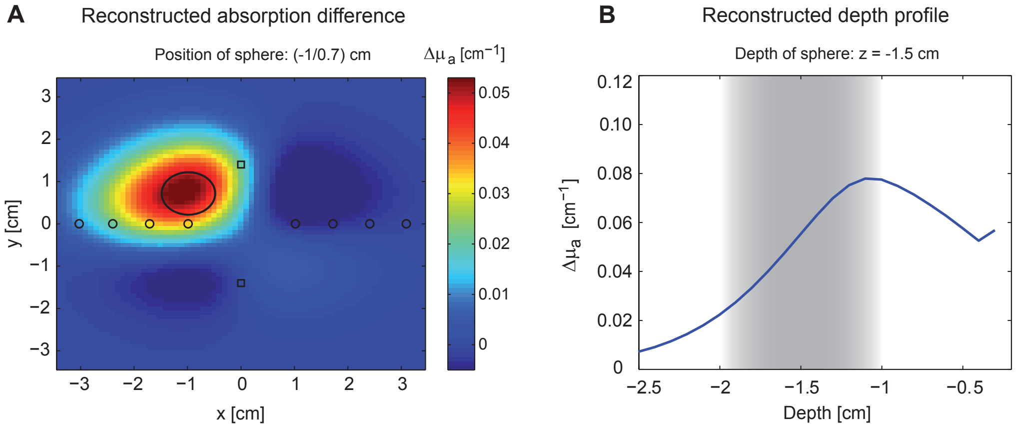

(c) Sphere position F

Figure 2.10 – Simulation of the image reconstruction process for three different sphere positions D, E and F. **A**: reconstructed absorption difference in the horizontal plane at a depth of 15 mm. The smaller black ellipses represent the position of the light sources and the black rectangle the position of the detectors. The larger black ellipse marks sphere's position. **B**: reconstructed depth profile (z axis) of the absorption difference. The location of the sphere is shaded in grey.

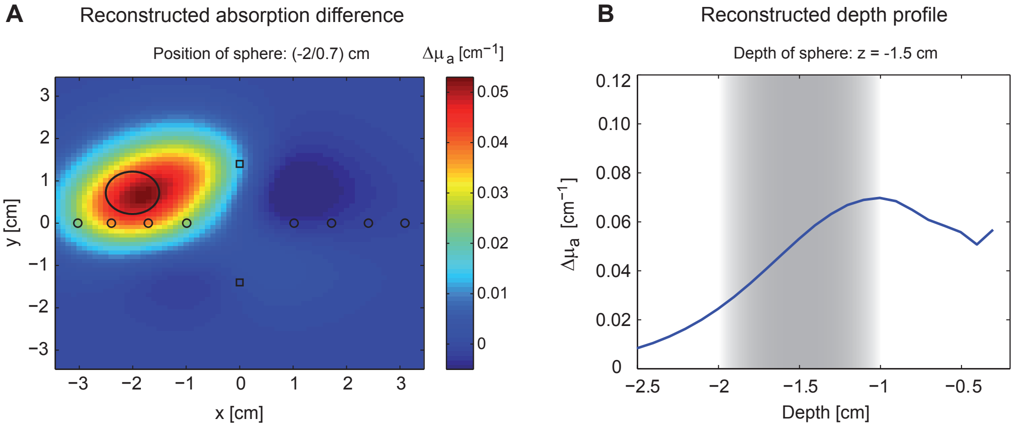

(a) Sphere position G

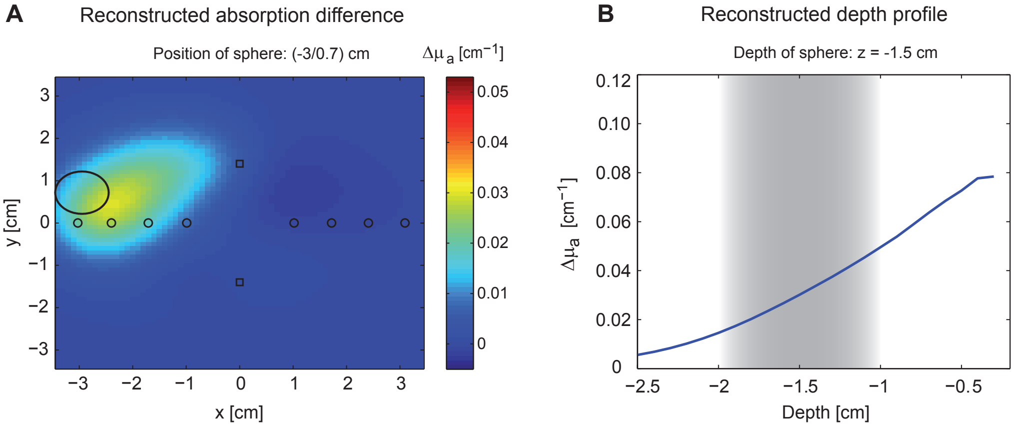

(b) Sphere position H

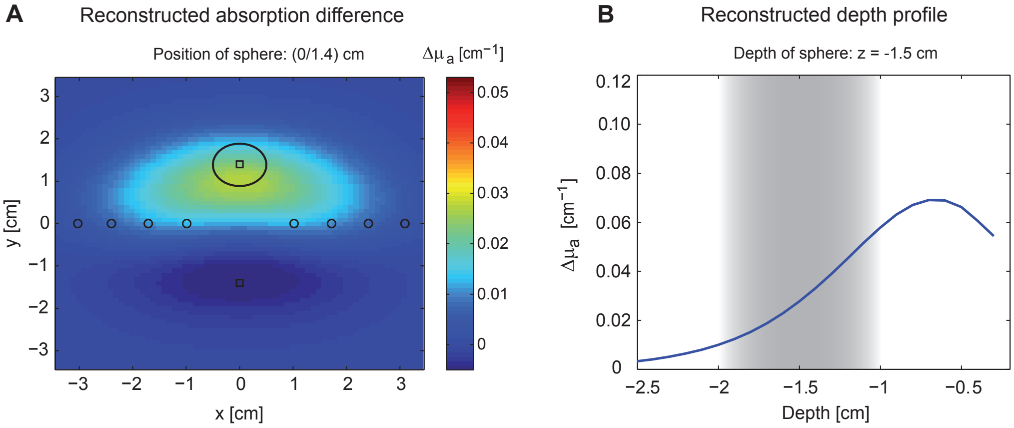

(c) Sphere position I

Figure 2.11 – Simulation of the image reconstruction process for three different sphere positions G, H and I. **A**: reconstructed absorption difference in the horizontal plane at a depth of 15 mm. The smaller black ellipses represent the position of the light sources and the black rectangle the position of the detectors. The larger black ellipse marks sphere's position. **B**: reconstructed depth profile (z axis) of the absorption difference. The location of the sphere is shaded in grey.

2.2.5 Conclusions: simulation A

The localization in the horizontal plane for all sphere positions agrees quite well with the real position, but the reconstructed geometry and the optical properties of the sphere depend highly on its position with respect to the optical sensor.

Reconstructed images and depth profiles are more accurate for sphere positions that are probed by multiple overlapping light paths, e.g. positions B, C, F and G,. In extreme cases, where only one light path probes the object, e.g. position D and H, the problem is undetermined. The missing information leads to a poor resolution in the horizontal plane and no information about the depth of the object can be obtained. In the case where the sphere is located in the middle of two sources and detectors - position A - the object gets equally sampled by all four source-detector combinations, but due to the short distance of 1.5 cm between source and detector each path measures only part of the object. Thus, lower absorption values are obtained for the sphere compared to other simulations.

For all depth profiles, the simulation results place the sphere closer to the surface than it is in reality. This is a common problem for measurements in the reflection mode and in reconstructions using a norm minimization (Boas, Dale and Franceschini 2004). Firstly, the reflection mode provides no measurements along the z-dimension and secondly, norm minimizations bias the solution towards smaller absorption amplitude, which is achieved by shifting the object closer to the surface and to regions with higher sensitivity (Boas, Dale and Franceschini 2004).

The real size of the object and its absorption coefficient cannot be determined since the solution of the problem is not unique and only the product $a^3\delta\mu_a$ is determinable and preserved (Boas et al. 1997).

The simulations present the best case scenario and do not consider instrumental and physiological noise. When reconstructing an in-vivo experiment, the signal-to-noise ratio plays an important role. Since solving the linear equation system is already ill posed, insufficient signal quality will lead to noisy and coincidental reconstructed images. Thus, diffuse optical imaging was also applied on in-vivo measurements (section 2.3, part in-vivo measurements).

Nevertheless, the resolution in the horizontal plane obtained in the simulations for the *Imager16* is comparable to simulations with other optical sensors (Haensse et al. 2005).

2.2.6 Simulation B: correlation between *real* and *reconstructed* depth for local activation volumes

In order to characterize the correlation between *real* and *reconstructed* depth of a sphere, simulations with varying sphere depth were performed. These simulations were conducted at the same sphere positions as in the section before but with varying object depths from -0.6 cm to -2.5 cm (object centre). The voxel dimension in z direction was reduced to 0.05 cm as compared to 0.1 cm in the earlier simulations to achieve a higher accuracy for the reconstructed depth. The maximal number of voxels and thus the minimal voxel length in all directions is limited by the memory capacity of the computer used.

For each object depth (*real* depth), a depth profile was plotted (analogue to Fig. 2.9-2.11B) and the depth at which the maximum absorption change occurred was calculated (*reconstructed* depth). The *reconstructed* versus the *real* depth was plotted for each sphere position (Fig. 2.12-2.14A). The relative error of the *reconstructed* depth to the *real*, $100 \cdot \frac{\textit{reconstructed}\ \text{depth} - \textit{real}\ \text{depth}}{\textit{real}\ \text{depth}}$ is shown in Fig. 2.12-2.14B. Sphere depths for which relative errors are smaller than 35% are shaded in grey.

2.2.7 Conclusions: simulation B

The correlation between the *real* and *reconstructed* depth and the relative error in Fig. 2.12 - 2.14 showed that in general the depth of an object cannot be accurately determined by the *Imager16* and DOI. The simulations demonstrated that for a restricted set of object depths and positions, relative position errors smaller than 35% can be obtained. At these positions, the object was probed by light of several source-detector combinations with different distances leading to overlapping measurements and a better defined problem. In the best case, where the sphere is positioned at (-1/0.7/-1), a minimum relative error of 18% is achieved.

It can be seen in Fig. 2.12 - 2.14 that the *reconstructed* depth is correlated with the *real* depth often in a highly non-linear manner. For *real* depths smaller than 0.9 cm the sphere is mostly reconstructed at the surface, since no measurement path, which measures the homogeneous medium above the sphere is available. The relative error is the smallest at sphere depths, which are probed by overlapping measurements. Increasing the sphere depth increasingly lowers the number of overlapping measurements and leads to increasing relative errors.

However, a step in the depth profiles between -0.6 cm and -1.0 cm can be observed for most sphere positions and thus, it may be possible to discriminate between superficial and deep changes. This was tested in phantom and in-vivo experiments (section 2.3).

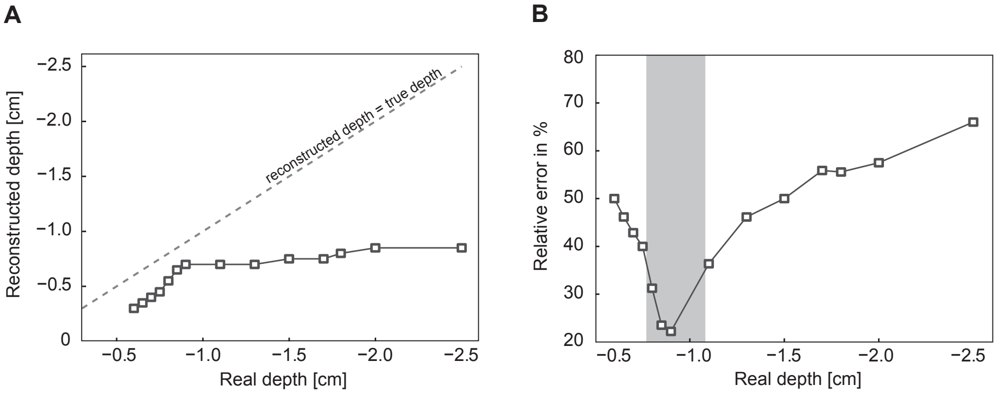

(a) Sphere position A

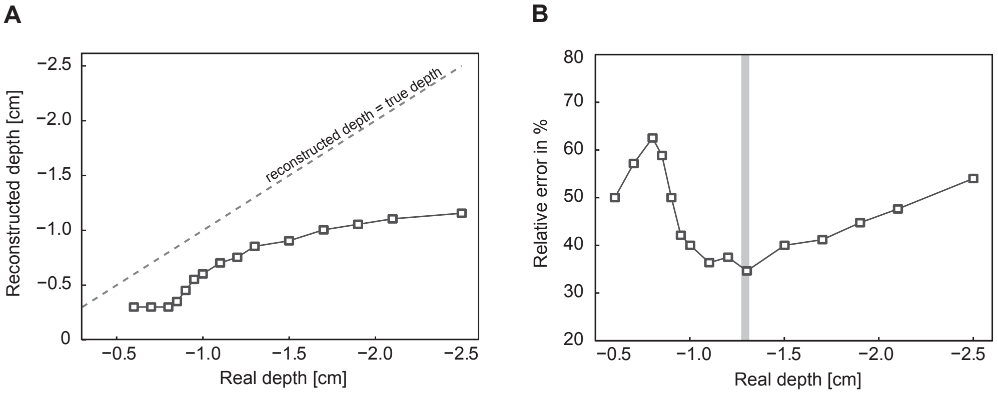

(b) Sphere position B

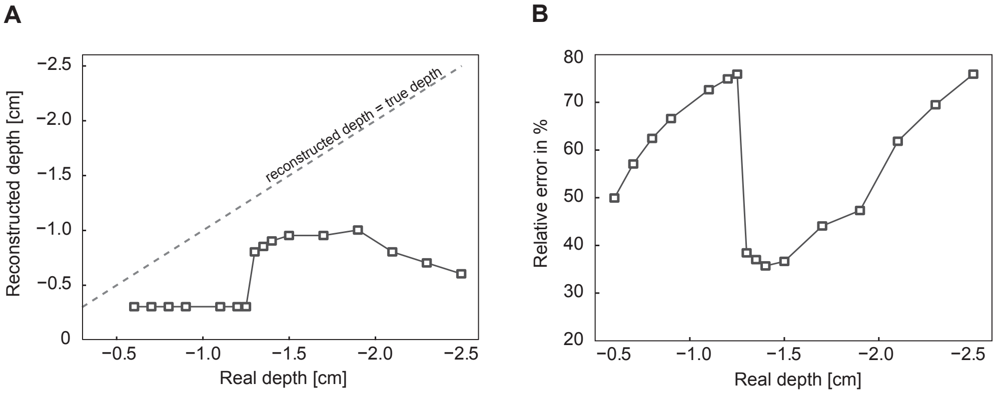

(c) Sphere position C

Figure 2.12 – Simulation of the image reconstruction. **A**: correlation between *real* and reconstructed depth. The dotted line describes the theoretical behavior if the reconstructed depth is equal the *real* object depth. **B**: relative error of the reconstructed depth. Grey shaded represents depths with a relative error smaller than 35%.

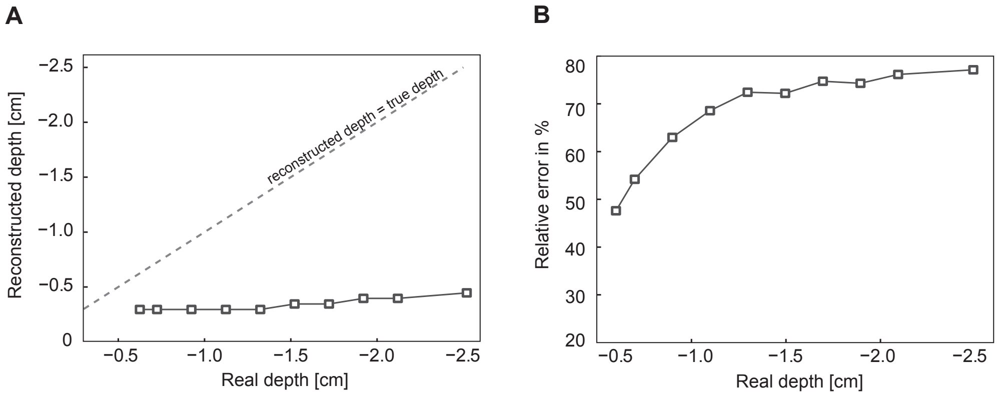

(a) Sphere position D

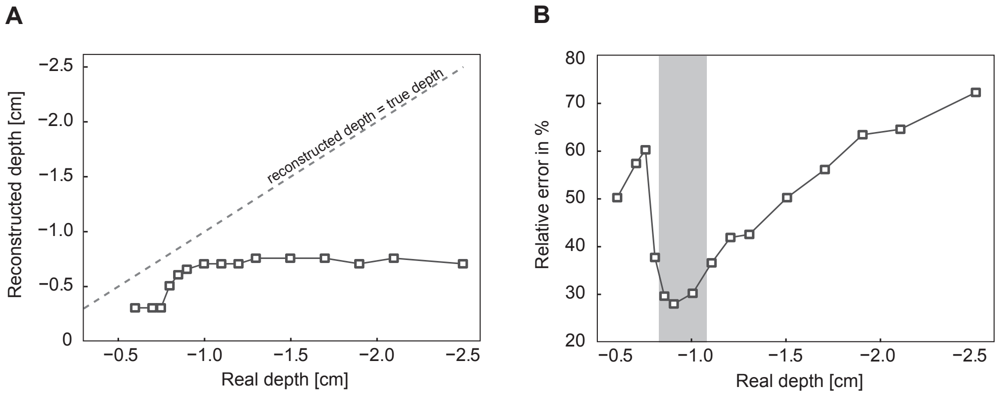

(b) Sphere position E

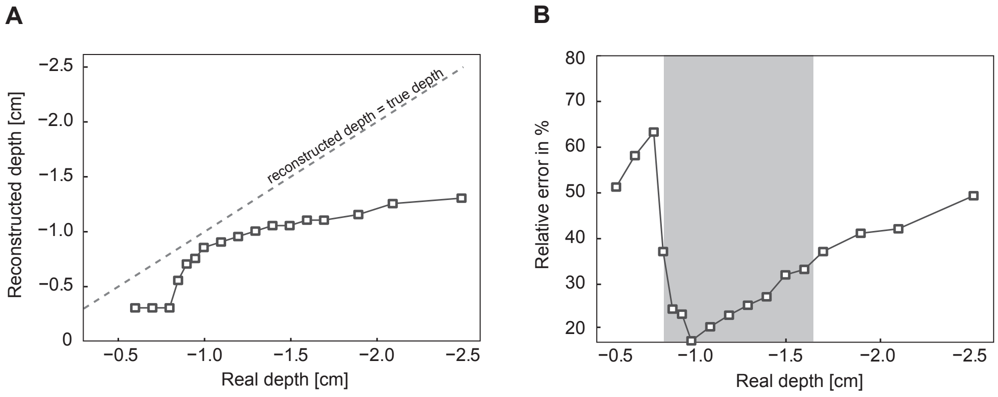

(c) Sphere position F

Figure 2.13 – Simulation of the image reconstruction. **A**: correlation between *real* and reconstructed depth. The dotted line describes the theoretical behaviour if the reconstructed depth is equal the *real* object depth. **B**: relative error of the reconstructed depth. Grey shaded represents depths with a relative error smaller than 35%.

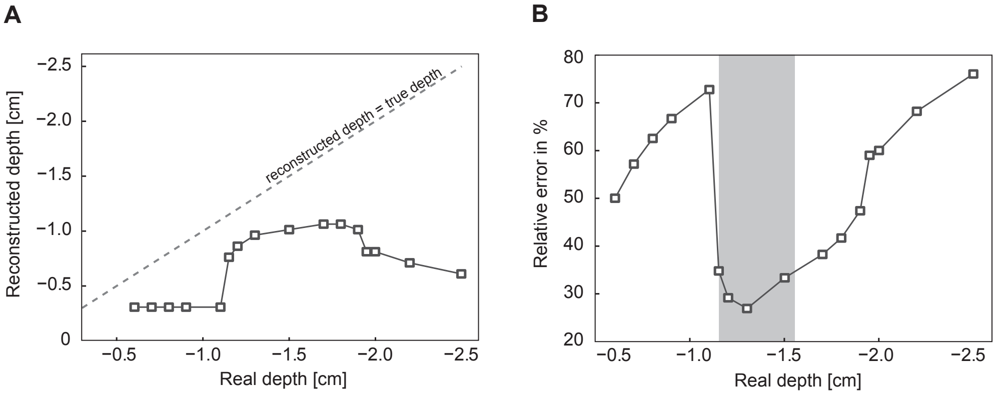

(a) Sphere position G

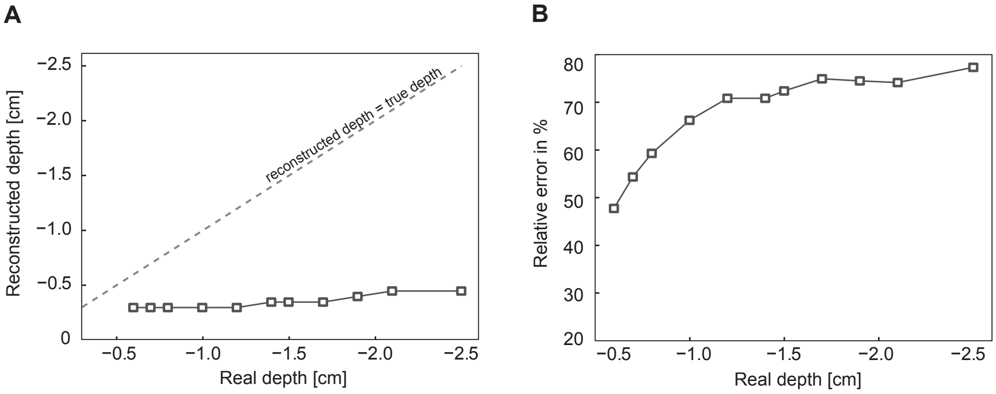

(b) Sphere position H

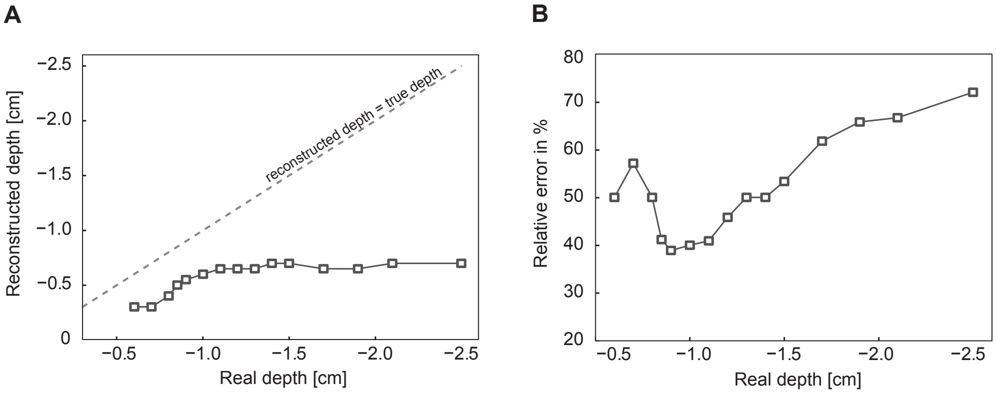

(c) Sphere position I

Figure 2.14 – Simulation of the image reconstruction. **A**: correlation between *real* and reconstructed depth. The dotted line describes the theoretical behaviour if the reconstructed depth is equal the *real* object depth. **B**: relative error of the reconstructed depth. Grey shaded represents depths with a relative error smaller than 35%.

2.2.8 Outlook

Dense imaging arrays (Boas, Chen, Grebert and Franceschini 2004, Zeff et al. 2007, Yamamoto et al. 2002, Bluestone et al. 2001), which became more popular in the past ten years, enhanced the spatial uniformity in the image resolution, image amplitude and improved the localization accuracy. However, although dense imaging arrays are a very promising imaging approach, as the optical sensor covers a larger surface area and the number of sources and detectors is higher, the equipment becomes more bulky and hence less practical. To date, all instruments with dense imaging arrays were custom-built in research laboratories.

Many efforts have been undertaken to improve imaging performance and several promising methods such as sophisticated brain models, use of a priori knowledge to define constraints and the use of a spatial deconvolution (Xu et al. 2005, Xu et al. 2007) were presented in the last years. The brain models range from schematic models taking the brain ayri into account (Okada et al. 1997) to models based on segmented anatomical MRI scans (Schweiger and Arridge 1999, Boas, Dale and Franceschini 2004, Custo et al. 2010). These models in combination with a priori spatial information about occurring concentration changes can be used to place constraints in the image reconstruction. For example, in functional measurements, the image reconstruction can be constrained to the cortex.

In addition, the computational power available today enables the application of more complex numerical models to describe photon transport in strongly diffusive tissues more accurately. For an overview of numerical models please refer to (Dehghani et al. 2009) and for a general overview of photon transport models and image reconstruction to (Arridge 1999).

The combination of dense imaging arrays, a priori structural information as spatial constraints and more complex numerical models will improve the image performance and accuracy of DOI. The future of DOI, especially if it is applied for clinical diagnosis and prognosis, will be determined by the achieved image quality and reliability of the reconstructed concentration changes.

Although dense imaging arrays seem promising, small planar sensors combined with methods described above will have some advantages in the future:

- Planar optical sensor are easy to handle and to attach.
- They are flexible and can be attached to different tissues or body parts, e.g. to muscles, the breast or head.
- The short time needed to attach the sensor allows to perform test measurements and to rearrange the sensor if necessary. This is especially useful for functional measurements, where the experimenter can record a test measurement and verify the correct placement.
- The system is compact, can be moved easily and allows measurement at the bedside of the patient.

2.3 Different approaches to obtain depth resolution

2.3.1 Background

In conventional NIRI brain studies, the depth of the measured hemodynamic signals remains unknown. Superficial fluctuations in the chromophore concentrations are not of interest in functional studies and Toronov et al. (2001) showed that the measured signal changes in response to a stimulus did originate from the brain.
However, for some NIRI research topics acquiring depth resolution is crucial and motivated by different aims:

- Separating the blood flow changes or oxygenation and hemoglobin concentration within the skin from those within the deeper tissue, e.g. the brain or the muscle.
- Improving the spatial correlation between fNIRI and fMRI.
- Localizing breast tumors or brain lesions with satisfying accuracy.

To achieve the second and third aim, more accurate photon transport models have been proposed. A priori information was incorporated in the models and multi-modal measurements were applied. Instead of a semi-infinite medium, photon transport can also be modeled in a multiple-layer medium (Okada et al. 1997, Alexandrakis et al. 1998, Kienle et al. 1998, Pham, Spott, Svaasand and Tromberg 2000) or in more sophisticated tissue models (Schweiger and Arridge 1999, Boas, Dale and Franceschini 2004, Custo et al. 2010). Although the models are very promising, they always require a priori knowledge about the thickness of the layers or accurate information about the underlying structure. To obtain subject-specific tissue models and to integrate them in the reconstruction process, fNIRI can be combined with anatomical MRI scans (Boas, Dale and Franceschini 2004, Schweiger and Arridge 1999).
The topic of separating superficial changes from changes in deeper tissue structures was approached by most research groups with the question how to eliminate superficial changes from the total optical signal (Saager and Berger 2005, Kohno et al. 2007). Saager and Berger (2005) proposed a least-square fitting method, in which the signal from a shorter source-detector distance is fitted to the signals measured at larger distances and afterwards subtracted to get rid of the superficial changes. This method is based on the assumption that the signal penetrates only the upper layer for short source-detector distances and thus is representative for the superficial changes. Another approach has been presented by Kohno et al. (2007), who showed that it is possible to extract the skin blood flow from the total NIRI signal by independent component analysis (ICA).
In clinical research, the most widely used approach is the multi-distance method (section 1.1), where optical changes in a superficial layer and the layer's optical properties cancel out for certain specific measurement configurations. Franceschini et al. (1998) used source-detector distances ranging from 1.5 to 4.5 cm and investigated the recovered optical properties in a two-layered turbid media in dependency of the thickness of the layer. They found that i) for a thickness of approximately 4 mm of the superficial layer, the optical properties were representative for the deeper layer and ii) for a thickness of approximately 13 mm of the superficial layer, the optical properties were representative

for this layer. For layer thicknesses in-between, the measured optical coefficients were a mixture of the optical properties of the superficial and deeper layer. These results also depend on the source-detector distances incorporated in the analysis (Choi et al. 2004). They performed measurements on the head of 30 volunteers and showed that for shorter source-detector distances, the optical coefficients of the scalp and skull were dominant. However, for longer source-detector distances the optical coefficients of the brain could be measured.

2.3.2 Discriminating superficial from deep changes

In the beginning of this thesis, the aim was to improve depth resolution methods to localize potential changes in the tissue. However, diffuse optical imaging based on a homogeneous semi-infinite medium which is the most promising method showed in simulations and measurements that it is unable to localize occurring changes accurately. It was found that for an accurate depth localization of absorption changes more sophisticated inversion algorithms and head models, such as subject-specific anatomical MR scans, are needed. Unfortunately the extra cost and work power needed exceeded by far the financial and temporal budgets of the project.

Thus, the aim was redefined to distinguish between superficial and deep effects, rather than to achieve accurate depth localization. This discrimination is important, because on the one hand the skin receives the highest dose of EMF and on the other hand the brain is a sensitive organ and results of previous studies indicated effects of EMF on rCBF (Huber et al. 2002, Huber et al. 2005). To achieve this discrimination, different approaches were evaluated in phantom and in-vivo measurements for the *Imager16*, which require no prior knowledge.

These approaches were:

A) The modified Lambert-Beer law (Eq. 2.3.3).

B) The slope comparison method based on the multi-distance approach (section 1.1).

C) Depth reconstruction based on DOI (section 2.2.2).

In the following chapters, the principle of the methods is explained, the performed measurements described and the results presented and discussed. The aim of this chapter is to demonstrate the ability of the *Imager16* to distinguish between superficial and deep structures. This ability is strongly dependent on the sensor geometry and the number of light paths and thus this chapter provides no conclusions about general NIRI performance, but rather for our specific NIRI sensor (section 2.1.2).

2.3.3 Principle

For measurements done in the reflection mode, depth resolution can be obtained due to the fact that different source-detector distances show a different depth sensitivity.

Following calculations assume a constant scattering coefficient.

The modified Lambert-Beer law

The modified Lambert-Beer law (Matcher, Elwell, Cooper, Cope and Delpy 1995, Wray et al. 1988)

$$\begin{pmatrix} \ln\left(\frac{I_{690nm}(t_1)}{I_{690nm}(t_0)}\right) \\ \ln\left(\frac{I_{830nm}(t_1)}{I_{830nm}(t_0)}\right) \end{pmatrix} = -\begin{pmatrix} \varepsilon^{\mathrm{HHb}}_{690nm} & \varepsilon^{\mathrm{O_2Hb}}_{690nm} \\ \varepsilon^{\mathrm{HHb}}_{830nm} & \varepsilon^{\mathrm{O_2Hb}}_{830nm} \end{pmatrix} \cdot d \cdot DPF \cdot \begin{pmatrix} \Delta[\mathrm{HHb}] \\ \Delta[\mathrm{O_2Hb}] \end{pmatrix},$$

can also be written as

$$\begin{pmatrix} \ln\left(\frac{I_{690nm}(t_1)}{I_{690nm}(t_0)}\right) \\ \ln\left(\frac{I_{830nm}(t_1)}{I_{830nm}(t_0)}\right) \end{pmatrix} = -d \cdot DPF \cdot \begin{pmatrix} \Delta\mu_{a,690nm} \\ \Delta\mu_{a,830nm} \end{pmatrix}, \tag{2.10}$$

where $I_{\lambda}(t_0)$ is the detected intensity of the light source with wavelength λ_i at the reference time point t_0. $I_{\lambda_i}(t_1)$ is the detected intensity of the light source with wavelength λ_i at any time t_1, $\varepsilon^{\mathrm{HHb}}_{\lambda_i}$ and $\varepsilon^{\mathrm{O_2Hb}}_{\lambda_i}$ are the extinction coefficients at wavelength λ_i for HHb and O_2Hb, Δ[HHb] and $\Delta[O_2\mathrm{Hb}]$ are the concentration changes in HHb and O_2Hb, $\Delta\mu_{a,\lambda_i}$ is the change in the absorption coefficient at wavelength λ_i, d is the source-detector distance and *DPF* the differential path length factor, which accounts for the longer path length the light traveled due to scattering.

Values for the *DPF* can either be taken from the literature (Duncan et al. 1995, Zhao et al. 2002) or can be calculated (Franceschini et al. 1998, Fantini, Hueber, Franceschini, Gratton, Rosenfeld, Stubblefield, Maulik and Stankovic 1999). To calculate *DPF* values, the absorption and scattering coefficient of the tissue must be known or must be calculated using the multi-distance approach (section 1.1). This approach assumes that the same amount of light is coupled into the tissue for the measurements on the phantom and the tissue. Yet, for investigations at the human head, the amount of light coupled into the tissue can vary due to local light attenuation by hair and hence, a reliable determination of the *DPF* is not possible anymore. Thus, for all in-vivo measurements the same literature *DPF* values as for the *UMTS exposure study* were used (Zhao et al. 2002): $DPF_{690nm} = 8.21$ and $DPF_{830nm} = 7.3$. For phantom measurements, absorption and scattering were known and thus the *DPF* values were calculated (Fantini, Hueber, Franceschini, Gratton, Rosenfeld, Stubblefield, Maulik and Stankovic 1999) using a semi-infinite medium

$$DPF(\lambda) = \frac{1}{2}\left(\frac{3\mu'_{sp}(\lambda)}{\mu_{a,initial}(\lambda)}\right)^{\frac{1}{2}}\left[1 - \frac{1}{\left(1 + d(3\mu'_{sp,initial}(\lambda)\cdot\mu_{a,initial}(\lambda))^{\frac{1}{2}}\right)}\right], \tag{2.11}$$

where $\mu_{a,initial}$ and $\mu'_{sp,initial}$ are the absorption and scattering coefficient of the homogeneous reference phantom and μ'_{sp} the calculated scattering coefficient of the phantom of interest.

Plotting $\Delta\mu_{a,690nm}$ and $\Delta\mu_{a,830nm}$ or Δ[HHb] and $\Delta[O_2\mathrm{Hb}]$ versus the distance d, should reveal if the changes are more pronounced at shorter or longer source-detector distances. Since longer source-detector distances are more sensitive to deeper structures, more pronounced changes at longer distances should indicate changes in deeper structures. This hypothesis was tested in phantom and in-vivo measurements and the results are shown in

section 2.3.5
Relative concentration changes calculated with the Lambert-Beer law are usually given the unit [μM] in the literature. However, in the case of localized activation, the absolute quantification is not reliable. In this case, the assumption of an homogeneous medium leads to an underestimation in the magnitude of the concentration change (Boas, Gaudette, Strangman, Cheng, Marota and Mandeville 2001), which depends on the optical path length covered within the activation compared to the optical path length within the whole tissue. This is called the *partial volume effect*. If global changes occur in the tissue of interest, the *partial volume effects* becomes small.
Since the penetration depth is not the same for different wavelengths, the *partial volume effect* becomes wavelength dependent, which can results in a cross-talk in the absorber concentrations (Uludag et al. 2002, Boas et al. 2001). For the wavelength pair used in the *UMTS exposure study* - 690 nm and 830 nm - the cross-talk between $\Delta[O_2Hb]$ and $\Delta[HHb]$ is significantly decreased (Sato et al. 2004).
Although no absolute values for local concentration changes can be obtained with the modified Lambert-Beer law, it provides some advantages. The approach is easy to comprehend and does not require huge computational resources. The obtained concentration changes provide an estimation of the minimal concentration changes, since the modified Lambert-Beer law tends to underestimate concentrations and also very importantly of the sign of changes.

The slope comparison method

The slope comparison method is based on the multi-distance method introduced in section 1.1. For a medium consisting of a superficial and deeper layer (see section 2.3.4), $\ln(U_{ac}r^2)$, $\ln(U_{dc}r^2)$ and φ (Fig. 1.2) in dependency of the distance r will not be linear anymore. For specific layer thicknesses, source-detector distances and optical properties of the superficial and deeper layer, the influence of the superficial and deeper layer on different measurement paths is approximatively the same and therefore the deviation from linearity is minimal (Franceschini et al. 1998, Choi et al. 2004). For these cases, it is not possible to discriminate between superficial and deep changes. Still, the aim was to test if this discrimination can be achieved with the *Imager16* and the optical conditions of the human head. For this purpose, the slopes between the two closest (short separation) and two farthest (long separation) source-detector distances were calculated and converted to optical coefficients. The performance of this method was tested in phantom and in-vivo measurements. For the phantom measurements the optical coefficients at short and long distances were compared to the optical coefficients of the deep and superficial layer.

Depth reconstruction based on DOI

The theory of diffuse optical imaging was described in section 2.2.2. As mentioned there, the depth reconstruction shows highly non-linear behaviour, but nonetheless it may be possible to distinguish between superficial (skin) and deep (cerebral) changes. The aim was to test this method in terms of discriminating superficial from deep changes for phantom and in-vivo measurements.
For the in-vivo measurements, the amplitude of the reconstructed $\Delta[O_2Hb]$ and $\Delta[HHb]$

have low absolute accuracy because the coefficients of the homogeneous medium cannot be estimated accurately and because of the underestimation of the amplitude in the case of localized absorption changes. For the phantom measurements, the optical coefficients were known and the properties of the deeper layer were used as background properties.

2.3.4 Methods

To investigate the performance of the proposed methods in discriminating superficial from deep changes, a two-layered configuration was chosen as model for the brain. A superficial layer mimics skin and skull, a thick block the brain, which can be assumed to be infinitely thick. This simplified model is relevant, since our work was focused on discriminating superficial from deep changes and not on an accurate depth localization.

Phantom kits were used as test systems, which consist of interchangeable blocks and layers. For the in-vivo experiments, a skin heating measurement was performed to induce localized superficial optical changes. In addition, a motor cortex activation measurement was carried out to induce cerebral changes. Both in-vivo measurements were carried out at the human head.

Phantom measurements

For the phantom measurements, phantom kits were manufactured, which consisted of a block and at least one layer (Fig. 2.15). One layer of each phantom kit was 8 mm thick and was used with the phantom block for the measurements. Several phantom kits were made to establish a phantom set for *BORL*. The optical properties have been measured with the ISS Oxiplex® and a commercial optical sensor (Tab. 2.4).

The phantom kits were manufactured following the instructions from the ISS Documentation (n.d.). A two-component silicone (Elastosil® RT 601, Wacker Chemie AG, Munich, Germany) was used as the basis of the solid phantoms. Adding a specific amount of carbon black powder and titanium dioxide (TiO_2) allows to adjust the absorption and scattering coefficient. Phantoms made of silicone, in contrast to those made e.g. of biological materials, feature constant optical properties on a long term scale.

Since phantom manufacturing is a complex procedure, it was very difficult to achieve exactly the same scattering coefficient for two phantom kits. Thus, the two phantom kits with the closest scattering but different absorption coefficients were chosen, namely phantom kit *D* and *I* (bold font in Tab. 2.4).

To calibrate the measurement on a phantom with known optical properties (also called calibration phantom), a commercially available solid silicone phantom from ISS Inc. (Champaign, Illinois, USA) was used. The optical coefficients are listed in Tab. 2.5.

Five different phantom measurements were carried out: one on the calibration phantom, one on block I with layer I on top (II), one on block D with layer D on top (DD), one on block I with layer D on top (ID) and one on block D with layer I on top (DI) (Fig. 2.15). The measurements were repeated three times. For all measurements, elastic bandages (Derma Plast®, IVF Hartmann AG, Neuhausen Switzerland) were used to assure a good and constant contact of the *Imager16* to the phantom. In addition, it should prevent the formation of an air layer between phantom block and layer.

Phantom kit	$\mu_{a,690nm}$ [cm^{-1}]	$\mu_{a,830nm}$ [cm^{-1}]	$\mu'_{s,690nm}$ [cm^{-1}]	$\mu'_{s,830nm}$ [cm^{-1}]
A	0.238	0.233	14.6	14.7
B	0.099	0.106	11.9	11.6
C	0.145	0.157	5.3	5.3
D	**0.14**	**0.144**	**5.9**	**5.8**
E	0.216	0.224	17.2	17.8
F	0.192	0.198	8.2	8.0
G	0.151	0.152	4.9	6.2
H	0.053	0.056	5.5	5.6
I	**0.096**	**0.10**	**5.7**	**5.6**
K	0.104	0.106	12.0	12.2
L	0.122	0.122	12.3	12.8

Table 2.4 – Optical properties of phantom basis set of BORL.

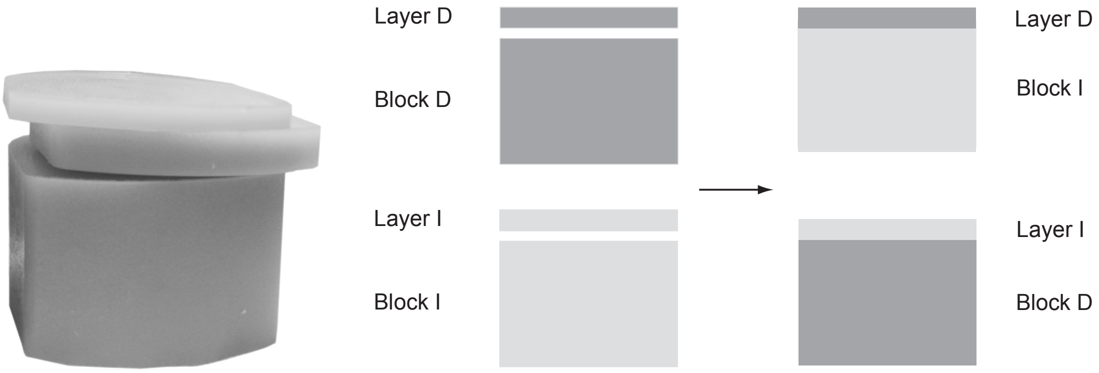

Figure 2.15 – Left side: picture of a solid silicone phantom kit containing one block and two layers. Right side: illustration of the use of the constructed solid silicone phantom kits. Performing a measurement on a layer-block combination belonging to the same kit and on a layer-block combination where the layer or the block is exchanged, one can mimic superficial or deep absorption changes.

	λ = 690 nm	λ = 830 nm
Absorption coefficient [cm^{-1}]	0.115	0.107
Scattering coefficient [cm^{-1}]	10.9	9.7

Table 2.5 – Optical coefficients of the calibration phantom.

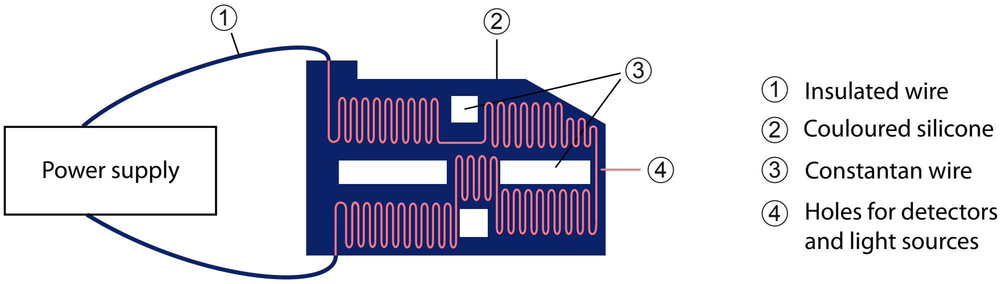

Figure 2.16 – Illustration of the heating coil used for the skin heating measurement. A power supply was connected to the heating coil to control the current in the circuit and the thermal energy released by the constantan wire. The heating coil was casted in black silicone to prevent direct skin contact.

The 15 phantom measurements were used for all depth analysis methods. However, the calibration measurements were only needed for the slope comparison method. For all analysis methods, mean and standard deviation were calculated over the three repetitions.

In-vivo measurements

Two in-vivo measurements were carried out: first, a motor cortex activation triggered changes in a deep tissue structure and second, localized heating of the skin induced optical changes in the superficial structures. Both measurements were performed at the same position on the human head.

For the skin heating measurement, a planar heating device was built, which was thin enough to place it between skin and *Imager16* (Fig. 2.16). A constantan wire, casted in black silicone, formed a heating coil. Since both, the heating device and the sensor were built from the same silicone, they kept together well, which prevented the formation of air layer between them. This is very important, because otherwise light may tunnel directly from source to detector, which would falsify the results.

The heating coil was connected to a power supply, which was used to control the current in the coil and thus the released thermal energy. For safety reasons, the current needed to achieve an increase in temperature of approximately four degrees was estimated in experiments before the real skin heating measurement took place.

For the motor cortex activation, a stimulation period of 20 s finger tapping and 20 s recovery was applied. The stimulation was repeated 15 times and before and after all repetitions a baseline of 2 minutes length was recorded (Fig. 2.17).

Both measurements were performed on one male test subject, who was positioned in a comfortable sitting position. The heating device was placed underneath the *Imager16* and both was attached with elastic bandages to the head with the center point located over C3 (in the international 10-20 EEG positioning system (Jasper 1958)).

The measurements were performed in the following order: first the measurement on the calibration phantom, then the performance of the motor cortex activation and skin heating followed by the calibration phantom. The sensor was attached to the head before the motor cortex activation and detached after the skin heating measurement. A temperature sensor was positioned between the sources closest to both detectors and the detectors.

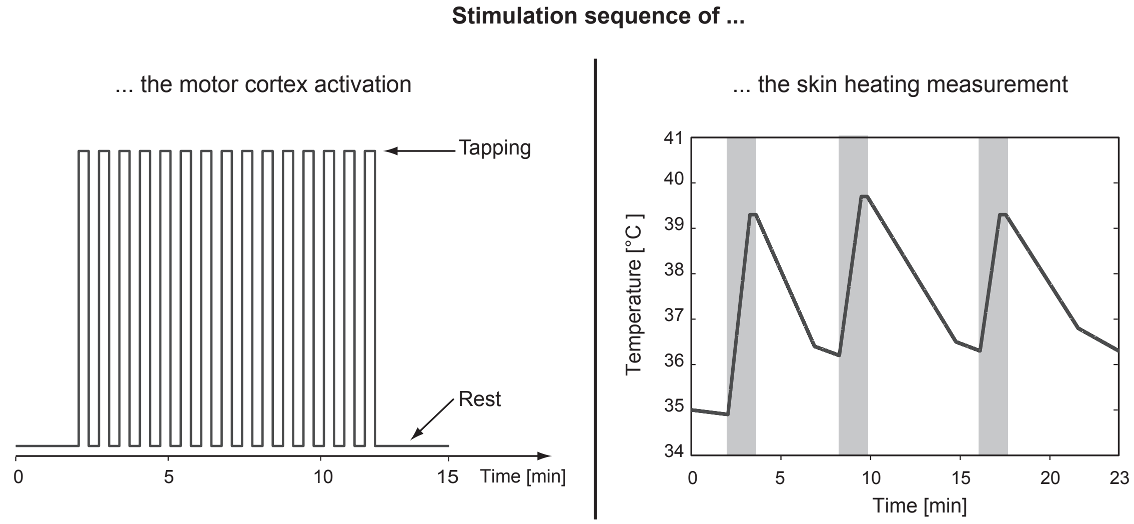

Figure 2.17 – Stimulation sequences for the motor cortex activation (left side) and the skin heating measurement (right side). Left side: the baseline was recorded before the first and after the last tapping. In between, 20 s finger tapping were followed by 20 s recovery. That was repeated 15 times. Right side: The stimulation sequence corresponded to the temperature measured beneath the *Imager16*. The time, in which the power supply was in use and thus thermal energy was released is shaded in grey.

Since the sensor itself insulated the skin from ambient air, the temperature decrease after the heating was very slow. To perform the measurement in a reasonable time, the next heating phase was initiated after the temperature dropped at least 3 degrees compared to maximum temperature reached in the previous heating phase. The maximum temperature was kept constant for about 30 s. In total, 3 heating phases were initiated resulting in a measurement duration of 23 minutes.

Since all depth analysis methods are based on representative values for the activation or heating phase and the rest phase, a mean over specific time slots was calculated for each stimulation segment: for the motor cortex measurements, the mean over the last 10 s tapping and over the last 10 s rest before tapping were calculated, for the skin heating measurement, the mean over the 30 s constant maximum temperature was calculated (heating phase) and the mean over the last 30 s before the start of the next heating event (rest).

In order to apply the slope comparison method, the first phantom measurement was used to calibrate the motor cortex activation and the second phantom measurement to calibrate the skin heating measurement.

For the motor activation and skin heating measurement, the mean and standard deviation of $\Delta[O_2Hb]$ and $\Delta[HHb]$ were calculated over the 15 stimulation segments or over the three heating phases, respectively.

2.3.5 Results

Phantom measurements

A) Modified Lambert-Beer law
The measured changes in the absorption coefficients ($\Delta\mu_{a,690nm}$ and $\Delta\mu_{a,830nm}$) are shown for all measurement paths in Fig. 2.18-2.20. These figures include one subfigure for each sensor quadrant. The phantoms used for the comparison are displayed using a color code above the reconstructed depth profiles; dark grey indicates stronger absorption (block D, layer D) as compared to the lightly greyed compartments (block I, layer I).
As expected, it can be seen in Fig. 2.18 that replacing the superficial layer with a layer of higher absorption leads to increased absorption at shorter source-detector distances. The opposite can be observed if the deep structure shows an increase in the absorption coefficient (Fig. 2.19). Comparing both figures, it can be seen that a superficial increase in μ_a influences the calculated $\Delta\mu_a$ of all source-detector distances, whereas a change in a depth over 8 mm has a relatively small impact on $\Delta\mu_a$ at the shortest source-detector distances. The same pattern, but with an opposite sign for $\Delta\mu_a$ can be observed for the comparisons of DD to DI and DD to ID (Fig. 2.21-2.20).
Overall, $\Delta\mu_a$ was maximal for comparisons, where superficial changes were induced. The obtained $\Delta\mu_a$ were in the range of 0.035 to 0.055 cm^{-1}, which corresponds well with the expected $\Delta\mu_a$ of 0.045 cm^{-1} between phantom II and DD. The variations between the quadrants may arise from errors in coupling constants.

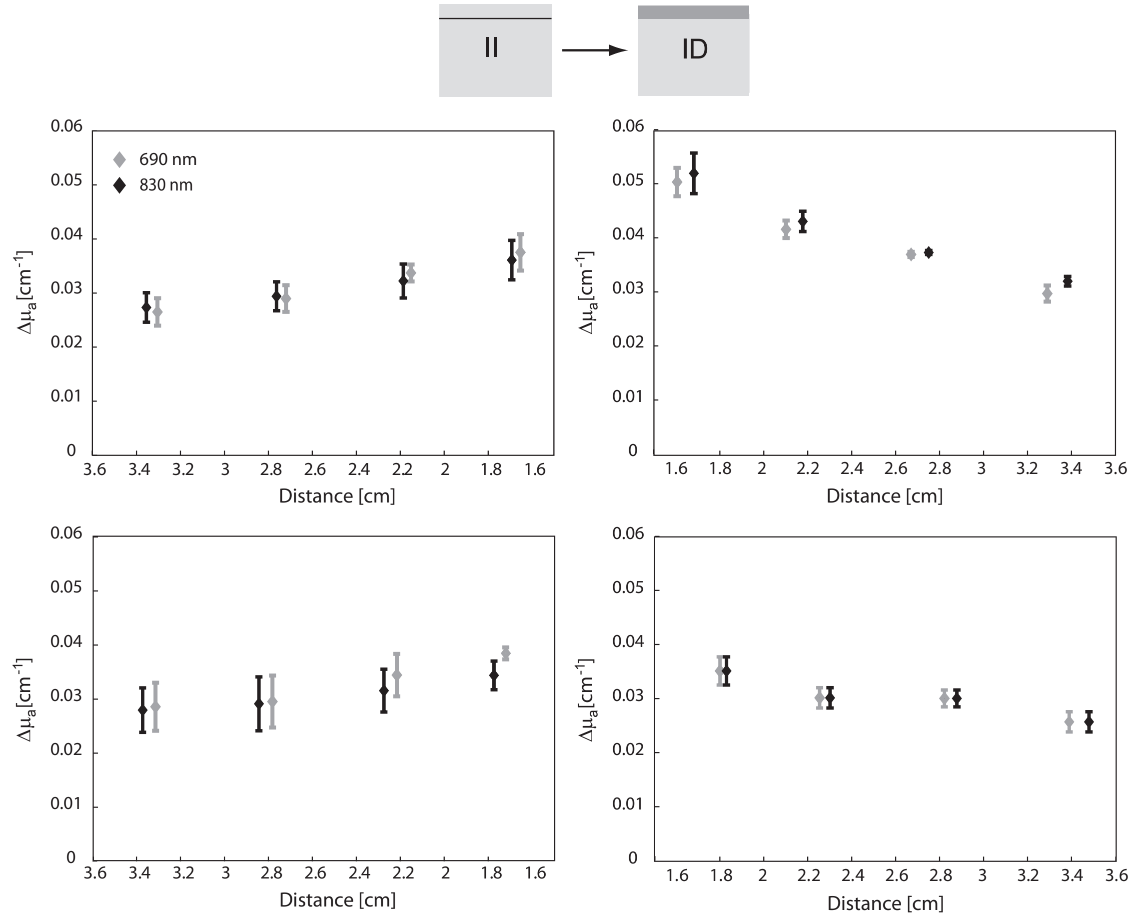

Figure 2.18 – Modified Lambert-Beer law applied on the II-ID phantom comparison (μ_a(690 nm) = 0.096 cm^{-1} for I and μ_a(690 nm) = 0.14 cm^{-1} for D). For each source-detector distance, the calculated mean changes ± the standard deviation in the absorption coefficients are displayed.

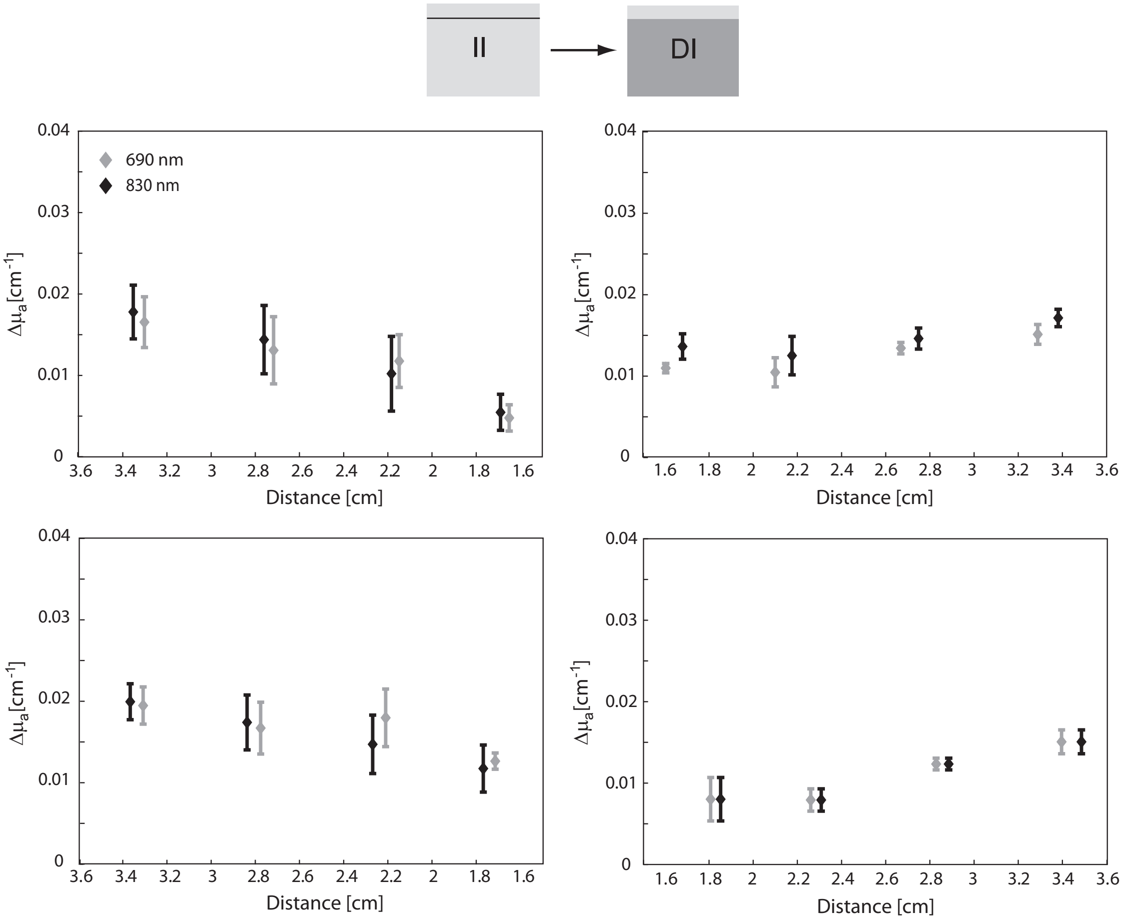

Figure 2.19 – Modified Lambert-Beer law applied on the II-DI phantom comparison (μ_a(690 nm) = 0.096 cm^{-1} for I and μ_a(690 nm) = 0.14 cm^{-1} for D). For each source-detector distance, the calculated mean changes ± the standard deviation in the absorption coefficients are displayed.

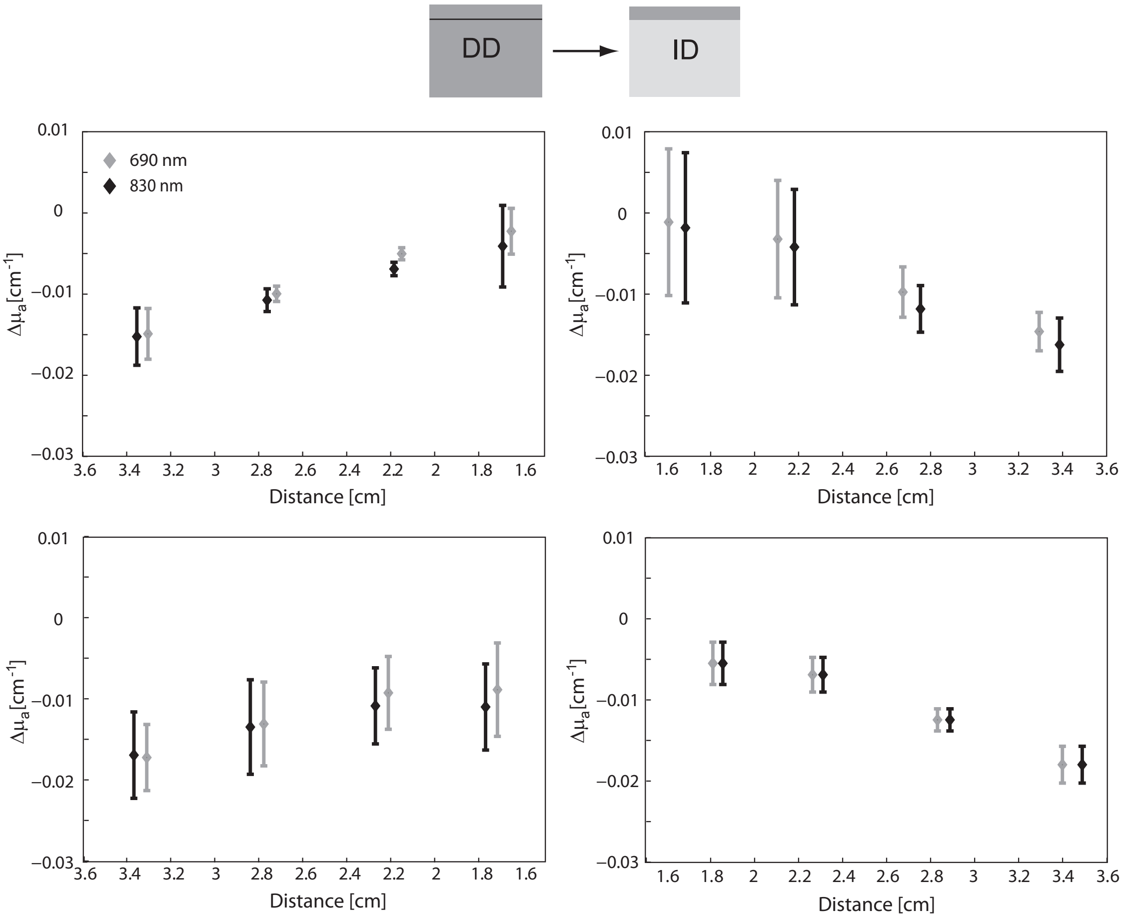

Figure 2.20 – Modified Lambert-Beer law applied on the DD-ID phantom comparison (μ_a(690 nm) = 0.096 cm^{-1} for I and μ_a(690 nm) = 0.14 cm^{-1} for D). For each source-detector distance, the calculated mean changes ± the standard deviation in the absorption coefficients are displayed.

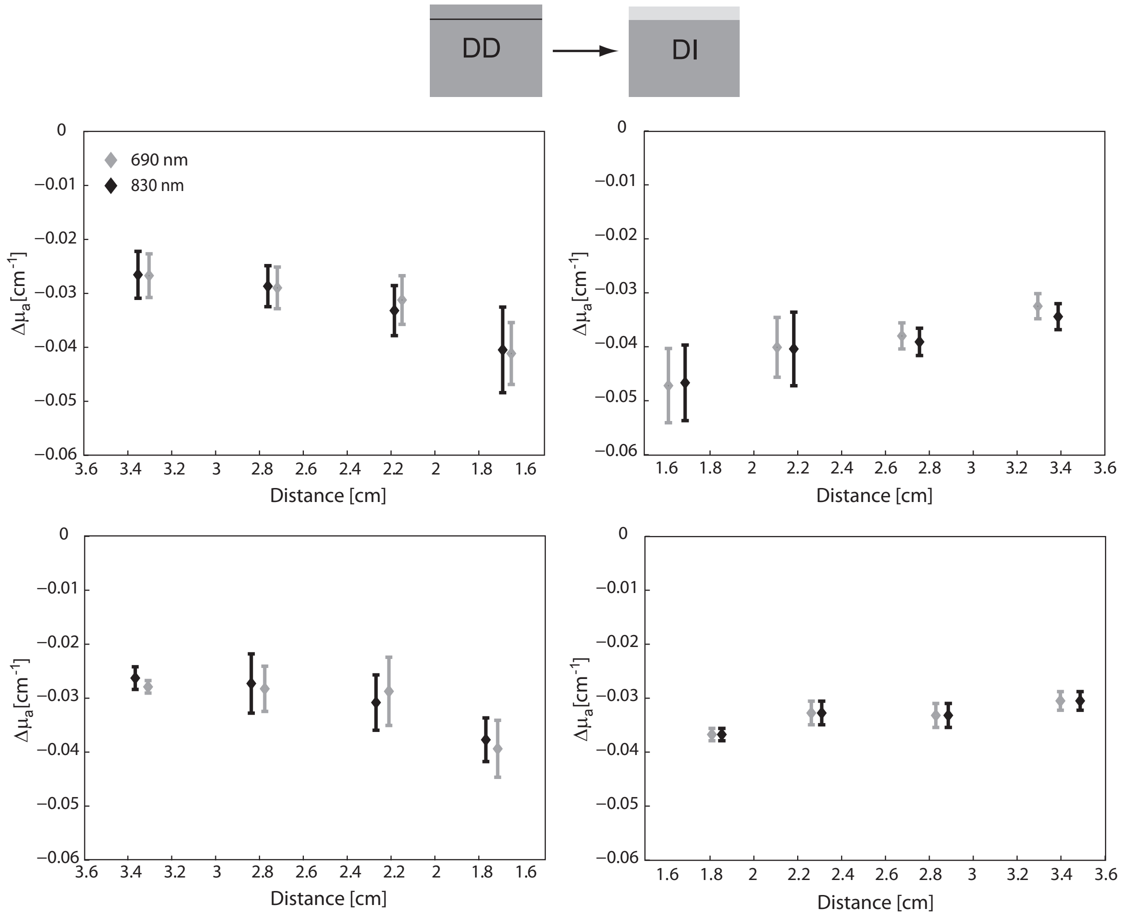

Figure 2.21 – Modified Lambert-Beer law applied on the DD-DI phantom comparison (μ_a(690 nm) = 0.096 cm^{-1} for I and μ_a(690 nm) = 0.14 cm^{-1} for D). For each source-detector distance, the calculated mean changes ± the standard deviation in the absorption coefficients are displayed.

B) Slope comparison method
The results for the slope comparison method are shown for each sensor quadrant in Fig. 2.22 and 2.23. The slopes of the two sources closest to the detectors was used to calculate the corresponding absorption coefficients, which are labelled *short separtion* in the figures. Accordingly, the absorption coefficients belonging to the two sources farthest from the detectors are labelled *long separation*. In addition to the mean μ_a ± standard deviation of the short and long distance, $\mu_a(690nm)$ of the homogeneous phantoms DD and II are indicated with a dotted grey line for better comparison. On the left side of the figures, the measured block-layer configuration is shown, which are displayed using a color code; dark grey indicates stronger absorption (block D, layer D) as compared to the lightly greyed compartments (block I, layer I).
For the block D with layer I (Fig. 2.22), four quadrants show the expected behavior for the 690 nm wavelength. Unexpectedly, for two quadrants, $\mu_a(830nm)$ are higher at the short distance. A possible explanation is a small curvature of block D's surface, which could have led to a localized air layer with a higher influence on the 830 nm wavelength, which penetrates deeper into tissue. Such air layers lead to light piping and erroneous results.
For the block I with layer D (Fig. 2.22), the experimental behavior is in good agreement with the expectations, meaning that longer distances show absorption coefficients closer to phantom II and shorter distances absorption coefficients closer to phantom DD. This indicates clearly that shorter distances are more sensitive to superficial changes.
Based on the presented results, the slope comparison method is suitable for phantom measurements to distinguish between superficial and deep changes.

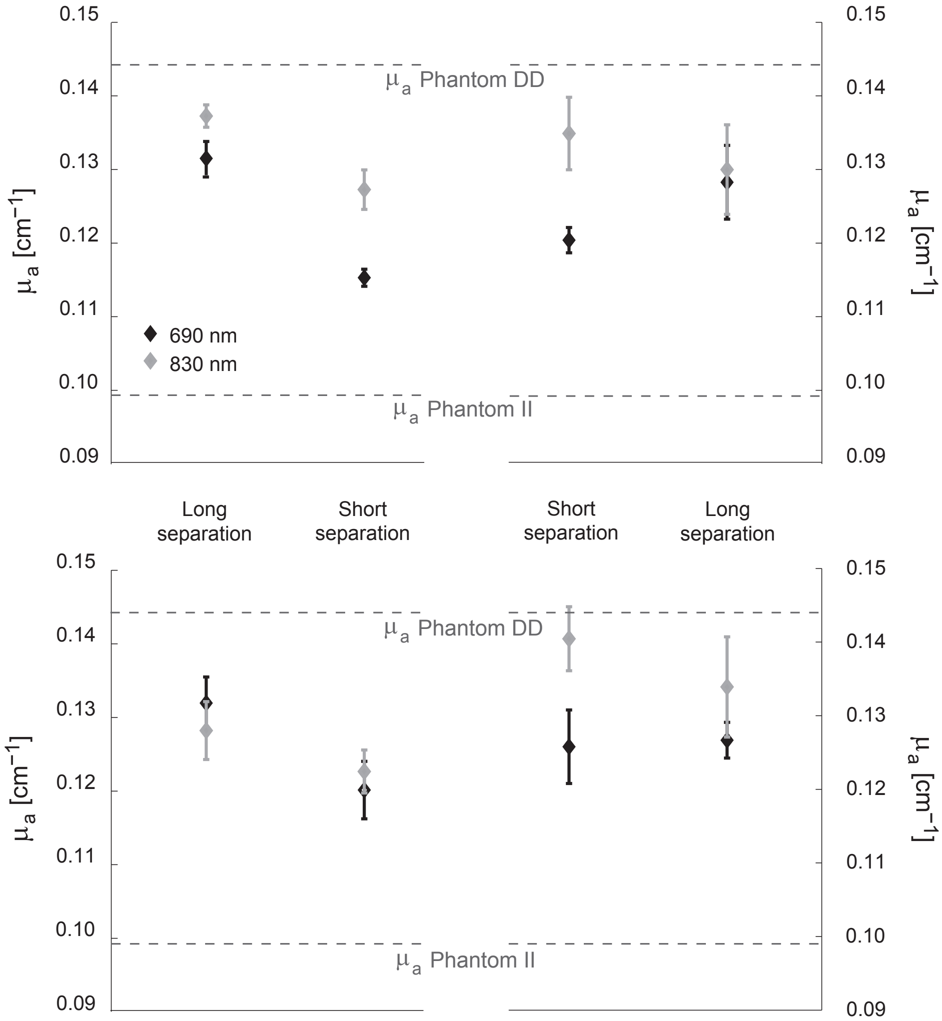

Figure 2.22 – Slope comparison method applied on the DI phantom. For the short and long source-detector distance, the calculated mean absorption coefficient μ_a ± the standard deviation are shown. The dotted grey line indicates the pure absorption coefficient of phantom DD and phantom II at wavelength λ = 690 nm.

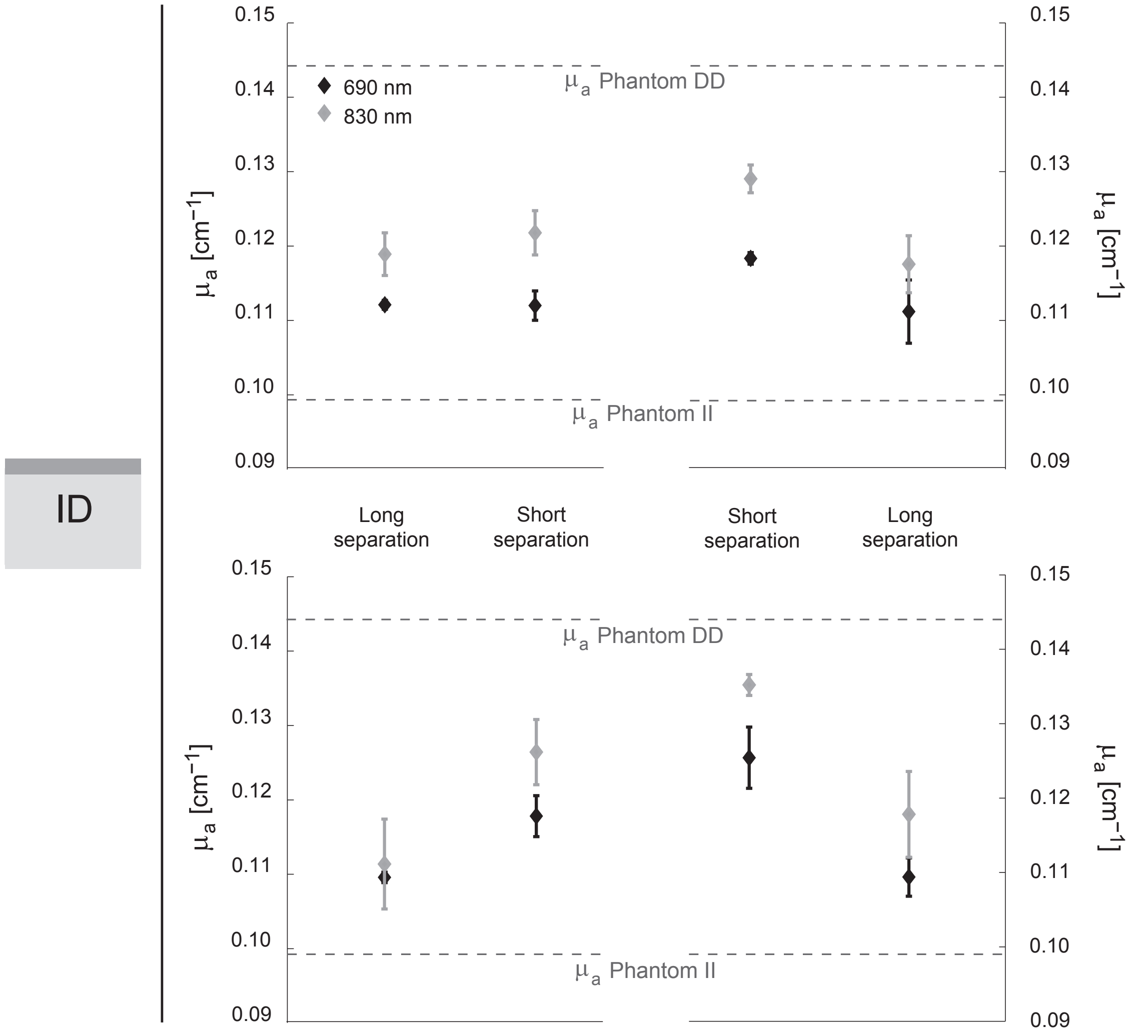

Figure 2.23 – Slope comparison method applied on phantom ID. For the short and long source-detector distance, the calculated mean absorption coefficient μ_a ± the standard deviation are shown. The dotted grey line indicates the pure absorption coefficient of phantom DD and phantom II at wavelength $\lambda = 690$ nm.

C) Depth reconstruction based on DOI

The results of the depth reconstructions based on DOI are shown in Fig. 2.24. The phantoms used for the comparison are displayed using a color code above the reconstructed depth profiles; dark grey indicates stronger absorption (block D, layer D) as compared to the lightly greyed compartments (block I, layer I).

The sign of the reconstructed $\Delta\mu_a$ was expected, whereas the depth profiles themselves provides no clear distinction between a superficial and deep changes. The depth profiles converge to zero for larger distances, because the depth sensitivity of a NIRI sensor is limited. Although, the depth profiles for deep changes show a maximum, which is below the surface, the same can be observed for the II - ID comparison. Also, the changes in $\Delta\mu_a$ are smaller and more broadly distributed over the depth for deep changes. However, without a direct comparison to a superficial change of the same magnitude, which is not possible for in-vivo measurements, no conclusions can be drawn.

This means that DOI in combination with our NIRI sensor is not a reliable method to distinguish between superficial and deep changes in phantom measurements.

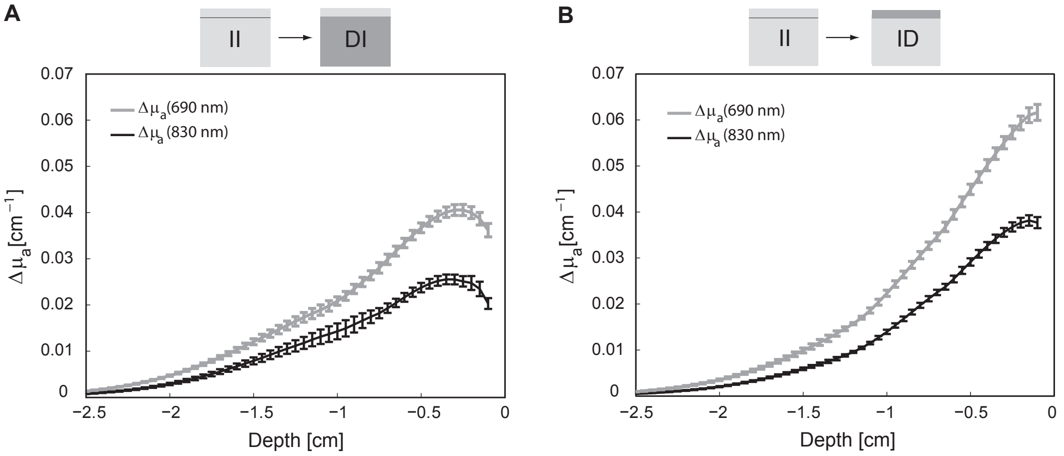

(a) DOI depth reconstruction for comparison of phantom II to ID (**A**) and phantom II to DI (**B**).

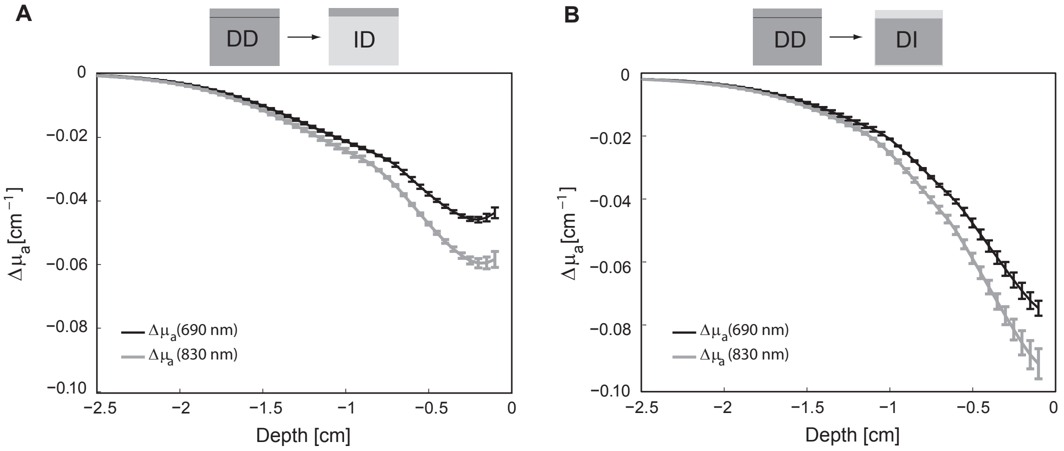

(b) DOI depth reconstruction for comparison of phantom DD to DI (**A**) and phantom DD to ID (**B**).

Figure 2.24 – DOI depth reconstruction applied on the phantom measurement data. $\Delta\mu_a(z) \pm$ standard deviation is plotted for 690 nm and 830 nm (block and layer I: μ_a(690 nm) = 0.096 cm^{-1}, block and layer D: μ_a(690 nm) = 0.14 cm^{-1}

In-vivo measurements

A) Modified Lambert-Beer law
Changes in O_2Hb and HHb were calculated from changes in the absorption coefficients and are shown in Fig. 2.25 for the motor cortex activation and in Fig. 2.26 for the skin heating measurement. All figures include a subfigure for each sensor quadrant.
For the motor cortex activation, $\Delta[O_2Hb]$ is increased and $\Delta[HHb]$ decreased at longer distances, which suggests an increase in cerebral blood flow (CBF) and in $CMRO_2$ at deep tissue layers (brain) (Hoshi et al. 2001, Wolf et al. 2002). For the skin heating measurement, $\Delta[O_2Hb]$ is increased at short distances, whereas $\Delta[HHb]$ shows no clear trend and the values are around zero. This may be interpreted as an increase in arterial blood flow and volume and will be discussed later on.
For the motor cortex activation, the concentration changes are largest for the left half of the sensor, whereas for the skin heating measurement, the largest concentration changes occur at the upper half of the sensor.
These results indicate that superficial and deep changes can be well distinguished for in-vivo measurements using the modified Lambert-Beer law.

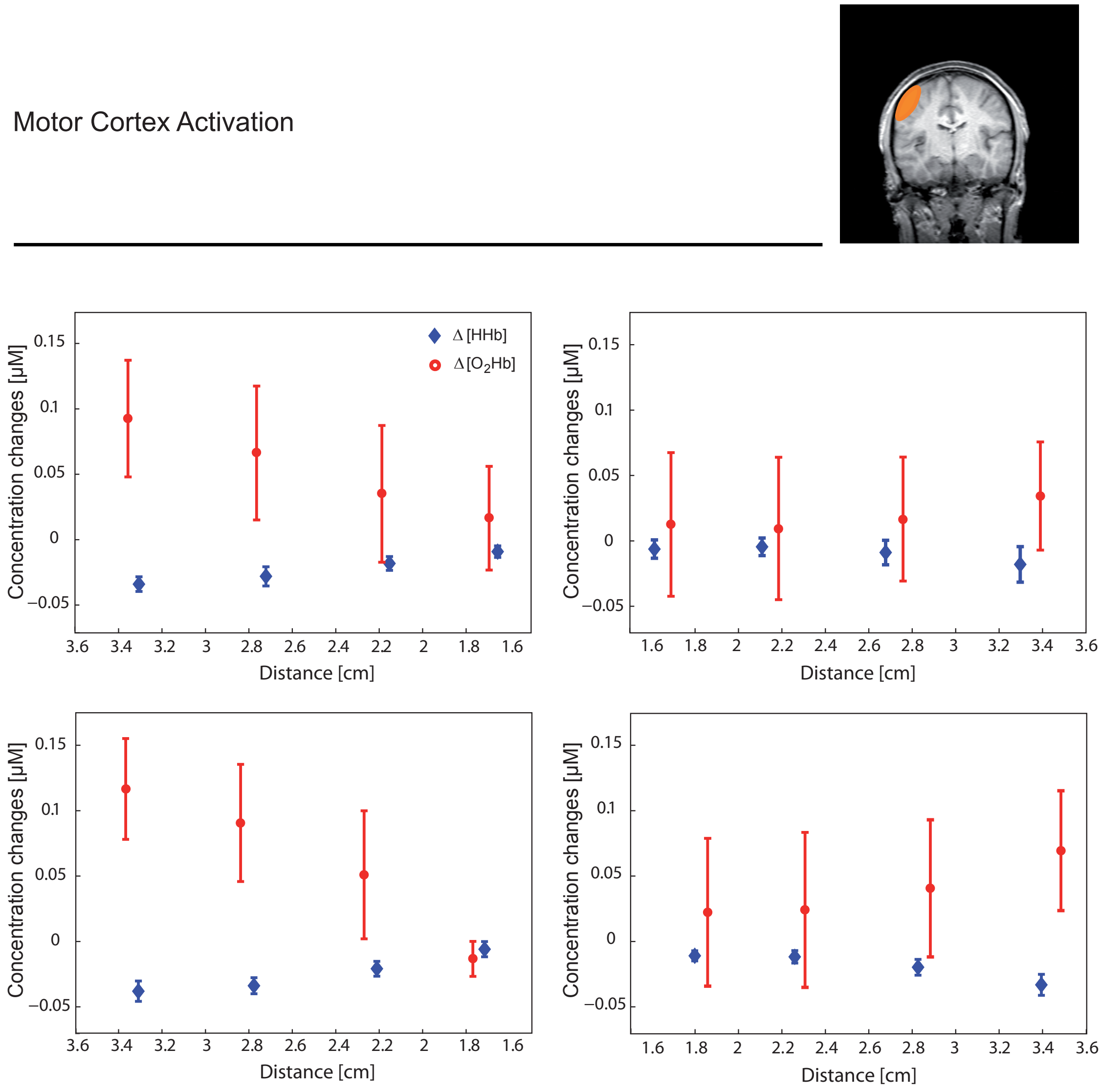

Figure 2.25 – Modified Lambert-Beer law applied on the motor cortex activation data. Displayed are for each sensor quadrant, the calculated mean changes in the chromophore concentrations ± the standard deviation in dependency of the source-detector distance.

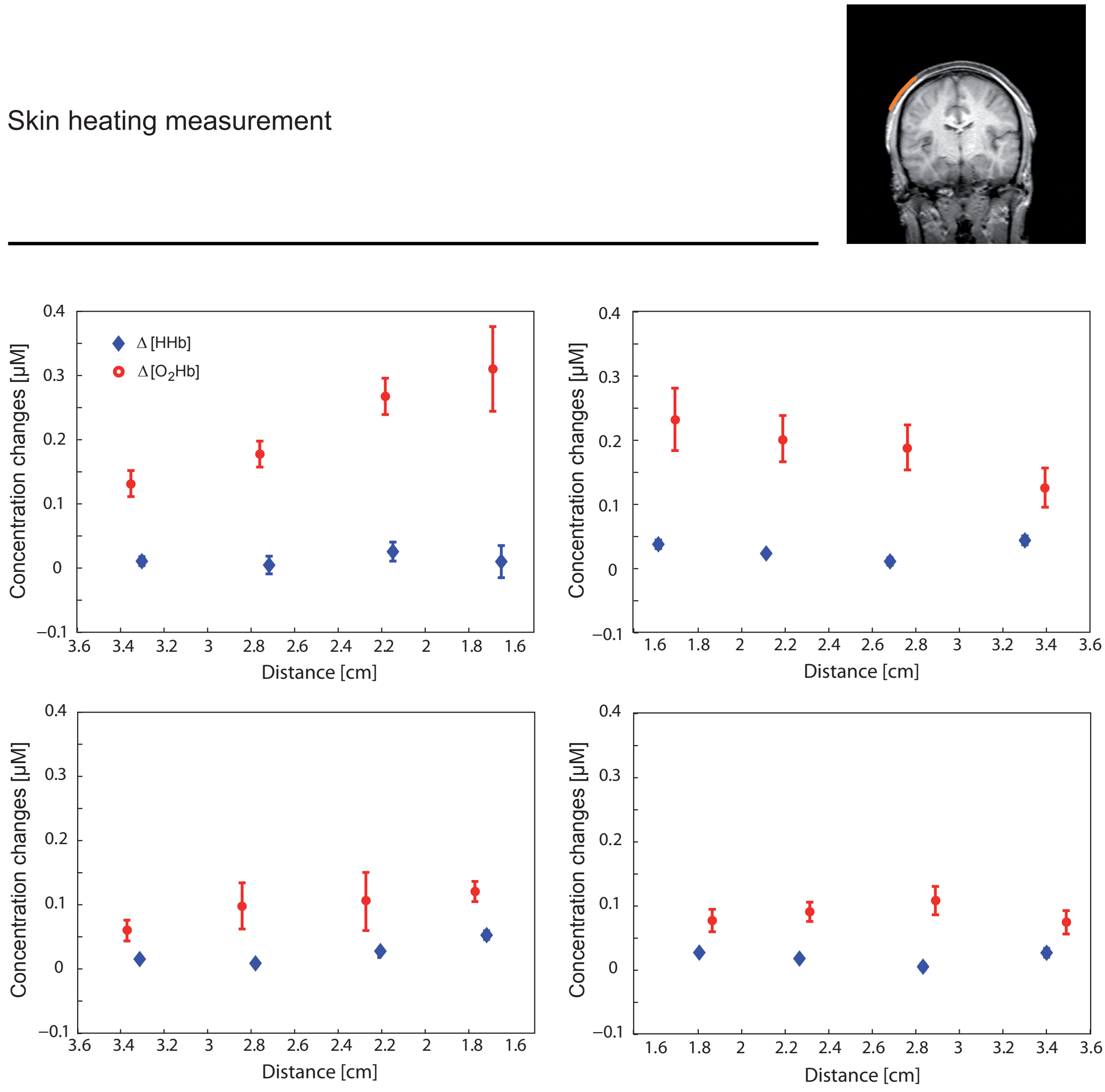

Figure 2.26 – Modified Lambert-Beer law applied on the skin heating measurement data. Displayed are for each sensor quadrant, the calculated mean changes in the chromophore concentrations ± the standard deviation in dependency of the source-detector distance.

B) Slope comparison method

The results of the slope comparison method are shown in Fig. 2.27. For each in-vivo measurement, a representative sensor quadrant illustrates the performance of the method. The calculated μ_a are quite different between the short and long separation, but between the rest and stimuli phase hardly any differences are detectable. In some cases, μ_a shows unreasonable values, e.g. being negative or as high as 0.3 cm^{-1}. Furthermore, the difference between rest and stimuli phase was calculated for short and long separation to investigate if this difference would be a meaningful indicator. However, no trend in the comparison of short to long separation was detected (data not shown). This indicates that the calculated μ_a values are erroneous. These erroneous values result from local light attenuation by hair. These local attenuations lead to unequal light coupling for different light sources and thus the basic assumption for the slope comparison method, having constant light coupling, is not valid anymore. Therefore, the slope comparison method is not suitable for in-vivo measurements, at least for measurement positions where the subjects exhibit hair.

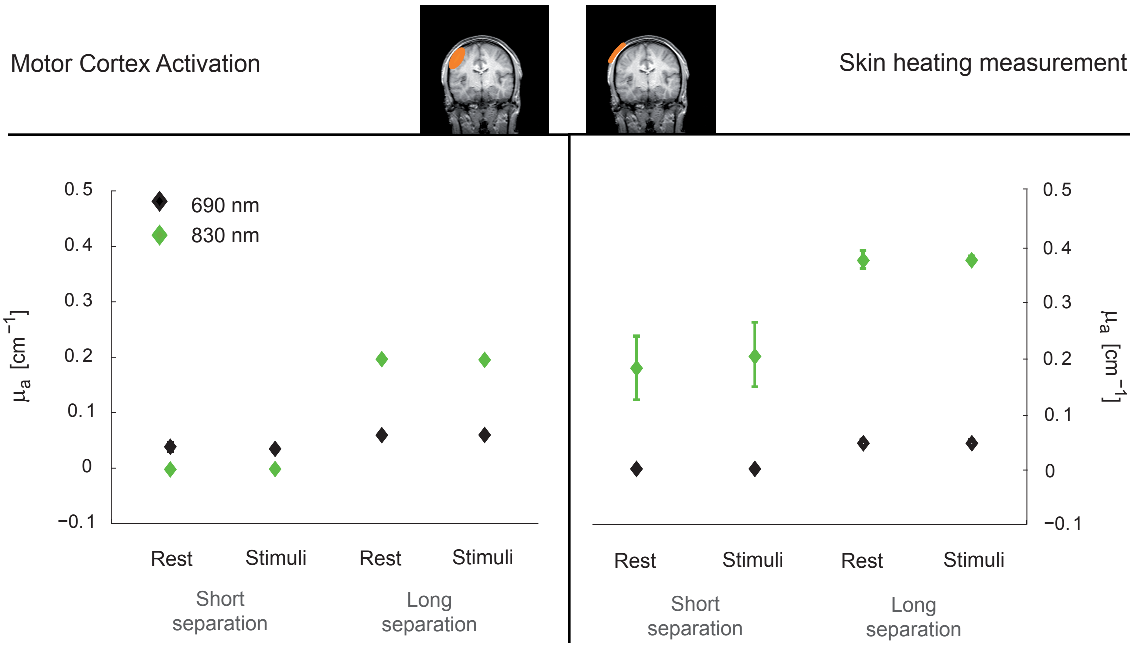

Figure 2.27 – Slope comparison method applied on the motor cortex activation (left side) and skin heating measurement (right side). $\mu_a \pm$ standard deviation are shown for the 690 nm and 830 nm wavelengths. μ_a is given for short and long distances as well as for rest and stimuli (finger tapping/heating) phases.

C) Depth reconstruction based on DOI

Fig. 2.28 shows on the left side the depth profile for the motor cortex activation and on the right side for the skin heating measurement. For the in-vivo measurements, not only a depth profile is provided as for the phantom measurements, but also reconstructions in the horizontal plane at different depths. This enhances the understanding of the spatial distribution of the stimuli response. In Fig. 2.29-2.30 the reconstructions in the horizontal plane at different depths are shown for the motor cortex activation and the skin heating measurement, respectively.

It must be noted, that a mean over the stimulation segments was calculated for the reconstructions in order to improve the signal-to-noise ratio and to minimize the occurrence of artifacts in the reconstructed image. Thus, the reconstructions and depth profiles shown in this section depict the mean response to the stimuli.

The results of the motor cortex activation - an increase in $\Delta[O_2Hb]$ and a decrease in $\Delta[HHb]$ - confirm the results of the modified Lambert-Beer law and, with respect to physiology, an increase in CBF and $CMRO_2$ (Hoshi et al. 2001, Wolf et al. 2002). And the spatial distribution of the change is in agreement with the modified Lamber-Beer law: the highest changes of $[O_2Hb]$ and [HHb] were detected on the left sensor half, together with small changes in the lower right sensor quadrant.

Furthermore, the results of the skin heating measurement are in good agreement with the results of the modified Lambert-Beer law. $\Delta[O_2Hb]$ is larger for the upper half of the sensor, whereas reconstructed $\Delta[HHb]$ values are relatively small when comparing the ratio between $\Delta[O_2Hb]/\Delta[HHb]$ for the motor cortex and skin heating measurement. Taking into account the coincidental pattern of reconstructed $\Delta[HHb]$ changes (Fig. 2.30), it can be concluded that the reconstruction shows probably noise. The high increase in $\Delta[O_2Hb]$ may result from an increase in arterial blood flow and volume to compensate the external heating. Vasodilation of small arteries, capillaries and small veins results in an increased blood volume and thus in an increased $[O_2Hb]$ and [HHb]. An increased blood flow leads to an increase in $[O_2Hb]$ and a decrease in [HHb] due to the wash-out effect. Both effects together results in an increase in $[O_2Hb]$ and a zero change in [HHb]. The physiological vasodilatory effect to an external heating source is commonly known and is utilized for example for the measurement of transcutaneous partial pressure of oxygen ($tcPO_2$).

By comparing the depth profile of the motor cortex activation with the one of the skin heating measurement, it can be seen that the motor cortex activation cause a concentration change below the surface, with a maximum at a depth of 0.2 cm, whereas the skin heating measurement shows a maximum at the surface. This indicates that a simple homogeneous semi-infinite model is sufficient to distinguish roughly between superficial and deep changes.

The amplitudes of the concentration changes are higher for the DOI reconstructions than for the modified Lambert-Beer law. Due to the overlapping measurements, DOI is less susceptible for *partial volume effects* and thus estimates the concentration changes closer to the real values (Boas et al. 2001).

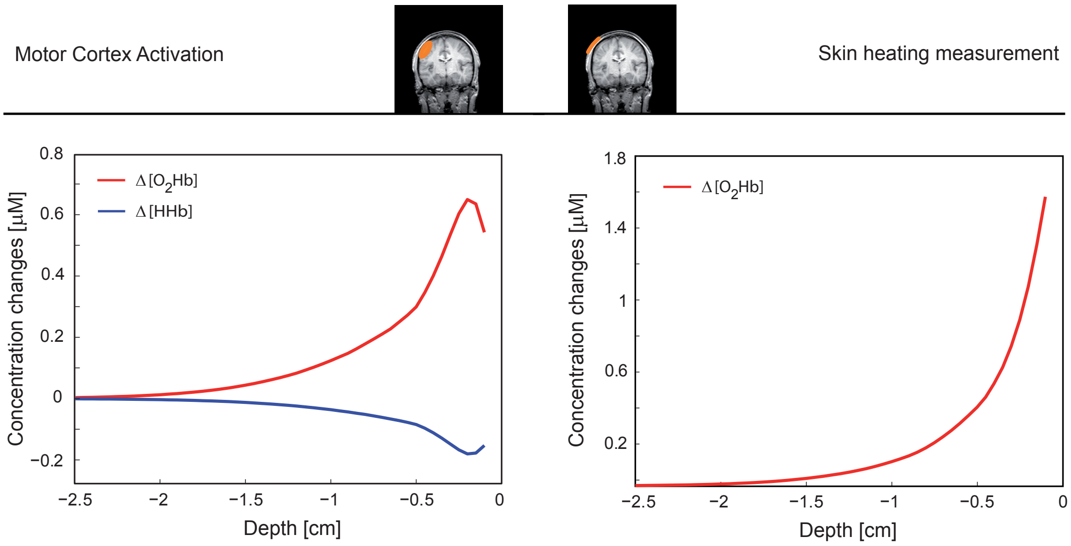

Figure 2.28 – Depth reconstruction based on DOI for the motor cortex activation (left side) and skin heating measurement (right side).

2.3.6 Conclusion

The performance of the different methods for discrimination between superficial and deep changes in phantom and in-vivo measurements is summarized in Tab. 2.6. As shown earlier, the modified Lambert-Beer law is suitable for distinguishing superficial and deep changes, for both phantom and in-vivo measurements. Since the modified Lambert-Beer law compares different time points of the same measurement, it is relatively robust against movement artifacts and thus suitable for analysis of in-vivo measurements. In contrast, the slope comparison method relies on constant light coupling for all light sources and is therefore very susceptible to localized light attenuation such as by hair. This explains why the slope comparison method works very well for measurement on phantoms, but fails in in-vivo measurements. Although the depth reconstruction using DOI provides some depth information for the in-vivo measurements, the reconstructed depth profiles are not that easy to interpret. And if the non-linearity of the depth reconstruction is taken in account (section 2.3), then the uncertainty of the interpretation increases even further.

All investigated approaches have the advantage that they require no a priori knowledge of the tissue structure, but this means that the probed tissue volume is assumed to be homogeneous. However, this does not apply for e.g. functional brain measurements, where increased neuronal activation results in localized perfusion changes. When using the modified Lambert-Beer law, the estimated absorption change is then highly dependent on the position of light sources and detectors with respect to the activation. Probing only a part of the activation volume with light leads to an underestimation of the magnitude of the absorption change. Furthermore, the DPF values could not be determined for the in-vivo measurements because of local light attenuation by hair. By using literature values for the DPF one may introduce an additional source of errors. Hence, the accuracy of the methods cannot be determined in-vivo since the real values are not known. This poses a problem when more sophisticated anatomical models and inversion algorithm are used: the optical properties of the different tissue structures in the human head are not

Method	Phantom measurement	In-vivo measurements
Mod. Lambert-Beer approach	YES	YES
Slope comparison method	YES	NO
Depth reconstructions using DOI	NO	YES, but difficult to interpret

Table 2.6 – Summary of results when discriminating superficial from deep changes. YES indicates that this method is suitable to distinguish superficial from deep changes and NO not. YES, but stands for results where the discrimination was possible, but difficult to interpret.

measurable in-vivo and postmortem evaluation may be erroneous.
However, as the results show, the modified Lamber-Beer law seems still the most reliable method for distinguishing between superficial and deep changes in phantom and in-vivo measurements. For that reason the modified Lambert-Beer law was applied in the *UMTS exposure study* (section 4.3). The so-called path analysis in the UMTS paper corresponds to the analysis presented for the modified Lambert-Beer law, where $\Delta[O_2Hb]$ and $\Delta[HHb]$ were calculated for each source-detector distance (Eq. 2.3.3) and plotted as shown in Fig. 2.26-2.25.

2.4 Conclusion

By modifying the ISS Oxiplex$^{\circledR}$, several improvements were achieved:

- The quadrupled number of measurement paths provides the possibility to achieve spatial resolution, which was not possible with the commercial instrument. This allows the experimenter to record functional activation and to reposition the optical sensor if the activation is slightly out of focus.
- In addition, the *Imager16* covers a larger surface and brain area, which makes the placement over the cortical area of interest easier.
- Due to the dip-switch on the back of the instrument,that allows to switch between the commercial and the newly implemented mode, the old instrument configuration is maintained but the range of applications of the instrument enhanced.

The localization of an absorbing object in the horizontal plane using DOI works well for the *Imager16*, although the shape of the object is distorted due to the sensor geometry. The reconstructed amplitude of absorption changes was found to be highly dependent on the position of the absorbing volume in respect to source and detector positions and the depth of the volume. This behavior - the spatial non-uniformity of the light probing the tissue - is caused by the limited number of sources and detectors.
The modified Lambert-Beer law has proven to be the most reliable method to distinguish between superficial and deep changes, for both phantom and in-vivo measurements. Yet, absolute quantification of concentration changes cannot be achieved.

The achieved depth resolution is quite limited and lower than anticipated in the beginning of the project. The *Imager4MRT* was developed and is applicable for combined NIRI and MRI measurements and might be used in future applications to improve depth resolution.

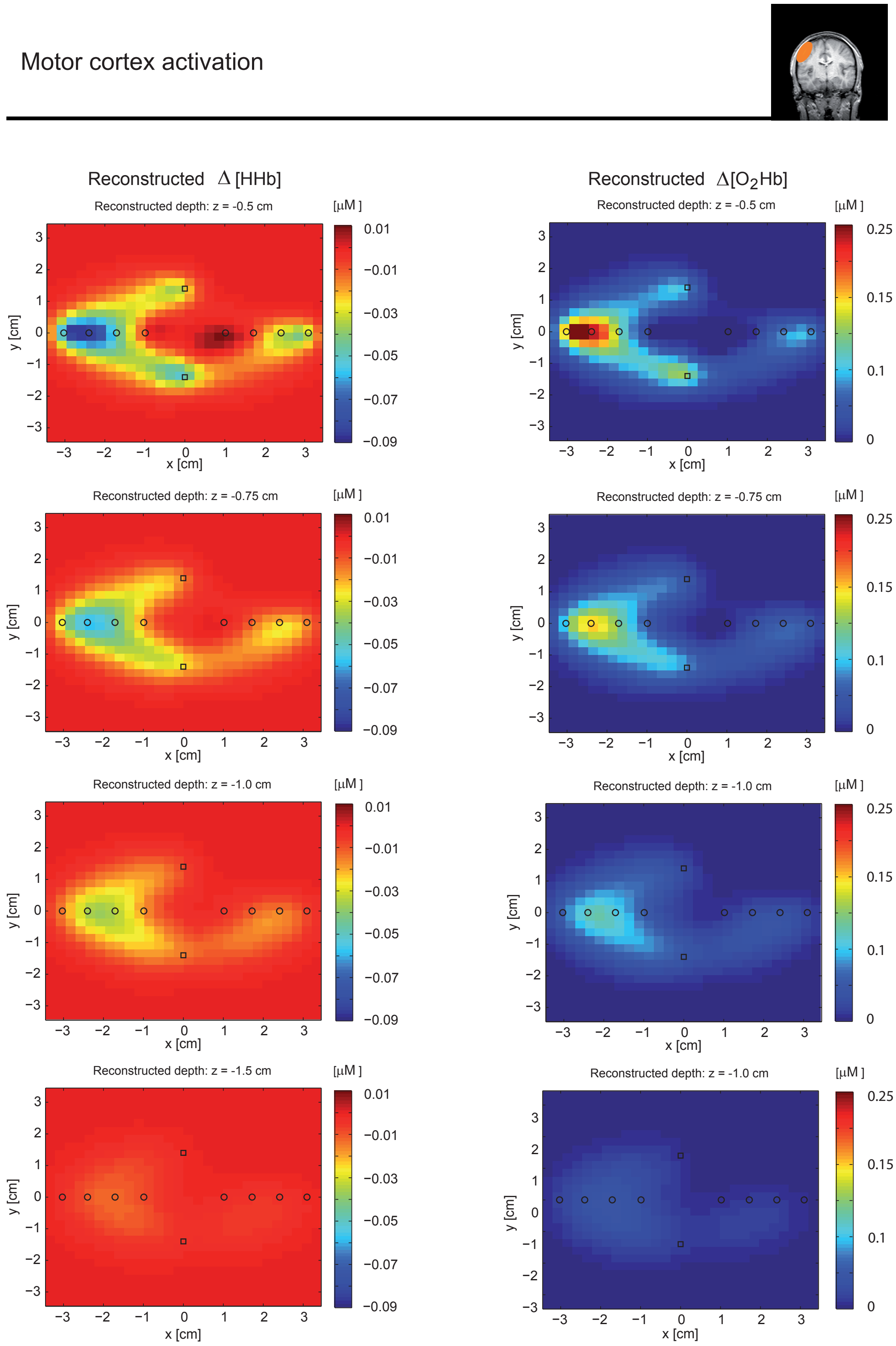

Figure 2.29 – DOI reconstruction at different depths (z = -0.5, -0.75, -1.0 and -1.5 cm) for the motor cortex activation. On the left side the reconstructed changes in [HHb] are shown and on the right side the reconstructed changes in [O_2Hb]. The black ellipses represent the position of the light sources and the black rectangle the position of the detectors. From top to bottom, the depth z increases.

Skin heating measurement

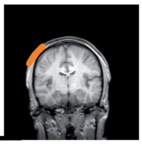

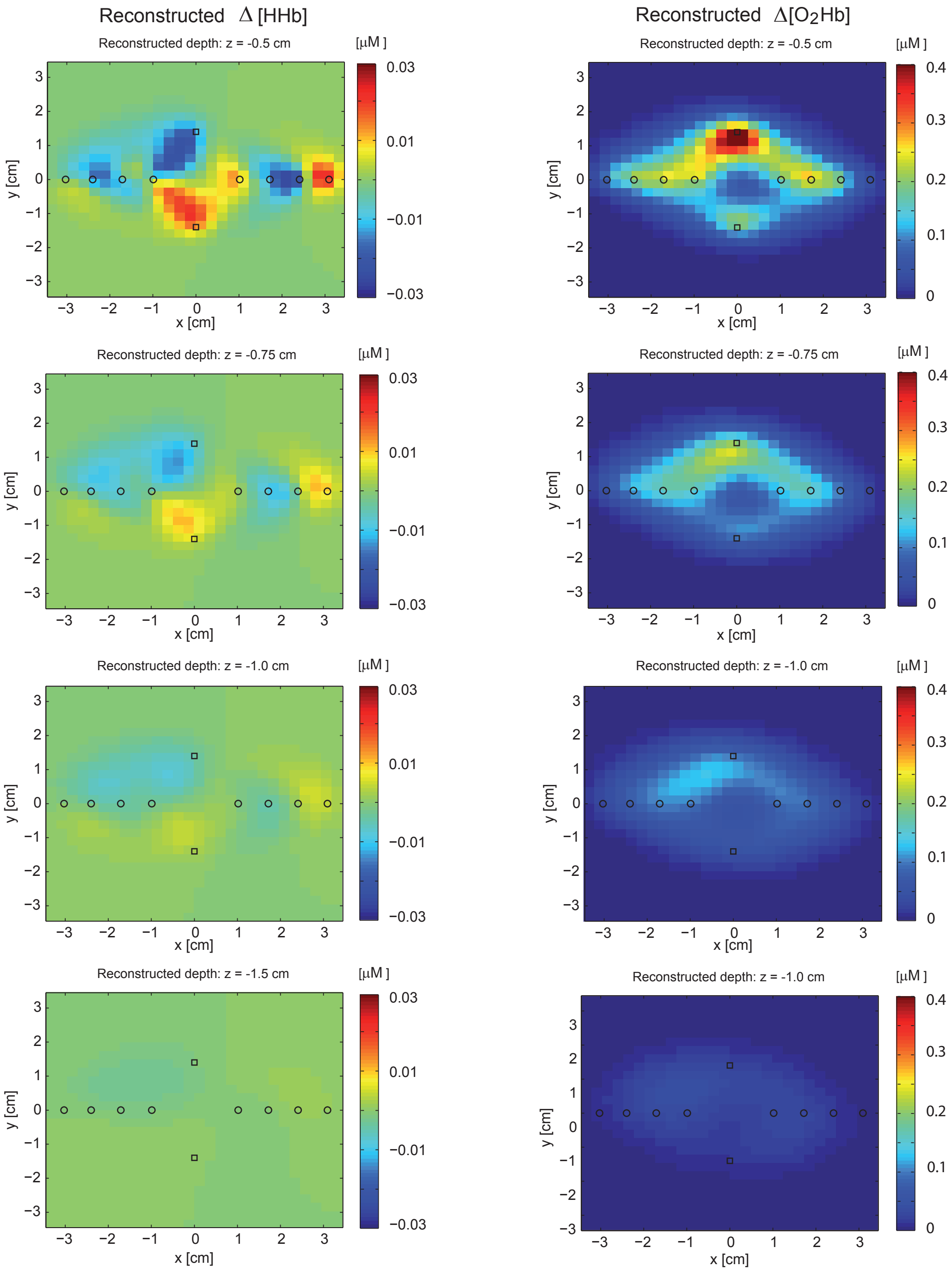

Figure 2.30 – DOI reconstruction at different depths (z = -0.5, -0.75, -1.0 and -1.5 cm) for the skin heating measurement. On the left side the reconstructed changes in [HHb] are shown and on the right side the reconstructed changes in [O_2Hb]. The black ellipses represent the position of the light sources and the black rectangle the position of the detectors. From top to bottom, the depth z increases.

3 Characterization of the multi-frequency FD-NIRS instrument

Multi-frequency frequency-domain spectrometer for tissue analysis

---

Sonja Spichtig[1,2], René Hornung[3], Derek W. Brown[1], Daniel Haensse[1,2] and Martin Wolf[1,2]

[1]Clinic of Neonatology, University Hospital Zurich, 8091 Zurich, Switzerland
[2]Institute for Biomedical Engineering, Swiss Federal Institute of Technology, 8092 Zurich, Switzerland
[3]Department of Obstetrics and Gynecology, Kantonsspital St. Gallen, 9007 St. Gallen, Switzerland

Published in: Rev. Sci. Instrum. 80, 024301 (2009)

Abstract

In this paper we describe the modification and assessment of a standard multi-distance FD-NIRS instrument to perform multi-frequency FD-NIRS measurements. The first aim of these modifications was to develop an instrument that enables measurement of small volumes of tissue, such as the cervix, which is too small to be measured using a multi-distance approach. The second aim was to enhance the spectral resolution to be able to determine the absolute concentrations of O_2Hb, HHb, tHb, water and lipids. The third aim was to determine the accuracy and error of measurement of this novel instrument in both in-vitro and in-vivo environments. The modifications include two frequency synthesizers with variable, freely adjustable frequency, broadband high-frequency amplifiers, the development of a novel APD detector and demodulation circuit, additional laser diodes with additional wavelengths and a respective graphic user interface to analyze the measurements. To test the instrument and algorithm, phantoms with optical properties similar to those of biological tissue were measured and analyzed. The results show that the μ_a can be determined with an error of $< 10\%$. The error of the scattering coefficient was smaller than 31%. Since the accuracy of the chromophore concentrations depends on the μ_a and not on the μ_s', the $< 10\%$ error is the clinically relevant parameter. In addition, the new APD had similar accuracy as the standard PMTs. To determine the accuracy of chromophore concentrations measurements we employed liquid Intralipid® phantoms that contained 99% water, 1% lipid, and an increasing concentration of hemoglobin in steps of 0.010 mM. Water concentration was measured with an accuracy of 6.5% and hemoglobin concentration with an error of 0.0024 mM independent of the concentration. The measured lipid concentration was negative, which shows that the current set-up is not suitable for measuring lipids. Measurements on the forearm confirmed reasonable values for water and hemoglobin concentrations, but again not for lipids. As an example of a future application, chromophore concentrations in the cervix were measured and comparable values to the forearm were found. In conclusion the modified instrument enables measurement of water concentration in addition to O_2Hb and HHb concentrations with a single source-detector distance in small tissue samples. Future work will focus on resolving the lipid component.

Introduction

Biological tissue exhibits relatively low absorption in the near-infrared range, 650 to 1000 nm, and light in this wavelength range penetrates tissue relatively deeply. NIRS has been successfully applied in medicine for a variety of non-invasive diagnostic purposes, e.g. to quantitatively investigate the oxygenation, blood flow, volume or function of tissues such as the breast, muscle or brain (Wolf et al. 2008, Leff et al. 2008, Ward et al. 2006, Wolf et al. 2007). Various techniques have been developed for this purpose. CW spectroscopy employs light sources with constant intensity to determine changes in attenuation. However, this enables only measurement of changes in chromophore concentrations and not absolute values. To determine absolute values the absorption (μ_a in $1/cm$) and reduced scattering (μ_s' in $1/cm$) coefficients of tissue must be quantified. Chromophore concentrations can then be calculated from μ_a values. Measurement of μ_a values is achieved either by TD spectroscopy, which records the dispersion of extremely short pulses of

light by tissue, or by FD spectroscopy, which assesses the phase shift (Θ) and amplitude (A) of intensity modulated light. Here, we focus on FD spectroscopy. There are two basic frequency-domain modes, the multi-distance mode, which measures Θ and A at several different source-detector distances, but at a single modulation frequency, and the multi-frequency mode, which measures Θ and A at a single source-detector distance, but at several different modulation frequencies (Fantini, Franceschini and Gratton 1994). The multi-distance method has a higher signal to noise ratio, but assumes a relatively large volume of homogeneous tissue of $\approx$250 ml. For many clinical applications this assumption is fulfilled. However, other clinical situations necessitate small volume measurements. To increase the scope of clinical applications and the potential of NIRS it is then desirable to enable measurements on smaller tissue volumes. The multi-frequency method is ideally suited for smaller volumes of tissue, in the range of $\approx$30 ml. This extends the range of clinical applications to smaller organs or tissues such as the cervix. While multi-distance instruments are commercially available (Fantini, Franceschini and Gratton 1994, *ISS Inc.* n.d.), multi-frequency instruments are not yet available on the market.
Therefore the aims of this work were to

- transform a commercial ISS Inc. (Champaign, Illinois, USA) FD multi-distance instrument to a multi-frequency mode instrument, which enables measurements on small tissues at a single source-detector distance,
- to enhance the spectral resolution to enable quantitative detection of O_2Hb, HHb and tHb, as well as water and lipid concentrations
- and finally to test the accuracy and error of measurements, thus characterizing the properties of the novel instrument in vitro and in vivo.

Instrumentation

The commercially available ISS Imagent® multi-distance instrument that was transformed originally featured four PMT as detectors and 32 laser diodes as light sources, 16 at 690 nm and 16 at 830 nm. The emitted light intensity is modulated at 110 MHz (*ISS Inc.* n.d.). The light sources are time multiplexed, i.e. only one light source is on at a time. The light is coupled to fibers (400 μm diameter) that guide light to the tissue. After penetrating the tissue the light is received and guided back to the instrument by another fiber (3 mm diameter), where it is detected by a PMT modulated at 110’005 kHz. The demodulated signal at 5 kHz is amplified and digitized in a computer (Datel PCI-416-M2 PCI ADC board). The computer also generates the timing signals (PCI-CTR05 PCI board). A software computes Θ and A by FFT and calculates the μ_a and μ_s' and absolute concentrations of O_2Hb, HHb and tHb and the regional tissue oxygen saturation StO_2. The sensor implements a multi-distance geometry, i.e. usually Θ and A are measured at four different distances, ranging from 1.5 to 5 cm. In theory, it is assumed that the tissue below the sensor is homogeneous (Fantini, Franceschini and Gratton 1994). Thus, this technique has been successfully applied in many types of tissue with a volume larger than 250 ml. It would, however, be advantageous to extend the range of applications to small volumes of tissue such as the cervix. Additionally, the commercial instrument’s detectors are insensitive to wavelengths above 880 nm and thus chromophores such as water and lipids, whose absorption peaks are above 900 nm, cannot be detected.

Modified ISS Inc. multi-frequency FD instrument

To extend the range of NIRS to smaller tissue volumes and to enable measurement of water and lipids, a commercially available Imagent® has been modified in collaboration with ISS Inc.

To enable the multi-frequency mode, the two original synthesizers with fixed frequencies were replaced by two frequency generators (PTS 500), whose frequency can be freely adjusted from 50 to 500 MHz. A new broad band amplifier delivers the modulation frequency to the laser diodes and detectors. The Boxy® (ISS Inc, Champaign, Illinois, USA) software that controls the instrument was modified to control the two frequency generators. Compared to network analyzers (Pham, Coquoz, Fishkin, Anderson and Tromberg 2000) our set-up decreases the sample time from $\approx$60 – 10 s and enables continuous measurements at a time resolution better suited for physiological measurements.

To be able to also measure water and lipid, the instrument was modified to measure at more, and also at higher, wavelengths. This required modifications of both the light sources and detectors. In the multi-frequency mode, only one laser diode is needed per wavelength. Thus, one laser board was equipped with 8 different laser diodes at the following wavelengths (in brackets the chromophore/s for which the respective wavelength is relevant): 690 nm (HHb), 692 nm (HHb), 764 nm (HHb), 831 nm (O_2Hb), 872 nm (O_2Hb), 888 nm (O_2Hb, lipid), 914 nm (lipid, water) and 980 nm (water).

The standard PMT detectors (R926, Hamamatsu Photonics, Japan) of the ISS Inc. instrument have several disadvantages. They are relatively expensive, fragile (an excess of light may destroy the PMT, a situation that can easily occur in a clinical environment), and need a high supply voltage of 1 kV. Their spectral sensitivity decreases rapidly at 800 nm which makes it impossible to detect water and lipid spectra above 880 nm. In addition the frequency response of the PMT decreases above 400 MHz. However, they have a high internal gain and a large detection area. For our low-level light application, we have chosen an APD as light detector, because it offers a broader spectral range including the wavelengths required for water and lipid detection. The APD also has a higher sensitivity, improved quantum efficiency compared to the PMT detector, and a higher signal to noise ratio than a PIN photodiode. To implement the APD two circuit boards were designed and produced, one to generate the high voltage for the APD and the APD demodulation board with the APD itself and all the filters.

The reverse bias voltage of the APD is delivered by the TR-0.2P high-voltage power supply (Matsusada). It has an output voltage of 0 to 200 V and temperature compensation. The voltage is controlled by a potentiometer.

The intensity of the laser diodes can be modulated from 50 to 500 MHz. The APD detector is modulated at a frequency that is always 5 kHz above the laser diodes. Thus, at the detector the frequency is mixed down to 5 kHz. This is achieved by heterodyne modulation of the reverse voltage of the APD. It consists of high-voltage and high-frequency elements. These are connected by inserting a capacitor as a DC-blocker on the high-

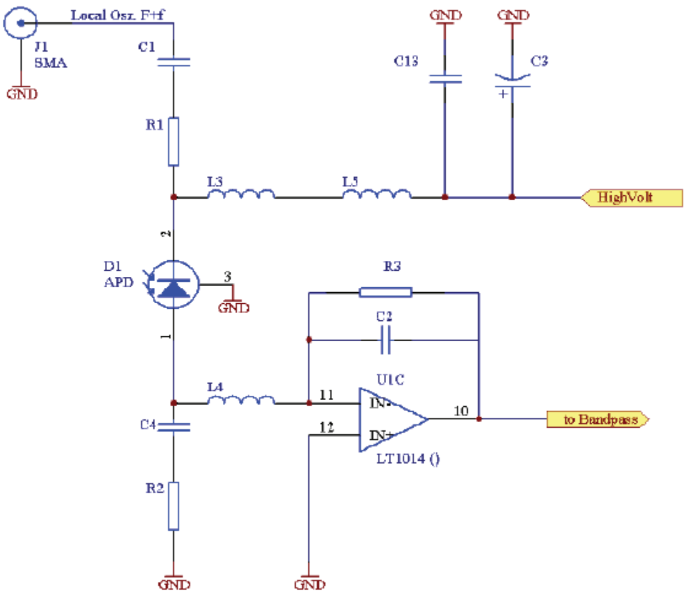

Figure 3.1 – APD demodulation board; high voltage and high frequency parts of APD, lowpass and transimpedance amplifier.

frequency element and inductivity as a high frequency-blocker on the high-voltage side on the APD demodulation board (Fig. 3.1).

For instance, when the incident light is modulated with 50 MHz and the APD with 50 MHz + 5 kHz, then the resulting signal contains the Θ and A information in a 5 kHz wave. The higher frequencies are suppressed by a lowpass filter (Yokoyama et al. 1995), which is attached to the anode of the APD. It is followed by a transimpedance amplifier to convert the current into a voltage. A feedback capacitance over the operational amplifier is applied in order to avoid oscillations of the system. The 5 kHz signal is connected to an active bandpass filter, which is implemented as a two-pole (4th order) multi-feedback filter (Lancaster 1996). It works with only one operational amplifier to serve the intended purpose. The source impedance must be low with respect to the input resistance, with the transimpedance amplifier as the source. This implementation only allows a Q value of 2 to 5 and the amplification is $-2Q^2$. To ensure the stability of the system, the amplification of the operational amplifier should be at least $20Q^2$ at the resonance frequency. An amplifier is connected to the output of the bandpass filter to enable reasonable values for the analog-digital converter board of the computer. The Θ and A are calculated digitally by fast Fourier Transform (FFT) .

The modified instrument is shown in Fig. 3.2.

Theory

In the following we describe how the concentration of O_2Hb, HHb, water and lipid can be calculated from the Θ and A,. The underlying theory of multi-frequency FD spectroscopy

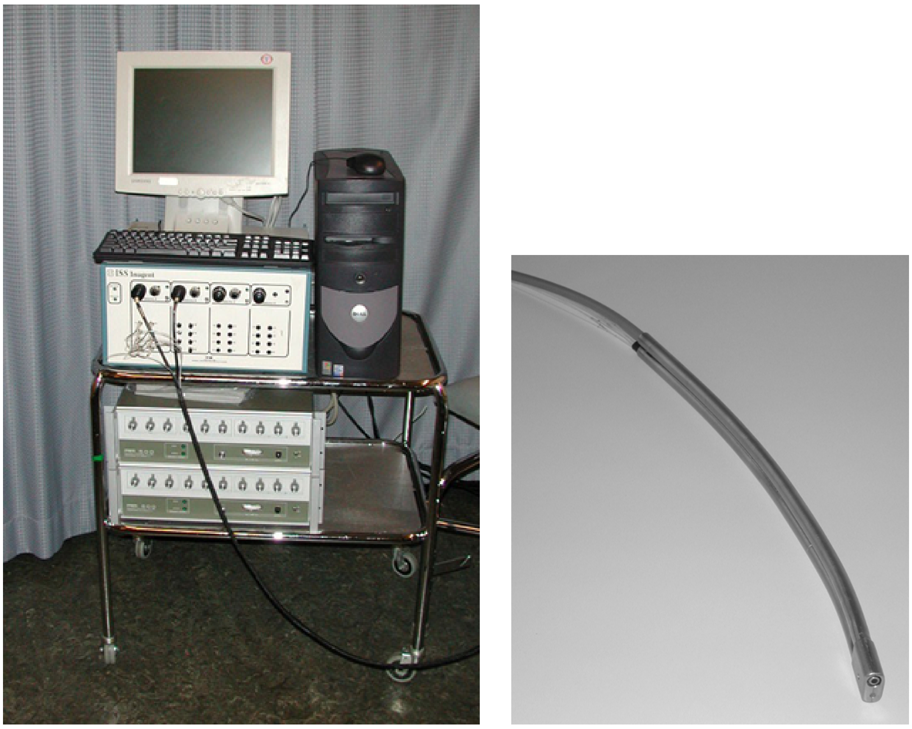

Figure 3.2 – Left side: ISS Imagent® and right side: optical cervix sensor.

has been described in detail elsewhere (Arridge 1999). Briefly, the propagation of light through a highly scattering medium ($\mu_a << \mu_s'$) is described by the diffusion approximation to the Boltzmann transportation equation. The diffusion equation describes the propagation of a photon density wave,

$$-D(r)\nabla^2\Phi(r,t) + \mu_a\Phi(r,t) + \frac{1}{c}\frac{\partial\Phi(r,t)}{\partial t} = q_0(r,t) \tag{3.1}$$

With r the source-detector distance, t the time, q_0 a modulated point source, D the diffusion coefficient, and $\Phi(r,t)$ the space- and time-dependent photon density. The light velocity in the medium can be calculated using c = (3 · 10^8 m/s)/n, where n is the refractive index for the medium.

The diffusion equation can be solved by assuming a semi-infinite medium, which approximately corresponds to the case in many clinical applications. The partial-current-extrapolated-boundary unification is an accurate representation of the boundary condition; for details about the theory and application see (Haskell et al. 1994).

The two measurable quantities of a photon density wave, the phase lag Θ^m_{lag} and the amplitude A^m_{att}, can be theoretically simulated: For a given μ_a, μ_s' and modulation frequency ω of the point source, the solution to the diffusion equation can be solved and the theoretical phase lag $\Phi^{th}_{lag}(\omega,\mu_a,\mu_s')$ and amplitude attenuation $A^{th}_{att}(\omega,\mu_a,\mu_s')$ calculated (Haskell et al. 1994).

Calibration and curve fitting

Since the various instrument factors such as source power, detector gain, losses due to the source and detector fiber are unknown and cannot be eliminated, the instrument needs to be calibrated. This calibration is done by measuring the phase lag Θ^{m}_{lag} and amplitude A^{m}_{att} over all employed modulation frequencies on a phantom with known optical properties similar to tissue. A comparison between the obtained values with the theoretical phase lag $\Phi^{th}_{lag}(\omega,\mu_a,\mu_s')$ and amplitude attenuation $A^{th}_{att}(\omega,\mu_a,\mu_s')$ leads to the modulation-frequency-dependent correction factor A^{c}_{att} and term Θ^{c}_{lag}:

$$A^{c}_{att}(\omega) = \frac{A^{m}_{att_{phantom}}(\omega)}{A^{th_{phantom}}(\omega)}, \quad \Theta^{c}_{lag}(\omega) = \Theta^{m}_{lag_{phantom}}(\omega) - \Theta^{th}_{lag_{phantom}}(\omega). \tag{3.2}$$

This correction factor and term are then applied to biological tissue measurements to eliminate the unknown instrumental factors,

$$A^{mc}_{att}(\omega) = \frac{A^{m}_{att}(\omega)}{A^{c}_{att}(\omega}, \quad \Theta^{mc}_{lag_{tissue}}(\omega) = \Theta^{m}_{lag_{tissue}}(\omega) - \Theta^{c}_{lag}(\omega). \tag{3.3}$$

A^{mc}_{att} and Θ^{mc}_{lag} are the calibrated measurement values of the tissue under investigation at a specific modulation frequency. A recursive fitting procedure is used to determine the $\mu_{a,tissue}$ and $\mu'_{s,tissue}$ for which the corresponding A^{th}_{att} and Θ^{th}_{lag} show the best agreement to the calibrated measurement values A^{mc}_{att} and Θ^{mc}_{lag}. More explicitly, a least square Gaussian-Newton algorithm with varying $\mu_{a,fit}$ and $\mu_{s',fit}$ is applied to minimize the following expression over all modulation frequencies ω_n:

$$\Big\{\sum_{n}([A^{th}_{att}(\omega_n,\mu_{a,fit},\mu'_{s,fit}) - A^{mc}_{att}(\omega_n,\mu_{a,tissue},\mu'_{s,tissue})]^2 + \dots$$
$$\alpha[\Theta^{th}_{lag}(\omega_n,\mu_{a,fit},\mu'_{s,fit}) - \Theta^{mc}_{lag}(\omega_n,\mu_{a,tissue},\mu'_{s,tissue})]^2\Big\} \tag{3.4}$$

The factor α adjusts the magnitude of the phase difference to that of the amplitude attenuation, meaning that differences in phase and amplitude have the same impact on the fitting procedure. It is also possible to fit Θ_{lag} or A_{att} by themselves (minimizing the differences for each variable separately), however, fitting both simultaneously increases the robustness of the fit (Pham, Coquoz, Fishkin, Anderson and Tromberg 2000).

Determining the physiological properties

Once μ_a and μ_s' of the measured tissue have been determined, the physiological concentrations of interest, mainly O_2Hb, HHb, water and lipid, can be calculated. For a given wavelength λ, the relation between μ_a and the concentration of the mentioned absorbers is,

$$\mu_a^{\lambda} = \varepsilon^{\lambda}_{HHb} \cdot c_{HHb} + \varepsilon^{\lambda}_{O_2Hb} \cdot c_{O_2Hb} + \varepsilon^{\lambda}_{H_2O} \cdot c_{H_2O} + \varepsilon^{\lambda}_{lipid} \cdot c_{lipid}, \tag{3.5}$$

where $\varepsilon^{\lambda}_{x}$ is the molar extinction coefficient of absorber x at wavelength λ and c_x is the concentration of absorber x. Equation 3.5 can also be written in the matrix form,

$$\vec{\mu_a} = ln(10) \cdot E \cdot \vec{c}, \tag{3.6}$$

where E is the extinction matrix and c the concentration vector (Cerussi et al. 2001),

$$E = \begin{pmatrix} \varepsilon_{HHb}^{\lambda_1} & \varepsilon_{O_2Hb}^{\lambda_1} & \varepsilon_{H_2O}^{\lambda_1} & \varepsilon_{lipid}^{\lambda_1} \\ \vdots & \vdots & \vdots & \vdots \\ \varepsilon_{HHb}^{\lambda_n} & \varepsilon_{O_2Hb}^{\lambda_n} & \varepsilon_{H_2O}^{\lambda_n} & \varepsilon_{lipid}^{\lambda_n} \end{pmatrix}, \quad \vec{c} \begin{pmatrix} c_{HHb} \\ c_{O_2Hb} \\ c_{H_2O} \\ c_{lipid}. \end{pmatrix} \tag{3.7}$$

To calculate the concentrations in Eq. 3.6, the equation and hence the extinction matrix have to be inverted. In this case where the system is overdetermined (more wavelengths than absorbers), the Gaussian normal equation, a least-squares procedure minimizing the error, is applied,

$$\vec{c} = \frac{1}{ln(10)}(E^T \cdot E)^{-1} E^T \cdot \mu_a. \tag{3.8}$$

To calculate chromophore concentrations, the values of the extinction coefficients of hemoglobin and water were taken from the literature (Wray et al. 1988, Matcher et al. 1994, Matcher, Elwell, Cooper, Cope and Delpy 1995, *Oregon Medical Laser Center* n.d.). For lipid we used the spectra of pork lipid (*Oregon Medical Laser Center*).

Graphical user interface

To analyze the data and calculate the optical properties a graphical user interface was programmed. It enables graphical inspection of the results of the calibration, measurement, and fitted lines. Furthermore, from the raw optical data the optical properties of the sample are calculated for each wavelength and the chromophore concentrations determined. Motion artifacts sometimes occur in clinical situations and may lead to unacceptable data. The graphic user interface enables immediate analysis and detection of such problems. Thus, often it will be possible to carry out another measurement without motion artifacts.

Measurements

To test the reproducibility, reliability, and accuracy of the modified instrument and algorithms, several experiments were performed:

- Measurements on silicone phantoms with known optical properties,
- Measurements of an Intralipid® solution with known chromophore concentrations
- In vivo measurement on a male human forearm for a comparison with values from the literature. Additionally, measurements on the human cervix were performed to show the feasibility of the method for small tissue investigations.

For all measurements a single-distance reflection sensor (Fig. 3.2) with a source-detector separation of 1.5 cm was used (mean penetration depth of ≈5 mm). The following eight laser diodes of the instrument were used: 980, 914, 888, 872, 805, 764, 692, and 690 nm. The measurements were recorded with modulation frequencies ranging from 130 to 490 MHz in 10 MHz steps. The modulation frequency range for the analysis of all measurements was constrained to $130-400$ MHz due to resonance effects below 130

MHz, significantly increasing noise for modulation frequencies above 400 MHz and to optimize the signal to noise ratio.

Silicone phantom measurements

An array of four silicone phantoms with known optical coefficients (Tab. 3.1) specified by the manufacturer ISS Inc. was selected to test the instrumental accuracy of the modified instrument. For comparison, the experiments were once performed with the APD and once with the PMT.

Each phantom was measured three times in an alternating order. First, the measurements were recorded by the PMT, then by the APD. For the analysis, a phantom (i.e., calibration phantom) was used to calibrate for the instrumental factors while optical properties of another phantom (i.e., measurement phantom) were measured. As the respective calibration phantom we chose the one with the μ_a closest to the one of the measurement phantom. The analysis was performed for each combination of a specific calibration-measurement phantom pair. For instance, for phantom 1 as measurement phantom and phantom 4 as calibration phantom, each measurement of phantom 1 was calibrated with each measurement of the calibration phantom 4. For three measurements on each phantom this yields nine combinations, i.e., nine estimates of μ_a and μ_s' for the measurement phantom 1. μ_a and μ_s' were averaged for each wavelength and the error $100 \cdot \frac{\text{measured value}-\text{actual value}}{\text{actual value}}$ and standard deviation (SD) of μ_a and μ_s' calculated.

Since the spectral range of the PMT is limited to 880 nm, the error for the wavelengths of 888, 914, and 980 nm were higher than 100% and increasing with the wavelength. For the other wavelengths, the error for μ_a was constant and $< 10\%$. The APD showed no wavelength-dependent change in the accuracy of the measured optical properties, i.e., the error was very similar for all wavelengths for μ_a and μ_s'. For μ_a the error was smaller than 10% for all wavelengths. Since the errors were very similar across wavelengths, in Tab. 3.1 the errors for μ_a and μ_s' were averaged across all wavelengths for the APD and across all wavelengths smaller than 880 nm for the PMT.

Tab. 3.1 shows that the error increases with the difference in the absorption between calibration and measurement phantom. For example the largest error was found for measurement phantom 3 and calibration phantom 1 with the largest $\Delta\mu_a = 0.021$ cm^{-1}. The same is true for the μ_s': the errors for μ_s' increase with the size of the $\Delta\mu_s'$ between calibration and measurement phantom (e.g. for phantom 1 versus phantom 4 $\Delta\mu_s' = 6$ cm^{-1} and for phantom 2 versus phantom 4 $\Delta\mu_s' = 0.1$ cm^{-1}). Since the accuracy of the chromophore concentrations depends on the μ_a and not on the μ_s', the error in $\mu_a < 10\%$ is the clinically relevant parameter.

This has implications for measurements on tissue. It is advisable to use a calibration phantom with similar optical properties as the tissue under investigation. The observed effect may be due to some instrumental nonlinearities which lead to calibration errors that depend on the difference between calibration and measurement phantoms.

Summarizing the results, for all wavelengths the APD provides approximately the same accuracy as the PMT. However, the APD enables detection of wavelengths above 880 nm, which includes absorption peaks of lipids and water. The small SD of the error demonstrates that the reproducibility of the measurements is high, demonstrating proper

Det.	Meas. phantom no.	μ_a* [cm^{-1}]	μ_s'* [cm^{-1}]	Cal. phantom no.	Error of μ_a ± SD in %	Error of μ_s' ± SD in %
PMT	1	0.125	4.9	4	4.77 ± 2.15	26.47 ± 4.37
	2	0.104	11.0	4	2.54 ± 1.82	0.63 ± 0.33
	3	0.146	4.1	1	10.00 ± 1.18	9.78 ± 2.81
	4	0.115	10.9	2	2.55 ± 1.87	0.63 ± 0.39
APD	1	0.125	4.9	4	3.70 ± 2.07	30.60 ± 3.29
	2	0.104	11.0	4	2.03 ± 0.98	1.63 ± 0.61
	3	0.146	4.1	1	9.90 ± 2.77	11.77 ± 3.54
	4	0.115	10.9	2	2.09 ± 1.00	1.65 ± 0.57

* measured at 690nm by the manufacturer ISS Inc.

Table 3.1 – Results of the measurements on the silicon phantoms for the APD and the PMT detector. The mean error and standard deviation (SD) of the measured optical properties compared to the optical properties at 690 nm specified by the manufacturer ISS Inc. are listed.

functioning of the instrument.

Intralipid® measurements

The main purpose of the measurements in an Intralipid® phantom was to test whether chromophore concentrations can be determined accurately. Thus, not only the instrumental accuracy but also the algorithms used to calculate optical properties and chromophore concentrations were tested. The Intralipid® phantom is a liquid emulsion, which has similar μ_a and μ_s' to human tissue, and the concentrations of water, lipids, and tHb are known.

The APD detector, the same frequency range, and wavelengths were used as described above. Again, the calibration was performed with two silicone phantoms from ISS Inc. (phantom 1 and 2 in Tab. 3.1). The Intralipid® phantom consisted of 99% water with 1% Intralipid® and an increasing amount of hemoglobin. Intralipid® without hemoglobin at this dilution is an emulsion of lipids, which has similar μ_s' as tissue, i.e., $\mu_s' = 9.71$ cm^{-1} at 633 nm (van Staveren et al. 1991). We added constant amounts of red cell concentrate [the hemoglobin content was determined beforehand by blood gas analysis (ABL 835, Radiometer Copenhagen)] in ten steps, increasing the tHb concentration by 0.010 mM with each step. This tHb is used as the reference value and is called the "actual concentration of tHb". The Intralipid® solution was maintained at a constant temperature of 37°C using a temperature controlled bath mixed with a magnetic mixer to ensure homogeneity of the solution and avoid sedation.

In total nine calibrations per silicone phantom were recorded: three before, three between, and three after the Intralipid® phantom measurements. Each specific tHb concentration in the Intralipid® phantom was also measured three times and for the analysis every single measurement was calibrated with two (both phantoms) times nine calibration measurements. The resulting 54 optical coefficients for each tHb concentration of the Intralipid®

phantom were then averaged to obtain mean and SD, which are displayed in Fig. 3.3. With our instrument we determined the optical coefficients of $\mu_a = 0.161\ \text{cm}^{-1}$ and $\mu_s' = 11.56\ \text{cm}^{-1}$ at 690 nm. These coefficients were measured with 0.010 mM of tHb. Since no data were recorded without hemoglobin in the Intralipid® phantom, we subtracted the absorption of the tHb and received $\mu_a = 0.049\ \text{cm}^{-1}$ for the pure Intralipid® phantom. Compared to the published optical coefficients (van Staveren et al. 1991) of $\mu_a = 0.0169\ \text{cm}^{-1}$ and $\mu_s' = 9.71\ \text{cm}^{-1}$ at 633 nm the measured ones show good agreement, taking into account that the optical coefficients vary from batch to batch.
The measured tHb correlated well with the actual values (Fig. 3.3), except for the 0.050 and 0.100 mM actual tHb. The reason for this error at 0.050 and 0.100 mM tHb is that the measured μ_s' for the 980 nm wavelength were overestimated by a factor $3-4$. This led to large errors in the water concentration but has also affected the tHb. Since our instrument is designed for tissue, which has a lower concentration of water than the Intralipid® phantom with 99% water concentration, the signal at the 980 nm wavelength was relatively small because the absorption peak of water is at this wavelength. Therefore the signal to noise ratio at 980 nm was comparably low, which leads to high sensitivity to motion artifacts and probably led to the large μ_s' values. In a real measurement in tissue, an error of this size would lead to the elimination and repetition of the measurement.

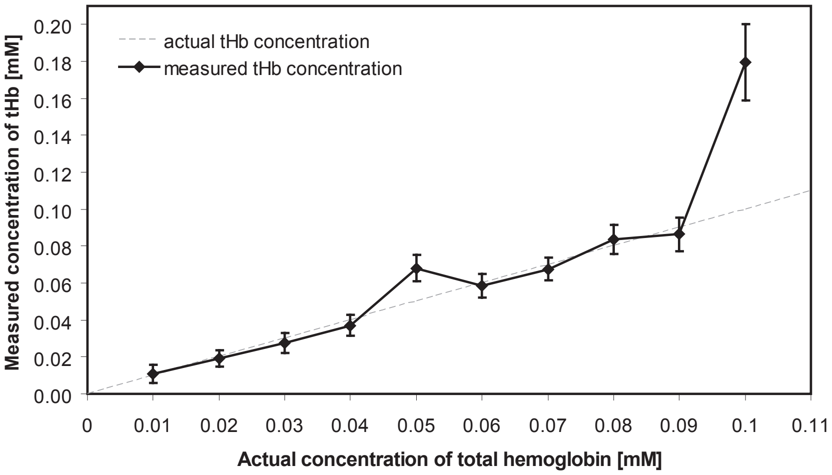

Figure 3.3 – Correlation of the actual tHb (dotted line) and the one measured by the modified NIRS instrument (solid line).

To analyze the agreement between the actual and measured tHb concentrations, we calculated the mean difference ± standard deviation between the two concentrations (measured - actual) according to the literature (Bland and Altman 1986): $\Delta[tHb] = 0.0088 \pm 0.02$ mM for all measurements (Fig. 3.4). These values are strongly affected by the two outliers 0.050 and 0.100 mM. When these were removed, a mean of the differences of -0.0012 ± 0.0024 mM was obtained, which was 5 – 10 times smaller than the lowest measured concentration. This indicates a high degree of accuracy of the measured concentrations, provided outliers are detected by their erroneous μ_s' and removed.

The concentration of water and lipid in the Intralipid® emulsion was nearly constant throughout the experimental series because the total volume of the solution was 400 ml and the addition of 0.010 mM of hemoglobin corresponded to an addition of only 1.6 ml of red cell concentrate. Therefore, for water as well as lipid all measurements were averaged, resulting in a water concentration of 58.6 ± 8.3 M. Since the Intralipid® phantom consisted of 99% water, a concentration of 55 M was expected. Thus, the water concentration was determined with a mean error of 6.5%.

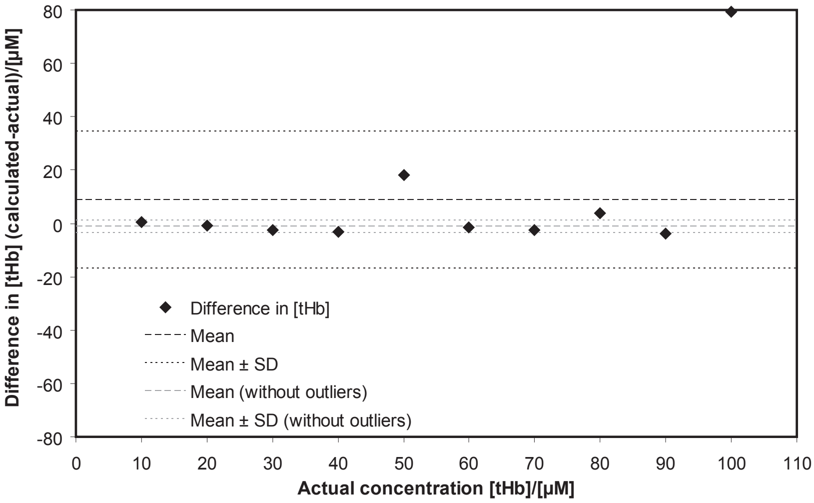

Figure 3.4 – Graphical representation of the difference in tHb concentration (measured-actual), the mean of the difference (prominent dotted line) ± standard deviation of the difference (dotted line) with and without outliers.

The lipid concentration of -408 ± 139 mM was negative instead of close to 0 mM, which is erroneous. Thus, this experiment revealed that the lipid cannot be accurately measured with the current setup. There are two possible reasons for these erroneous results: (1) the implemented spectrum of porcine lipid may not match the actual spectrum of Intralipid® and (2) the silicone of the phantom has an absorption peak at 910 nm close to the wavelength of 914 nm. Although we have tried to correct for this absorption peak, the interpolation may not match the actual spectrum and we did not have the means to measure the actual spectrum of the calibration phantoms. We simulated small variations in the calibration of this peak and they considerably affected the measured lipid concentrations. Therefore we will measure the spectrum of the calibration phantom in the future in an attempt to overcome this problem. Once the spectra are obtained, the measured data can still be reanalyzed, but for the moment we conclude that the measurement of the lipid concentration is inaccurate.

In summary, the experiment demonstrates the importance of testing the accuracy of the instrument and algorithm. It also shows the feasibility of reliably and accurately measuring the tHb and water concentration but not lipid concentration by our instrument.

	Optical Properties		Chromophore concentrations	
λ [nm]	μ_a [cm^{-1}]	μ_s' [cm^{-1}]		
690	0.129 ± 0.003	8.10 ± 0.91	[HHb]	0.0173 ± 0.0006 mM
692	0.124 ± 0.007	7.49 ± 0.75	[O_2Hb]	0.0421 ± 0.005 mM
764	0.141 ± 0.006	7.03 ± 0.77	[tHb]	0.0594 ± 0.005 mM
831	0.130 ± 0.007	6.88 ± 0.74	StO_2	70.7 ± 2.7 %
872	0.164 ± 0.014	6.58 ± 0.78	H_2O	22.98 ± 1.34 M
888	0.192 ± 0.017	6.46 ± 0.71	lipid	-116.6 ± 137.3 mM
914	0.172 ± 0.018	5.9 ± 0.63		
980	0.330 ± 0.007	5.87 ± 0.55		

Table 3.2 – Measured optical coefficients and chromophore concentrations for the forearm of a male subject.

In vivo measurements

To test the modified instrument and analysis with an in vivo application, measurements on a male human forearm were performed and the results were compared to values previously presented in the literature. The APD detector, the same frequency range, and wavelengths were used as described above. For the calibration, two silicone phantoms from ISS Inc. (phantoms 1 and 2 of Tab. 3.1) were used.

The measurements were performed in the following order: forearm, phantom 1, and phantom 2. The procedure was repeated three times. Each forearm measurement was calibrated with each phantom measurement and the mean and SD for each wavelength and chromophore concentration were calculated (Tab. 3.2).

The measured concentrations of HHb, O_2Hb, tHb, and StO_2 values values are similar to published data (Casavola et al. 2000). Also the SDs of the hemoglobin and water concentrations are small, corresponding to an error of measurement of 3.5% for HHb, 11.9% for O_2Hb, 8.4% for tHb, and 3.8% for StO_2. Since it is expected that the concentration of the chromophores is not completely stable in living tissue, the true error may even be smaller. A water concentration of 23.0 ± 1.3 M was obtained, which corresponds to a tissue water content of 41.37 ± 2.41%. From the literature, water concentration of 78 ± 4% in the male human forearm muscle and 20 ± 9% in the adipose tissue have been published (Matcher et al. 1994). Since adipose tissue is present between muscle and the skin and due to the small mean penetration depth (0.5 cm) of the sensor, it is likely that mixture of muscle and adipose tissue was measured. A tissue water content of 41.37%, i.e., a value between adipose tissue and muscle, seems reasonable. It is quite clear, however, that this is only a relatively imprecise estimate. The SD of repeated measurements and thus the error of measurement at 5.8% were small for water.

As in the Intralipid$^{\circledR}$ experiment, the estimation of the actual lipid concentration yielded a negative value and thus was inaccurate. Possible reasons have been discussed above.

Thus, we conclude that for the HHb, O_2Hb, tHb, StO_2, and water, the in vivo measurement

	Test subject 1	Test subject 2
[HHb]	0.0220 mM	0.0145 mM
[O_2Hb]	0.0734 mM	0.060 mM
[tHb]	0.0954 mM	0.0745 mM
StO_2	76.9 %	80.5 %
[H_2O]	24.95 M	19.56 M
[lipid]	-730.61 mM	-766.65 mM

Table 3.3 – Measured chromophore concentrations for the cervix of two test subjects.

yields reasonable values and an acceptable error of measurement for clinical research applications.

To show that the method is suitable for investigations of small tissue volumes, the same setup was used to perform measurements of the cervix on two test subjects. The results are shown in Tab. 3.3. Since no other data on cervix chromophore concentrations have previously been published, we can only demonstrate the feasibility but not the accuracy of the method.

The measured HHb, O_2Hb, and tHb are higher than the values on the male human forearm but still within a reasonable range. Water concentrations also compare favorably to those measured in the male human forearm. As before, estimation of the measured lipid concentration yielded a negative value and thus was inaccurate. Possible reasons for this have been discussed above.

In conclusion, in the cervix reasonable values for O_2Hb, HHb, and water were obtained.

Conclusions

In this work we present the modification and assessment of a commercially available FD NIRS instrument adapted from a multi-distance instrument to a multi-frequency FD NIRS instrument to enable measurements in small volume of tissue. The algorithms used to determine optical coefficients and concentrations of HHb, O_2Hb, tHb, lipid, and water were implemented in a graphical user interface. The instrument was tested in solid and liquid phantoms as well as in in vivo settings. The results show that thorough testing in vitro and in vivo is essential to assess the strengths and weaknesses of an instrument and they demonstrate the capability of the modified instrument to accurately quantify both μ_a and μ_s' and all chromophore concentrations (except for lipids) in highly scattering media, thus providing the necessary background information for further clinical investigations. There are numerous clinical applications for this noninvasive method, which include, but are not limited to, organs with small volumes such as the hand, foot, tongue, and cervix, the latter to monitor cervical ripening during pregnancy (Baños et al. 2007).

Acknowledgements

We gratefully acknowledge funding from the Swiss National Research Foundation.

4 Application of the multi-distance FD-NIRS instruments

4.1 Movement artifact reduction

How to detect and reduce movement artifacts in near-infrared imaging using moving standard deviation and spline interpolation

---

Felix Scholkmann[1,2], Sonja Spichtig[1,3], Thomas Muehlemann[1,3] and Martin Wolf[1,3]

[1]Clinic of Neonatology, University Hospital Zurich, 8091 Zurich, Switzerland
[2]Institute of Informatics, University of Zurich, 8050 Zurich, Switzerland
[3]Institute for Biomedical Engineering, Swiss Federal Institute of Technology, 8092 Zurich, Switzerland

Published in: Physiol. Meas. 31, 649-662 (2010)

Abstract

NIRI is a neuroimaging technique which enables to non-invasively measure hemodynamic changes in the human brain. Since the technique is very sensitive, the movement of a subject can cause movement artifacts (MAs), which affect the signal quality and results to a high degree. No general method is yet available to reduce these MAs effectively. The aim was to develop a new MA reduction method. A method based on moving standard deviation and spline interpolation was developed. It enables the semi-automatic detection and reduction of MAs in the data. It was validated using simulated and real NIRI signals. The results show that a significant reduction of MAs and an increase in signal quality is achieved. The effectiveness and usability of the method is demonstrated by the improved detection of evoked hemodynamic responses. The presented method cannot only be used in the postprocessing of NIRI signals but also for other kinds of data containing artifacts, for example electrocardiography (ECG) or EEG signals.

Introduction

Since Jöbsis (1977) first demonstrated the possibility of non-invasively measuring changes in concentrations of oxyhemoglobin ($\Delta[O_2Hb]$), deoxyhemoglobin ($\Delta[HHb]$) and total hemoglobin ($\Delta[tHb] = \Delta[HHb] + \Delta[O_2Hb]$) in the human brain using NIRS, this technique has been continuously developed and the scope of applications in medicine and neuroscience expanded (Boushel et al. 2001, Ferrari et al. 2004, Wolf et al. 2007, Hoshi 2007, Hamaoka et al. 2007, Muehlemann et al. 2008, Gibson and Dehghani 2009).

Since NIRI is a very sensitive method, head and body movements lead to changes in light coupling to the head and therefore to movement artifacts (MAs) in the signals. This is well known and can lead to the exclusion of whole data sets from a clinical study. This is a problem especially if the subject is unable to avoid movements deliberately, which is the case for neonates or animals.

To solve this problem, simple linear filtering techniques are not effective because $\Delta[O_2Hb]$, $\Delta[HHb]$ and $\Delta[tHb]$ (in the following summarized as "NIRI signals") as well as MAs are highly non-stationary multicomponent signals.

Up to now, different methods where suggested to overcome this problem. According to Cui, Bray and Reiss (2010), these methods can be categorized as: (i) methods based on the *temporal* characteristics of the signal, (ii) methods based on the *spatial* characteristics of the signal, and (iii) methods that use external signals for MA removal by adaptive filtering.

Generally three methods have been published in relation to the *first* category: Wiener filtering (Izzetoglu et al. 2005), wavelet minimum description length (Wavelet-MDL) detrending (Jang et al. 2009) and a correlation-based signal improvement (CBSI) method (Cui et al. 2010). A *Wiener filter* does not need an external input signal because the filter coefficients are only estimated based on the statistics of the measured signal. This requires two calibration measurements before the actual measurement: one measurement without MAs, and one with MAs. The disadvantage is that the only types of MAs eliminated are those present in the calibration measurement. Additionally, in animals or neonates, it is difficult to avoid MAs during the calibration measurement. *Wavelet-MDL detrending* outperforms the conventional detrending approaches. The disadvantage is that the fine structure of the signal is lost due to detrending and it has yet to be investigated whether strong and short MAs can be removed effectively. The *CBSI method* proposed by Cui et al. (2010) is based on the assumption that the time courses of the true $\Delta[O_2Hb](t)$ and $\Delta[HHb](t)$ time series should be maximally negatively correlated. It improves signals with large amounts of noise in particular.

The *second* category comprises methods based on eigenvalue decomposition (Zhang et al. 2005, Wilcox et al. 2005, Nozawa and Kondo 2009). These methods need a set of signals from the same measurement in order to calculate the spatial covariance of the signals to design spatial filters. According to the results presented by Zhang et al. (2005), Wilcox et al. (2005) and Nozawa and Kondo (2009), these methods work quite well. Nevertheless, it is not easy to select components with characteristic features of MAs and the methods are difficult to apply in a real-time signal-processing environment.

Methods of the *third* category use adaptive filters to subtract the noise and MAs from the signals. Input signals for the adaptive filters can be (i) externally measured body movements (Izzetoglu et al. 2003), or (ii) signals that come from optode channels with a very short emitter-receiver distance (to ensure that the light changes detected are not caused by brain activity because the light cannot pass through the brain at this short distance) (Zhang et al. 2007*a*, Zhang et al. 2007*b*, Zhang et al. 2009). One drawback of the methods in this category is that the effectiveness of the adaptive filtering depends strongly on the external input signal. If information (such as time of occurrence and intensity) about the MAs is incomplete, the adaptive filter obviously cannot remove the MAs completely.

In general, all filtering approaches have the disadvantage that the filter needs a specified sample size to estimate the filter coefficients and thus the first samples of the measured time series remain unchanged.

The aim of our work was to develop a new method to reduce MAs in NIRI signals, which overcomes the disadvantages of the methods mentioned and extends the range of available methods for MA reduction by introducing a new approach for signals especially heavily affected by MAs.

Materials and methods

A.) Near-infrared imaging

For an NIRI measurement a specified number of light-sources and light-detectors are placed on the tissue. Then the light attenuation at multiple wavelengths is measured, enabling the calculation of concentration changes of O_2Hb, HHb and tHb. The volume and depth of the tissue investigated depends on the wavelength and the distance between source and detector. The concentration changes of O_2Hb, HHb and tHb are calculated using (i) the modified Lambert-Beer law (Delpy et al. 1988, Sassaroli and Fantini 2004) or (ii) the diffusion approximation of the Boltzmann transport equation for the semi-infinite boundary condition (Arridge et al. 1992). NIRI enables the measurement of evoked hemodynamic responses during stimulation of areas of the brain like the visual cortex (Karen et al. 2008), motor cortex (Haensse et al. 2005), auditory cortex (Zaramella et al. 2001) and olfactory cortex (Fladby et al. 2004). In this context, the terms fNIRS or fNIRI are used. The evoked hemodynamic response is a change in the NIRI signals due to an increase in $CMRO_2$, rCBF and rCBV (Wolf et al. 2002).

B.) The new movement artifact reduction algorithm

Our movement artifact reduction algorithm (MARA) is implemented in MATLAB$^{\text{TM}}$ and based on six data processing steps (see figure 4.1 and 4.2):

1. Calculation of the moving standard deviation (MSD) $s(t)$ of the discrete time series $x(t) = \{x(t_i)\}$, $t_i = i\Delta t$, $i = 1,2,\ldots,N$, where Δt is the sampling period and N the number of sampling points.

2. Detection of the start and endpoints of the MAs. The indices of the corresponding sample points are stored in the vector $\xi(n) = \{\xi(n_i)\}$, $i = 1,2,\ldots,M$, where M is twice the number of detected MAs.

3. Segmentation of $x(t)$ into parts with MAs ($x_{\text{MA}}(t)$) and without MAs ($x_{\text{ok}}(t)$), where $x_{\text{MA}}(t) = \{x_{\text{MA},k}(t)\}$, $k = 1,2,\ldots,L$ with $L = M/2$ the total number of segments stored in $x_{\text{MA}}(t)$, and $x_{\text{ok}}(t) = \{x_{\text{ok},k'}(t)\}$, $k' = 1,2,\ldots,L'$ with L' the total number of segments stored in $x_{\text{ok}}(t)$.

4. Spline interpolation of each k-th segment stored in $x_{\text{MA}}(t)$.

5. Subtraction of the spline interpolation function $x_{\text{S},k}(t)$ of each k-th segment of $x_{\text{MA}}(t)$ to get the denoised segment $x_{\text{D},k}(t)$.

6. Reconstruction of the whole time series by reconnecting all segments.

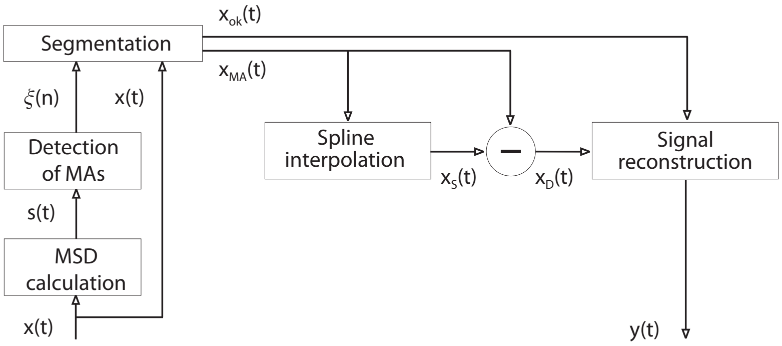

Figure 4.1 – Flow chart of the MARA. $x(t)$: original signal (containing MAs), $s(t)$: moving standard deviation, $\xi(n)$: indices with the start and endpoints of the MAs, $x_{\text{ok}}(t)$: segments of $x(t)$ without MAs, $x_{\text{MA}}(t)$: segments of $x(t)$ which contain MAs, $x_{\text{S}}(t)$: spline interpolation function of $x_{\text{MA}}(t)$, $x_{\text{D}}(t) = x_{\text{MA}}(t) - x_{\text{S}}(t)$, $y(t)$: denoised signal.

B.1.) Calculation of the moving standard deviation

The two-sided moving standard deviation is given by

$$s(t) \quad = \quad \frac{1}{2k+1}\left[\sum_{j=-k}^{k} x^2(t+j) - \frac{1}{2k+1}\left(\sum_{j=-k}^{k} x(t+j)\right)^2\right]^{\frac{1}{2}} \qquad (4.1)$$

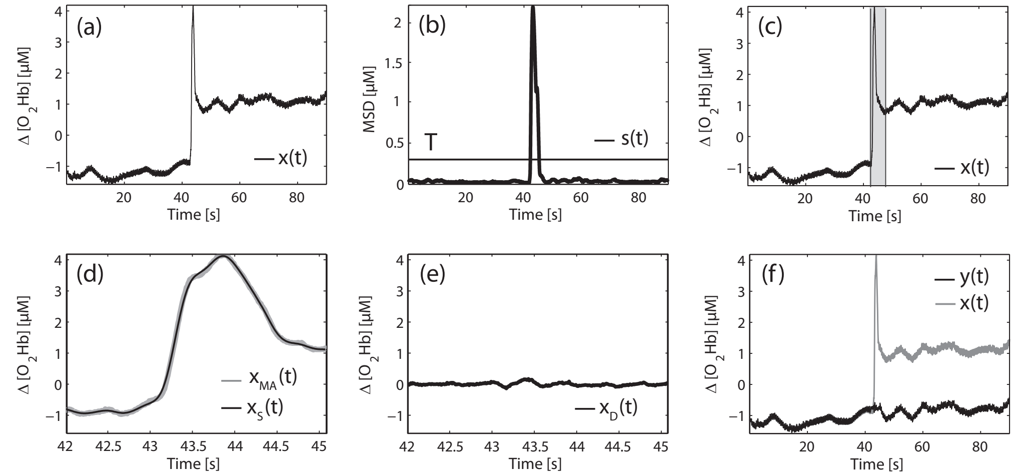

Figure 4.2 – Illustration of the MA reduction algorithm steps. (a): original signal $x(t)$ containing a MA; (b): calculated moving standard deviation $s(t)$ and indicated threshold level T; (c): original signal $x(t)$ with marked MA; (d): enlarged plot of the segment $x_{\mathrm{MA}}(t)$ of $x(t)$ which contains a MA, $x_{\mathrm{S}}(t)$: spline interpolation function of $x_{\mathrm{MA}}(t)$; (e) residual signal $x_{\mathrm{D}}(t) = x_{\mathrm{MA}}(t) - x_{\mathrm{S}}(t)$; (f) original signal $x(t)$ and denoised signal $y(t)$ after applying MARA to $x(t)$.

for $t = k+1, k+2, \ldots, N-k$ with N the length of the time series $x(t)$ and $W = 2k+1$ the sliding window length. W has to be an odd value.

B.2.) Detection of the start and endpoints of the MAs

In the next step, the moving standard deviation time series $s(t)$ is processed by using a threshold value T, which can be specified by the user. All values of $s(t)$ smaller than T are set to zero so that the remaining non-zero values in $s(t)$ correspond to segments of $x(t)$ which are part of an MA. The first and last samples of the non-zero values in $s(t)$ are than extracted. Using the parameters T and W the user can adjust the MARA specifically for the MAs occurring in a certain NIRI signal.

B.3.) Segmentation of the time series

Using the start and endpoints of the MAs, the time series $x(t)$ is segmented. If the first segment contains no MA and the last segment contains one, $x(t)$ can be expressed as

$$x(t) = \{x_{\mathrm{ok},1}(t), x_{\mathrm{MA},1}(t), x_{\mathrm{ok},2}(t), x_{\mathrm{MA},2}(t), \ldots, x_{\mathrm{ok},L'}(t), x_{\mathrm{MA},L}(t)\}, \tag{4.2}$$

with $x_{\mathrm{ok},k}(t)$ the k-th segment of $x(t)$ which contains no MA, $x_{\mathrm{MA},k}(t)$ the k-th segment of $x(t)$ which contains a MA, and $L = L' = M/2$ the half number of all segments.

B.4.) Spline interpolation

In the next step, each segment containing an MA ($x_{\mathrm{MA},k}(t)$) is spline interpolated. The main advantages of this interpolation are that it is efficiently computed and more stable than polynomial interpolation by avoiding the problem of Runge's phenomenon (Biran and Breiner 1999). The cubic spline interpolation method (`csaps`) implemented in MATLAB$^{\mathrm{TM}}$

is used. The accuracy of the interpolation can be specified by choosing an adequate degree of the spline function by defining the value of the parameter p that is in the range [0,1]. For $p = 1$ a least-squares straight line fit is applied, whereas for $p = 0$ a natural cubic spline interpolation is conducted. The appropriate p value depends on the specific type of MA to be removed from the signal. A p value of 0.01 will give a good result for most MAs.
Tests with other interpolation and fitting methods (such as moving average interpolation or Savitzky–Golay smoothing) showed that in principal these methods can be used as alternatives to spline interpolation.

B.5.) Subtraction of the spline interpolation function

The spline interpolation function $x_{\mathrm{S},k}(t)$ for each segment $x_{\mathrm{MA},k}(t)$ is subtracted from $x_{\mathrm{MA},k}(t)$. The difference represents the denoised segment and is stored in $x_{\mathrm{D},k}(t)$. Figure 4.2 (e) illustrates this step. According to Eq. 4.2, the new signal $x'(t)$ is:

$$x'(t) = \{x_{\mathrm{ok},1}(t), x_{\mathrm{D},1}(t), x_{\mathrm{ok},2}(t), x_{\mathrm{D},2}(t), \ldots, x_{\mathrm{ok},L'}(t), x_{\mathrm{D},L}(t)\}. \tag{4.3}$$

B.6.) Reconstruction of the whole time series

Since the spline subtraction leads to different signal levels of $x_{\mathrm{ok},k}(t)$ and $x_{\mathrm{D},k}(t)$, a correction algorithm has been implemented to ensure a continuous signal. In general, each segment $x_{\mathrm{p},m+1}(t)$, $m = 1,2,\ldots,L+L'-1$ of $x'(t)$ is parallel-shifted with respect to its mean value and the mean value of the previous segment $x_{\mathrm{p},m}(t)$, considering also the length of both segments to calculate the mean value. Hence, the number of samples used to determine the mean value of a segment depends on the actual segment length. We defined three cases of segment length: the segment has (i) fewer or equal than α samples, (ii) more than α samples but less than β samples, and (iii) more or equal than β samples. This leads to nine different cases to determine the value by which the segment $x_{\mathrm{p},m+1}(t)$ has to be parallel-shifted (see table 4.1). The parameters α and β can be determined using the empirically found equations $\alpha = 3^{-1}\mathrm{Hz}^{-1} f_s$ and $\beta = 2\,\mathrm{Hz}^{-1} f_s$ with f_s the sampling frequency corresponding to the recorded NIRS signal $x(t)$. If the solutions of the equations are not integers, the value is rounded to an integer value. For example, $f_s = 100$ Hz yields the values $\alpha = 33$ and $\beta = 200$.
The resulting time series $y(t) = \{y(t_i)\}$, $i = 1,2,\ldots,N$ with the total length N is the denoised (MAs reduced) time series $x(t)$, which can be expressed, according to (3), as

$$y(t) = \{x_{\mathrm{ok},1}(t), x_{\mathrm{D},1}(t) + \vartheta_1, x_{\mathrm{ok},2}(t) + \vartheta_2, x_{\mathrm{D},2}(t) + \vartheta_3, \ldots, x_{\mathrm{ok},L'}(t) + \vartheta_{L+L'-2}, x_{\mathrm{D},L}(t) + \vartheta_{L+L'-1}\}, \tag{4.4}$$

with ϑ the value of the vertical shift. Figure 4.2 (f) visualises these steps of the algorithm.

	$x_{\mathrm{p},m}(t_i)$ $i = 1,2,\ldots,\lambda_1$, $\lambda_1 \leq \alpha$	$x_{\mathrm{p},m}(t_i)$ $i = 1,2,\ldots,\lambda_1$, $\alpha < \lambda_1 < \beta$	$x_{\mathrm{p},m}(t_i)$ $i = 1,2,\ldots,\lambda_1$, $\lambda_1 \geq \beta$
$x_{\mathrm{p},m+1}(t_i)$ $i = 1,2,\ldots,\lambda_2$, $\lambda_2 \leq \alpha$	$a = \sum_{i=1}^{\lambda_1} x_{\mathrm{p},m}(t_i)$, $b = \sum_{i=1}^{\lambda_2} x_{\mathrm{p},m+1}(t_i)$,	$a = \sum_{i=\lambda_1-\alpha}^{\lambda_1} x_{\mathrm{p},m}(t_i)$, $b = \sum_{i=1}^{\lambda_2} x_{\mathrm{p},m+1}(t_i)$,	$a = \sum_{i=\lambda_1-\theta_1}^{\lambda_1} x_{\mathrm{p},m}(t_i)$, $b = \sum_{i=1}^{\lambda_2} x_{\mathrm{p},m+1}(t_i)$,
$x_{\mathrm{p},m+1}(t_i)$ $i = 1,2,\ldots,\lambda_2$, $\alpha < \lambda_2 < \beta$	$a = \sum_{i=1}^{\lambda_1} x_{\mathrm{p},m}(t_i)$, $b = \sum_{i=1}^{\alpha} x_{\mathrm{p},m+1}(t_i)$,	$a = \sum_{i=\lambda_1-\alpha}^{\lambda_1} x_{\mathrm{p},m}(t_i)$, $b = \sum_{i=1}^{\alpha} x_{\mathrm{p},m+1}(t_i)$,	$a = \sum_{i=\lambda_1-\theta_1}^{\lambda_1} x_{\mathrm{p},m}(t_i)$, $b = \sum_{i=1}^{\alpha} x_{\mathrm{p},m+1}(t_i)$,
$x_{\mathrm{p},m+1}(t_i)$ $i = 1,2,\ldots,\lambda_2$, $\lambda_2 \geq \beta$	$a = \sum_{i=1}^{\lambda_1} x_{\mathrm{p},m}(t_i)$, $b = \sum_{i=1}^{\theta_2} x_{\mathrm{p},m+1}(t_i)$,	$a = \sum_{i=\lambda_1-\alpha}^{\lambda_1} x_{\mathrm{p},m}(t_i)$, $b = \sum_{i=1}^{\theta_2} x_{\mathrm{p},m+1}(t_i)$,	$a = \sum_{i=\lambda_1-\theta_1}^{\lambda_1} x_{\mathrm{p},m}(t_i)$, $b = \sum_{i=1}^{\theta_2} x_{\mathrm{p},m+1}(t_i)$,

Table 4.1 – Table with the rules to determine the proper magnitude of the shift for each segment $x_{\mathrm{p},m+1}(t)$, $m = 1,2,\ldots,L+L'-1$ with respect to the length of the previous segment $x_{\mathrm{p},m}(t)$. The new segment $x^{\mathrm{new}}_{\mathrm{p},m+1}(t)$ is than calculated as $x^{\mathrm{new}}_{\mathrm{p},m+1}(t) = x_{\mathrm{p},m+1}(t) + \vartheta_m$, with the shift parameter $\vartheta_m = a - b$. The constants α and β define the threshold values for the case differentiation, whereas θ_1 and θ_2 represent the next integer values of the solution of equations $\theta_1 = \lambda_1/10$ and $\theta_2 = \lambda_2/10$.

C.) Validation of the MARA with simulated NIRI signals

An NIRI signal containing typical oscillations of systemic hemodynamic changes was simulated. This signal was composed of four sine waves and additional white Gaussian noise $\sigma(t)$:

$$x_{\mathrm{NIRI}}(t) = \sum_{i=1}^{n} \Big(\mu_i \sin(\omega_i t) + \gamma_i \sigma(t)\Big), \tag{4.5}$$

with $n = 4$, $\omega = 2\pi f$, μ: amplitude of the sine wave oscillation, γ: amplitude of $\sigma(t)$. $x_{\mathrm{NIRI}}(t)$ is in the range [-1,1]. The amplitude and frequency values of each sine wave were defined according to the mean frequencies of real NIRI signals (Elwell et al. 1999, Obrig et al. 2000, Müller et al. 2003): (i) very high frequency oscillation (heart rate, $\langle f \rangle = 1$ Hz, $\mu = 0.6$, $\gamma = 0.01$), (ii) high frequency oscillation (respiration, $\langle f \rangle = 0.25$ Hz, $\mu = 0.2$, $\gamma = 0.01$), (iii) low frequency oscillation ($\langle f \rangle = 0.1$ Hz, $\mu = 0.9$, $\gamma = 0.01$), and (iv) very low frequency oscillation ($\langle f \rangle = 0.04$ Hz, $\mu = 1$, $\gamma = 0.05$). The sampling frequency of the simulated NIRI signal ($x_{\mathrm{NIRI}}(t)$) was set to 20 Hz and the length to 5000 samples (about 4 min).

The three time series $x_{\mathrm{MA}_1}(t)$, $x_{\mathrm{MA}_2}(t)$ and $x_{\mathrm{MA}_3}(t)$ were defined having the same length as $x_{\mathrm{NIRI}}(t)$, which simulate three typical forms of MAs: base shifts (MA_1), short impulses (MA_2) and temporally low frequency oscillation (MA_3). These simulated MAs were added to $x_{\mathrm{NIRI}}(t)$ (see figure 4.3).

In a next step, these simulated MA afflicted NIRI signals were processed with MARA.

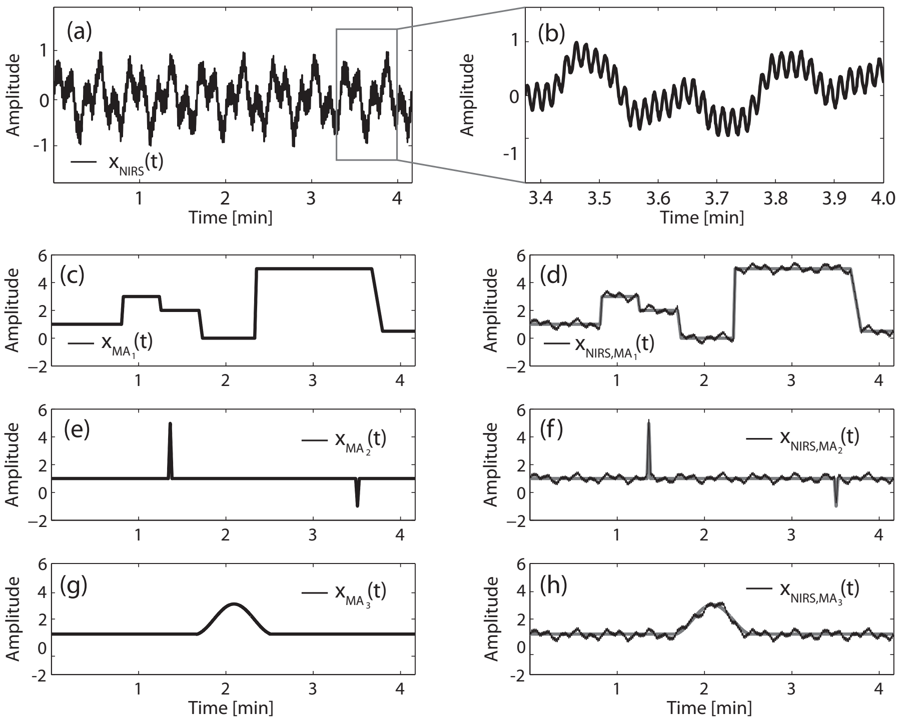

Figure 4.3 – Simulated NIRI signal (a) and zoomed in section (b); simulated MAs (c), (e) and (g); (d), (f), (h): signals obtained by adding (a) to the MAs (c), (e) (g).

Therefore the following empirically generated values for the parameters T and W are used: (i) $y_{\mathrm{NIRI,MA_1}}(t)$: $T = 0.25$, $W = 100$; (ii) $y_{\mathrm{NIRI,MA_2}}(t)$: $T = 0.25$, $W = 100$; (iii) $y_{\mathrm{NIRI,MA_3}}(t)$: $T = 0.22$, $W = 1800$. In all cases the parameter p was set to $p = 0.01$.
To estimate the degree of agreement between the MA reduced NIRI signals $y_{\mathrm{NIRI,MA_1}}(t)$, $y_{\mathrm{NIRI,MA_2}}(t)$, $y_{\mathrm{NIRI,MA_3}}(t)$ and the simulated NIRI signal $x_{\mathrm{NIRI}}(t)$, the percent root difference (*PRD*), the root mean square error (*RMSE*) and the Pearson product-moment correlation coefficient (r) are calculated, as in Liu et al. (2008). The parameters are defined as:

$$RMSE = \sqrt{\frac{1}{N}\sum_{i=1}^{N}\Big(x(t_i) - y(t_i)\Big)^2}, \tag{4.6}$$

$$PRD = 100\,\% \times \sqrt{\sum_{i=1}^{N}\Big(x(t_i) - y(t_i)\Big)^2 \left(\sum_{i=1}^{N} x^2(t_i)\right)^{-1}}, \tag{4.7}$$

$$r = \frac{1}{M}\sum_{i=1}^{N}\left(\frac{x(t_i) - \langle x(t)\rangle}{s_x}\right)\left(\frac{y(t_i) - \langle y(t)\rangle}{s_y}\right), \quad \text{with} \tag{4.8}$$

$$s_x = \sqrt{\frac{1}{M}\sum_{i=1}^{N}\Big(x(t_i) - \langle x(t)\rangle\Big)^2}, \quad s_y = \sqrt{\frac{1}{M}\sum_{i=1}^{N}\Big(y(t_i) - \langle y(t)\rangle\Big)^2},$$

whereby $x(t)$ and $y(t)$ are the time series which should be compared, $M = N - 1$ and N the length of $x(t)$ and $y(t)$ respectively. The *agreement* between $x(t)$ and $y(t)$ is evaluated by the parameters *PRD* and *RMSE*, r determines the *similarity* between the two signals.

The smaller the *PRD* and *RMSE* values and the larger the r value, the better the correspondence between the signals.

D.) Validation of the MARA with real NIRI signals

In order to test if the MARA is applicable on real NIRI signals, the algorithm was applied on three NIRI data sets affected with three types of MAs: short impulses (first data set), base shifts (second data set) and temporally limited low frequency oscillations (third data set). The NIRI data sets originated from two measurements with a multidistance near-infrared spectroscopy instrument developed at our laboratory (Haensse et al. 2005). The time series represent data which would have been excluded from an analysis due to the MAs. In particular, data set three originated from an experiment whereby evoked hemodynamic responses in the motor cortex of a subject were measured. In this experiment the subject performed a finger tapping excercise (20 s tapping, 60 s rest) repeated 16 times.

All three data sets were processed in a two step procedure: (i) calculation of the relative changes of oxyhemoglobin and deoxyhemoglobin ($\Delta[O_2Hb]$, $\Delta[HHb]$) according to the approach presented in Haensse et al. (2005), (ii) application of the MARA. For the time series of the third data set, a block average was calculated to assess brain activation.

The empirically generated values used for the parameters t, W and p are mentioned in the legends of the figures 4.5-4.7.

Results

A.) Validation of the MARA with simulated NIRI signals

The effectiveness of the MARA is shown in figure 4.4 and table 4.2. As one can see from the relative changes of these parameters with and without applied MARA, MARA yielded in all three cases an improvement of the signal quality. The efficacy of the denoising depends on the type of MA. Whereas for short impulses (MA_2) ΔPRD and $\Delta RMSE$ decreased at the most, Δr increased most of all for base shifts (MA_3).

Signal	*PRD*	*RMSE*	r	MARA	ΔPRD	$\Delta RMSE$	Δr
$x_{\mathrm{NIRI}}(t)$	0 %	0	1	without			
$x_{\mathrm{NIRI,MA_1}}(t)$	236.4 %	2.43	0.07	without	89.3 % ↓	89.3 % ↓	90.8 % ↑
$y_{\mathrm{NIRI,MA_1}}(t)$	25.4 %	0.26	0.76	with			
$x_{\mathrm{NIRI,MA_2}}(t)$	25.0 %	0.26	0.67	without	95.2 % ↓	96.2 % ↓	33 % ↑
$y_{\mathrm{NIRI,MA_2}}(t)$	1.2 %	0.01	1.00	with			
$x_{\mathrm{NIRI,MA_3}}(t)$	54.4 %	0.56	0.36	without	84.6 % ↓	83.9 % ↓	60.9 % ↑
$y_{\mathrm{NIRI,MA_3}}(t)$	8.4 %	0.09	0.92	with			

Table 4.2 – *PRD*, *RMSE* and r values for the comparison between the simulated NIRI signal without MAs ($x_{\mathrm{NIRI}}(t)$), with MAs ($x_{\mathrm{NIRI,MA_1}}(t)$, $x_{\mathrm{NIRI,MA_2}}(t)$, $x_{\mathrm{NIRI,MA_3}}(t)$) and with reduced MAs ($y_{\mathrm{NIRI,MA_1}}(t)$, $y_{\mathrm{NIRI,MA_2}}(t)$, $y_{\mathrm{NIRI,MA_3}}(t)$). The Δ values correspond to the percental changes comparing the results without and with MARA usage.

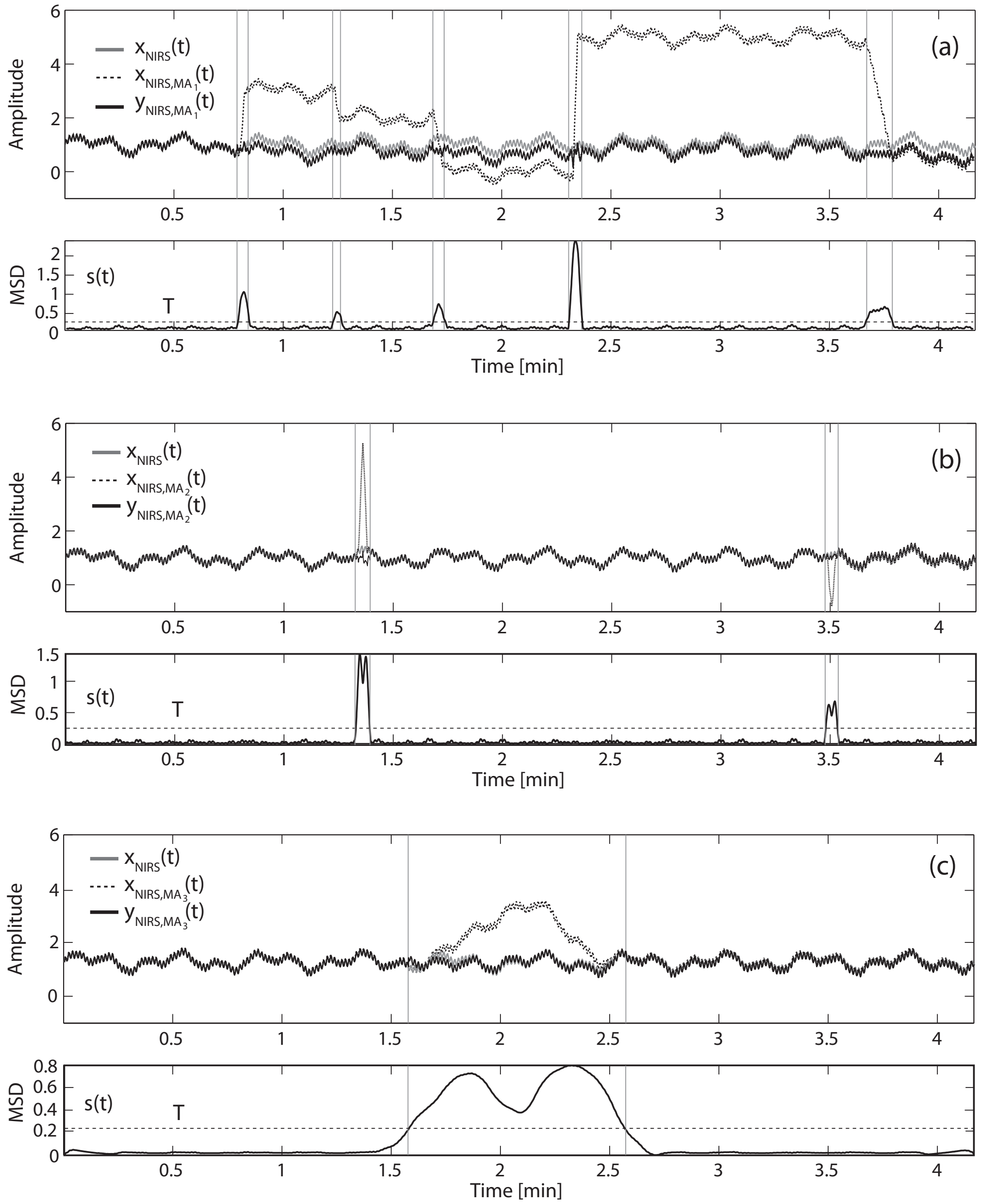

Figure 4.4 – Results of the MARA. The figures (a)–(c) show the simulated NIRI signals without MAs (grey lines), with MAs (dashed black lines) and the artifact reduced signals (black lines). MSD: moving standard deviation $s(t)$, T: threshold value.

B.) Validation of the MA reduction algorithm with real NIRI signals

The effects of the MARA on the three real NIRI data sets are shown in figure 4.5 – 4.7. It is obvious that the MAs are reduced considerably. For the case of the brain activity measurement, the improvement in the quality leads to a better signal-to-noise ratio of evoked hemodynamic responses (see figure 4.7).

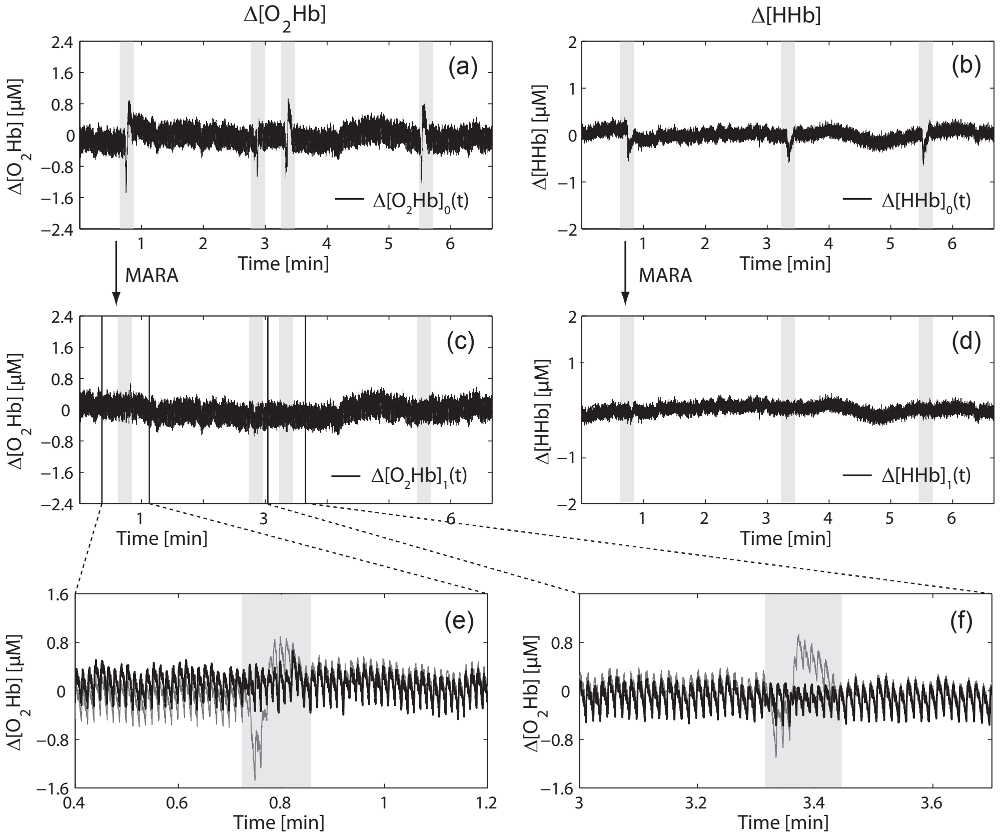

Figure 4.5 – Illustration of the MA reduction performed on MA affected data ($\Delta[\mathrm{O_2Hb}]_0(t)$, $\Delta[\mathrm{HHb}]_0(t)$). Original data: (a, b); corrected data: (c, d). The shaded areas denote parts of the NIRI signal afflicted by MAs. (e) and (f) show enlarged parts of the $\Delta[\mathrm{O_2Hb}](t)$ time series (grey lines: original time series, black lines: corrected time series). The empirically generated values used for the parameters T, W and p are (i) $T = 0.4$, $W = 195$, $p = 0.01$ for the $\Delta[\mathrm{O_2Hb}]_0(t)$ signal, and (ii) $T = 0.25$, $W = 195$, $p = 0.01$ for the $\Delta[\mathrm{HHb}]_0(t)$ signal.

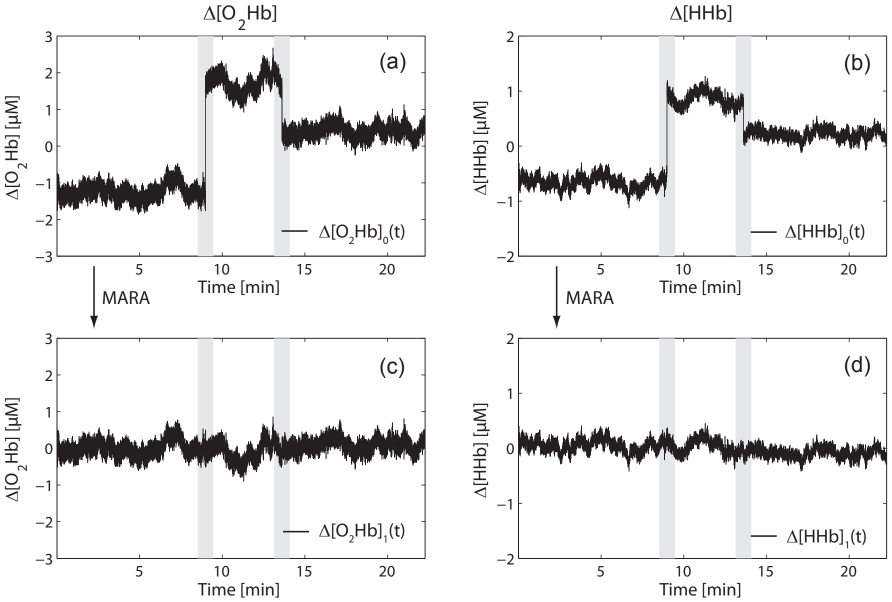

Figure 4.6 – Illustration of the MA reduction process performed on the second MA afflicted time series of O_2Hb (a, c) and HHb (b, d). The empirically generated values used for the parameters T, W and p are (i) $T = 0.3$, $W = 705$, $p = 0.01$ for the $\Delta[O_2Hb]_0(t)$ signal, and (ii) $T = 0.2$, $W = 705$, $p = 0.01$ for the $\Delta[HHb]_0(t)$ signal.

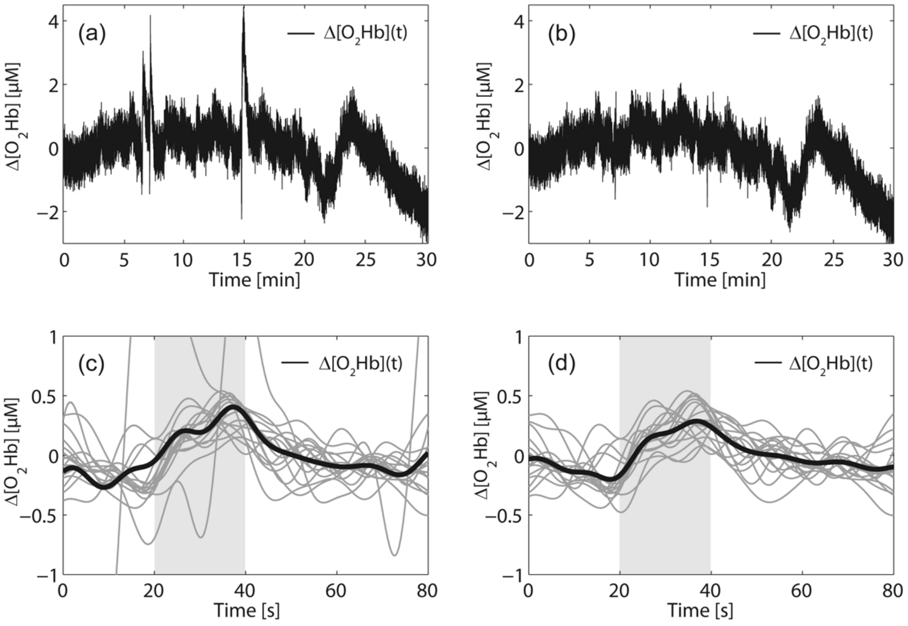

Figure 4.7 – Illustration of the MA reduction performed on the MA afflicted signal of O_2Hb from the functional motor cortex experiment. Shown are the original (a) and MA reduced (b) signals and the corresponding evoked hemodynamic responses using the original data (c) or the MA reduced data (d). The time period in which the subject performed the finger tapping task is highlighted with a grey area starting at 20 s and ending at 40 s. The bold black curve represents the mean of all time series, and the sixteen grey curves in (c) and (d) show the time series of each stimulation segment. The empirically generated values used for the parameters T, W and p are (i) $T = 0.8$, $W = 495$, $p = 0.01$

Discussion and conclusion

The MARA presented in this paper was tested on simulated and real NIRI signals. In both cases the MARA reduces MAs siginificantly and without changing the signal characteristics.

The advantages of the MARA are (i) the automatical detection of MAs, (ii) the efficiency of MA reduction without affecting the non-MA part and (iii) the option to adapt the algorithm to different types of MAs by choosing the optimal parameters (W, T, p). This option may be also regarded as a disadvantage, because the optimal parameters are not chosen automatically. However, manual selection of parameters ensures the quality of the reduction in MAs because a person can best distinguish MA-free data from MA-afflicted data. Another limitation of the MARA is that the variances of the MAs have to be greater than the variances of the physiological signal components in order to ensure the correct detection and reduction of MAs. However, if the variance of the MA is smaller than the one of physiological signals, this also means that it is not a severe MA.

Furthermore, one has to keep in mind that the reconstructed time series is always an estimation of the time series without MAs.

MARA is particulary appropriate for long NIRI measurements ($>$ 1 h) where the likelihood of MAs is high, e.g. in sleep research. Here it may enable further data analysis, e.g. extraction of the sleep-stage-dependent hemodynamic changes or sleep apneas by using advanced signal decomposition techniques for non-linear and non-stationary time series (such as empirical mode decomposition (EMD) (Huang et al. 1998) or non-linear singular spectrum analysis (NLSSA) (Hsieh and Wu 2002) for example) which are not efficient when signals include strong MAs.

For further improvement, it would be interesting to test how different interpolation methods affect the MA reduction process. Instead of spline interpolation (which tends to cause an overshoot in the interpolated data), Akima interpolation (Akima 1970) might be an interesting alternative worth testing.

In conclusion, the proposed algorithm provides an efficient and practical method to semi-automatically detect and reduce MAs in NIRI data. In principle, the algorithm can also be applied to other kinds of signals containing artifacts, for example ECG or EEG signals.

Acknowledgement

The authors gratefully acknowledge funding of the Swiss National Science Foundation. For support and fruitful discussions the authors wish to thank Ivo Trajkovic, Rachel Folkes, Andreas Metz and Jochen Rößler.

4.2 Exploratory study

Assessment of potential short-term effects of intermittent UMTS electromagnetic fields on blood circulation in an exploratory study, using near-infrared imaging

---

Sonja Spichtig[1,2], Felix Scholkmann[1], Lydia Chin[1,2], Hugo Lehmann[3] and Martin Wolf[1,2]

[1]Biomedical Optics Research Laboratory, Division of Neonatology, Department of Obstetrics and Gynecology, University Hospital Zurich, 8091 Zurich, Switzerland
[2]Institute for Biomedical Engineering, Swiss Federal Institute of Technology, 8092 Zurich, Switzerland
[3]Swisscom (Switzerland) Ltd, Innovation Competence Centre, Environment & Electromagnetic Compatibility, 3050 Bern, Switzerland

Submitted to: Conference of the International Society on Oxygen Transport to Tissue (ISOTT) 2010, Ascona, Switzerland

---

Abstract

Potential short-term effects of intermittent UMTS electromagnetic fields (UMTS-EMF) on the cerebral blood circulation were assessed by near-infrared imaging. Different UMTS-EMF signals and exposure positions were applied in an exploratory study on 8 subjects. Since no significant changes were found, the UMTS-EMF signal and the exposure position with the maximum changes in the measurement variables were estimated.

Introduction

We investigated potential short-term effects (occurring within 80 s) of intermittent Universal Mobile Telecommunications System electromagnetic fields (UMTS-EMF) on blood circulation in the human head using near-infrared imaging (NIRI). NIRI measures changes in oxy, deoxy and total hemoglobin concentration ($\Delta[O_2Hb]$, $\Delta[HHb]$ and $\Delta[tHb]$), which reflect changes in cerebral activity, perfusion and/or oxygenation. Its insensitivity to EMF, the high temporal resolution and the flexibility in choosing the exposure sequence makes NIRI an excellent tool to study immediate physiological effects of continuous and intermittent EMF.
The aim of this exploratory study was i) to investigate several UMTS signal types and exposure positions in 8 subjects for potential effects, and ii) to define a final protocol for a more extensive study.

Materials and Methods

Optical Setup

Hardware and software changes on the commercially available ISS Oxiplex® (ISS Inc., Champaign, Illinois, USA) quadrupled the number of detector and light source combinations available for a single optical sensor. The available 2 detectors and 8 source positions enable to collect in total 16 light bundles, also called light paths. Each light bundle comprised light at two wavelengths, namely 690 nm and 830 nm. The NIRI sensor was custom-built in our lab and contains no active parts to be insensitive to UMTS-EMF. 10 m long optical fibres were used for the NIRI sensor to enable the placement of the NIRI instrument outside of the exposure chamber and therefore to minimize potential electrical interferences. For more details about the modifications on the ISS Oxiplex® refer to Spichtig (2010).

Exposure Setup

The measurements were carried out in an experimental room located in the base-ment of the University Hospital Zurich, where the electromagnetic background fields were determined to be very low (@1.9 GHz the background electrical field strength was 0.0002 V/m). The noticeable contributions to the background elec-trical field strength were a GSM downlink signal (@900 MHz: 0.005 V/m), a FM radio signal (@88 MHz: 0.0005 V/m) and the hospital pager (@451 MHz: 0.0003 V/m). Absorber walls were arranged around the subject's bench to minimize poss-ible UMTS-EMF reflections of the exposure setup.

The electronics was programmed to produce 4 different UMTS signal types with a carrier frequency of 1.9 GHz: i) continuous wave (cw), ii) base station-like (bs, as in the TNO-study (Zwamborn et al. 2003)), iii) W-CDMA uplink 1 communication channel (1up; similar to the signal proposed by (Mbonjo et al. 2004)), iv) W-CDMA uplink 6 communication channels (6up; as proposed by (Mbonjo et al. 2004)). Two exposure positions were defined, one lo-cated close to the ear (Fig. 4.8: T3) and the other (Fig. 4.8: B-C3) midway between the motor cortex and position B where previously a change in the regional cerebral blood flow was reported for a Global System for Mobile Communications (GSM) signal (Huber et al. 2002, Huber et al. 2005). The center point of the optical sensor was positioned directly on these positions and a planar patch antenna (SPA 2000/80/8/0/V, Huber & Suhner, Switzerland) emitting the EMF at a distance of 4 cm.

The spatial peak specific absorption rate (SAR) over 10 g of the exposure setup was simulated with SEMCAD X (Version 13, Schmid and Partner Engineering, Zurich, Switzerland) using the Specific Anthropomorphic Mannequin (SAM) phantom defined in CENELEC 50361 (CENELEC 2001). The simulation results were verified with an experimental SAR measurement using the DASY5 Dosimetric Assessment System (Schmid and Partner Engineering, Zurich, Switzerland) at the IT'IS foundation in Zurich. The simulated and experimental data showed deviations smaller than $\pm$ 5% and thus a high agreement. Maximum peak SAR (over 10 g) applied was 1.8 W/kg, which is below the ICNIRP guidelines. For more information about the exposure system and dosimetry see (Lehmann et al. to be published).

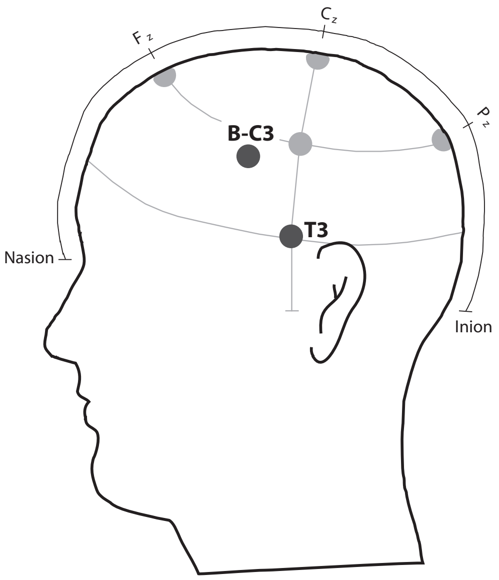

Figure 4.8 – Graphical representation of the exposure positions T3 and B-C3 in the international 10–20 EEG positioning system (Jasper 1958)

Subjects and study protocol

Eight right-handed male subjects (age: 28.6 ± 2.9 y) participated after giving written informed consent. They were asked to abstain from coffee, cigarettes and mobile phone use within two hours before a measurement. Each subject underwent eight measurements on different days experiencing all possible combinations of UMTS signal types and exposure positions in a single-blind paradigm.

A measurement consisted of 15 cycles, the exposure segments, 20 s of UMTS-EMF exposure alternated with 60 s recovery. Before and after the cycles a base-line was recorded for 3 minutes. In total, a measurement lasted 26 min.

Data analysis

Data were band pass filtered (0.008–0.8 Hz) to remove high frequency noise and very low physiological contributions. $\Delta[O_2Hb]$ and $\Delta[HHb]$ were calculated using the modified Lambert-Beer law. The differential pathlength factors (DPF) for C3 given in the literature (Zhao et al. 2002) were linearly interpolated to $DPF_{690nm} = 8.21$ and $DPF_{830nm} = 7.3$ and used in the modified Lambert-Beer law.

To reduce present movement artifacts, the algorithm presented by Scholkmann et al. (2010) was applied to the concentration time series of $\Delta[O_2Hb]$ and $\Delta[HHb]$. The sum of the MA reduced $\Delta[O_2Hb]$ and $\Delta[HHb]$ yielded $\Delta[tHb]$.

The last 10 s of UMTS-EMF exposure (ON) and recovery (OFF) were averaged. The difference between ON-OFF was modeled using a linear mixed-effects model with the factors signal type (levels: cw, bs, 1up and 6up), exposure position (levels: T3, B–C3), light path (defined as the different source-detector combinations; levels: light path 1 to light path 16) and exposure segments (levels: exposure segment 1 to exposure segment 15). The subject was defined as random factor.

Parameter	Position	Signal	[μM]
Max(Δ[O_2Hb])	C3	1up	0.1357
Min(Δ[O_2Hb])	T3	downlink	-0.1818
Max(Δ[HHb])	C3	cw	0.0418
Min(Δ[HHb])	T3	cw	-0.0380
Max(Δ[tHb])	T3	downlink	0.1421
Min(Δ[tHb])	T3	downlink	-0.1752

Table 4.3 – Maximum and minimum concentration changes in μM described by a linear mixed-effects model.

Results

The histograms for the difference between ON and OFF are displayed in Fig. 4.9 for Δ[O_2Hb], Δ[HHb] and Δ[tHb] with all 15'360 observations. They show normally distributed concentration differences with a mean close to zero. No statistically significant differences between exposure and recovery were found for any condition and measurement parameter.

The signal type and exposure position with maximum and minimum differences (ON–OFF) in Δ[O_2Hb], Δ[HHb] and Δ[tHb] are summarized in Tab. 4.3.

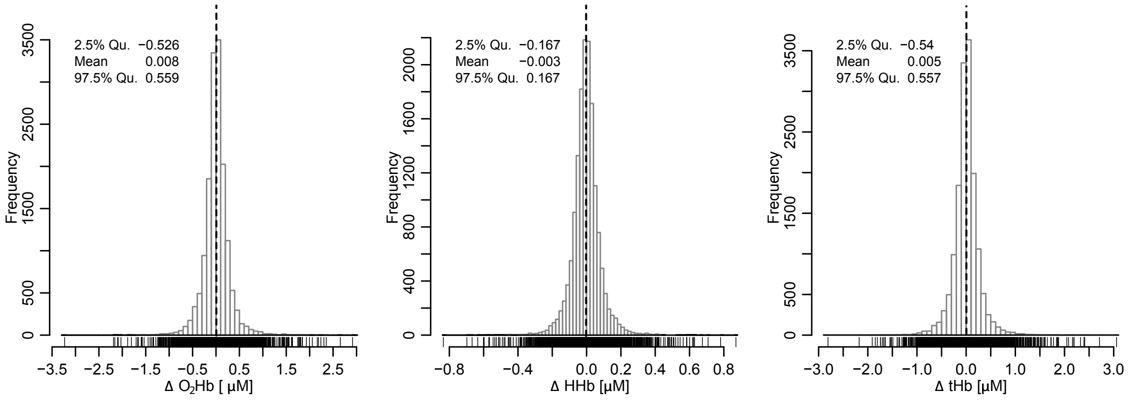

Figure 4.9 – Histograms of Δ[O_2Hb], Δ[HHb] and Δ[tHb] for all observations. Mean (black dotted vertical line), 2.5% and 97.5% quantiles are given for each distribution.

Discussion and Conclusion

The largest differences in Δ[O_2Hb], Δ[HHb] and Δ[tHb] (Tab. 4.3) occurred for the majority of cases at the position T3 and the signal type bs. Hence, this signal type and exposure position were selected for the protocol of a more extensive study.

To set the size of the obtained changes in perspective, we compared them to concentration changes elicited by functional activation of the brain, e.g. for a motor cortex activation their size is approximately 0.8 μM for Δ[O_2Hb], 0.15 μM for Δ[HHb] and 0.65 μM for Δ[tHb]. These values are reference values based on the literature including the results of functional measurements on adults in several studies (Wolf et al. 2006). The changes presented in Tab. 4.3 were 4 to 6 times smaller.

There could be different reasons why no significances were detected: firstly, the effect could be very small as the detected maximum and minimum differences indicate and the number of subjects was too low to detect the effect with statistical measures. Thus the power of the study was not sufficient to detect such small effects. And secondly, it could be that there is no effect of UMTS-EMF on the blood circulation at this measurement positions or anywhere.

To further investigate this, a more extensive study with enhanced power (twice the number of subjects) and the exposure parameters mentioned above will be carried out.

Acknowledgments

The authors gratefully acknowledge the support of the Swiss National Foundation (National Research Programme NRP 57). We thank Massimo Merlini (Statistician, ETH Zurich) for his valuable comments and great support.

4.3 Main study

Assessment of the short and medium-term effects of intermittent UMTS electromagnetic fields on blood circulation, using near-infrared imaging

Sonja Spichtig[1,2], **Felix Scholkmann**[1], **Lydia Chin**[1,2], **Hugo Lehmann**[3] **and Martin Wolf**[1,2]

[1]Biomedical Optics Research Laboratory, Division of Neonatology, Department of Obstetrics and Gynecology, University Hospital Zurich, 8091 Zurich, Switzerland
[2]Institute for Biomedical Engineering, Swiss Federal Institute of Technology, 8092 Zurich, Switzerland
[3]Swisscom (Switzerland) Ltd, Innovation Competence Centre, Environment & Electromagnetic Compatibility, 3050 Bern, Switzerland

Submitted to: Bioelectromagnetics

Abstract

The aim of the present study was to assess the potential effects of UMTS-EMF on blood circulation in the human head using NIRI in the short-term (effects occurring within 80 s) and in the medium-term (effects occurring within 80 s to 30 min). For the first time, we measured potential immediate effects of UMTS-EMF in real-time without any interference during exposure. Three different exposures (sham, 0.18 W/kg, 1.8 W/kg) were applied in a controlled, randomized, crossover and double-blind paradigm on 16 healthy volunteers. In addition to [O_2Hb], [HHb] and [tHb], the heart rate (HR), subjective well-being, tiredness and counting performance were recorded. During exposure to 0.18 W/kg, we found a significant short-term increase in Δ[O_2Hb] and Δ[tHb], which is small ($\approx$17%) compared to a functional brain activation. A significant decrease in the medium-term response of Δ[HHb] to 0.18 W/kg and 1.8 W/kg exposures was detected, which is in the range of physiological fluctuations. The medium-term ΔHR was significantly higher (+1.84 bpm) for 1.8 W/kg than for sham exposure. The other parameters showed no significant effects. Our results suggest that intermittent exposure to UMTS-EMF has small short and medium-term effects on cerebral blood circulation and HR and the reason for this should be investigated in further studies.

Introduction

The growing use of mobile phones in today's communication increases the duration that individuals are exposed to radiofrequency electromagnetic fields (RF-EMF). To assess the potential effects of RF-EMF exposure, several studies have been performed for different exposed biosystems ranging from cells to humans (Vecchia et al. 2009). Since the head is the part of the body receiving the highest RF-EMF dose during mobile phone calls, the investigation of neurophysiological effects (Valentini et al. 2007) is of great importance. Important studies have been performed using EEG and have shown a significant effect of GSM RF-EMF on sleep EEG (Borbely et al. 1999, Huber et al. 2000, Huber et al. 2002, Regel, Tinguely, Schuderer, Adam, Kuster, Landolt and Achermann 2007) and on waking EEG (Huber et al. 2002, Croft et al. 2008, Curcio et al. 2005, Regel, Gottselig, Schuderer, Tinguely, Retey, Kuster, Landolt and Achermann 2007), whereas in other studies no effects were found (Röschke and Mann 1997, Hietanen et al. 2000, Hinrichs and Heinze 2006, Kleinlogel et al. 2008). Using PET rCBF was significantly increased (various locations) 30 minutes after exposure (Huber et al. 2002, Huber et al. 2005), and decreased (close to the antenna) during (Aalto et al. 2006) exposure to GSM-like signals. The signal used in these studies was equivalent to either a mobile phone or a base station in terms of their carrier frequency and modulation but not intensity. Another study reported a decrease in rCBF, although this is probably a spurious auditory effect (Haarala et al. 2003). For UMTS-EMF only one study was performed, which observed no change in rCBF (Mizuno et al. 2009).

PET has a low time resolution (15 – 30 min) and is therefore only suited to study slow effects. Another technique to measure rCBF changes with a much higher temporal resolution ($\approx$100 Hz) is NIRI. NIRI is based on the low light absorption of biological tissue in the optical window (650 – 950 nm). The use of at least two wavelengths makes it possible to measure $\Delta[O_2Hb]$, $\Delta[HHb]$ and $\Delta[tHb]$. They represent changes in CBF, CBV and $CMRO_2$. $[O_2Hb]$, [HHb] and [tHb] are very sensitive to physiological changes, i.e. changes in temperature, metabolism and brain activity due to neurovascular coupling. Several studies showed a high level of agreement between fNIRI, fMRI (Kleinschmidt et al. 1996, Strangman et al. 2002, Toronov et al. 2001) and PET (Hock et al. 1997, Villringer et al. 1997) measures.

NIRI and fNIRI sensors can be built completely from optical parts, which make them insensitive to EMF. Thus NIRI enables to investigate potential immediate and long-lasting effects of EMF exposure. So far, immediate (Wolf et al. 2006) and long-lasting (Curcio et al. 2009) effects of GSM-EMF on $[O_2Hb]$, [HHb] and [tHb] have been studied. Wolf et al. (2006) found small borderline significant short-term changes in $[O_2Hb]$ and [HHb], which correspond to a decrease of CBF and CBV. No effect was found over 20 minutes of exposure. Curcio et al. (2009) found a significant linear increase in [HHb] during 40 minutes of exposure.

Since near-infrared light also penetrates superficial tissue, it provides simultaneous information on cerebral and superficial effects. However, these need to be separated. Since longer source-detector distances probe deeper tissue layers, it is possible to estimate whether an effect is more likely to be superficial or cerebral.

NIRI signals also contain the heart rate (HR). Three studies on the effects of GSM exposure on HR have been published so far. Braune et al. (2002) measured no effect on the HR using a randomized crossover study design. Huber et al. (2003) showed a small reduction of the HR and Tahvanainen et al. (2004) found no effect. Two studies (Eltiti et al. 2007, Eltiti et al. 2009) were carried out with a continuous 2020 MHz UMTS signal and found no effect.

Despite the rapid replacement of GSM by UMTS, few exposure studies using UMTS signals exist, although effects of GSM on CBF and CBV were demonstrated. Thus, we decided to investigate potential effects of UMTS-EMF using NIRI. The studies conducted with NIRI and GSM-EMF (Curcio et al. 2009, Wolf et al. 2006) indicate that the effects of RF-EMF may depend on the time the individuals are exposed. Therefore, we choose to incorporate two different time scales in this study.

Since EMF sensitive individuals claim to experience a variety of symptoms (Röösli et al. 2004) and due to inconsistent data about potential effects on cognitive performance (Vecchia et al. 2009), we included a self-evaluation questionnaire and a counting performance test in our study.

We tested the following hypotheses:

1. There is a short-term response of [O_2Hb], [HHb], [tHb] and/or HR to UMTS-EMF occurring within 80 s.
2. There is a medium-term response of [O_2Hb], [HHb], [tHb] and/or HR to UMTS-EMF occurring within 80 s to 30 minutes.
3. There is a dose-dependent response of [O_2Hb], [HHb], [tHb] and/or HR.
4. There is a dependence of subjective self-evaluations and counting performance on UMTS-EMF.

In addition, to set potential short-term changes in relation to normal brain activity, results were compared to a motor activation measurement.

Materials and methods

A.) Subjects

Sixteen healthy, right-handed, male non-smokers (mean age ± SD: 26.8 ± 3.9 y, weight: 83.2 ± 11.3 kg, height: 182.5 ± 8.8 cm, mobile phone use/day: 7.1 ± 4.5 minutes, mobile phone use since: 8.4 ± 2.5 y) participated after giving written informed consent. The protocol was approved by the ethical committee of the Canton of Zurich. Subjects were briefed to abstain from alcohol, medication and sport and to maintain constant waking times, sleep hours and coffee levels for each study day. Additionally, subjects had to switch off their mobile phone on the evening before the experiment to inhibit use on the measurement day. There were no withdrawals or drop-outs.

B.) Study design

Each subject encountered four different conditions on four different days at the same day time: i) maximum peak SAR of 1.8 W/kg, ii) maximum peak SAR of 0.18 W/kg, iii) sham and iv) motor activation measurement. The three types of exposure took place on

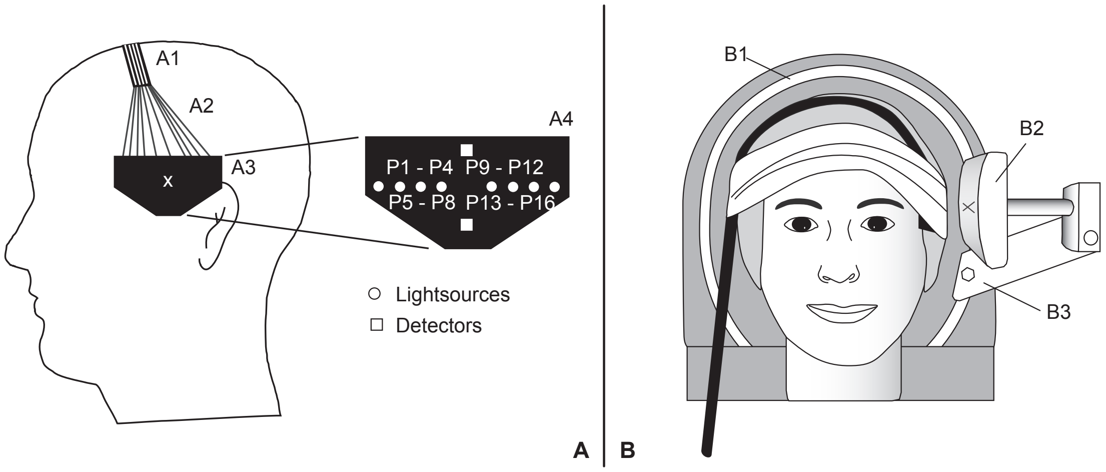

Figure 4.10 – A: Lateral view of sensor placement at the head. A1: 10 m long bundle, A2: optical fibres, A3: optical sensor, A4: sensor geometry with source and detector positions and B: frontal view of arrangement of patch antenna and subjects head. B1: track for the antenna slide, B2: patch antenna and B3: antenna slide for positioning.

study day 1-3 and in a controlled, randomized, crossover and double-blind paradigm. On study day 4 a motor activation measurement was performed. Before each measurement, subjects answered a questionnaire about activities, tiredness and well-being. Subjects had to insert earplugs to avoid potential external auditory stimuli, since the chosen position was located close to the auditory cortex. Afterwards, the center of the optical sensor was fixed at position T3 (Fig. 4.10A) according to the international 10–20 EEG positioning system (Jasper 1958) for exposure experiments and at C3–1.5 cm for the motor activation experiment. Subjects were placed in comfortable supine position. They were asked not to talk and to avoid unnecessary movements.

A measurement consisted of 16 cycles, the exposure/stimulation segments, 20 s of UMTS-EMF exposure (ON) or finger tapping were alternated with 60 s recovery (OFF). Beforehand a baseline was recorded for 3 minutes, afterwards for 6 minutes. A measurement lasted 31 minutes in total. During the exposure measurements, subjects were asked to perform a counting performance test consisting of the task to count back from 2000. Additionally, this task should ensure that subjects were mentally focused and did not fall asleep. To assess the counting, an acoustic signal was emitted after 12 minutes and subjects reported the number reached (*Mid_Exp*) and continued counting. Tiredness and well-being, the number reached at the end of measurement (*End_Exp*) and the subject's guess about the exposure condition was recorded after the measurement. The Karolinska sleepiness scale (Åkerstedt and Gillberg 1990) was used to evaluate tiredness and an analogue scale (10 steps) to evaluate well-being.

C.) Near-infrared system

The commercially available ISS Oxiplex® (ISS Inc., Champaign, Illinois, USA) was specifically adapted for this study. Modifications to hardware and software quadrupled the number of detector and light source combinations available for a single optical sensor. This provided information on location and depth of concentration changes. The optical

NIRI sensor was custom built without active parts to be insensitive to UMTS-EMF. It consisted of 2 detectors and 8 sources enabling 16 measurement paths (Fig. 4.10A). Each source position included light at two wavelengths (690 nm, 830 nm) to detect both O_2Hb and HHb. Data acquisition rate was 25 Hz. 10 m long glass-fibres connected the sensor to the NIRI instrument, which was placed behind absorber walls in the measurement room to minimize potential electrical interferences. An interference test, where the optical sensor fixed to an optical phantom was exposed to intermittent UMTS-EMF, demonstrated the insensitivity of the NIRI setup to UMTS-EMF.

E.) UMTS exposure system

The measurements were carried out in the basement of the University Hospital Zurich, where electromagnetic background was very low (@1.9 GHz the background electrical field strength was 0.0002 V/m). The bench for the subject was laterally shielded by pyramidal radio frequency absorbers (Emerson & Cuming ECCOSORB VHP-12) in order to minimize the possible UMTS-EMF reflexions of the exposure setup. The background EMF from 5 Hz to 30 kHz at the experimental location was <90 nT and the only noticeable background EMF contributions are a GSM downlink signal in the 900 MHz band of 0.005 V/m, a FM radio signal at 88 MHz of 0.0005 V/m and the hospital pager (@451 MHz) with an electrical field strength of 0.0003 V/m.

The signal generator (Rhode & Schwarz SMIQ 03B), power amplifier (Swisscom RCS 1900 amplifier 20 W), couplers and switching matrixes required to generate UMTS-EMF as well as the control laptop were located outside this exposure chamber.

UMTS-EMF was transmitted to the subject's head by a planar patch antenna (SPA 2000/80 /8/0/V, Huber & Suhner, Switzerland), centered on T3 at a distance of 4 cm to the head (Fig. 4.10B). This led to a homogeneous SAR distribution over the measurement area and left space for the NIRI sensor (Fig. 4.11).

The patch antenna emitted a wideband code division multiple access (W-CDMA) downlink signal (Zwamborn et al. 2003) with a carrier frequency of 1.9 GHz, similar to a base station. Three different exposure conditions were set: i) sham (maximum peak SAR over 10 g of 0.0 W/kg), ii) low dose maximum peak SAR over 10 g of 0.18 W/kg) and iii) high dose (maximum peak SAR over 10 g of 1.8 W/kg). The SAR value of the high dose condition was below the SAR limit of the (ICNIRP 1998).

To evaluate SAR distribution in the human head, numerical dosimetry was performed using SEMCAD X (Version 13, Schmid and Partner Engineering, Zurich, Switzerland). The Specific Anthropomorphic Mannequin (SAM) phantom defined in CENELEC 50361 (CENELEC 2001) was used for the simulation of the spatial peak SAR over 10 g generated by the setup. The simulations were verified by an experimental SAR evaluation with the DASY5 Dosimetric Assessment System (Schmid and Partner Engineering, Zurich, Switzerland) at IT'IS foundation in Zurich. The simulated and experimental data showed a high agreement (deviations smaller than ± 5%). For more details about the exposure system, dosimetry, signals and positions see Lehmann et al. (to be published).

The type of signal (downlink) and measurement position (T3) were selected based on an exploratory study (EP), where potential effects of four different UMTS signals (continuous wave, downlink signal, W-CDMA uplink with 1 communication channel and W-CDMA uplink with 6 communication channels (Mbonjo et al. 2004) were studied in 8

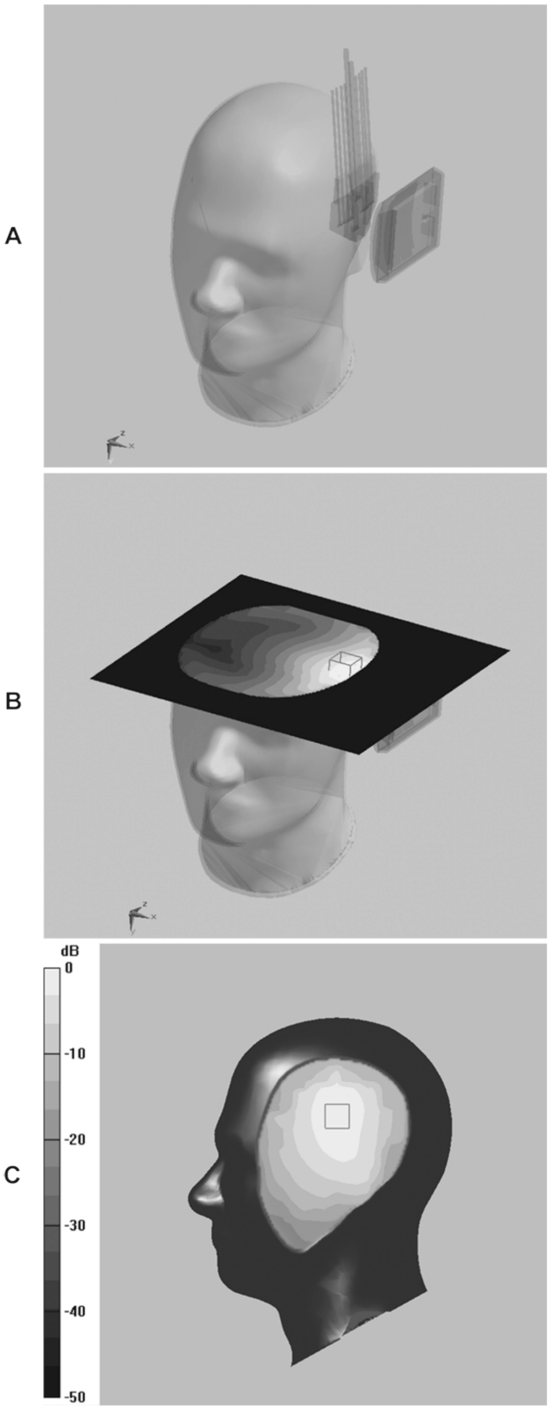

Figure 4.11 – A: model used for the simulations: SAM phantom with optical sensor placed at T3 and the patch antenna at a distance of 4 cm to the head surface. B and C: SAR distributions through cross-sections with the maximum spatial peak SAR averaged over 10g. The cube marks the location of the maximum peak SAR values, i.e. equal to 1.8 W/kg (over 10 g) for the high dose and 0.18 W/kg (over 10 g) for the low dose.

subjects. The center of the antenna and sensor were located at two positions, T3 and B-C3. The first corresponds to the closest position to the ear accessible with the optical sensor and the latter represents the middle point, where Huber et al. (2005) found an effect on rCBF, and C3, the motor cortex. For all four UMTS signals, a maximum peak SAR-value over 10 g of 1.8 W/kg was applied. The EP was carried out to investigate potential short-term effects of intermittent UMTS-EMF on [O_2Hb], [HHb] and [tHb] and to define the protocol for the main study presented in this paper. The difference between the last 10 s of exposure and the last 10 s before exposure was calculated and modeled using a linear mixed-effects model depending on the factors signal type, exposure position, measurement path and exposure segment. No statistically significant short-term effect was found for any UMTS-EMF signal and measurement position. For position T3 and the downlink signal, changes in [O_2Hb], [HHb] and [tHb] were greatest and therefore selected for the current study. The exposure system was controlled by software written in LabView 7® (National Instruments Corporation, Austin, Texas, USA). The software ran in two modes, open mode for testing purposes and random mode for controlled, randomized, crossover and double-blind studies. In random mode, the exposure conditions (sham, low dose and high dose) were automatically randomized by computer for each subject. The exposure condition and forward and reverse UMTS-EMF power were encrypted. A password encoded program deblinded the conditions after data analysis was completed.

F.) NIRI data analysis

Optical intensity data was converted to concentration changes using the modified Lambert-Beer law (Matcher, Elwell, Cooper, Cope and Delpy 1995, Wray et al. 1988). To calculate the DPF used in the modified Lambert-Beer law, a calibration measurement on a phantom with known optical properties is needed. Due to attenuation differences for different light sources, the assumption of constant coupling on the phantom and the human head is not valid anymore and the DPF cannot be determined. Therefore, the DPF values for position C3 (DPF_{759nm} = 7.75; DPF_{834nm} = 7.25) found in literature (Zhao et al. 2002) were linearly interpolated to DPF_{690nm} = 8.21 and DPF_{830nm} = 7.3 and used for the analysis of all measurements.

F.1.) Short-term: [O_2Hb], [HHb] and [tHb]

MAs in Δ[O_2Hb] and Δ[HHb] were reduced according to Scholkmann et al. (2010). The moving window length was adjusted manually for each data set to remove MAs most effectively. The algorithm significantly reduced MAs and improved the signal quality, but not all MAs were removed completely. The MA-reduced Δ[O_2Hb] and Δ[HHb] were band pass-filtered (0.008 – 0.4 Hz). The number of sampling points was reduced to a final sampling frequency of 1 Hz. 10 data points were smoothed and each exposure/stimulation segment was linearly detrended. To identify the remaining MAs, all data was visually inspected for MAs. Segments containing MAs and exposure segment 8, where the subject reported the number reached in the counting task, were removed from further analysis (17.9% of segments for Δ[O_2Hb] and 17.4% for Δ[HHb]). For all paths and measurements, at least 8 segments contained no MAs.

For each path a block average over the remaining segments was calculated for Δ[O_2Hb] and Δ[HHb]. The sum of Δ[O_2Hb] and Δ[HHb] yielded Δ[tHb]. A mean over 10 s was calculated for $\Delta[O_2Hb]$, $\Delta[HHb]$ and $\Delta[tHb]$ and used as input for the statistics.

F.2.) Short-term: heart rate

The HR was calculated from intensity data. Each exposure segment was divided into eight 10 s-long parts. A peak detection was applied to extract integer multiples of the HR period within these 10 s-long parts. This procedure was applied to enhance the accuracy of the FFT, which was the method used to determine the HR. To determine HR we used the optical path with the highest signal to noise ratio, i.e. the highest ratio between the power in the HR band (0.7–1.4 Hz) and noise-band (5–5.7 Hz).
A block average of the HR was calculated and used as input for the statistics.

F.3.) Medium-term: [O_2Hb], [HHb] and [tHb]

$\Delta[O_2Hb]$ and $\Delta[HHb]$ were low pass-filtered (cut-off frequency: 0.0125 Hz). A mean was calculated over every exposure segment (80 s), except for the 8th segment where the subject reported the number reached. Additionally, the baseline was divided into 80 s segments: two before the first exposure segment and four after the last one. All segments were baseline corrected by subtracting the mean of the first baseline segment.
MAs may have a considerable influence on the mean values of segments and hence also on the medium-term analysis. To reduce MAs, they were detected for each path by calculating the concentration change between two segments. Changes exceeding three standard deviations were defined as artifacts and were set to the mean difference between segments. The following segments were shifted accordingly. The algorithm was applied repeatedly until no further MAs were found (twice for $\Delta[O_2Hb]$ and three times for $\Delta[HHb]$). 0.72% of all segments were corrected for $\Delta[O_2Hb]$ and 0.98% for $\Delta[HHb]$. $\Delta[tHb]$ was calculated from the corrected $\Delta[O_2Hb]$ and $\Delta[HHb]$.

F.4.) Medium-term: heart rate

The HR was calculated for the same time segments as described in section F.3 and analogously to section F.2 an FFT was applied to determine the HR. The changes in the HR were calculated by subtracting the HR of the first segment.

F.5.) Counting and self-evaluations

The difference between subjective tiredness (T) and well-being (S) before and after measurements was calculated and named *Exp_T*, *Exp_S*, respectively. The number reached at the beginning of the 8^{th} exposure segment (*Mid_Exp*) and the number reached at the end of the measurement (*End_Exp*) was recorded by the experimenter, respectively the subject.

G.) Statistical analysis

The statistical analysis was carried out by R (R Developement Core Team 2009) and a p-value < 0.05 indicated significance. Exposure conditions were not deblinded until data analysis (sections F.1 – F.5) was completed. Thus, all exposure conditions were analyzed in the same way and bias by the experimenter can be excluded.
Linear mixed-effects models were applied to changes in measurement variables to test the influence of all known factors: time (*Time*), exposure condition (*Exposure*) and measurement path (*Path*) and known covariables: heart rate (*HR*), *Exp_T*, *Exp_S*, *Age*, *Weight*,

Height, *Health*, caffeine on measurement day (*Caffeine*), daytime of measurement (*Meas-_time*), awake time (*Awake_time*), hours of sleep the night before (*Sleep_h*), EMF perception (*EMF_perception*), EMF hypersensitivity (*EHS*), number reached mid-experiment (*Mid_Exp*), number reached at the end of experiment (*End_Exp*) and also the interactions between *Exposure*, *Path* and *Time* were considered. A step-wise exclusion procedure based on the AIC criteria (Akaike 1973) was performed to determine one final model for each measurement variable.

For all linear mixed-effects models, a residue analysis was performed to check its validity. The influence of the subjects was considered as a random factor.

If the factor *Exposure* was significant for the models, a multiple comparison of means with the Tukey correction would be applied to determine the differences between exposure types. Additionally, for all time points we calculated: 1.) the mean effect and 99% confidence interval and performed 2.) a multiple comparison of means with Tukey correction to test for significant differences between the exposure types.

Potential short-term effects were compared to a motor activation. For the motor cortex only the size of the effect was of interest, hence it was modeled in dependency of the predictor *Time*. Only subjects showing a significant activation (14 of 16 for O_2Hb, 12 of 16 for HHb and 14 of 16 for tHb) were considered in the model. To enable direct comparison between exposure and motor activation measurement, data were analysed and modeled the same way. This means that for the motor activation not only the paths showing an activation but all paths were included in the model. This leads to lower mean effects than the values found in the literature. For this reason, we also stated the maximal change elicited by the activation, which are comparable to literature values.

G.1.) Counting and self-evaluations

Self-evaluations and counted numbers were used as predictors for concentration changes and were also estimated by their own mixed-model, because well-being and tiredness changes during measurement and the influences on counting performance could affect the cerebral oxygenation and these variables themselves may depend on several monitored variables such as awake time.

The reporting of *Mid_Exp* was used to test the subject's counting and thus only was a predictor. *End_Exp*, *Exp_T* and *Exp_S* were viewed as performance measures and estimated by a linear mixed-effects model. The analysis of *Exp_S* was discarded because most of the subjects reported no difference in well-being before and after the measurement. Only in 4 out of 48 measurements (2x sham, 1x low and 1x high-dose exposure) did subjects report that they experienced EMF. These occurrences were distributed in a random pattern over the exposure conditions and subjects and no statistical method can be applied due to the low number of occurrences.

G.2.) Responder analysis

To test for responders at an individual level, the last ten seconds UMTS on and off of each exposure segment without MA were compared with a paired Wilcoxon signed rank test over one measurement path. The number of significant paths per exposure condition and subject was calculated and the number of occurrences per exposure condition compared within a subject.

Variable	Factors	numDF	$F_{\text{numDF,denDF}=6105}$	p-value
Δ[HHb]	Time	7	15.06	< 0.001
	Exposure	2	10.11	< 0.001
	Time:Exposure	14	7.00	< 0.001
Δ[O_2Hb]	Time	7	19.43	< 0.001
	Exposure	2	42.11	< 0.001
	Time:Exposure	14	15.24	< 0.001
Δ[tHb]	Time	7	14.25	< 0.001
	Exposure	2	41.71	< 0.001
	Time:Exposure	14	14.42	< 0.001

Table 4.4 – Main study: F- and p-values for the different linear mixed-effects models of Δ[O_2Hb], Δ[HHb] and Δ[tHb] for the short-term analysis

Results

A.) Short-term

For the short-term analysis we obtained the following models:

$$\begin{aligned}\Delta[\mathrm{O_2Hb}] &\sim Time + Exposure + Time : Exposure\\ \Delta[\mathrm{HHb}] &\sim Time + Exposure + Time : Exposure\\ \Delta[\mathrm{tHb}] &\sim Time + Exposure + Time : Exposure\end{aligned} \tag{4.9}$$

For ΔHR no significant dependency was found. Results are included in Tab. 4.4. Graphs are shown in Fig. 4.12A, for graphs with 99% confidence interval at each time point, please refer to Fig. 4.14 in the supplementary information at the end of this chapter. The asterisks mark significant differences ($p < 0.01$) compared to sham. Mean effects and confidence intervals at *40 s* are included in Tab. 4.5A.

To account for negative responses during motor stimulation, not only the mean effect but also the mean of the absolute effects was calculated as a measure of changes induced by the activation (Tab. 4.5A). The maximum response in a single path was 0.567 μM Δ[O_2Hb], 0.251 μM Δ[HHb] and 0.610 μM Δ[tHb] and the minimum response: -0.245 μM for Δ[O_2Hb], -0.110 μM for Δ[HHb] and -0.355 μM for Δ[tHb].

The mean effect of the exposures at 40 s was compared to the motor activation and confidence intervals calculated with error propagation according to Doerffel (1984) (Tab. 4.5B). These values are an upper limit for the estimation, because the mean response over all paths during motor stimulation was calculated independent of an activation.

The multiple comparisons of means with Tukey correction between exposures for each path revealed no significant differences. This means that no regional effects were found.

A	$\Delta[O_2Hb]$ in μM		Δ[HHb] in μM		Δ[tHb] in μM	
Condition	Mean Effect	CI [0.5%, 99,5%]	Mean Effect	CI [0.5%, 99,5%]	Mean Effect	CI [0.5%, 99,5%]
Sham	-0.011	[-0.017, -0.004]	-0.003	[-0.005, -0.001]	-0.013	[-0.020, -0.006]
0.18 W/kg	0.013	[0.006, 0.02]	-0.004	[-0.006, -0.001]	0.010	[0.002, 0.017]
1.8 W/kg	-0.005	[-0.012, 0.002]	-0.002	[-0.004, 0.001]	-0.007	[-0.014, 0.001]
Motor Cortex	0.072	[0.086, 0.100]	-0.011	[-0.0114, -0.0106]	0.077	[0.062, 0.092]
Motor Cortex abs(Effect)	0.126	[0.113, 0.139]	-0.022	[-0.025, -0.019]	0.118	[0.104, 0.132]
B	$\Delta[O_2Hb]$ in %		Δ[HHb] in %		Δ[tHb] in %	
0.18 W/kg vs. Motor Cortex	17.4	[-60.2, 94.9]	5.3	[-1109.1, 1119.6]	17.3	[-70.6, 105.1]
1.8 W/kg vs. Motor Cortex	4.2	[-70.2, 78.6]	-5.0	[-1118.9, 1109.0]	5.1	[-79.4, 89.6]

Table 4.5 – Short-term analysis of the mean effects of $\Delta[O_2Hb]$, Δ[HHb] and Δ[tHb]. A: mean effect and estimated confidence interval [0.5%, 99.5%] in μM for $\Delta[O_2Hb]$, Δ[HHb] and Δ[tHb] at 40 s for all measurement conditions. B: mean effect of exposure for $\Delta[O_2Hb]$, Δ[HHb] and Δ[tHb] at 40s compared to the motor activation given in percent.

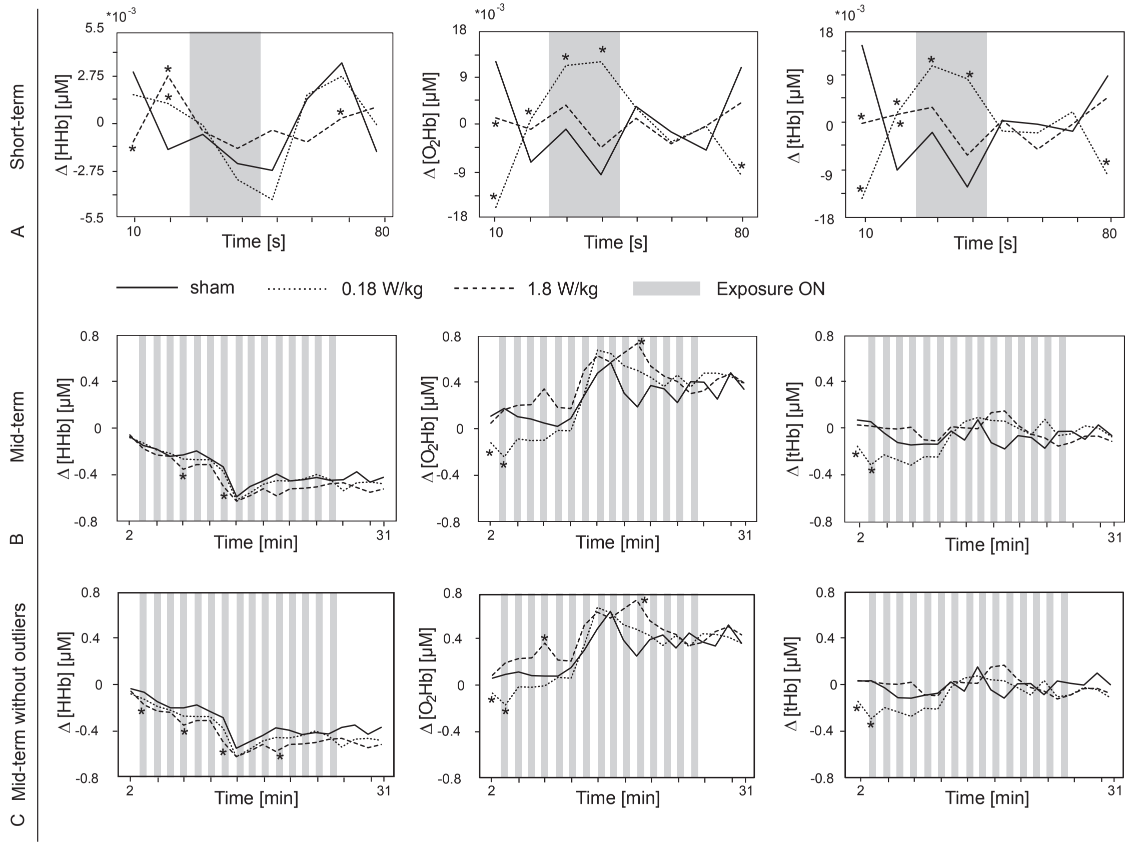

Figure 4.12 – Time-evolution of mean effects for Δ[O_2Hb], Δ[HHb] and Δ[tHb] for the different exposures displayed for the short-term (**A**), medium-term analysis (**B**) and the medium-term analysis without outliers (**C**). Significant results ($p < 0.01$) comparing 0.18 W/kg or 1.8 W/kg to sham are marked with an asterisk beneath the corresponding mean effect.

B.) Medium-term

For the medium-term analysis we obtained the following models:

$$\begin{aligned}
\Delta[\mathrm{O_2Hb}] &\sim Time + Exposure + Path + HR + Exp\_T + Exp\_S + Awake\_time + Sleep\_h \\
&\quad + Mid\_Exp + End\_Exp + Exposure : Path \\
\Delta[\mathrm{HHb}] &\sim Time + Exposure + Path + HR + Exp\_T + Exp\_S + Meas\_time + Sleep\_h \\
&\quad + End\_Exp + Exposure : Path \\
\Delta[\mathrm{tHb}] &\sim Time + Exposure + Exp\_S + Awake\_time + Mid\_Exp + End\_Exp \\
\Delta\mathrm{HR} &\sim Time + Exposure + Exp\_S + Awake\_time + Mid\_Exp + End\_Exp
\end{aligned} \tag{4.10}$$

In contrast to the short-term analysis, the medium-term ΔHR showed a significant dependency on several predictors and was thus modelled analogously to $\Delta[\mathrm{O_2Hb}]$, Δ[HHb] and Δ[tHb]. F and p-values for the factors of the different mixed-models are included in Tab. 4.6.

A multiple comparison of means with Tukey correction was performed and we found the following significant mean differences between sham and exposures: $\Delta[\mathrm{O_2Hb}]$(sham - 0.18 W/kg) = 0.78 [0.43, 1.12] μM ($p < 0.001$), Δ[HHb](sham - 0.18 W/kg) = -0.16 [-0.3, 0.03] μM (p = 0.001), Δ[HHb](sham - 1.8 W/kg) = -0.20 [-0.34, -0.06] μM ($p < 0.001$) and Δ[tHb](sham - 0.18 W/kg) = 0.70 [0.34, 1.05] μM ($p < 0.01$). For ΔHR the difference between sham and 1.8 W/kg of 1.84 [1.16, 2.52] bpm was significant ($p < 0.001$).

Graphs with mean effects for $\Delta[\mathrm{O_2Hb}]$, Δ[HHb] and Δ[tHb] are shown in Fig. 4.12 and for ΔHR in Fig. 4.13. The asterisks mark significant differences ($p < 0.01$) to sham. For graphs with 99% confidence interval at each time point, please again refer to Fig. 4.15 - 4.17 in the supplementary information at the end of this chapter.

During the analysis and before deblinding, six relevant outlying traces (out of 768) were identified (2x sham, 3x low dose and 1x high dose exposure). Since there was no reason to consider these traces as artifacts, we decided to perform the statistical analysis with and without them to investigate their influence on the results.

Without the outliers, the factor Exposure was no longer significant for $\Delta[\mathrm{O_2Hb}]$ and Δ[tHb]. For Δ[HHb] a multiple comparison of means with Tukey correction showed significant mean differences between sham and exposures: Δ[HHb](sham - 0.18 W/kg) = -0.14 [-0.28, -0.006] μM (p = 0.007) and Δ[HHb](sham - 1.8 W/kg) = -0.19 [-0.33, -0.05] μM ($p < 0.001$). Remarkably, the number of significant time points increased for Δ[HHb] for 1.8 W/kg exposure. The number of significant time points stayed approximately the same for $\Delta[\mathrm{O_2Hb}]$ and Δ[tHb]. The results so far refer to differences between exposure conditions.

Independent of exposure condition, [HHb] decreases, $[\mathrm{O_2Hb}]$ increases and [tHb] is unchanged over time. For the sham condition in three out of four sensor quadrants, the mean effect for $\Delta[\mathrm{O_2Hb}]$ and Δ[tHb] at the last time point was significantly higher for the shortest source-detector distances than for the longest source-detector distances. This indicates that the trend during the measurement, which was observed for all conditions, has its origin in superficial changes.

Variable	Factors	numDF	Influence	$F_{\text{numDF,denDF}}$	p-value
Δ[HHb] (denDF = 14952)	Time	19		73.49	< 0.001
	Exposure	2		9.88	< 0.001
	Path	15		76.68	< 0.001
	Exposure:Path	30		7.79	< 0.001
	HR	1	-	654.22	< 0.001
	Exp_T	1	-	528.84	< 0.001
	Exp_S	1	-	21.10	< 0.001
	Waking_time	1	-	53.53	< 0.001
	Sleep_h	1	-	91.53	< 0.001
	End_Exp	1	+	472.59	< 0.001
Δ[O$_2$Hb] (denDF = 14954)	Time	19		18.22	< 0.001
	Exposure	2		26.44	< 0.001
	Path	15		53.68	< 0.001
	Exposure:Path	30		7.37	< 0.001
	HR	1	+	134.09	< 0.001
	Exp_T	1	+	52.21	< 0.001
	Exp_S	1	+	229.74	< 0.001
	Waking_time	1	+	86.24	< 0.001
	Sleep_h	1	+	20.11	< 0.001
	Mid_Exp	1	+	56.91	< 0.001
	End_Exp	1	-	7.60	< 0.001
Δ[tHb] (denDF = 14954)	Time	19		1.62	0.042
	Exposure	2		20.81	< 0.001
	Path	15		76.45	< 0.001
	Exposure:Path	30		6.84	< 0.001
	HR	1	+	27.87	< 0.001
	Exp_S	1	+	251.88	< 0.001
	Meas_Time	1	-	158.44	< 0.001
	End_Exp	1	+	215.33	< 0.001
ΔHR (denDF = 899)	Time	20		3.47	< 0.001
	Exposure	2		24.72	< 0.001
	Exp_S	1	-	3.96	0.047
	Waking_time	1	-	5.23	0.022
	Mid_Exp	1	+	131.13	< 0.001
	End_Exp	1	-	44.64	< 0.001

Table 4.6 – Medium-term analysis: F- and p-values for all factors of the different linear mixed-effects models of Δ[O$_2$Hb], Δ[HHb] and Δ[tHb]. For each covariable, the influence column indicates which direction it influences the measurement variable.

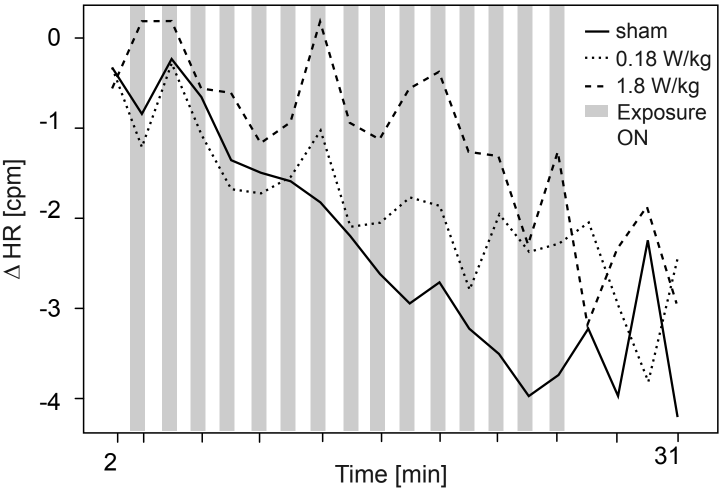

Figure 4.13 – Time-evolution of mean effects for the medium-term ΔHR displayed for the different exposures. No significant results ($p < 0.01$) comparing 0.18 W/kg or 1.8 W/kg to sham were found for single time points. The overall comparison for the factor *Exposure* shows a significant difference of 1.84 bpm when comparing 1.8 W/kg to sham.

C.) Counting and self-evaluations

The mixed model analysis for *End_Exp* and *Exp_T* showed no significant dependence on any predictor.

D.) Responder analysis

We did not find any difference between the exposure conditions for any of the subjects. Over all subjects, the total number of significant paths was close to the 5 percent of stochastically expected significances.

Discussion

A.) General considerations and limitations

The current study applied a W-CDMA downlink signal at 1.9 GHz in repetitive cycles to assess potential alterations in blood circulation. The study was carried out with a homogenous population to minimize inter-individual variations and to enhance sensitivity to detect potential effects.

Near-infrared light has a limited penetration depth depending on the source-detector distance and the optical properties of the tissue. For a tissue with $\mu_a = 0.1$ cm^{-1} and $\mu_s' =$ 8 cm^{-1}, the mean penetration depth of light travelling from a source to detector with a separation of 1.5 cm is 5 mm and for a separation of 3.5 cm it is 8 mm. But photons travel much deeper as Toronov et al. (2001) has shown: information about brain activity from a depth of 2.5 cm was detected. Depth information about concentration changes can be obtained with NIRI if different source-detector distances are employed. Thus, NIRI is able to study both changes in superficial and cerebral blood circulation at the same time. Since near-infrared light is highly scattered in human tissue the accuracy of this depth information is limited.

The high temporal resolution and the unique insensitivity to EMF enable continuous measurements and a high flexibility in the choice of exposure sequences. To the best of our knowledge, NIRI is the only technique able to study short-term effects and to detect significant changes within a single subject.

B.) Short-term changes

We found a significant short-term response of $\Delta[O_2Hb]$, $\Delta[HHb]$ and $\Delta[tHb]$, which can be modelled with the factors *Time*, *Exposure* and the interaction *Time*:*Exposure* (Tab. I). This interaction indicates that the concentration changes during the different exposure conditions vary significantly over time (Fig. 4.12A). All time series were detrended in the analysis and thus have a mean over time equal to zero. This ensures that the variance between measurements is different from zero at every time point. The other option is to set the last value before exposure to zero. In this case the variance at this time point is equal to zero, which is statistically problematic. The detrending leads to a balance between positive and negative concentration changes and values different from zero before the exposure. It represents the more conservative estimate of potential effects.

In a comparison of means between the exposures, significant differences were obtained for several time points (Fig. 4.12A): i) for the high dose $[O_2Hb]$ and [tHb] are significantly lower than in the sham condition for the first 10 s or first 20 s (Fig. 4.12A) and [HHb] is significantly different for the first 20 s and at 70 s. This can be explained by the high $[O_2Hb]$ and [tHb] values at 10 s in the sham condition, which contributes to the significance for the high dose. For [HHb], it is noteworthy that the amplitude of changes during sham exposure is similar to the amplitude during EMF exposure. This may indicate spurious changes. ii) for the low dose $[O_2Hb]$ and [tHb] are significantly higher during exposure than in sham condition and $[O_2Hb]$ and [tHb] are significantly lower for the first and last 10 s. This pattern during exposure indicates an increase in blood flow (Hoshi et al. 2001). The low $[O_2Hb]$ and [tHb] values at 10 s seem to imply that the increase already starts before the exposure onset. However, it has to be kept in mind that the value at 80 s is connected to the value at 10 s, because exposure was repeated. This could be interpreted as an increase during exposure and a decrease after exposure, which recovers to baseline levels only at 20 s. iii) For the sham condition for $[O_2Hb]$ and [tHb] the change between the first and second time point is relatively high compared to the other concentration changes. This high concentration change in the sham exposure may indicate a spurious effect.

The pattern of short-term results - no effect at the high dose and an effect at the low dose - and the results of the EP - no effect at the high dose for all signal types and measurement positions - indicate that there may also be short-term effects for the other UMTS signal types used in the EP at the lower dose.

Although some signs for spurious effects or coincidences are present, it has to be kept in mind that the probability of such effects is low ($< 1\%$). The comparison with the amplitude of the motor response showed that the short-term effects are small($\approx 17\%$ for $[O_2Hb]$ and [tHb]). The effects did not show any regional dependency.

To the best of our knowledge, the only study investigating short-term effects of intermittent EMF was performed in our group (Wolf et al. 2006). A decrease in blood flow was found with a lower significance level. The study was not comparable due to the carrier frequency, modulation, SAR value and exposure protocol (2 s on followed by 2 s off for 20 s instead of 20 s on) and the interference present during the 2 s of exposure.

For the present short-term effects, a thermal effect is unlikely, because thermal effects are expected to show a proportional dependency on the field intensity. The results indicate an intensity dependent effect, similar to the one found in wound healing (dependent on the applied electrical current) (Zhao et al. 2006). It is also possible that the non-linear dependency on the field intensity is caused by two interfering effects showing a linear dose-dependency but with opposite signs.

In summary, our results suggest a short-term effect of UMTS-EMF, whose amplitude is quite small compared to the response to a functional activation ($\approx$17% for [O_2Hb] and [tHb]).

C.) Medium-term changes

ΔHR decreased with time for all exposure conditions, because the subjects relaxed in a supine position (Fig. 4.13). We found a significant difference in ΔHR between sham and the high dose of 1.84 [1.16, 2.52] bpm, taking into account all time points. This increased HR indicates that the subjects relaxed less. One GSM study Huber et al. (2003) showed a reduction in HR during waking and stage 1 sleep, whereas **?** found no effect of GSM-EMF on the HR in randomized crossover trials. In contrast to our results Eltiti et al. (2007) and Eltiti et al. (2009) did not find an effect on HR using a base-station-like UMTS signal, which had a different carrier frequency of 2020 MHz and was continuous. Based on the literature cited, we conclude that the possible influence of RF exposure on HR is still unclear.

During the measurement, [O_2Hb] increased, [HHb] decreased and [tHb] remained stable independent of the exposure condition. These findings agree with Wolf et al. (2006), but disagree with Curcio et al. (2009), who found a decrease in [O_2Hb] and an increase in [HHb]. The analysis indicated that these changes represent a superficial increase in blood flow. One likely explanation is that the temperature below the sensor on the head increased due to the shielding of skin from ambient air and thus superficial blood flow increased. Another explanation is that the pressure exerted by the sensor on the skin initially inhibited blood flow. This may have induced physiological reactions to increase blood flow. However, these effects affect all exposure conditions in the same way.

Since the outliers influence the medium-term results of [O_2Hb] and [tHb] significantly, there is some uncertainty in our interpretation. The number of outliers per exposure indicates that they are not due to EMF effects, but more likely due to non-identified artifacts and thus we think that the analysis without these six outliers is more trustworthy. The significant difference in [O_2Hb] and [tHb] was only found for the analysis including the outliers and it disappeared when the outliers were removed. Thus we think that this effect is spurious. The analysis without outliers at each time point revealed several significances: i) Δ[O_2Hb] and Δ[tHb] were significant for the low dose at the first 4 minutes, even before the exposure started and hence indicate spurious effects, ii) both significances for Δ[O_2Hb] of the high dose seem to be distributed over time in a random manner with no clusters formed at any time point.

Independent of the analysis, Δ[HHb] was significantly lower for both exposures compared to sham and with a slightly larger effect for the higher dose. The analysis without outliers at each time point revealed several significances distributed over time and forming no clusters. However, the effect is always a decrease in Δ[HHb] and is supported by the significant decrease of Δ[HHb] taking into account all time points. This effect can be interpreted as a decrease in oxygen consumption. No dependencies on the light path and thus no regional effects were observed.

Wolf et al. (2006) found no significant difference in [HHb] between sham and GSM exposure, whereas Curcio et al. (2009) presented a significant increase in [HHb] over time for the GSM exposure. These differences may be explained by different exposure types, doses and times.

Three PET studies, using GSM-EMF, showed an increase in rCBF (Huber et al. 2005, Huber et al. 2005, Aalto et al. 2006) and one a decrease, which was interpreted as a spurious auditory effect (Haarala et al. 2003). Thus for GSM an increase of rCBF is likely. For UMTS-EMF only one study was performed, which observed no change in rCBF (Mizuno et al. 2009) in agreement with our results.

D.) Counting and self-evaluations

We found no significant dependence on the exposure condition for the increase in tiredness during the measurement (*Exp_T*). This corresponds to Koivisto et al. (2001) and Rubin et al. (2006), who employed GSM-EMF. Besides the EMF type, the studies had different study designs. Koivisto et al. (2001) assessed tiredness and other subjective measures only in relation to the exposure conditions and neglected the influence of sleeping hours, time awake, coffee level and similar factors. Rubin et al. (2006) assessed subjective measures such as tiredness > 24 h after the exposure session and not directly after the measurement.

We also found no significant dependence of the counted number on the exposure condition. To the best of our knowledge no similar study has been performed.

Conclusion

For the first time, a NIRI instrument inert to EMF enabled the measurement of potential effects of intermittent UMTS-EMF exposure.

In summary, based on our hypotheses we found:

1. A significant short-term response of [O_2Hb] and [tHb] to the low-dose exposure within 80 s, which is small ($\approx$17%) compared to a functional activation.
2. A significant medium-term response of [HHb] to the low and high-dose UMTS-EMF exposure, which is in the range of normal physiological fluctuations and also a medium-term response of HR to the high-dose exposure within 80 s to 30 minutes.
3. A slightly larger, but not significant medium-term response of [HHb] for the high dose.
4. No significant dependence between the self-evaluation and UMTS-EMF exposure and counting performance and exposure.

Disclosure/Conflicts of interest

We have no financial interest and no conflict of interests. The equipment was borrowed from Swisscom (Switzerland) Ltd.. They performed dosimetric simulations and measurements for verification in collaboration with IT'IS, Zurich. Swisscom (Switzerland) Ltd. had no influence on the data acquisition or analysis.

Acknowledgements

The authors gratefully acknowledge the support of the Swiss National Foundation (National Research Programme NRP 57). We thank Massimo Merlini (Statistician, ETH Zurich) for his valuable comments and great support, Rachel Folkes for professional proofreading, and all study participants.

Supplementary Information

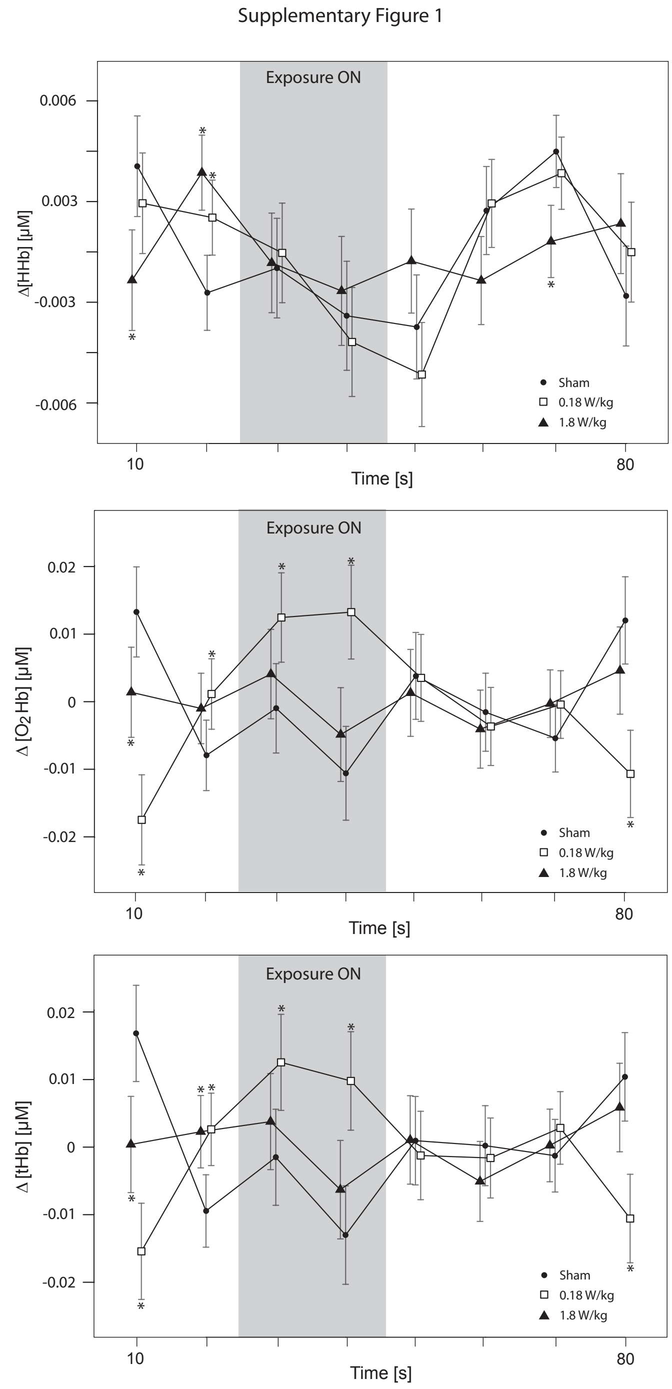

Figure 4.14 – Short-term analysis: Time evolution of mean effects and 99% confidence intervals for Δ[O_2Hb], Δ[HHb] and Δ[tHb] for the different exposures displayed. Significant results ($p < 0.01$) comparing 0.18 W/kg or 1.8 W/kg to sham are marked with an asterisk.

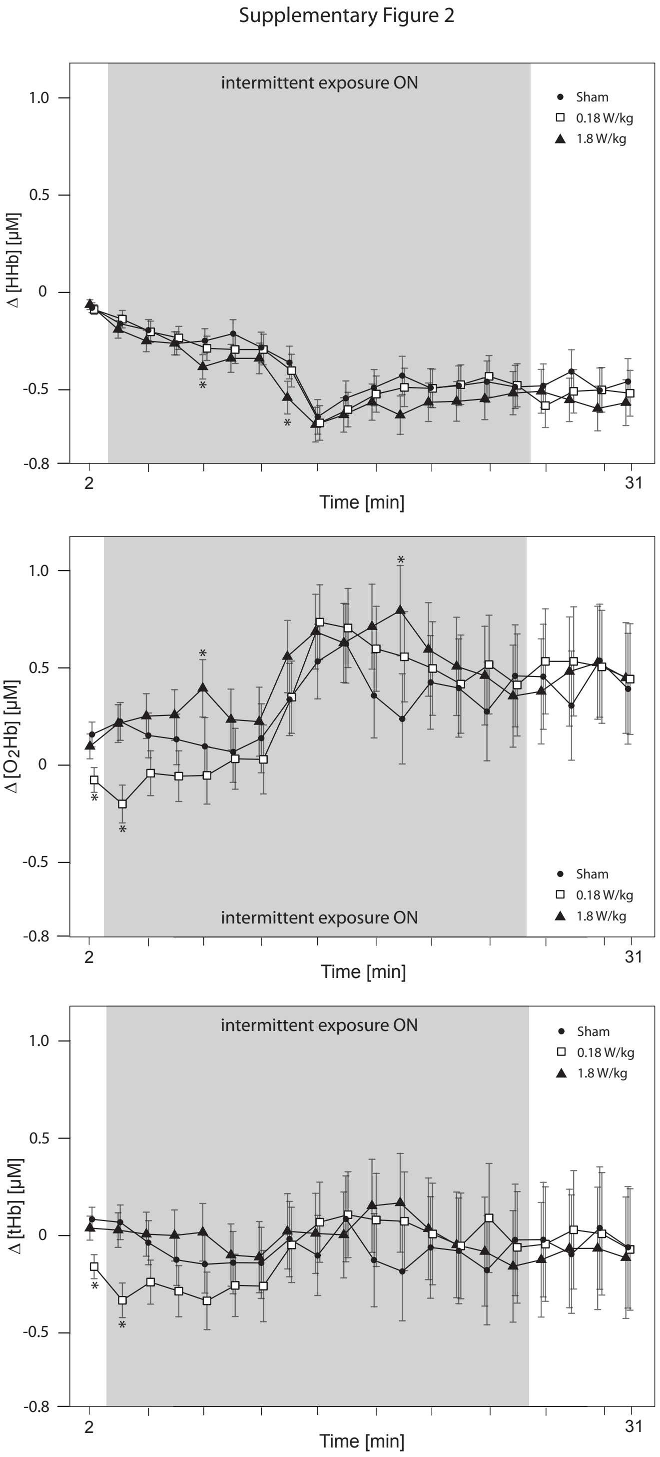

Figure 4.15 – Medium-term analysis: Time evolution of mean effects and 99% confidence intervals for Δ[O_2Hb], Δ[HHb] and Δ[tHb] for the different exposures displayed. Significant results ($p < 0.01$) comparing 0.18 W/kg or 1.8 W/kg to sham are marked with an asterisk.

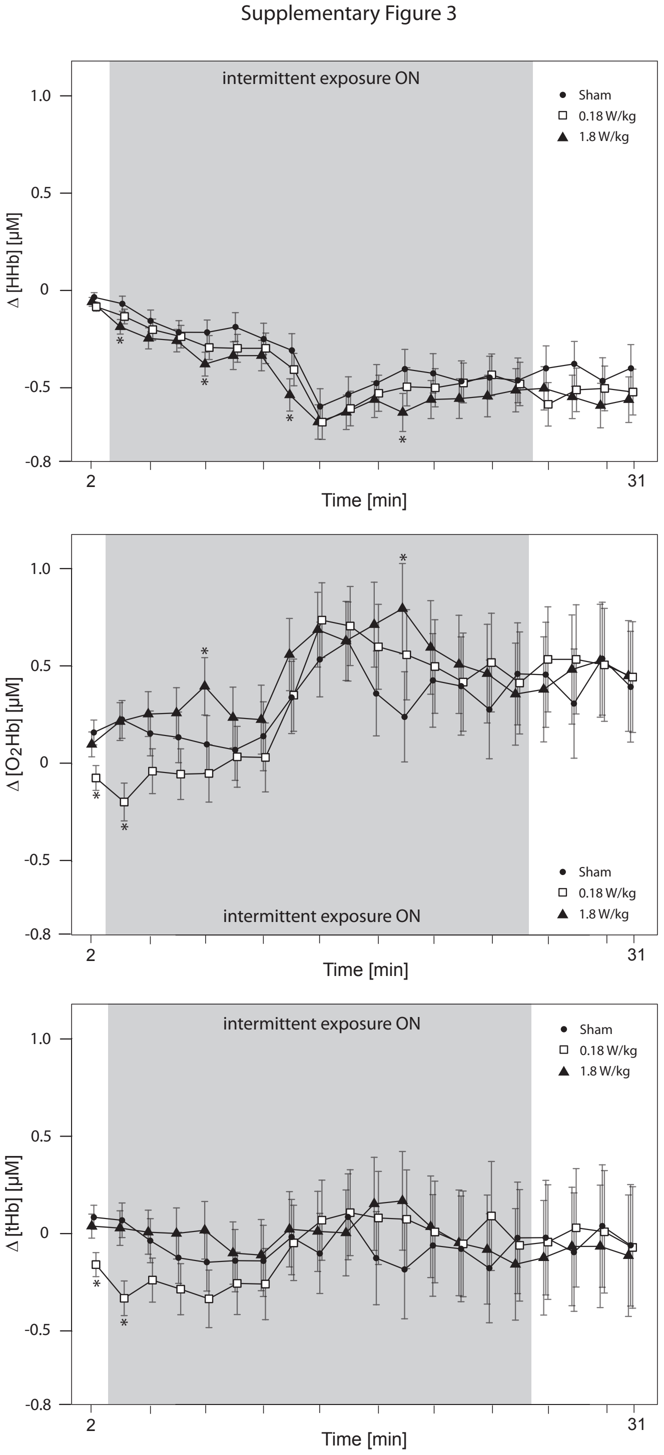

Figure 4.16 – Medium-term analysis without outliers: Time evolution of mean effects and 99% confidence intervals for $\Delta[O_2Hb]$, $\Delta[HHb]$ and $\Delta[tHb]$ for the different exposures displayed. Significant results ($p < 0.01$) comparing 0.18 W/kg or 1.8 W/kg to sham are marked with an asterisk.

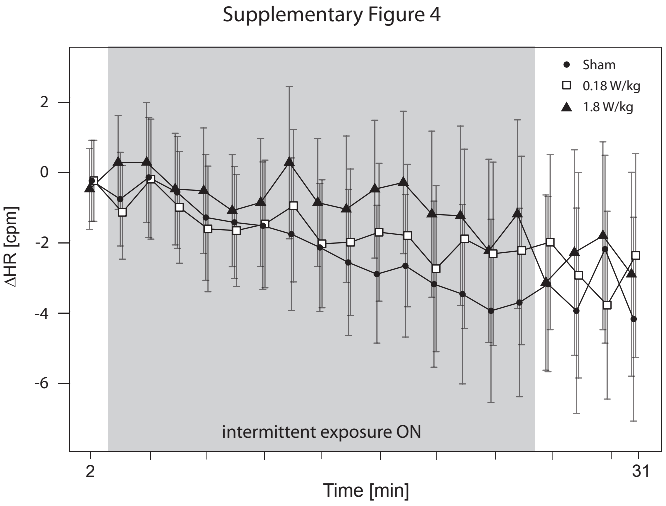

Figure 4.17 – Medium-term analysis for HR: Time evolution of mean effects and 99% confidence intervals for HR for the different exposures displayed. No significant results ($p < 0.01$) were found for single time points.

5 Application of the multi-frequency FD-NIRS instruments

Frequency domain near-infrared spectroscopy of the uterine cervix during regular pregnancies

---

René Hornung[1], Sonja Spichtig[2], Ana Baños[3], Michèle Stahel[3], Roland Zimmermann[3], and Martin Wolf[2]

[1]Department of Obstetrics and Gynecology, Kantonsspital St. Gallen, Switzerland
[2]Biomedical Optics Research Laboratory, Division of Neonatology, Department of Obstetrics and Gynecology, University Hospital Zurich, 8091 Zurich, Switzerland
[3]Department of Obstetrics and Gynecology, University Hospital Zurich, Switzerland

Submitted to: Lasers Med Sci

Abstract

Objective: Preterm labor is a common obstetric complication. Clinical evaluation of cervical ripening to predict preterm labor is very inaccurate. We used FD-NIRS to non-invasively investigate the changes of the optical properties (i.e. μ_a and μ_s') in the uterine cervix during regular pregnancies.
Methods: Optical properties of uterine cervices were measured in 13 patients at various time points of regular pregnancies. For each gestational trimester, mean values with 95% confidence intervals were calculated for O_2Hb, HHb, tHb, StO_2 and water content and statistically significant differences between the trimesters were determined. The wavelength-dependent scattering (scatter power) was calculated by an exponential fit.
Results: O_2Hb and tHb showed an increase and SP an decrease as a function of the gestational age. Differences between the second and the third trimester were statistically significant. HHb and the water content showed no significant change over time.
Conclusion: Our results show that FD-NIRS is a promising diagnostic tool to provide information about cervical content of hemoglobin, water and extracellular matrix proteins. We propose this technology to assess the cervical ripening and eventually to predict preterm labor.

Introduction

Preterm labor is responsible for 70% of perinatal mortality and nearly half of long-term neurological morbidity (Goldenberg et al. 2000) and is probably one of the most challenging problems in modern obstetrics and gynecology. In the United States, more than half a million infants are born preterm annually, a rate of 12,8% (Martin et al. 2007). One of the keys to treating preterm labor and preventing severe neonatal complications would be early identification of women at risk. This would allow the initiation of important interventions to delay delivery and to improve neonatal outcome. Clinical evaluation of cervical ripening in the first, second and third trimester of pregnancy to predict preterm labor has a substantial inter- and intraobserver variability and does not provide accurate diagnosis, prediction, or insight into the pathopyhsiology. Although excellent research has been performed to understand the etiology of spontaneous and preterm delivery, a more accurate method to determine the cervical status and diagnose preterm cervical ripening would be invaluable.

Cervical ripening may be induced by local infection, cervical incompetence or uterine contractions. Undoubtedly, cervical ripening is associated with many biochemical and physiological changes of the cervical tissue. Changes in blood perfusion and water content could well be reflected in changes in optical properties (i.e. μ_a and μ_s') of the uterine cervix during pregnancy and labor. In a recent study we demonstrated that drug-induced cervical ripening resulted in a significant decrease in tHb, a significant decrease in oxyhemoglobin O_2Hb, a highly significant increase in water content and a significant increase of SP (Baños et al. 2007). We also demonstrated that hormonal changes in human uterine cervices and breasts can be monitored as changes in optical properties (Matzinger et al. 2009, Stahel et al. 2009).

NIRS is used to non-invasively characterize optical properties of thick tissues in vivo (Patterson, Pogue and Wilson 1993). Optical properties can be quantitatively defined in terms of μ_a and μ_s'. These parameters are sensitive to the tissue concentration of light absorbing molecules and light scattering structures. The primary tissue contributors to light absorption are O_2Hb, HHb, water (H_2O), lipids, cytochromes and melanin (Cope 1991). Light scatterers are tissue structural elements, such as cellular components and fibrous materials in the extracellular matrix (e.g. collagen/elastin).

The main limitation of NIRS was the inability to make quantitative measurements because of the difficulty to separately measure μ_a and μ_s'. FD-NIRS is a NIRS technique capable of solving this problem and quantifying absolute tissue μ_a and μ_s' values and absolute concentrations of O_2Hb, HHb, tHb and H_2O and StO_2 (Tromberg et al. 1996). The instrumentation and theoretical background for FD-NIRS have been described elsewhere (Fishkin et al. 1997, Chance et al. 1998).

The present study is based on the hypothesis that optical properties of cervices change from trimester to trimester in regular pregnancies, and that the quantification of the optical properties in vivo by means of FD-NIRS will provide insight into physiology of cervices during regular pregnancies.

We therefore used FD-NIRS technology to study the optical properties of the uterine cervix in healthy pregnant volunteers scheduled for regular pregnancy controls.

This appears to be the first clinical study which measured non-invasively and quantitatively the μ_a and μ_s' as well as the physiological properties of the uterine cervix along the entire pregnancy.

Materials and Methods

The FD-NIRS instrument used at the Department of Obstetrics and Gynecology, University Hospital of Zurich, is a modified Imagent® (ISS Inc., Champaign, Illinois, USA). It is equipped with 7 near infrared diode lasers (emitting at 690 nm, 730 nm, 750 nm, 808 nm, 870 nm, 920 nm and 970 nm) and one APD detector. The instrument includes a pair of frequency synthesizers (PTS 500 Frequency Synthesizer, Programmed Test Sources Inc., Littleton, USA) working in the range of 130 – 490 MHz and capable of switching frequencies within less than 1 ms. One frequency synthesizer modulates the intensity of the laser diodes, while the other modulates the detector at a frequency which is 5 kHz different from the source modulation, thus demodulating the frequency at the detector. The instrument is equipped with a complete software package Boxy® (ISS Inc., Champaign, Illinois, USA) for data acquisition and two calibration blocks with known optical properties. Once data acquisition is initiated the photon density wave's phase and amplitude is measured as a function of frequency from 130 to 490 MHz in steps of 10 MHz and fitted to analytically derived model functions in order to calculate μ_a and μ_s' for each wavelength.

The wavelength-dependence of absorption enables to calculate O_2Hb, HHb, tHb, StO_2 and H_2O (Spichtig et al. 2009). μ_s' were measured for the different wavelengths. In addition, the wavelength-dependent decrease of scattering, the so called SP, was calculated by an exponential fit.

The software also provides measures of the quality of the fitting, which enables to discard measurements with low quality. The system is fully automated and data acquisition time is approximately 40 s. The instrument is described in detail elsewhere (Spichtig et al. 2009).

For the present study we used a vaginal probe specifically designed for measurements of the human uterine cervix (Baños et al. 2007, Matzinger et al. 2009, Hornung, Pham, Keefe, Berns, Tadir and Tromberg 1999). The vaginal probe was slightly bent allowing good visualization during placement on the cervix. Eight multimode silica fibers (400 μm diameter, 3M FT 400 EMT, Thorlabs Inc., USA) were coupled to the laser sources to transmit the light to the tip of the probe. One glass fiber bundle (3 mm diameter) conducts the light from the tip of the probe to the detector. The source-detector separation is 10 mm.

Condom-like latex-covers were used to prevent transfection from patient to patient. The latex cover did not affect light transmission as investigated in some pilot measurements (data not shown).

A total of 13 healthy pregnant volunteers scheduled for routine pregnancy controls were included in the study after written informed consent was obtained. The study was approved by the local ethical committee under the protocol StV 19/2003.

Age was 28.4 ± 5.2 years (mean ± SD), 5 patients were nulliparous, 5 patients primiparous and 3 patients multiparous.

All patients underwent a routine obstetrical examination. Optical properties of the uterine cervix were determined at every visit in the hospitals outpatient clinic, typically in intervals of one month. The uterine cervix was cleaned using a dry cotton swab to remove mucous and detritus in order to allow optimal light penetration and signal detection. The vaginal probe was inserted into the vagina using regular specula and placed on the vaginal portion of the uterine cervix with a gentle pressure ensuring good probe-cervix contact. Measurements were performed once on the anterior and once on the posterior cervical lip. For technical reasons and patients discomfort the anterior cervical lip was more suitable to FD-NIRS measurements. On the posterior lip, fit errors were also higher. This is why we restricted data analysis to those of the anterior cervical lip.

The statistical analysis was carried out with R (R Developement Core Team 2009) and a p-value < 0.05 was considered as significant and $p < 0.005$ as highly significant. The gestational age was divided into three gestational trimesters: the first trimester from week 0 to 13, the second trimester from week 14 to 26 and the third trimester from week 27 to 39. In a first step, the calculated concentrations were plotted against the gestational age and a suitable regression function, its correlation coefficient and p-value were determined. In a second step, an analysis of variance (ANOVA) model in dependency of the factor *trimester* was performed and a multiple comparison of means with Tukey correction was carried out to test for significant differences between the gestational trimesters. For each trimester and measurement variable, mean values and a confidence interval of 95% are given [2.5%, 97.5%].

Results

The absolute concentration of HHb (in μmol/l) in dependency of the gestational age is shown in Figure 5.1. HHb showed no statistically significant relationship to the gestational age (weeks in pregnancy). HHb was 23.6 [13.7, 33.4] μmol/l in the first trimester, 18.1 [13.2, 23.1] μmol/l in the second trimester and 24.5 [21.0, 28.0] μmol/l in the third trimester.

O_2Hb showed a significant linear correlation to the gestational age (Figure 5.2). O_2Hb was 65.2 [40.9, 90.0] μmol/l in the first trimester, 76.9 [64.8, 89.1] μmol/l in the second trimester and 96.6 [88.0, 105.2] μmol/l in the third trimester. The difference between the second and third trimester was significant (p = 0.027).

tHb showed a significant linear correlation to the gestational age (Figure 5.3). tHb was 88.8 [63.2, 114.3] μmol/l in the first trimester, 95.1 [82.3, 107.9] μmol/l in the second trimester and 121.1 [112.1, 130.1] μmol/l in the third trimester. The difference between the second and third trimester was significant (p = 0.027).

StO_2 was stable throughout the entire pregnancy and showed no statistically significant relationship to the gestational age. StO_2 was 71.5 [62.3, 80.7]% in the first trimester, 79.3 [74.7, 83.9]% in the second trimester and 77.9 [74.6, 81.1]% in the third trimester.

H_2O showed no statistically significant relationship to the gestational age (Figure 5.4). H_2O was 38.7 [28.2, 49.2]% in the first trimester, 30.0 [24.8, 35.3]% in the second trimester and 31.5 [27.8, 35.2]% in the third trimester.

SP showed a statistically significant polynomial correlation to the gestational age (Figure 5.5). SP was 1.14 [0.92, 1.36] cm^{-1} in the first trimester, 0.51 [0.39, 0.62] cm^{-1} in the second trimester and 0.34 [0.26, 0.43] cm^{-1} in the third trimester. The difference between the first and second trimester is highly significant ($p < 0.005$) and the difference between the second and third trimester is close to significance (p = 0.067).

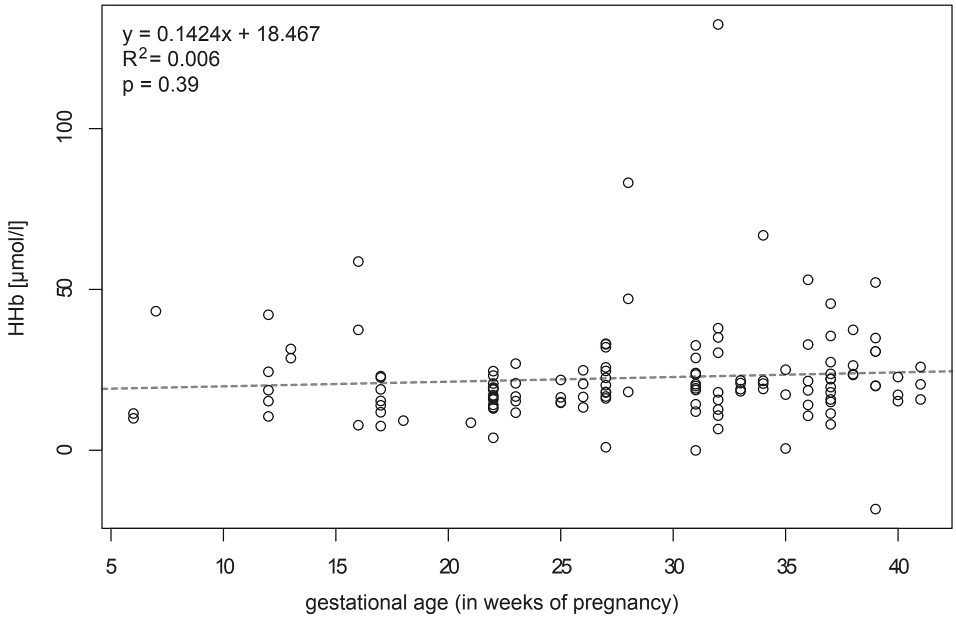

Figure 5.1 – The concentrations of HHb in μmol/l in the tissue of the uterine cervix as a function of the gestational age (in weeks of pregnancy) is shown. The statistically not significant linear regression function is shown as a dotted grey line and its correlation coefficient R^2 and p-value are given.

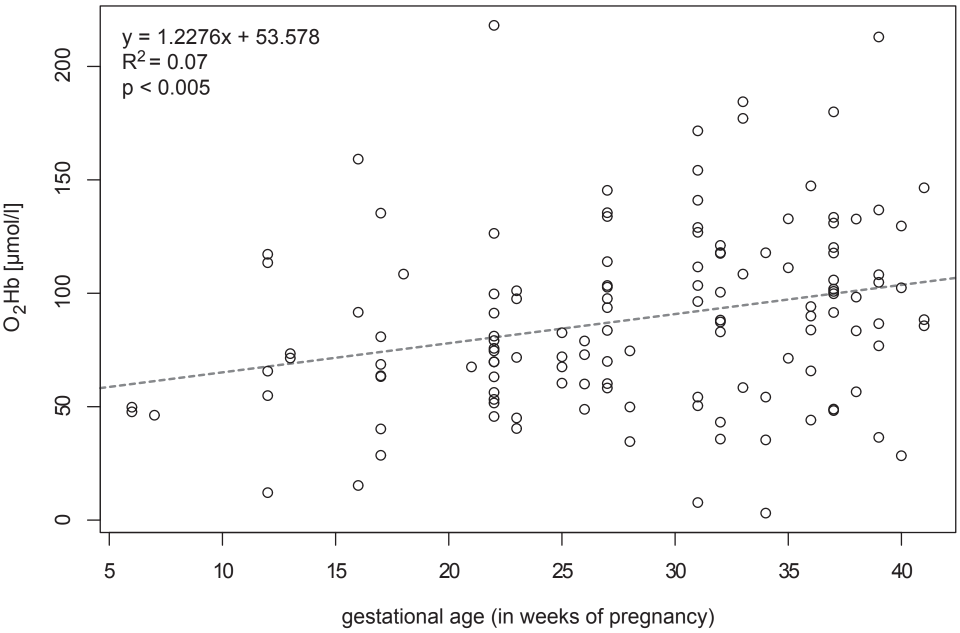

Figure 5.2 – The concentration of O_2Hb in μmol/l in the tissue of the uterine cervix as a function of the gestational age (in weeks of pregnancy) is shown. The statistically significant linear regression function is shown as a dotted grey line and its correlation coefficient R^2 and p-value are given.

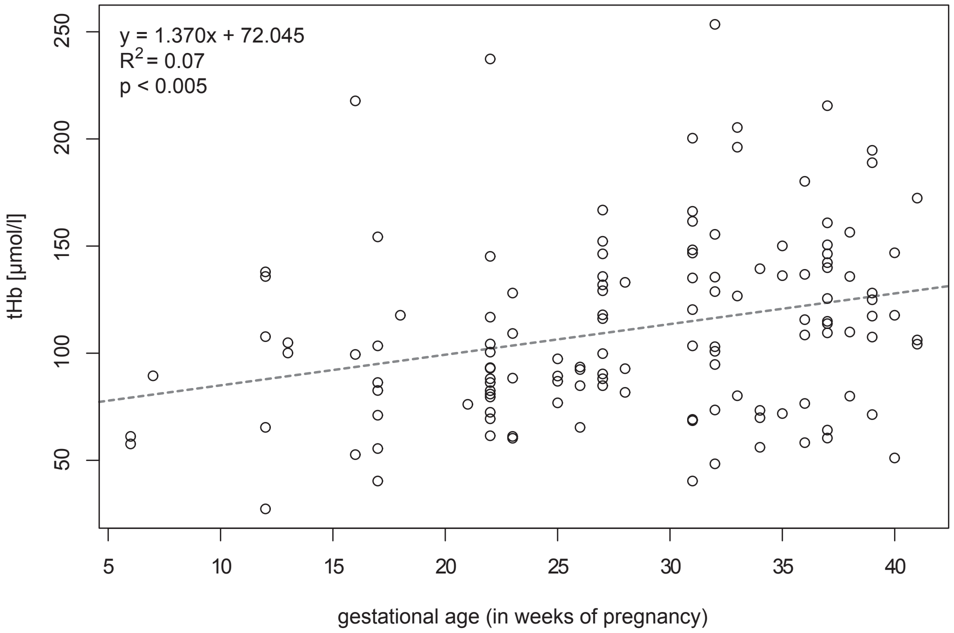

Figure 5.3 – The concentration of tHb in μmol/l in the tissue of the uterine cervix as a function of the gestational age (in weeks of pregnancy) is shown. The statistically significant linear regression function is shown in as a dotted grey line and its correlation coefficient R^2 and p-value are given.

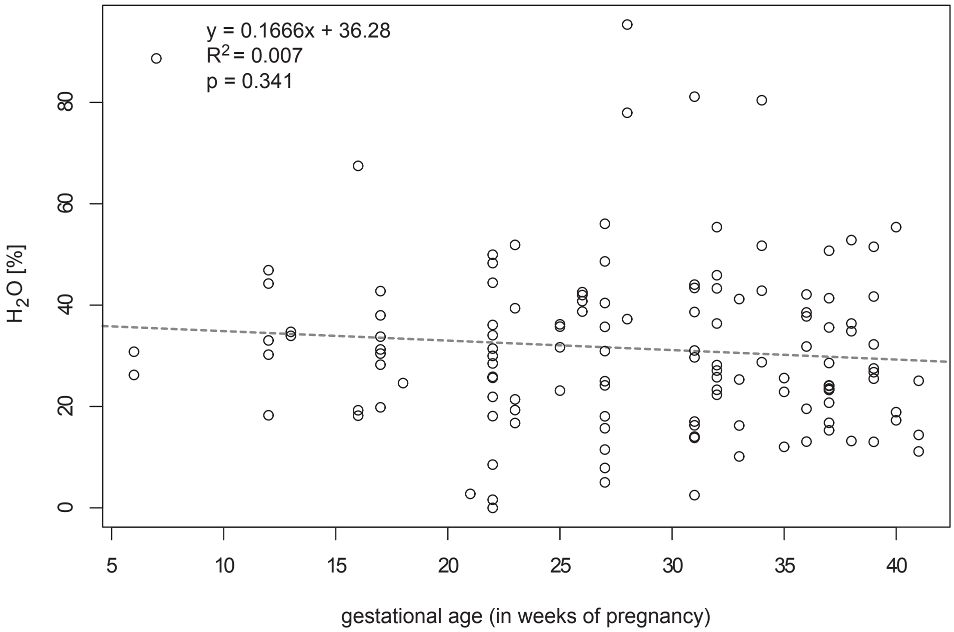

Figure 5.4 – The relative water content (H_2O in %) in the tissue of the uterine cervix as a function of the gestational age (in weeks of pregnancy) is shown. The statistically not significant linear regression function is shown as a dotted grey line and its correlation coefficient R^2 and p-value are given.

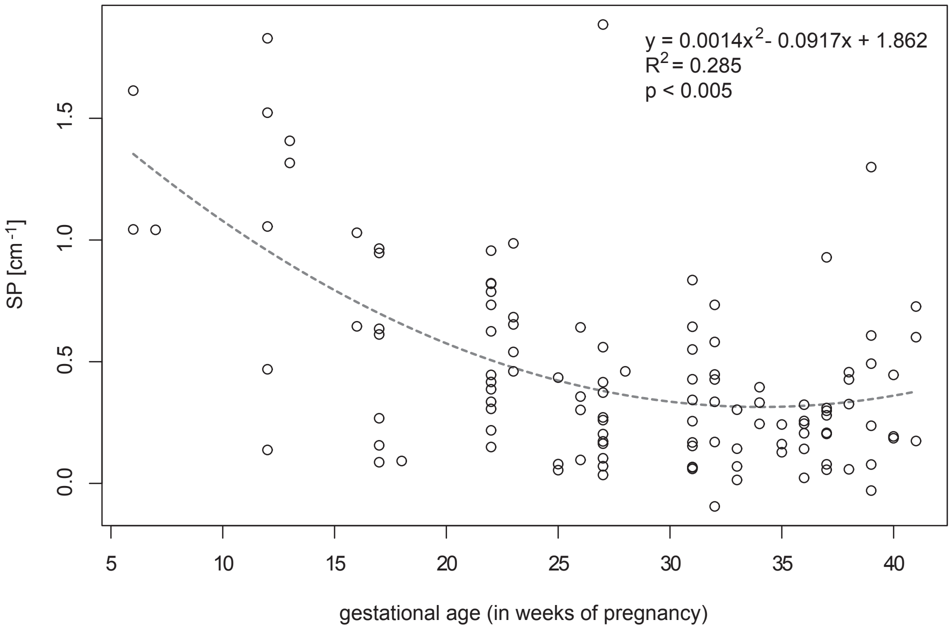

Figure 5.5 – The SP in cm^{-1} in the tissue of the uterine cervix as a function of the gestational age (in weeks of pregnancy) is shown. The statistically significant polynomial regression function is shown in as a dotted grey line and its correlation coefficient R^2 and p-value are given.

Discussion

The uterine cervix challenges several opposing purposes: on one hand it has to form a slim tunnel to allow the sperms to pass into the uterus and on the other hand it has to be closed to protect the pregnancy from ascending infections and preterm delivery. At the end of the pregnancy the cervix is softening and has to form a ten centimeter wide opening to allow the fetus to pass through the birth channel. Consequently, the human uterine cervix is a complex tissue, which is capable of adapting to these various situations. It is composed of an extracellular matrix consisting predominantly of collagen (about 70% type I collagen) with elastin and proteoglycans, and a cellular component consisting of smooth muscle and fibroblasts, epithelium, and blood vessels (Ludmir and Sehdev 2000, Schlembach et al. 2009). Hormones regulate cervical consistence to preserve the pregnancy and ultimately to induce cervical ripening for delivery (Leppert 1995).

This study employed FD-NIRS, a modern technology to measure optical properties of the human uterine cervix in volunteers scheduled for routine controls during regular pregnancies. We thus aim to provide new insights into the physiological changes of the uterine cervix during pregnancy. Absolute values of the present study are in reasonable agreement with previously published data from not pregnant patients and from pregnant patients scheduled for abortion (Baños et al. 2007, Matzinger et al. 2009). Not surprisingly, HHb, O_2Hb and tHb values of not pregnant uterine cervices were lower than those for pregnant women. In not pregnant patients, HHb of the uterine cervix was 16.0 μmol/l (Matzinger et al. 2009). HHb was 20.4 μmol/l in patients scheduled for abortion (Baños et al. 2007) and 23.6 μmol/l in the first trimester of the present study. This good consistency with previous results indicates the reliability of the method.

As expected, O_2Hb and tHb of the uterine cervix increased continuously over time during a regular pregnancy (Figures 5.2 and 5.3).This represents the dramatic increase of the uterine perfusion during the pregnancy to provide a sufficient supply for the growing fetus. The growing fetus is increasingly building up pressure on the uterine cervix. The cervix, in turn, has to withstand this pressure to prevent a preterm dilation of the birth channel by increasing the levels of total sulphated glycosaminoglycans, hyaluronic acid, and collagen solubility (Myers et al. 2009).

Scattering of light is a boundary phenomenon. Photons propagating in tissues are deflected as they experience changes in the index of refraction at boundaries, such as cellular membranes or extracellular matrix proteins (i.e. mainly collagen). This is the reason for the scattering of light. The SP is negatively correlated with the size of the scatterer. In our measurements SP significantly decreased as a function of the gestational age (Fig. 5.5). In part, this may be explained by the increasing size of cervical cells that is very likely to occur as the uterus grows during the pregnancy. To maintain structural integrity and avoid preterm cervical ripening the cellular synthesis of proteins has to be activated, requiring more and bigger cellular organelles and structures. In addition, collagen fibers are aligned, increase in size with reduced collagenolytic activity and an increase of insoluble collagen concentration. This is well reflected in Fig. 5.5 of the present study. The SP showed a substantial decrease as a function of the gestational age. In addition, we found a slight but not significant decrease in water content that may be explained by the increased collagen concentration. During cervical ripening, in contrast, the concentration of collagen changes from the insoluble to the more soluble form by an increase in collagenolytic activity during cervical ripening. The collagen is dispersed and remodeled with a net loss in collagen fiber alignment and a decrease in fiber length (Schlembach et al. 2009, Leppert 1995, Myers et al. 2009, Myers et al. 2008). This shift was observed in our previous study on drug-induced cervical ripening (Baños et al. 2007), which resulted in a significant increase in SP.

One major clinical aim in obstetrics is the identification of women at risk of preterm delivery. The current state of labor monitoring is highly subjective and no currently used method has been successful at predicting preterm delivery so far.

Bimanual vaginal and transvaginal ultrasonographic assessment of the uterine cervix as well as the determination of fetal fibronectin (FFN) have emerged as the major clinical predictors of preterm birth (Leitich and Kaider 2003).

Advances have been made in measuring the length of the uterine cervix by transvaginal ultrasound (Berghella et al. 2009, Volumenie et al. 2004). Furthermore, the tissue specific mean grey scale value of the cervix determined by quantitative ultrasound has been shown to be a better predictor for preterm birth than cervical length measurements (Tekesin et al. 2005). Our data may, in part, clarify the grey level analysis, which reflects cervical tissue composition. The combination of transvaginal sonography with its capability to measure the cervical length, grey scale and perfusion may reveal additional information when combined with FD-NIRS.

A cervicotonometer to measure cervical distensibility showed significantly elevated distensibility in women who had a preterm delivery (Cabrol et al. 1991, Mazza et al. 2006) and may be able to detect early changes associated with pathologic conditions. Another non-invasive method, a 'Collascope', to measure the decrease in collagen content has been developed (Maul, Saade and Garfield 2005, Maul, Olson, Fittkow, Saade and Garfield 2003), where fluorescence of the cervical collagen is determined. The correlation between gestational age and cervical tissue collagen content is high and the clinical evaluation is still in progress. A combination of absorption, scattering and fluorescence may deepen our insight into cervical physiology in pregnancy.

Uterine electro-myography acquires uterine electrical signals taken non-invasively from the abdominal surface (Garfield et al. 2002, Garfield et al. 2005) and may predict labor and subsequent delivery.

A biochemical approach for the assessment of the cervix requires cervical biopsies and cannot be used in practice. An indirect approach is the measurement of biomarkers involved in cervical ripening. Among many markers evaluated, FFN is an effective short-term marker of preterm delivery (Leitich and Kaider 2003, Vogel et al. 2005) and may be part of a 'multiple marker' approach (Simhan 2005).

There are two main limitations of the present study. First, since this study was designed as a feasibility study, the number of subjects included is low. Second, the positioning of the probe on the uterine cervix of a pregnant woman using the speculum although technically straight forward, leads to discomfort for the patient. It was not easy for the volunteers to remain motionless, which led to some movement artifacts in the measurements. Such artifacts can be detected and discarded by looking at the fit errors. On the other hand, the probe design will be improved in the future to increase comfort for the patient.

Conclusion

Our encouraging results indicate that FD-NIRS is a promising diagnostic tool to measure cervical O_2Hb, HHb, tHb and water, representing perfusion. In combination with the scattering properties, FD-NIRS provides useful information on the status of the cervix and its ripening. The potential benefits of FD-NIRS include a better understanding of physiology and biochemistry of the uterine cervix during pregnancy as well as cervical ripening and eventually a prediction of preterm labor.

In the present feasibility study we measured the optical properties of the uterine cervix during regular pregnancies. These normal values will be compared to the data of patients at risk for preterm delivery in the future. We propose to apply this technology to assess the cervix for the prediction of preterm labor or for distinguishing between true and false labor. In our ongoing studies we investigate the uterine cervix in pregnancies at risk for preterm delivery to determine the ability of FD-NIRS to predict preterm labor. In addition, FD-NIRS together with the collascope may be combined with ultrasound measurements of the cervical length to predict preterm delivery.

Acknowledgement

Statistical support by Mr. Massimo Merlini (Statistical Seminar, Swiss Federal Institute of Technology Zurich, Switzerland) is highly acknowledged.

Conclusion and Outlook

The ability of NIRI to non-invasively assess various parameters such as the μ_a and μ_s' of tissue, changes in hemoglobin, water and fat content, the oxygenation of tissue and functional brain activation, make NIRI a promising technique in a broad field of applications. This thesis describes two projects: i) assessing potential effects of UMTS-EMF on blood circulation in the human head and ii) monitoring structural and compositional changes of the human cervix during normal pregnancies. To achieve these aims, the commercially available instruments were modified according to the study requirements. Then measurements were performed, the data analysis was improved and applied and the appropriate statistics carried out.

Potential effects of electromagnetic fields on blood circulation in the human head

The implementation of the *switch16* mode for the multi-distance instrument ISS Oxiplex®, which can be activated by a dip-switch on the backside of the instrument, quadrupled the number of available light paths and enabled to obtain spatial resolution with the novel NIRI sensors, *Imager16* and *Imager4MRT* (section 2.1).

The characterization of the novel sensors in terms of horizontal and depth resolution showed good resolution in the horizontal plane, but a non linear depth resolution over the probed volume (section 2.2). The object is usually projected closer to the surface and the reconstructed amplitude of $\Delta\mu_a$ depends highly on the position of an object with respect to source and detector positions. If the number of light paths which penetrate an object is increased, the position of the object can be reconstructed more accurately. Testing different methods for their ability to distinguish superficial from deep changes showed that the results obtained with the modified Lambert-Beer law are the most reliable in both phantom and in-vivo measurements (section 2.3). Obtaining absolute quantification of absorption changes is still an important research issue in NIRI and DOI. Indeed, absolute quantification and the uniformity of the sensor sensitivity is better for dense imaging arrays (Zeff et al. 2007) and it can further be improved by incorporating subject-specific head models in photon transport modeling. However dense imaging arrays require custom-built instruments and subject-specific head models cost-intensive MR scanner time.

Quantitative phantom and in-vivo functional measurements showed that the *Imager4MRT* is suitable for NIRI measurements simultaneously to MRI scanning. This opens a wide range of multi-modal applications, which have the potential to benefit both modalities. Anatomical MR images can be incorporated as subject-specific head models in the photon transport modeling to improve quality and accuracy of NIRI. The hemodynamic parameters measured with NIRI provide additional information for the hemodynamic forward model used in fMRI for the analysis of effective connectivity with DCM (Friston, Harrison and Penny 2003).

A novel motion artifact reduction algorithm (MARA) was developed within the scope of the UMTS exposure study and has proven to be an efficient method to reduce movement artifacts in NIRI data (section 4.1). In the future, the algorithm can be expanded to apply other than spline interpolation methods and statistical methods can be incorporated to predict the signal characteristics within the MA-afflicted segments.

Within an exploratory study (section 4.2), no significant short-term effect of intermittent UMTS-EMF (maximum peak SAR-value of 1.8 W/kg) on blood circulation was found for any signal type or exposure position. This signal type *downlink* and exposure position *T3* were applied in the main study because this configuration showed the most pronounced (yet not significant) change in the measurables due to EMF. A homogeneous study population (young, non-smoking, healthy men) was chosen for the main study. Small significant short-term effects on [O_2Hb] and [tHb] for low dose (0.18 W/kg) were found, medium-term effects on [HHb] for low and high dose (1.8 W/kg) and medium-term effects on HR for the high dose.
The amplitude of the short-term effects found were relatively small ($\approx$17%) compared to the amplitude of changes related to normal functional activation. In addition, the difference in the medium-term heart rate of +1.84 bpm was also small when comparing it to changes elicited by physical activity or by stress. However, the results must be interpreted carefully and we suggest that a replication study should be performed as effects of EMF exposure are a controversial subject and premature conclusions of results may cause confusion in the general public. The research of intermittent EMF exposure should also be applied to other study populations.
Since the mechanisms of interaction are not known, translating the scientific results to health implications is not possible. But considering the small effect size and the state of knowledge, a negative impact on human health is unlikely, but cannot be excluded. Since the effects were found in a healthy male population, no conclusions about the whole population can be drawn.
Although the measured effects are small, they indicate that there may be an effect of intermittent UMTS-EMF exposure, which justifies that intermittent EMF exposure receives more scientific attention in the future.

The inertness of NIRI to EMF makes it an excellent tool to study immediate effects of intermittent EMF. The modified NIRI instrument and flexible exposure setup are suitable to be used in several future applications such as the investigation of potential effects of EMFs at various frequencies on blood circulation and the hemodynamic response to neuronal activation.

Monitoring of structural and compositional changes of the uterine cervix

The ISS Imagent® was modified to operate as a multi-frequency instrument and the spectral range of the instrument was enhanced to enable, in principle, the determination of O_2Hb, HHb, tHb, water and lipid concentration. Validation measurements of our instrument showed that it is feasible to determine reliable and accurate measures for tHb and water concentration, but not for lipid (section 3). The implementation of the multi-frequency setup with a single distance enables measurements on small tissue structures, such as the cervix and can be used in future applications for the tongue, hand or foot. But to be able to determine the lipid component as well, absorption and scattering spectra of different human lipids must be available.

The results of the cervix study (section 5) showed a significant increase in [O_2Hb] and [tHb] from the second to the third trimester, which may be explained by the large increase of the uterine perfusion which guarantees a sufficient supply for the growing fetus. No significant changes were observed for StO_2, [H_2O] and [HHb]. The SP decreased significantly between the first and second trimester, which indicates an increase in the size of scatter particles. This may be explained by an increasing size and number of cervical cells and the consolidation and alignment of collagen (Ludmir and Sehdev 2000).

Although, strong movement artifacts were present in NIRS data, we have shown that structural and compositional changes in the uterine cervix during normal pregnancy are correlated to changes of the optical signal. To further reduce data variability and the amount of movement artifacts a pressure feedback should be integrated in the optical sensor. This will provide a better control for the clinicians and guarantees constant light coupling over the whole measurement duration.

The values for normal pregnancies will be compared to pregnancies at risk for preterm labor in an ongoing study. This comparison will determine the ability of FD-NIRS to predict preterm labor. To enhance the diagnostic value, several methods can also be combined: due to their similarity with respect to the design of the vaginal probe, the collascope and the cervical length measurement using ultrasound can be combined with FD-NIRS in the future.

References

Aalto, S., Haarala, C., Bruck, A., Sipila, H., Hamalainen, H. and Rinne, J. O. (2006), 'Mobile phone affects cerebral blood flow in humans', *J Cereb Blood Flow Metab* **26**(7), 885–890.

Akaike, H. (1973), 'Information theory and an extension of the maximum likelihood principle', *Proceedings of the Second International Symposium on Information Theory Budapest: Akademiai Kiado* pp. 267–281.

Akima, H. (1970), 'A new method of interpolation and smooth curve fitting based on local procedures', *J. Assoc. Comput. Mach.* **17**(4), 589–602.

Alexandrakis, G., Farrell, T. and Patterson, M. (1998), 'Accuracy of the diffusion approximation in determining the optical properties of a two-layer turbid medium', *Applied Optics* **37**(31), 74017409.

Arridge, S. R. (1999), 'Optical tomography in medical imaging', *Inverse Problems* **15**, R41–R93.

Arridge, S. R. and Hebden, J. C. (1997), 'Optical imaging in medicine: II. Modelling and reconstruction', *Phys Med Biol* **42**(5), 841–853.

Arridge, S., Schweiger, M. and Delpy, D. T. (1992), 'Iterative reconstruction of near infrared absorption images', *SPIE Vol. 1767 Inverse Problems in Scattering and Imaging* .

Baños, A., Wolf, M., Grawe, C., Stahel, M., Haensse, D., Fink, D. and Hornung, R. (2007), 'Frequency domain near-infrared spectroscopy of the uterine cervix during cervical ripening', *Lasers Surg Med* **39**(8), 641–646.

Berghella, V., Baxter, J. K. and Hendrix, N. W. (2009), 'Cervical assessment by ultrasound for preventing preterm delivery', *Cochrane Database Syst Rev* (3), CD007235.

Biran, A. and Breiner, M. (1999), *MATLAB 5 für Ingenieure*, Munich: Adison-Wesley-Longman.

Bland, J. M. and Altman, D. G. (1986), 'Statistical methods for assessing agreement between two methods of clinical measurement', *Lancet* **1**(8476), 307–310.

Bluestone, A., Abdoulaev, G., Schmitz, C., Barbour, R. and Hielscher, A. (2001), 'Three-dimensional optical tomography of hemodynamics in the human head', *Opt Express* **9**(6), 272–286.

Boas, D. (1997), 'A fundamental limitation of linearized algorithms for diffuse optical tomography', *Opt Express* **1**(13), 404–413.

Boas, D. A., Chen, K., Grebert, D. and Franceschini, M. A. (2004), 'Improving the diffuse optical imaging spatial resolution of the cerebral hemodynamic response to brain activation in humans', *Opt Lett* **29**(13), 1506–1508.

Boas, D. A., Gaudette, T., Strangman, G., Cheng, X., Marota, J. J. and Mandeville, J. B. (2001), 'The accuracy of near infrared spectroscopy and imaging during focal changes in cerebral hemodynamics', *Neuroimage* **13**(1), 76–90.

Boas, D. A., O'Leary, M. A., Chance, B. and Yodh, A. G. (1997), 'Detection and characterization of optical inhomogeneities with diffuse photon density waves: a signal-to-noise analysis', *Appl Opt* **36**(1), 75–92.

Boas, D., Dale, A. and Franceschini, M. (2004), 'Diffuse optical imaging of brain activation: approaches to optimizing image sensitivity, resolution, and accuracy', *NeuroImage* **23**, 275–288.

Borbely, A. A., Huber, R., Graf, T., Fuchs, B., Gallmann, E. and Achermann, P. (1999), 'Pulsed high-frequency electromagnetic field affects human sleep and sleep electroencephalogram', *Neurosci Lett* **275**(3), 207–210.

Boushel, R., Langberg, H., Olesen, J., Gonzales-Alonzo, J., Bülow, J. and Kjaer, M. (2001), 'Monitoring tissue oxygen availability with near infrared spectroscopy (NIRS) in health and disease', *Scand. J. Med. Sci. Sports* **11**(4), 213–222.

Braune, S., Riedel, A., Schulte-Monting, J. and Raczek, J. (2002), 'Influence of a radiofrequency electromagnetic field on cardiovascular and hormonal parameters of the autonomic nervous system in healthy individuals', *Radiat Res* **158**(3), 352–6.

Cabrol, D., Carbonne, B., Ledieu, C. and Lussiana, F. (1991), 'Relationship between mechanical properties of the uterine cervix and occurrence of postdate pregnancy', *Gynecol Obstet Invest* **32**(1), 36–38.

Casavola, C., Paunescu, L. A., Fantini, S. and Gratton, E. (2000), 'Blood flow and oxygen consumption with near-infrared spectroscopy and venous occlusion: spatial maps and the effect of time and pressure of inflation', *J Biomed Opt* **5**(3), 269–276.

CENELEC (2001), Basic standard for the measurement of specific absorption rate related to human exposure to electromagnetic fields from mobile phones (300 MHz-3 GHz), Technical report, Brussels, Belgium: EN50361, 2001.

Cerussi, A. E., Berger, A. J., Bevilacqua, F., Shah, N., Jakubowski, D., Butler, J., Holcombe, R. F. and Tromberg, B. J. (2001), 'Sources of absorption and scattering contrast for near-infrared optical mammography', *Acad Radiol* **8**(3), 211–218.

Chance, B., Cope, M., Gratton, E., Ramanujam, N. and Tromberg, B. (1998), 'Phase measurement of light absorption and scatter in human tissue', *Rev Sci Instrum* **69 (10)**, 3457–3481.

Chandrasekhar, R. (1950), *Radiative Transfer*, Oxford: Clarendon Press.

Choi, J., Wolf, M., Toronov, V., Wolf, U., Polzonetti, C., Hueber, D., Safonova, L., Gupta, R., Michalos, A., Mantulin, W. and Gratton, E. (2004), 'Noninvasive determination of the optical properties of adult brain: near-infrared spectroscopy approach', *J Biomed Opt* **9**(1), 221–229.

Cope, M. (1991), 'The development of a near infrared spectroscopy system and its application for non invasive monitoring of cerebral blood and tissue oxygenation in the newborn infant', PhD thesis.

Croft, R. J., Hamblin, D. L., Spong, J., Wood, A. W., McKenzie, R. J. and Stough, C. (2008), 'The effect of mobile phone electromagnetic fields on the alpha rhythm of human electroencephalogram', *Bioelectromagnetics* **29**(1), 1–10.

Cui, X., Bray, S. and Reiss, A. L. (2010), 'Functional near infrared spectroscopy (NIRS) signal improvement based on negative correlation between oxygenated and deoxygenated hemoglobin dynamics', *NeuroImage* **49**(4), 3039–3046.

Curcio, G., Ferrara, M., Limongi, T., Tempesta, D., Di Sante, G., De Gennaro, L., Quaresima, V. and Ferrari, M. (2009), 'Acute mobile phones exposure affects frontal cortex hemodynamics as evidenced by functional near-infrared spectroscopy', *J Cereb Blood Flow Metab* **29**(5), 903–910.

Curcio, G., Ferrara, M., Moroni, F., D'Inzeo, G., Bertini, M. and De Gennaro, L. (2005), 'Is the brain influenced by a phone call? An EEG study of resting wakefulness', *Neurosci Res* **53**(3), 265–270.

Custo, A., Boas, D. A., Tsuzuki, D., Dan, I., Mesquita, R., Fischl, B., Grimson, W. E. L. and Wells, W. (2010), 'Anatomical atlas-guided diffuse optical tomography of brain activation', *Neuroimage* **49**(1), 561–567.

Dehghani, H., White, B. R., Zeff, B. W., Tizzard, A. and Culver, J. P. (2009), 'Depth sensitivity and image reconstruction analysis of dense imaging arrays for mapping brain function with diffuse optical tomography', *Appl Opt* **48**(10), D137–D143.

Delpy, D. T., Cope, M., van der Zee, P., Arridge, S., Wray, S. and Wyatt, J. (1988), 'Estimation of optical pathlength through tissue from direct time of flight measurement', *Phys Med Biol* **33**(12), 1433–1442.

Doerffel, K. (1984), *Statistik in der analytischen Chemie*, third edn, Verlag Chemie, Weinheim, DE.

Duncan, A., Meek, J. H., Clemence, M., Elwell, C. E., Tyszczuk, L., Cope, M. and Delpy, D. T. (1995), 'Optical pathlength measurements on adult head, calf and forearm and the head of the newborn infant using phase resolved optical spectroscopy', *Phys. Med. Biol.* **40**, 295–304.

Edmonds, H. L., Ganzel, B. L. and Austin, E. H. (2004), 'Cerebral oximetry for cardiac and vascular surgery', *Semin Cardiothorac Vasc Anesth* **8**(2), 147–166.

Eltiti, S., Wallace, D., Ridgewell, A., Zougkou, K., Russo, R., Sepulveda, F. and Fox, E. (2009), ‘Short-term exposure to mobile phone base station signals does not affect cognitive functioning or physiological measures in individuals who report sensitivity to electromagnetic fields and controls’, *Bioelectromagnetics* **30**(7), 556–563.

Eltiti, S., Wallace, D., Ridgewell, A., Zougkou, K., Russo, R., Sepulveda, F., Mirshekar-Syahkal, D., Rasor, P., Deeble, R. and Fox, E. (2007), ‘Does short-term exposure to mobile phone base station signals increase symptoms in individuals who report sensitivity to electromagnetic fields? A double-blind randomized provocation study’, *Environ Health Perspect* **115**(11), 1603–1608.

Elwell, C. E., Springett, R., Hillman, E. and Delpy, D. T. (1999), ‘Oscillations in cerebral haemodynamics. Implications for functional activation studies’, *Adv. Exp. Med. Biol.* **471**, 57–65.

Fantini, S., Franceschini, M. A. and Gratton, E. (1994), ‘Semi-infinite-geometry boundary problem for light migration in highly scattering media: a frequency-domain study in the diffusion approximation’, *J. Opt. Soc. Am. B* **11 (10)**, 2128–2138.

Fantini, S., Franceschini, M. A., Maier, J. S., Walker, S. A., Barbieri, B. and Gratton, E. (1995), ‘Frequency-domain multichannel optical detector for noninvasive tissue spectroscopy and oximetry’, *Optical Engineering* **34 (1)**, 32–42.

Fantini, S., Franceschini, M., Gratton, E., Hueber, D., Rosenfeld, W., Maulik, D., Stubblefield, P. and Stankovic, M. (1999), ‘Non-invasive optical mapping of the piglet brain in real time’, *Opt Express* **4**(8), 308–314.

Fantini, S., Francheschini, M., Fishkin, J., Barbieri, B. and Gratton, E. (1994), ‘Quantitative determination of the absorption-spectra of chromophores in strongly scattering media - a light-emmiting-diode based technique’, *Applied Optics* **33**(22), 5204–5213.

Fantini, S., Hueber, D., Franceschini, M. A., Gratton, E., Rosenfeld, W., Stubblefield, P. G., Maulik, D. and Stankovic, M. R. (1999), ‘Non-invasive optical monitoring of the newborn piglet brain using continuous-wave and frequency-domain spectroscopy.’, *Phys Med Biol* **44**(6), 1543–1563.

Ferrari, M., Mottola, L. and Quaresima, V. (2004), ‘Principles, techniques, and limitations of near infrared spectroscopy’, *Can. J. Appl. Physiol.* **29**(4), 463–487.

Fishkin, J. B., Coquoz, O., Anderson, E. R., Brenner, M. and Tromberg, B. J. (1997), ‘Frequency-domain photon migration measurements of normal and malignant tissue optical properties in a human subject’, *Appl Opt* **36**(1), 10–20.

Fishkin, J. B. and Gratton, E. (1993), ‘Propagation of photon-density waves in strongly scattering media containing an absorbing semi-infinite plane bounded by a straight edge’, *J Opt Soc Am A* **10**(1), 127–140.

Fladby, T., Bryhn, G., Halvorsen, O., Rosé, I., Wahlund, M., Wiig, P. and Wetterberg, L. (2004), ‘Olfactory response in the temporal cortex of the elderly measured with near-infrared spectroscopy: a preliminary feasibility study’, *J. Cereb. Blood. Flow. Metab.* **24**(6), 677–680.

Franceschini, M., Fantini, S., Paunescu, L., Maier, J. and E., G. (1998), ‘Influence of a superficial layer in the quantitative spectroscopic study of strongly scattering media’, *Applied Optics* **37**(31), 7447–7458.

Franceschini, M., Toronov, V., Filiaci, M., Gratton, E. and Fantini, S. (2000), ‘On-line optical imaging of the human brain with 160-ms temporal resolution’, *Opt Express* **6**(3), 49–57.

Friedman, L. and Glover, G. (2006), ‘Report on a multicenter fMRI quality assurance protocol’, *J. of Magn. Res. Img.* **23**, 827–839.

Friston, K. J., Harrison, L. and Penny, W. (2003), ‘Dynamic causal modelling.’, *Neuroimage* **19**(4), 1273–1302.

Furutsu, K. (1980), ‘Diffusion equation derived from space-time transport equation’, *J. Opt. Soc. Am. A* **70 (4)**, 360–366.

Garfield, R. E., Maner, W. L., MacKay, L. B., Schlembach, D. and Saade, G. R. (2005), ‘Comparing uterine electromyography activity of antepartum patients versus term labor patients’, *Am J Obstet Gynecol* **193**(1), 23–29.

Garfield, R. E., Maul, H., Maner, W., Fittkow, C., Olson, G., Shi, L. and Saade, G. R. (2002), ‘Uterine electromyography and light-induced fluorescence in the management of term and preterm labor’, *J Soc Gynecol Investig* **9**(5), 265–275.

Garfield, R. E., Maul, H., Shi, L., Maner, W., Fittkow, C., Olsen, G. and Saade, G. R. (2001), ‘Methods and devices for the management of term and preterm labor’, *Ann N Y Acad Sci* **943**, 203–224.

Gaudette, R., Brooks, D., DiMarzio, C., Kilmer, M., Miller, E., Gaudette, T. and Boas, D. (2000), ‘A comparison study of linear reconstruction techniques for diffuse optical tomographic imaging of absorption coefficient’, *Phys. Med. Biol.* **45**, 1051–1070.

Gibson, A. and Dehghani, H. (2009), ‘Diffuse optical imaging’, *Philos Transact A Math Phys Eng Sci* **367**(1900), 3055–3072.

Gibson, A., Hebden, J. and Arridge, S. (2005), ‘Recent advances in diffuse optical imaging’, *Phys. Med. Biol.* **50**, R1–R43.

Goldenberg, R. L., Hauth, J. C. and Andrews, W. W. (2000), ‘Intrauterine infection and preterm delivery’, *N Engl J Med* **342**(20), 1500–1507.

Haarala, C., Aalto, S., Hautzel, H., Julkunen, L., Rinne, J. O., Laine, M., Krause, B. and Hamalainen, H. (2003), ‘Effects of a 902 MHz mobile phone on cerebral blood flow in humans: a PET study’, *Neuroreport* **14**(16), 2019–2023.

Haensse, D., Szabo, P., Brown, D., Fauchère, J.-C., Niederer, P., Bucher, H.-U. and Wolf, M. (2005), ‘A new multichannel near infrared spectrophotometry system for functional studies of the brain in adults and neonates’, *Opt Express* **13**(12), 4525–4538.

Hamaoka, T., McCully, K. K., Quaresima, V., Yamamoto, K. and Chance, B. (2007), ‘Near-infrared spectroscopy/imaging for monitoring muscle oxygenation and oxidative metabolism in healthy and diseased humans’, *J. Biomed. Opt.* **12**(6), 062105.

Haskell, R. C., Svaasand, L. O., Tsay, T. T., Feng, T. C., McAdams, M. S. and Tromberg, B. J. (1994), 'Boundary conditions for the diffusion equation in radiative transfer', *J Opt Soc Am A Opt Image Sci Vis* **11**(10), 2727–2741.

Hebden, J. C., Arridge, S. R. and Delpy, D. T. (1997), 'Optical imaging in medicine: I. Experimental techniques', *Phys Med Biol* **42**(5), 825–840.

Heekeren, H. R., Obrig, H., Wenzel, R., Eberle, K., Ruben, J., Villringer, K., Kurth, R. and Villringer, A. (1997), 'Cerebral haemoglobin oxygenation during sustained visual stimulation–a near-infrared spectroscopy study', *Philos Trans R Soc Lond B Biol Sci* **352**(1354), 743–750.

Hietanen, M., Kovala, T. and Hämäläinen, A. M. (2000), 'Human brain activity during exposure to radiofrequency fields emitted by cellular phones', *Scand J Work Environ Health* **26**(2), 87–92.

Hinrichs, H. and Heinze, H. (2006), 'High frequency GSM-1800 fields with various modulations and field strengths: No short term effect on human awake EEG', *Edition Science (Research Association for Radio Applications* **23**, 1–11.

Hock, C., Villringer, K., Muller-Spahn, F., Wenzel, R., Heekeren, H., Schuh-Hofer, S., Hofmann, M., Minoshima, S., Schwaiger, M., Dirnagl, U. and Villringer, A. (1997), 'Decrease in parietal cerebral hemoglobin oxygenation during performance of a verbal fluency task in patients with alzheimer's disease monitored by means of near-infrared spectroscopy (NIRS)–correlation with simultaneous rCBF-PET measurements', *Brain Res* **755**(2), 293–303.

Hornung, R., Pham, T. H., Keefe, K. A., Berns, M. W., Tadir, Y. and Tromberg, B. J. (1999), 'Quantitative near-infrared spectroscopy of cervical dysplasia in vivo', *Hum Reprod* **14**(11), 2908–2916.

Hoshi, Y. (2007), 'Functional near-infrared spectroscopy: current status and future prospects', *J. Biomed. Opt.* **12**(6), 062106.

Hoshi, Y., Kobayashi, N. and Tamura, M. (2001), 'Interpretation of near-infrared spectroscopy signals: a study with a newly developed perfused rat brain model', *J Appl Physiol* **90**(5), 1657–1662.

Hsieh, W. W. and Wu, A. (2002), 'Nonlinear singular spectrum analysis', *Proc. of the 2002 Int. Joint Conference on Neural Networks, IJCNN '02.* **3**, 2819–2824.

Huang, N. E., Shen, Z., Long, S. R., Wu, M. C., Shih, H. H., Zheng, Q., Yen, N.-C., Tung, C. C. and Liu, H. H. (1998), 'The empirical mode decomposition and the hilbert spectrum for nonlinear and non-stationary time series analysis', *Proc. R. Soc. Lond. A* **454**(1971), 903–995.

Huber, R., Graf, T., Cote, K. A., Wittmann, L., Gallmann, E., Matter, D., Schuderer, J., Kuster, N., Borbely, A. A. and Achermann, P. (2000), 'Exposure to pulsed high-frequency electromagnetic field during waking affects human sleep EEG', *Neuroreport* **11**(15), 3321–3325.

Huber, R., Schuderer, J., Graf, T., Jutz, K., Borbely, A. A., Kuster, N. and Achermann, P. (2003), 'Radio frequency electromagnetic field exposure in humans: Estimation of SAR distribution in the brain, effects on sleep and heart rate', *Bioelectromagnetics* **24**(4), 262–276.

Huber, R., Treyer, V., Borbely, A. A., Schuderer, J., Gottselig, J. M., Landolt, H. P., Werth, E., Berthold, T., Kuster, N., Buck, A. and Achermann, P. (2002), 'Electromagnetic fields, such as those from mobile phones, alter regional cerebral blood flow and sleep and waking EEG', *J Sleep Res* **11**(4), 289–295.

Huber, R., Treyer, V., Schuderer, J., Berthold, T., Buck, A., Kuster, N., Landolt, H. P. and Achermann, P. (2005), 'Exposure to pulse-modulated radio frequency electromagnetic fields affects regional cerebral blood flow', *Eur J Neurosci* **21**(4), 1000–1006.

Hueber, D. M., Franceschini, M. A., Ma, H. Y., Zhang, Q., Ballesteros, J. R., Fantini, S., Wallace, D., Ntziachristos, V. and Chance, B. (2001), 'Non-invasive and quantitative near-infrared haemoglobin spectrometry in the piglet brain during hypoxic stress, using a frequency-domain multidistance instrument', *Phys Med Biol* **46**(1), 41–62.

ICNIRP (1998), Guidelines for limiting exposure to time varying electric, magnetic and electromagnetic fields (to 300 GHz), Technical report.

ISS Documentation (n.d.), Specification, ISS-documentation: 96-0027 rev. 3, confidential, Technical report, ISS, Inc.

ISS Inc. (n.d.). Champaign, Illinois, USA, See http://www.iss.com/products/imagent/index.html for more information about the original version of the modified ISS instrument.

Izzetoglu, M., Devaraj, A., Bunce, S. and Onaral, B. (2005), 'Motion artifact cancellation in NIR spectroscopy using Wiener filtering', *IEEE Trans. Biomed. Eng.* **52**(5), 934–938.

Izzetoglu, M., Devaraj, A., Izzetoglu, M., Bunce, S. and Onaral, B. (2003), 'Motion artifact removal in fNIR signals using adaptive filtering', *Proc. of the 2003 BMES Annual Meeting of the Biomedical Engineering Society, Nashville, TN, USA* pp. 5333–5336.

Jang, K. E., Tak, S., Jung, J., Jang, J., Jeong, Y. and Ye, J. C. (2009), 'Wavelet minimum description length detrending for near-infrared spectroscopy', *J. Biomed. Opt.* **14**(3), 034004.

Jasper, H. (1958), 'Report of the committee on methods of clinical examination in electroencephalography', *Electroenceph. Clin. Neurophysiol.* **Vol. 10**, 370–375.

Jöbsis, F. F. (1977), 'Noninvasive, infrared monitoring of cerebral and myocardial oxygen sufficiency and circulatory parameters', *Science* **198**(4323), 1264–1267.

Kak, A. C. and Slaney, M. (2001), *Principles of Computerized Tomographic Imaging*, Society of Industrial and Applied Mathematics. http://www.slaney.org/pct/.

Karen, T., Morren, G., Haensse, D., Bauschatz, A. S., Bucher, H. U. and Wolf, M. (2008), 'Hemodynamic response to visual stimulation in newborn infants using functional near-infrared spectroscopy', *Hum. Brain Mapp.* **29**(4), 453–460.

Kienle, A., Patterson, M. S., Dögnitz, N., Bays, R., Wagnivres, G. and van den Bergh, H. (1998), 'Noninvasive determination of the optical properties of two-layered turbid media', *Appl Opt* **37**(4), 779–791.

Kleinlogel, H., Dierks, T., Koenig, T., Lehmann, H., Minder, A. and Berz, R. (2008), 'Effects of weak mobile phone - electromagnetic fields (GSM, UMTS) on event related potentials and cognitive functions.', *Bioelectromagnetics* **29**(6), 488–497.

Kleinschmidt, A., Obrig, H., Requardt, M., Merboldt, K. D., Dirnagl, U., Villringer, A. and Frahm, J. (1996), 'Simultaneous recording of cerebral blood oxygenation changes during human brain activation by magnetic resonance imaging and near-infrared spectroscopy', *J Cereb Blood Flow Metab* **16**(5), 817–826.

Kohno, S., Miyai, I., Seiyama, A., Oda, I., Ishikawa, A., Tsuneishi, S., Amita, T. and Shimizu, K. (2007), 'Removal of the skin blood flow artifact in functional near-infrared spectroscopic imaging data through independent component analysis', *J Biomed Opt* **12**(6), 062111.

Koivisto, M., Haarala, C., Krause, C. M., Revonsuo, A., Laine, M. and Hamalainen, H. (2001), 'GSM phone signal does not produce subjective symptoms', *Bioelectromagnetics* **22**(3), 212–215.

Kondepati, V. R., Heise, H. M. and Backhaus, J. (2008), 'Recent applications of near-infrared spectroscopy in cancer diagnosis and therapy', *Anal Bioanal Chem* **390**(1), 125–139.

Lakowicz, J. R. and Berndt, K. (1990), 'Frequency domain measurements of photon migration in tissues', *Chem. Phys. Lett.* **166**, 246–252.

Lancaster, D. (1996), *Active Filter Cookbook*, second edn, Newnes.

Leff, D. R., Warren, O. J., Enfield, L. C., Gibson, A., Athanasiou, T., Patten, D. K., Hebden, J., Yang, G. Z. and Darzi, A. (2008), 'Diffuse optical imaging of the healthy and diseased breast: a systematic review', *Breast Cancer Res Treat* **108**(1), 9–22.

Lehmann, H., Pollara, L., Spichtig, S., Kühn, S. and Wolf, M. (to be published), 'Head exposure system for a human provocation study to assess the possible influence of UMTS-like electromagnetic fields on cerebral blood circulation using near infrared imaging (NIRI)'.

Leitich, H. and Kaider, A. (2003), 'Fetal fibronectin – how useful is it in the prediction of preterm birth?', *BJOG* **110 Suppl 20**, 66–70.

Leppert, P. C. (1995), 'Anatomy and physiology of cervical ripening', *Clin Obstet Gynecol* **38**(2), 267–279.

Liebert, A., Wabnitz, H., Steinbrink, J., Obrig, H., Möller, M., Macdonald, R., Villringer, A. and Rinneberg, H. (2004), 'Time-resolved multidistance near-infrared spectroscopy of the adult head: intracerebral and extracerebral absorption changes from moments of distribution of times of flight of photons', *Appl Opt* **43**(15), 3037–3047.

Liu, S., He, Q., Gao, R. X. and Freedson, P. (2008), 'Empirical mode decomposition applied to tissue artifact removal from respiratory signal', *Conf. Proc. IEEE Eng. Med. Biol. Soc.* pp. 3624–3627.

Ludmir, J. and Sehdev, H. M. (2000), 'Anatomy and physiology of the uterine cervix', *Clin Obstet Gynecol* **43**(3), 433–439.

Martin, J. A., Hamilton, B. E., Sutton, P. D., Ventura, S. J., Menacker, F., Kirmeyer, S., Munson, M. L., for Disease Control, C. and for Health Statistics National Vital Statistics System, P. N. C. (2007), 'Births: final data for 2005', *Natl Vital Stat Rep* **56**(6), 1–103.

Matcher, S. J., Cope, M. and Delpy, D. T. (1994), 'Use of the water absorption spectrum to quantify tissue chromophore concentration changes in near-infrared spectroscopy', *Phys Med Biol* **39**(1), 177–196.

Matcher, S. J., Elwell, C. E., Cooper, C. E., Cope, M. and Delpy, D. T. (1995), 'Performance comparison of several published tissue near-infrared spectroscopy algorithms', *Anal Biochem* **227**(1), 54–68.

Matcher, S., Kirkpatrick, P., Nahid, K., Dope, M. and Delpy, D. T. (1995), 'Absolute quantification methods in tissue near-infrared spectroscopy', *SPIE Vol. 2389* pp. 486–495.

Matzinger, B., Wolf, M., Baños, A., Fink, D. and Hornung, R. (2009), 'Optical properties, physiologic parameters and tissue composition of the human uterine cervix as a function of hormonal status', *Lasers Med Sci* **24**(4), 561–566.

Maul, H., Olson, G., Fittkow, C. T., Saade, G. R. and Garfield, R. E. (2003), 'Cervical light-induced fluorescence in humans decreases throughout gestation and before delivery: preliminary observations', *Am J Obstet Gynecol* **188**(2), 537–541.

Maul, H., Saade, G. and Garfield, R. E. (2005), 'Prediction of term and preterm parturition and treatment monitoring by measurement of cervical cross-linked collagen using light-induced fluorescence', *Acta Obstet Gynecol Scand* **84**(6), 534–536.

Mazza, E., Nava, A., Bauer, M., Winter, R., Bajka, M. and Holzapfel, G. A. (2006), 'Mechanical properties of the human uterine cervix: an in vivo study', *Med Image Anal* **10**(2), 125–136.

Mbonjo, H. N. M., Streckert, J., Bitz, A., Hansen, V., Glasmachers, A., Gencol, S., Rozic, D. and for Radio Waves, G. R. F. (2004), 'Generic UMTS test signal for RF bioelectromagnetic studies', *Bioelectromagnetics* **25**(6), 415–425.

Meerstetter, M. and Jacoma, M. (2004), Frequency-domain near-infrared spectroscopy: Developement of a multi-frequency instrument, Master's thesis, ETH Zurich.

Mizuno, Y., Moriguchi, Y., Hikage, T., Terao, Y., Ohnishi, T., Nojima, T. and Ugawa, Y. (2009), 'Effects of W-CDMA 1950 MHz EMF emitted by mobile phones on regional cerebral blood flow in humans', *Bioelectromagnetics* **30**(7), 536–544.

Mourant, J. R., Fuselier, T., Boyer, J., Johnson, T. M. and Bigio, I. J. (1997), 'Predictions and measurements of scattering and absorption over broad wavelength ranges in tissue phantoms', *Appl Opt* **36**(4), 949–957.

Muehlemann, T., Haensse, D. and Wolf, M. (2008), 'Wireless miniaturized in-vivo near infrared imaging', *Opt. Express* **16**(14), 10323–10330.

Müller, T., Timmer, J., Reinhard, M., Oehm and Hetzel, A. (2003), 'Detection of very low-frequency oscillations of cerebral haemodynamics is influenced by data detrending', *Med. Biol. Eng. Comput.* **41**(1), 69–74.

Myers, K. M., Paskaleva, A. P., House, M. and Socrate, S. (2008), 'Mechanical and biochemical properties of human cervical tissue', *Acta Biomater* **4**(1), 104–116.

Myers, K., Socrate, S., Tzeranis, D. and House, M. (2009), 'Changes in the biochemical constituents and morphologic appearance of the human cervical stroma during pregnancy', *Eur J Obstet Gynecol Reprod Biol* **144 Suppl 1**, S82–S89.

Nozawa, T. and Kondo, T. (2009), A comparison of artifact reduction methods for real-time analysis of fNIRS data, Vol. 5618 of *Lecture Notes in Computer Science*, Springer, pp. 413–422.

Obrig, H., Hirth, C., Junge-Hülsing, J. G., Döge, C., Wolf, T., Dirnagl, U. and Villringer, A. (1996), 'Cerebral oxygenation changes in response to motor stimulation', *J Appl Physiol* **81**(3), 1174–1183.

Obrig, H., Neufang, M., Wenzel, R., Kohl, M., Steinbrink, J., Einhäupl, K. and Villringer, A. (2000), 'Spontaneous low frequency oscillations of cerebral hemodynamics and metabolism in human adults', *NeuroImage* **12**(6), 623–639.

Okada, E., Firbank, M., Schweiger, M., Arridge, S. R., Cope, M. and Delpy, D. T. (1997), 'Theoretical and experimental investigation of near-infrared light propagation in a model of the adult head', *Appl Opt* **36**(1), 21–31.

O'Leary, M. A. (1996), 'Imaging with diffuse photon density waves', PhD thesis, University of Pennsylvania. http://www.lrsm.upenn.edu/pmi/theses/oleary/oleary-diss.htm.

Oregon Medical Laser Center (n.d.). See http://omlc.ogi.edu/spectra/.

Patterson, M., Pogue, B. and Wilson, B. (1993), *SPIE Opt. Eng. Press, Medical Optical Tomography: Functional Imaging and Monitoring* **Volume IS11**. Part 4. In: G. Müller BC, R. Alfano, S. Arridge, J. Beuthan, E. Gratton, M. Kaschke, B. Masters, S. Svanberg, P. van der Zee, R.F. Potter.

Pham, T., Coquoz, O., Fishkin, J., Anderson, E. and Tromberg, B. (2000), 'Broad bandwidth frequency domain instrument for quantitative tissue optical spectroscopy', *Rev Sci Instrum* **71**(6), 2500–2513.

Pham, T., Spott, T., Svaasand, L. and Tromberg, B. (2000), 'Quantifying the properties of two-layer turbid media with frequency-domain diffuse reflectance', *Applied Optics* **39**(25), 4733.

R Developement Core Team (2009), 'R: A language and environment for statistical computing'.

Åkerstedt, T. and Gillberg, M. (1990), 'Subjective and objective sleepiness in the active individual', *Int J Neurosci* **52**(1-2), 29–37.

Regel, S. J., Gottselig, J. M., Schuderer, J., Tinguely, G., Retey, J. V., Kuster, N., Landolt, H. P. and Achermann, P. (2007), 'Pulsed radio frequency radiation affects cognitive performance and the waking electroencephalogram', *Neuroreport* **18**(8), 803–807.

Regel, S. J., Tinguely, G., Schuderer, J., Adam, M., Kuster, N., Landolt, H. P. and Achermann, P. (2007), 'Pulsed radio-frequency electromagnetic fields: dose-dependent effects on sleep, the sleep EEG and cognitive performance', *J Sleep Res* **16**(3), 253–258.

Rorden, C. (n.d.), 'MRIcro, see http://www.mricro.com'.

Röschke, J. and Mann, K. (1997), 'No short-term effects of digital mobile radio telephone on the awake human electroencephalogram', *Bioelectromagnetics* **18**(2), 172–176.

Röösli, M., Moser, M., Baldinini, Y., Meier, M. and Braun-Fahrlander, C. (2004), 'Symptoms of ill health ascribed to electromagnetic field exposure – a questionnaire survey', *Int J Hyg Environ Health* **207**(2), 141–150.

Rubin, G. J., Hahn, G., Everitt, B. S., Cleare, A. J. and Wessely, S. (2006), 'Are some people sensitive to mobile phone signals? Within participants double blind randomised provocation study', *BMJ* **332**(7546), 886–891.

Saager, R. B. and Berger, A. J. (2005), 'Direct characterization and removal of interfering absorption trends in two-layer turbid media', *J Opt Soc Am A Opt Image Sci Vis* **22**(9), 1874–1882.

Sassaroli, A. and Fantini, S. (2004), 'Comment on the modified Beer-Lambert law for scattering media', *Phys. Med. Biol.* **49**(14), N255–N257.

Sato, H., Kiguchi, M., Kawaguchi, F. and Maki, A. (2004), 'Practicality of wavelength selection to improve signal-to-noise ratio in near-infrared spectroscopy.', *Neuroimage* **21**(4), 1554–1562.

Schecklmann, M., Ehlis, A.-C., Plichta, M. M. and Fallgatter, A. J. (2008), 'Functional near-infrared spectroscopy: a long-term reliable tool for measuring brain activity during verbal fluency', *Neuroimage* **43**(1), 147–155.

Schlembach, D., Mackay, L., Shi, L., Maner, W. L., Garfield, R. E. and Maul, H. (2009), 'Cervical ripening and insufficiency: from biochemical and molecular studies to in vivo clinical examination', *Eur J Obstet Gynecol Reprod Biol* **144 Suppl 1**, S70–S76.

Scholkmann, F., Spichtig, S. and Wolf, M. (2010), 'How to detect and reduce movement artifacts in near-infrared imaging using moving standard deviation and spline interpolation', *Physiol. Meas.* **31**, 649–662.

Schweiger, M. and Arridge, S. R. (1999), 'Optical tomographic reconstruction in a complex head model using a priori region boundary information', *Phys Med Biol* **44**(11), 2703–2721.

Simhan, H. N. (2005), 'Serum biomarkers of spontaneous preterm birth', *Acta Obstet Gynecol Scand* **84**(6), 545–546.

Spichtig, S. (2006), Frequency-Domain Nahinfrarot Spektrophotometrie – Messung der Cytochrome Oxidase im Gewebe mit Licht, Master's thesis, ETH Zurich.

Spichtig, S. (2010), Multi-distance and multi-frequency frequency-domain near-infrared spectroscopy: Characterization and Application. PhD thesis No 19006, PhD thesis, Swiss Federal Institute of Technology Zurich.

Spichtig, S., Hornung, R., Brown, D. W., Haensse, D. and Wolf, M. (2009), 'Multifrequency frequency-domain spectrometer for tissue analysis', *Rev Sci Instrum* **80**(2), 024301.

Stahel, M. C., Wolf, M., Baños, A. and Hornung, R. (2009), 'Optical properties of the breast during spontaneous and birth control pill-mediated menstrual cycles', *Lasers Med Sci* **24**(6), 901–907.

Strangman, G., Culver, J. P., Thompson, J. H. and Boas, D. A. (2002), 'A quantitative comparison of simultaneous BOLD fMRI and NIRS recordings during functional brain activation', *Neuroimage* **17**(2), 719–731.

Tahvanainen, K., Nino, J., Halonen, P., Kuusela, T., Laitinen, T., Lansimies, E., Hartikainen, J., Hietanen, M. and Lindholm, H. (2004), 'Cellular phone use does not acutely affect blood pressure or heart rate of humans', *Bioelectromagnetics* **25**(2), 73–83.

Tekesin, I., Wallwiener, D. and Schmidt, S. (2005), 'The value of quantitative ultrasound tissue characterization of the cervix and rapid fetal fibronectin in predicting preterm delivery', *J Perinat Med* **33**(5), 383–391.

Toronov, V., Webb, A., Choi, J. H., Wolf, M., Michalos, A., Gratton, E. and Hueber, D. (2001), 'Investigation of human brain hemodynamics by simultaneous near-infrared spectroscopy and functional magnetic resonance imaging', *Med Phys* **28**(4), 521–527.

Tromberg, B., Coquoz, O., Fishkin, J. B., Anderson, E., Pham, D., Brenner, M. and Svaasand, L. O. (1996), Frequency-domain photon migration (FDPM) measurements of normal and malignant cell and tissue optical properties, *in* 'Biomedical Optical Spectroscopy and Diagnostics (BOSD)'.

Tuchin, V. (2000), *Tissue Optics, Light-scattering methods and instruments for medical diagnosis*, first edn, SPIE.

UCL, Departement of Medical Physics and Bioengineering (n.d.). see http://www.medphys.ucl.ac.uk/research/borl/research/NIR_topics/spectra/spectra.htm.

Uludag, K., Kohl, M., Steinbrink, J., Obrig, H. and Villringer, A. (2002), 'Cross talk in the lambert-beer calculation for near-infrared wavelengths estimated by monte carlo simulations', *J Biomed Opt* **7**(1), 51–59.

Valentini, E., Curcio, G., Moroni, F., Ferrara, M., De Gennaro, L. and Bertini, M. (2007), 'Neurophysiological effects of mobile phone electromagnetic fields on humans: a comprehensive review', *Bioelectromagnetics* **28**(6), 415–432.

van Staveren, H., Moes, C., Van Marle, J., Prahl, S. and Vangemert, M. (1991), 'Light-scattering in intralipid-10% in the wavelength range of 400–1100 nm', *Applied Optics* **30**(31), 4507–4514.

Vardi, M. and Nini, A. (2008), 'Near-infrared spectroscopy for evaluation of peripheral vascular disease. a systematic review of literature', *Eur J Vasc Endovasc Surg* **35**(1), 68–74.

Vecchia, P., Matthes, R., Ziegelberger, G., Lin, J., Saunders, R. and Swerdlow, A. (2009), Exposure to high frequency electromagnetic fields, biological effects and health consequences (100 kHz – 300 GHz), review of the scientific evidence on dosimetry, biological effects, epidemiological observations, and health consequences concerning exposure to high frequency electromagnetic fields (100 kHz to 300 GHz), Report 978-3-934994-10-2.

Villringer, K., Minoshima, S., Hock, C., Obrig, H., Ziegler, S., Dirnagl, U., Schwaiger, M. and Villringer, A. (1997), 'Assessment of local brain activation. a simultaneous PET and near-infrared spectroscopy study', *Adv Exp Med Biol* **413**, 149–153.

Vogel, I., Thorsen, P., Curry, A., Sandager, P. and Uldbjerg, N. (2005), 'Biomarkers for the prediction of preterm delivery', *Acta Obstet Gynecol Scand* **84**(6), 516–525.

Volumenie, J.-L., Luton, D., Spirlet, M. D., Sibony, O., Blot, P. and Oury, J.-F. (2004), 'Ultrasonographic cervical length measurement is not a better predictor of preterm delivery than digital examination in a population of patients with idiopathic preterm labor', *Eur J Obstet Gynecol Reprod Biol* **117**(1), 33–37.

Ward, K. R., Ivatury, R. R., Barbee, R. W., Terner, J., Pittman, R., Filho, I. P. and Spiess, B. (2006), 'Near infrared spectroscopy for evaluation of the trauma patient: a technology review', *Resuscitation* **68**(1), 27–44.

Wilcox, T., Bortfeld, H., Woods, R., Wruck, E. and Boas, D. A. (2005), 'Using near-infrared spectroscopy to assess neural activation during object processing in infants', *J Biomed Opt* **10**(1), 011010.

Wolf, M., Ferrari, M. and Quaresima, V. (2007), 'Progress of near-infrared spectroscopy and topography for brain and muscle clinical applications', *J Biomed Opt* **12**(6), 062104.

Wolf, M. and Greisen, G. (2009), 'Advances in near-infrared spectroscopy to study the brain of the preterm and term neonate', *Clin Perinatol* **36**(4), 807–834.

Wolf, M., Haensse, D., Morren, G. and Froehlich, J. (2006), 'Do GSM 900 MHz signals affect cerebral blood circulation? A near-infrared spectrophotometry study', *Opt Express* **14**(13), 6128–41.

Wolf, M., Morren, G., Haensse, D., Karen, T., Wolf, U., Fauchére, J. and Bucher, H. (2008), 'Near infrared spectroscopy to study the brain: an overview', *Opto-Electronics Review* **16**(4), 413–419.

Wolf, M., Wolf, U., Toronov, V., Michalos, A., Paunescu, L. A., Choi, J. H. and Gratton, E. (2002), 'Different time evolution of oxyhemoglobin and deoxyhemoglobin concentration changes in the visual and motor cortices during functional stimulation: a near-infrared spectroscopy study', *Neuroimage* **16**(3 Pt 1), 704–712.

Wray, S., Cope, M., Delpy, D. T., Wyatt, J. S. and Reynolds, E. O. (1988), 'Characterization of the near infrared absorption spectra of cytochrome aa3 and haemoglobin for the non-invasive monitoring of cerebral oxygenation', *Biochim Biophys Acta* **933**(1), 184–192.

Xu, Y., Graber, H. and Barbour, R. (2007), 'Image correction algorithm for functional three-dimensional diffuse optical tomography brain imaging', *Applied Optics* **46**(10), 1693–1704.

Xu, Y., Pei, Y., Graber, H. L. and Barbour, R. L. (2005), 'Image quality improvement via spatial deconvolution in optical tomography: time-series imaging', *J Biomed Opt* **10**(5), 051701.

Yamamoto, T., Maki, A., Kadoya, T., Tanikawa, Y., Yamad, Y., Okada, E. and Koizumi, H. (2002), 'Arranging optical fibres for the spatial resolution improvement of topographical images', *Phys Med Biol* **47**(18), 3429–3440.

Yokoyama, S., Okamoto, A., Araki, T. and Suzuki, N. (1995), 'Examination to eliminate undesirable phase delay of an avalanche photodiode (APD) for intensity-modulated light', *Rev Sci Instrum* **66**(11), 5331–5336.

Zaramella, P., Freato, F., Amigoni, A., Salvadori, S., Marangoni, P., Suppjei, A., Schiavo, B. and Chiandetti, L. (2001), ‘Brain auditory activation measured by near-infrared spectroscopy (NIRS) in neonates’, *Pediatr. Res.* **49**(2), 213–219.

Zeff, B. W., White, B. R., Dehghani, H., Schlaggar, B. L. and Culver, J. P. (2007), ‘Retinotopic mapping of adult human visual cortex with high-density diffuse optical tomography’, *Proc Natl Acad Sci U S A* **104**(29), 12169–12174.

Zhang, Q., Brown, E. N. and Strangman, G. E. (2007*a*), ‘Adaptive filtering for global interference cancellation and real-time recovery of evoked brain activity: a Monte Carlo simulation study’, *J. Biomed. Opt.* **12**(4), 044014.

Zhang, Q., Brown, E. N. and Strangman, G. E. (2007*b*), ‘Adaptive filtering to reduce global interference in evoked brain activity detection: a human subject case study’, *J Biomed Opt.* **12**(6), 064009.

Zhang, Q., Strangman, G. E. and Ganis, G. (2009), ‘Adaptive filtering to reduce global interference in non-invasive NIRS measures of brain activation: how well and when does it work?’, *NeuroImage* **45**(3), 788–794.

Zhang, X., Toronov, V. and Webb, A. (2005), ‘Simultaneous integrated diffuse optical tomography and functional magnetic resonance imaging of the human brain’, *Opt Express* **13**(14), 5513–5521.

Zhao, H., Tanikawa, Y., Gao, F., Onodera, Y., Sassaroli, A., Tanaka, K. and Yamada, Y. (2002), ‘Maps of optical differential pathlength factor of human adult forehead, somatosensory motor and occipital regions at multi-wavelengths in NIR’, *Phys Med Biol* **47**(12), 2075–2093.

Zhao, M., Song, B., Pu, J., Wada, T., Reid, B., Tai, G., Wang, F., Guo, A., Walczysko, P., Gu, Y., Sasaki, T., Suzuki, A., Forrester, J. V., Bourne, H. R., Devreotes, P. N., McCaig, C. D. and Penninger, J. M. (2006), ‘Electrical signals control wound healing through phosphatidylinositol-3-oh kinase-gamma and PTEN’, *Nature* **442**(7101), 457–60.

Zwamborn, A., Vossen, S., Van Leersum, B., Ouvens, M. and Maekel, W. (2003), Effects of global communication system radio-frequency fields on well being and cognitive functions of human subjects with and without subjective complaints, Technical report.

List of publications

Spichtig S, Hornung R, Brown DW, Haensse D and Wolf M, (2009), ’Multifrequency frequency-domain spectrometer for tissue analysis’, *Rev Sci Instrum.* **80**(2), 024301

Spichtig S, Scholkmann F, Chin L, Lehmann H and Wolf M, (2010) ’Assessment of the short and medium-term effects of intermittent UMTS electromagnetic fields on blood circulation, using near-infrared imaging’, submitted to *Bioelectromagnetics*

Spichtig S, Piccirelli M, Vorburger R, and Wolf M, (2010) ’Simultaneous NIRI and MRI measurements - a novel optical sensor with improved handling and direct localization in the MRI’, in preparation

Spichtig S, Scholkmann F, Chin L, Lehmann H and Wolf M, (2010) ’Assessment of potential short-term effects of intermittent UMTS electromagnetic fields on blood circulation in an exploratory study, using near-infrared imaging’, submitted for the *conference proceedings of the international society on oxygen transport to tissue 2010*

Hornung R, Spichtig S, Banos A, Stahel M, Zimmermann R, and Wolf M, (2010) ’Frequency domain near-infrared spectroscopy of the uterine cervix during regular pregnacies’, submitted to *Lasers Med Sci*

Scholkmann F, Spichtig S, Muehlemann T and Wolf M, (2010) ’How to detect and reduce movement artifacts in near-infrared imaging using moving standard deviation and spline interpolation’, *Phys. Meas.* 31, 649-662

Rothmaier M, Selm B, Spichtig S, Haensse D and Wolf M, (2008) ’Photonic textiles for pulse oximetry’, *Opt Express* **16**(17), 12973-86.

Lehmann H, Pollara L, Spichtig S, Kühn S, Wolf M, (2010) ’Head exposure system for a human provocation study to assess the possible influence of UMTS-like electromagnetic fields on cerebral blood circulation using near infrared imaging’, submitted to *Bioelectromagnetics*

Scholkmann F, Trajkovic I, Spichtig S and Wolf M, ’Using ensembled empirical mode decomposition to extract evoked hemodynamic responses from functional near-infrared neuroimaging data’, in preparation

Danksagung

An dieser Stelle möchte ich mich bei allen Personen bedanken, die zum Gelingen dieser Arbeit beigetragen haben. Mein Dank gilt insbesondere:

- Prof. Markus Rudin, für die Betreuung meiner Doktorarbeit, das motivierende wissenschaftliche Ambiente an den Progress Reports und die wertvollen Inputs.
- Prof. Hans-Ulrich Bucher, für die Bereitstellung der Infrastruktur und die Ermöglichung der Doktorarbeit.
- PD Martin Wolf, für das entgegengebrachte Vertrauen, die Ermöglichung und Betreuung der Doktorarbeit.
- Prof. Peter Achermann, für die wertvollen Inputs zur Studiendurchführung und das Korreferat.
- Dr. Hugo Lehmann, für die freundschaftliche und professionelle Kollaboration.
- Dennis Hueber von ISS Inc., für die fachkundige Beantwortung meiner Fragen zu Hard- und Software der ISS Instrumente und zur Herstellung von optischen Sensoren.
- Thomas, für die unzähligen Arbeitsstunden eingesetzt für das Wohl des Forschungsteams, die unglaubliche Geduld bei der Beantwortung von Fragen und seine moralische Unterstützung.
- Felix, für die Einweihung in immer neue Ansätze der Signalverarbeitung, die unschlagbare Zeit in Davos und die Unterstützung bei den UMTS Messungen.
- Martin Biallas für seine Hilfsbereitschaft und die sportliche Kameradschaft auf dem Wasser und in hohen Lüften.
- Ivo, für das Erhalten vom seelischen Gleichgewicht dank regelmässigen gemeinsamen Joggingrunden.
- Sandro, für die unterhaltsamen Gespräche über Diffusionstheorie und die Welt und seinen Einsatz im Rahmen seines Zivildienstes.
- Juan, fürs Gegenlesen einiger Teile der vorliegenden Doktorarbeit.
- Marco Piccirelli, für den Einsatz am MR Scanner und seine unkomplizierte und aufstellende Art.

- Laboratory for Social and Neural Systems Research (SNS Lab), für das Benutzen vom MR-Scanner und der Küchen-Infrastruktur.
- Samuel Godina, Marcel Meerstetter und Martial Jacoma für die Modifizierungen am Multi-Frequenz FD-NIRS Gerät.
- Daniel Haensse, für die Einführung in die grosse unbekannte Welt der Elektronik.
- Jürg Fröhlich, für anregende Gespräche und kritisches Gegenlesen der vorliegenden Doktorarbeit.
- Thomas Schröter, für die Bereitstellung der Serverinfrastruktur, welche das Arbeiten von zuhause sehr erleichterte.
- Massimo Merlini, für die geduldigen Erklärungen zum Thema Linear Mixed-Effects Models und die Unterstützung bei der statistischen Auswertung der UMTS-Studie.
- Andreas Metz, für seine Unbeschwertheit und seinen beispielslosen Einsatz als Proband.
- René Hornung, für die Zusammenarbeit im Rahmen der Cervix-Studie.
- Ana Banos, fürs Durchführen der Messungen der Cervix-Studie.
- Sandra und Barbara, die für eine freundschafliche Büroatmospäre sorgten.
- Cornelia, für die spannenden Gespräche über klinische MRI, EEG und Ultraschall Diagnostik und die Englischkorrekturen.
- meinem Partner Nico, für den Glauben an mich in guten und schweren Zeiten der Doktorarbeit.
- meinen Eltern, welche meinen für sie ungewöhnlichen Werdegang jederzeit voll unterstützten.
- meiner Schwester, für die aufmunternden unterstützenden Worte und den Glücksbringer.
- Claudia, die es immer schafft mich mit ihrer unbeschwerten und lebensfrohen Art zum Lachen zu bringen.
- allen Probanden und Probandinnen, die an der UMTS Expositions- oder Cervix-Studie teilgenommen haben.
- sowie allen weiteren momentanen oder ehemaligen Mitarbeitern: Dorli, Iris, Anita, Jean-Claude, Brigitte, Mark, Andreas, Damien, Lukas, Robert, Lydia, Bernhard, Carmen, Omar, Manuel, Geert, Ruben, Christian, Rafael, Stephan, Oliver, Thomas, Beat
- dem ganzen NEO-Team für die Gastfreundschaft auf der Station und in der NEO-Küche.

Curriculum Vitae

I was born as the daughter of Alfred and Klara Spichtig on 1^{st} of October in Sarnen, Switzerland. I grew up in Giswil, where I also attended elementary school. In Summer 2001, I graduated from the 'Kantonsschule Obwalden' (high school), Sarnen.

A few months later, I started studying intermediate nature science at the Swiss Federal Institute of Technology (ETH) in Zurich. During my studies, I specialized in the topics of physical chemistry and optics. In summer 2004, I had the opportunity to work as an au pair in the USA and to perform simultaneously a semester thesis at the college of Charleston (South Carolina) entitled '*Conformational Analysis, vibrational assignment, theoretical infrared and Raman spectra, ab initio molecular orbital energy and comparison study of allylgermane and its chloro- and fluoroderivatives*'. During my diploma thesis I worked on '*Frequency Domain Nahinfrarot Spektrophotometrie, Messung der Cytochrome Oxidase im Gewebe mit Licht*' in the biomedical optics research laboratory (BORL) headed by PD Martin Wolf. I graduated in September 2006 at ETH Zurich receiving a diploma (Masters) in Natural Science.

In January 2007, I started my PhD at BORL under the supervision of Prof. Markus Rudin and PD Martin Wolf. My work was focused on adjusting and applying frequency-domain near-infrared spectroscopy instruments within two main studies: firstly, assessing potential effects of UMTS-EMF on blood circulation in the human head and secondly, monitoring structural and compositional changes of the human cervix in regular pregnancies.